

*In Situ* Resonance Raman Studies  
of Molybdenum Oxide Based  
Selective Oxidation Catalysts

von Martin Dieterle

Vom Fachbereich Chemie  
der Technischen Universität Berlin  
zur Erlangung des akademischen Grades

Doktor der Naturwissenschaften

Dr. rer. nat.

genehmigte Dissertation

Tag der mündlichen Prüfung: 20.03.2001

Promotionsausschuß:

Vorsitzender: Prof. Dr. rer. nat. Martin Lerch

Berichter: Prof. Dr. rer. nat. Reinhard Schomäcker

Prof. Dr. rer. nat. Robert Schlögl

Berlin, März 2001

D83

## Abstract

The preparation (aqueous chemistry and the thermal activation of polyoxometalates) and the structures of promoted molybdenum oxide catalysts are investigated under the condition of selective propene oxidation by *in situ* Raman spectroscopy. The influences of V and/or W-promoters on the structures of mixed MoVW oxides and their catalytic properties are investigated by XRD, TEM, SEM, *in situ* Raman spectroscopy and TPRS. V addition causes high propene conversions and the formation of an oxide with  $\text{Mo}_5\text{O}_{14}$  structure is observed. Minor amounts of W in the molybdenum oxides matrix inhibit structural reorganisation processes which is explained by preferred octahedral coordination of the redox stable W. The combined XRD, TEM and Raman spectroscopic identification of the oxide of  $\text{Mo}_5\text{O}_{14}$  structure points to its relevant role for the selective propene oxidation.

A resonance Raman effect is proven to be operative in oxygen defective molybdenum oxides. For an excitation wavelength of 632 nm (1.96 eV), the observed Raman cross section varies as a function of the degree of reduction of five different  $\text{MoO}_{3-x}$  samples. A model of the electronic transitions in  $\text{MoO}_{3-x}$  based on crystal field theory explains the electronic transitions observed by DR-UV/VIS spectroscopy. The observed resonant Raman scattering is coupled to the IVCT transition at about 2 eV arising from oxygen vacancies present in the materials. Due to the local nature of the absorption process, the developed model is valid for intermediate oxides too. Resonant Raman scattering was proven for  $\text{Mo}_4\text{O}_{11}$  and  $\text{MoO}_2$  too.

Hence, the experimentally observed Raman intensity bears information about the degree of reduction of the molybdenum oxide. *In situ* Raman spectroscopy of  $\text{MoO}_{3-x}$  catalysts during propene partial oxidation indicates that the propene conversions and the selectivities are a function of the degree of reduction of the catalyst.

It is attempted to control the spatial elemental distribution within the polyoxometalate catalyst precursor by the formation of molecularly defined species in solution by addition of acetate, oxalate or tartrate. Due to the low stability of the acetate complexes, the addition of acetate only leads to minor amounts of monomeric species beside mixed and pure polyoxometalates. The formation of stable monomeric oxometalate oxalate and tartrate complexes is observed, which are expected to lead to the formation of a catalyst precursor with a homogeneous elemental distribution.

Diese Arbeit entstand in der Zeit von September 1997 bis Januar 2001 am Fritz-Haber-Institut der Max Planck Gesellschaft in Berlin in der Abteilung von Prof. Dr. Schlögl und der Arbeitsgruppe von Dr. Mestl. Beiden möchte ich an dieser Stelle für ihr Interesse sowie das Vertrauen in meine Arbeit danken. Herrn Prof. Dr. Schomäcker gilt mein Dank für die Übernahme des Referats.

Danken möchte ich auch allen Kollegen der Abteilung AC. Besonders Bettina.

Finanziell wurde meine Arbeit vom Bundesministerium für Bildung, Wissenschaft, Forschung und Technologie im Rahmen des BMBF-Verbundvorhabens " Heterogene Partialoxidation von ungesättigten Aldehyden: Einfluß von Katalysator- und Eduktstruktur" dankenswerter Weise unterstützt. Dank auch an die Kooperationspartner: der BASF AG sowie den Arbeitskreisen von Prof. Vogel und Prof. Gaube an der TU Darmstadt.

Besonders danken möchte ich meinen Eltern.

*FÜR MEINE ELTERN*

# Contents

<b>Introduction</b>	<b>1</b>
<b>1 Resonance Raman Spectroscopy of molybdenum oxides</b>	<b>6</b>
1.1 Structural Characterisation of Oxygen Defects in $\text{MoO}_{3-x}$	6
1.1.1 Introduction	6
1.1.1.1 Theory of Raman Scattering	10
1.1.2 Experimental	14
1.1.3 Results and Discussion	16
1.1.3.1 SEM and XRD	16
1.1.3.2 UV/VIS Spectroscopy	18
1.1.3.3 Raman Micro-Spectroscopy	24
1.1.4 Conclusions	30
1.2 Resonance Raman Spectroscopic Characterisation $\text{Mo}_4\text{O}_{11}$ and $\text{MoO}_2$	31
1.2.1 Introduction	31
1.2.2 Experimental	35
1.2.3 Results and Discussion	35
1.2.3.1 XRD	35
1.2.3.2 Raman Microscopy	36
1.2.3.3 UV/VIS Spectroscopy	39
1.2.4 Discussion of the Resonance Raman Effect	41
1.2.5 Conclusions	42
1.3 Summary	42

<b>2</b>	<b>Catalytic and Physico-Chemical Characterisation of a Molybdenum Oxide Based Partial Oxidation Catalyst</b>	<b>44</b>
2.1	Thermally Induced Oxygen Deficiency, Elemental and Structural Heterogeneity and the Relation to Catalytic Performance . . . . .	45
2.1.1	Introduction . . . . .	45
2.1.2	Experimental . . . . .	48
2.1.3	Results and Discussion . . . . .	50
2.1.3.1	Thermal Activation of the Untreated Mixed Oxide . . . . .	50
2.1.3.2	Temperature Programmed Reaction Spectroscopy (TPRS) . . . . .	50
2.1.3.3	Physicochemical Characterisation . . . . .	52
2.1.3.4	SEM/EDX Analysis . . . . .	52
2.1.3.5	X-ray diffraction of the MoVW Mixed Oxide . . . . .	54
2.1.3.6	Confocal Raman Microspectroscopy . . . . .	56
2.1.4	Conclusions . . . . .	58
2.2	Combined X-Ray Diffraction, Electron Microscopy and Raman Investigation of the Phase Stability of Oxides of $\text{Mo}_5\text{O}_{14}$ Structure. . . . .	62
2.2.1	Introduction . . . . .	62
2.2.2	Experimental . . . . .	63
2.2.3	Results and Discussion . . . . .	65
2.2.3.1	XRD . . . . .	65
2.2.3.2	HRTEM . . . . .	67
2.2.3.3	Raman Spectroscopy . . . . .	73
2.2.4	Summary and Conclusion . . . . .	77
2.3	Summary . . . . .	79
<b>3</b>	<b>Thermal Activation of Molybdenum Polyoxometalates</b>	<b>82</b>
3.1	<i>In situ</i> Characterisation of the Thermal Activation of Ammonium Heptamolybdate by TG/DTA, XRD and Raman Spectroscopy . . . . .	82
3.1.1	Introduction . . . . .	82
3.1.2	Experimental . . . . .	83
3.1.3	Results and Discussion . . . . .	84

3.1.3.1	Thermal Analysis . . . . .	84
3.1.3.2	XRD . . . . .	87
3.1.3.3	Raman spectroscopy . . . . .	89
3.1.4	Summary . . . . .	93
3.2	Thermal Activation of V and W Promoted Mo-Oxide Based Catalysts . . . . .	93
3.2.1	Introduction . . . . .	93
3.2.2	Experimental . . . . .	95
3.2.2	Results and Discussion . . . . .	95
3.2.2.1	TG/DTA-MS . . . . .	95
3.2.2.2	XRD . . . . .	95
3.2.2.3	<i>in situ</i> Raman Spectroscopy . . . . .	100
3.3	Conclusions . . . . .	103
<b>4</b>	<b><i>In situ</i> Raman investigations on molybdenum oxide based catalysts</b>	<b>104</b>
4.1	<i>In situ</i> Raman Studies on the Reduction of MoO <sub>3</sub> . . . . .	107
4.1.1	Introduction . . . . .	107
4.1.2	Experimental . . . . .	107
4.1.3	Results and Discussion . . . . .	108
4.1.4	Conclusions . . . . .	110
4.2	<i>In situ</i> Raman Spectroscopy Studies Combined with Temperature Programmed Reaction Spectroscopy (TPRS) of V and W Promoted Molybdenum Oxide Catalysts . . . . .	111
4.2.1	Experimental . . . . .	114
4.2.2	Results and Discussion . . . . .	116
4.2.2.1	Pure Molybdenum Catalyst . . . . .	116
4.2.2.2	W-promoted Mo-Oxide Catalyst (Mo9W1) . . . . .	122
4.2.2.3	<i>in situ</i> Raman Spectroscopy Results . . . . .	123
4.2.2.4	V-promoted Mo-Oxide Catalyst (Mo9V1) . . . . .	125
4.2.2.5	V,W-promoted Mo-Oxide Catalyst (Mo8V1W1) . . . . .	129
4.2.2.6	V,W-promoted Mo-Oxide Catalyst (Mo6V3W1) . . . . .	132

4.2.2.7	Comparison of the Catalytic Performances of the V-Promoted Catalysts and <i>in situ</i> Raman Results . . . . .	134
4.2.3	Summary . . . . .	138
4.2.3.1	The role of the V and W promoters . . . . .	138
4.2.3.2	Model for the Propene Oxidation over MoVW Oxide Catalysts . . . . .	139
<b>5</b>	<b><i>In situ</i> Raman Studies on Mixed Metal-Oxygen-Clusters (Mo, V, W) and Carboxylates in Aqueous Solution</b>	<b>141</b>
5.0.4	Introduction . . . . .	141
5.0.4.1	Raman spectroscopy of Polyoxometalates in Aqueous Solutions . . . . .	143
5.0.4.2	Isopolyoxomolybdates in Aqueous Solution . . . . .	143
5.0.4.3	Isopolyoxovanadates in Aqueous Solution . . . . .	144
5.0.4.4	Isopolyoxotungstates in Aqueous Solution . . . . .	146
5.0.4.5	Assignment of Raman Bands . . . . .	146
5.1	Experimental . . . . .	148
5.2	Results and Discussion . . . . .	150
5.2.1	Pure Molybdate Solutions . . . . .	150
5.2.2	Mixed Mo/Carboxylate Solutions . . . . .	151
5.2.2.1	Mo/Acetate Solution . . . . .	152
5.2.2.2	Mo/Oxalate Solution . . . . .	152
5.2.2.3	Mo/Tartrate Solution . . . . .	153
5.2.3	Pure Vanadate Solutions . . . . .	156
5.2.4	Mixed V/Carboxylate Solutions . . . . .	157
5.2.4.1	Vanadate/Acetate Solution . . . . .	157
5.2.4.2	Vanadate/Oxalate Solution . . . . .	158
5.2.4.3	Mixed Vanadate/Tartrate Solution . . . . .	159
5.2.5	Tungstate Solutions . . . . .	160
5.2.5.1	W/Carboxylate Solutions . . . . .	161
5.2.6	Mixed Binary Metalate Solutions . . . . .	161



5.2.6.1	Mixed Mo/V and Mo/W Solutions . . . . .	161
5.2.7	Mixed Ternary Metalate Solutions . . . . .	163
5.2.7.1	Mixed Mo/V/W Solution . . . . .	163
5.2.7.2	Mixed Mo/V/W/Acetate Solution . . . . .	165
5.2.7.3	Mixed Mo/V/W/Oxalate Solution . . . . .	166
5.2.7.4	Mixed Mo/V/W/Tartrate Solution . . . . .	167
5.3	Conclusions . . . . .	168

<b>6</b>	<b>Summary</b>	<b>170</b>
----------	----------------	------------

# Introduction

Catalytic selective oxidation reactions belong to the most important industrial processes. About one quarter of the value produced world-wide *via* catalytic reactions stems from partial oxidation reactions and considerably contribute to the gross national products of industrialised countries.<sup>1</sup> Thus, it is highly important to further develop not only the performance of such industrial processes but also the fundamental understanding of such multielement and multiphasic catalysts, *e.g.* the role of each phase and their interaction under catalytic action. This information is prerequisite for future material science tailoring of molecularly defined selective catalysts.

Molybdenum oxides generally are of great technical interest. The interesting optical and electronic properties of molybdenum oxides<sup>2-6</sup> make them attractive as electrochromic devices for information displays.<sup>7, 8</sup> Molybdenum oxide based materials are highly important compounds in selective oxidation catalysis.<sup>9-14</sup> Such catalysts are industrially used for partial oxidation of hydrocarbons *e.g.* unsaturated aldehydes to carbon acids.<sup>15, 16</sup> The production of industrially valuable products like acrylonitrile and acrylic acid are performed over molybdenum oxide based catalysts.<sup>16, 17</sup> The world production of acrylic acid is about 2 bill. tons/a which are used as intermediates in the chemical industry.<sup>18</sup> The main products formed from acrylic acid are acrylic esters and polyacrylic acid based superabsorbers.<sup>19</sup> The modern industrial production of acrylic acid is a two-step selective oxidation of propene. In the first step, the propene oxidation to acrolein is carried out over Bi-Mo catalysts at 603-673 K. In the second step V and W promoted molybdenum oxide based catalysts are employed for the selective oxidation of acrolein to acrylic acid.

The use of *in situ* techniques for the characterisation of catalysts and the development of these techniques has gained remarkable interest in the last decade.<sup>20-25</sup> *In situ* studies assure that the observed time dependent, structural changes are related to the changes of the catalytic activity.

Therefore, direct correlations can be established between the structural and chemical features and the performances of catalysts under different process conditions.

Photon in/out techniques are particularly suitable for *in situ* characterisations. *In situ* Raman spectroscopy provides many advantages (many catalytic active transition oxides are Raman active, extreme pressure or high temperature *in situ* conditions are possible and a simple *in situ* cell setup can be used). Therefore, Raman spectroscopy serves as a unique tool to investigate catalysts based on molybdenum oxide and to get structural information about molybdenum oxides.<sup>10, 26</sup> However, several disadvantages of *in situ* Raman spectroscopy like sensitivity limitations due to the small Raman cross section of the materials under investigation, impossibility of quantification due to unknown Raman cross sections may limit the application of *in situ* Raman spectroscopy.<sup>27</sup>

The structural chemistry of molybdenum oxides  $\text{MoO}_x$  with  $2 < x < 3$  was studied by Magéli and Kihlberg.<sup>28</sup> They determined the crystal structures of  $\text{MoO}_2$  and  $\text{MoO}_3$  and the intermediate oxides  $\text{Mo}_4\text{O}_{11}$  (monoclinic),  $\text{Mo}_4\text{O}_{11}$  (orthorhombic),  $\text{Mo}_{17}\text{O}_{47}$ ,  $\text{Mo}_5\text{O}_{14}$ ,  $\text{Mo}_8\text{O}_{23}$ ,  $\text{Mo}_9\text{O}_{26}$ . None of the oxides has an extended homogeneity range as can be seen in Figure 1 from the formation temperature versus oxygen/metal ratio diagram (taken from Ref. 29).

Although, numerous intermediate molybdenum oxide phases exist, mostly Raman or infrared (IR) spectroscopic characterisations of the stoichiometric oxides  $\text{MoO}_3$ <sup>30, 31</sup> and  $\text{MoO}_2$ <sup>32</sup> have been reported. A correlation has not been reported so far of the structure of catalytically important reduced molybdenum oxides like  $\text{Mo}_4\text{O}_{11}$  or  $\text{Mo}_5\text{O}_{14}$ <sup>33, 34, 35</sup> as determined by *in situ* Raman spectroscopy

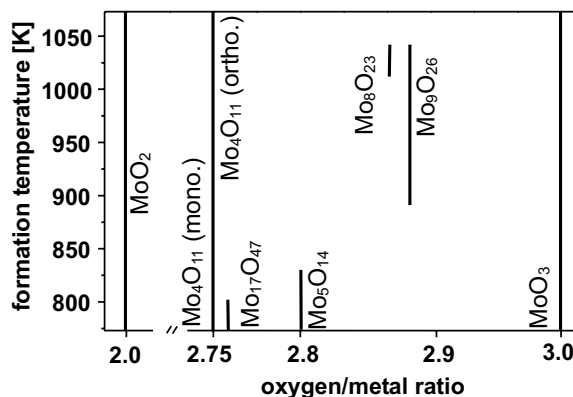


**Fig. 1:** Formation temperature v. composition diagram of known molybdenum oxides.

and their catalytic behaviour. One reason for this may be the often reported small Raman scattering efficiency of intermediate molybdenum oxides.<sup>36</sup> Therefore, a relation of *in situ* Raman spectroscopic results and catalytic activities may not unambiguously deducible because phases or compounds present in the catalyst may escape Raman detection. Especially in case of molybdenum intermediate oxide phases with their estimated small Raman cross sections, *in situ*

Raman detection may be limited. Therefore, experimental solutions have to be found for *in situ* Raman spectroscopy to overcome this problem. One way to increase the efficiency of the Raman scattering process is resonant coupling of the Raman scattering to electronic transitions of the material investigated. Resonance Raman spectroscopy makes use of an excitation frequency close to an electronic absorption. Under these conditions the Raman scattering cross section may be enhanced by several orders of magnitude.<sup>37-39</sup> Because not all electronic transitions of a material do lead to a resonance enhancement of the Raman scattering, a detailed knowledge of its electronic properties is necessary for resonant coupling of the Raman scattering by a proper choice of the excitation wavelength with respect to electronic transitions present in the material. The first Chapter of this thesis is focused on the question, how to invoke resonant Raman scattering in molybdenum oxides by a proper choice of the excitation wavelength and how to prove such a resonance enhancement. The influence of the degree of reduction of  $\text{MoO}_{3-x}$  samples on structural and electronic properties and, thus on their Raman spectra are investigated by SEM, XRD, diffuse reflectance UV/VIS and Raman spectroscopy in order to develop a model to explain the nature of the observed electronic transitions in  $\text{MoO}_{3-x}$ . This model explains resonant enhancement of Raman scattering in catalytically important intermediate oxide like  $\text{Mo}_4\text{O}_{11}$ , which is the objective of the second part of the first Chapter.

Catalyst optimisation often produces complex mixtures of many elements. Doping is a fundamental method to modify the physico-chemical and, hence, catalytic properties of a transition metal oxide catalyst. The influence of minor quantities - *i.e.* promoters - of additional transition metals in the main catalyst material is manifold. Promoters may act as structural promoters (for example extend the surface area of the catalyst material) and/or may directly be involved in the catalytic cycle due to their different redox or acid/base properties as compared to the major component. The catalytic properties of a mixed transition metal oxide catalyst are a function of its structure and the compositional range tolerated by that structure. Therefore, the catalytic properties of such multielement mixed oxide catalysts are a complex function of the added elements.

Already the binary oxides of molybdenum, vanadium or tungsten have a broad structural variability.<sup>40, 41</sup> It is known for molybdenum oxides that they tolerate different amounts of other transition metal oxides like  $\text{V}^{42}$ ,  $\text{W}^{43, 44, 45, 46}$ ,  $\text{Nb}^{47}$  or  $\text{Ta}^{48}$  within their structure. The addition of such transition metal promoters to molybdenum oxide based catalysts leads to phases which

persist of a wide range of composition. A deeper understanding of the principal role and effect of each single element on the geometric structure of the catalyst and its physical-chemical properties, or its influence on the activation process of the catalyst or on its catalytic performance are usually unknown.

Promoters with a lower formal charge as compared to  $\text{Mo}^{6+}$  induces oxygen non-stoichiometry. Therefore, such promoted catalysts are usually poorly crystallised and have a high degree of defects. Therefore, a wide range of analytical methods is used to characterise especially the physico-chemical properties of such catalysts. Such a multidisciplinary concept builds the frame of the second Chapter of this thesis.

The catalytic and physico-chemical properties of a mixed Mo/V/W oxide, with a composition close to industrial catalysts are investigated by SEM/EDX, XRD and Raman spectroscopy. Of all possible oxides there may only be one single structurally defined oxide which exhibits the highest catalytic selectivity and activity. The identification of such a the target structure, which presence is strongly related to high catalytic activity and selectivity, is the centre of the second Chapter. Thermal activation is used to invoke changes of the catalytic and physico-chemical properties of the catalyst in order to develop a model of the structural properties of the catalyst under operation. The results of the investigation of this complex, multielement catalyst invokes questions which are the objectives of Chapters 3-5.

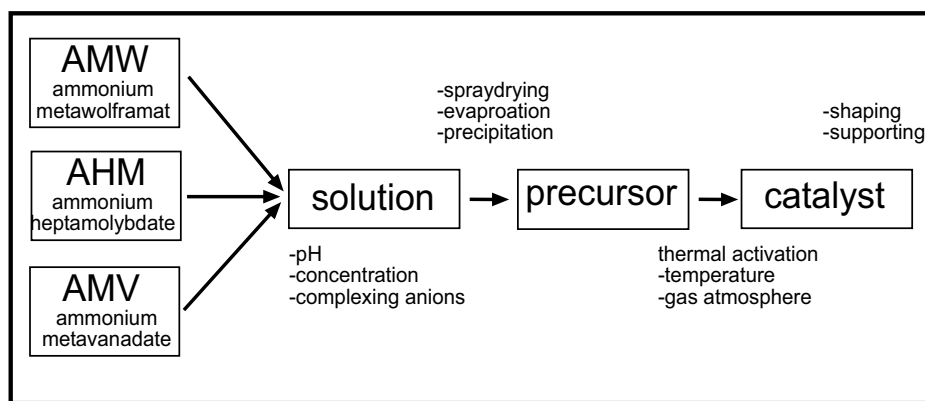


**Fig. 2:** General preparation Scheme for molybdenum oxide based catalysts.

Catalyst precursor preparation and activation of the precursors definitely is of importance for the final structure of the catalyst, its degree of reduction and its elemental and structural homogeneity. The synthesis of active catalysts typically involves a complex series of chemical and physical transformations, such as precipitation, drying and activation. Most Mo-oxide based catalysts are prepared from aqueous mixed ammonium metalate solutions. After drying, these

precursors are activated by well-defined thermal procedures under well-defined gas atmospheres (see the Scheme in Figure 2). The influence of added promoters on such preparation steps and their elemental distribution in the catalyst material are usually unknown.

In order to deeper understand V- and W- promoter effects it is necessary to study separately the influence of added V and W. Therefore, polyoxometalate catalyst precursors with V and/or W promoters have been prepared. The dynamic influence of V- and W- promoters on the thermal activation process of such pure and mixed Mo-oxide catalysts is investigated in Chapter 3 by thermoanalytical methods, *in situ* XRD and Raman spectroscopy.

Chapter 4 is dedicated to the question about the role of V- and W promoters on the catalytic and structural properties of molybdenum oxide catalysts. The catalytic properties of these catalysts are investigated as a function of the added transition metal by combined TPRS/*in situ* Raman spectroscopy experiments. Results obtained in Chapter 1 are used to obtain information about the degree of the reduction of the catalysts as a function of their activities and selectivities by *in situ* Raman spectroscopy.

In order to improve the elemental homogeneity of the final activated catalyst, a deeper understanding is needed of the species in solution of concentrated pure and mixed polyoxometalate solutions. Especially group IV, V, VI transition cations exhibit a unique and complex aqueous polyoxometalate chemistry.<sup>41, 49, 50</sup> In Chapter 5 the catalyst preparation, *e.g.* the chemistry in aqueous solutions of pure and mixed molybdate, vanadate and tungstate solutions are investigated by *in situ* Raman spectroscopy in order to control the formation of a defined species in solution and, hence, a molecularly well defined polyoxometalate catalyst precursor.

## Chapter 1

# Resonance Raman Spectroscopy of molybdenum oxides

Raman spectroscopy is especially suited for the characterisation of molybdenum oxides.<sup>20, 51</sup> The Raman cross section generally depends on properties as crystallinity or the concentration of oxygen defects present in the material. Most catalysts based on molybdenum oxides are poorly crystallised on one hand and on the other have a high degree of oxygen defects. As a consequence these materials are dark coloured and strongly absorbing. Strong absorption leads in generally to low Raman efficiencies. Therefore, conditions have to be found to increase the Raman cross section. The proper choice of the excitation wavelength may induce a resonant coupling of the Raman scattering which leads to a drastic increase of the Raman cross section. In this Chapter\* two ways to prove a Resonance Raman effect operative in molybdenum oxides will be presented. Further, a model of the electronic transitions in  $\text{MoO}_{3-x}$  will be developed, which will serve as the base to explain resonant Raman effects in molybdenum oxides.

## 1.1 Structural Characterisation of Oxygen Defects in $\text{MoO}_{3-x}$

### 1.1.1 Introduction

The oxygen defect concentration of molybdenum oxides is thermodynamically determined by the oxygen partial pressure and temperatures of the preparation method.<sup>52-54</sup> Further, the crystal

---

\* Parts of this Chapter will be published in M. Dieterle, G. Weinberg, G. Mestl, Raman spectroscopy of molybdenum oxides (Part I): Structural Characterisation of oxygen defects in  $\text{MoO}_{3-x}$  by DRUV/VIS-, Raman Spectroscopy and X-ray Diffraction and M. Dieterle and G. Mestl, Raman spectroscopy of molybdenum oxides (Part II): Resonance Raman spectroscopic characterisation of the molybdenum oxides  $\text{Mo}_4\text{O}_{11}$  and  $\text{MoO}_2$  (both submitted to *Phys. Chem. Chem. Phys.*)

morphology is a function of the preparation temperature and the oxygen partial pressure too.<sup>55</sup> As a consequence, both, crystal morphology and the amount of oxygen vacancies cannot be altered independently at the same time.

Samples which exhibited different relative areas of the exposed surface planes have been used to investigate the structure sensitivity of catalytic reactions over  $\text{MoO}_3$ . These samples were prepared under different temperatures, oxygen or water partial pressures.<sup>56-66</sup> Due to thermodynamics, it is expected that these different  $\text{MoO}_{3-x}$  samples also contained different oxygen defect concentrations. However, these probably varying degrees of reduction were not taken into account in interpretations to deduce structure-activity relations for  $\text{MoO}_3$ . Future structure-activity investigations should, therefore, consider different oxygen vacancy concentration in materials with different ratios of exposed surfaces.

$\text{MoO}_{3-x}$  can readily exchange lattice oxygen with gas phase oxygen and provide lattice oxygen for catalytic oxidation reactions.<sup>67</sup> Thermal treatment under low oxygen partial pressures or mechanical activation of  $\text{MoO}_3$  induces oxygen deficiency defects and leads to  $\text{MoO}_{3-x}$ .<sup>68-70</sup> Gay-Boys et al.<sup>70</sup> showed that surface oxygen defects are induced upon reduction with propene or  $\text{H}_2$  up to 670 K. At temperatures around 670 K, the temperature at which many of the molybdenum oxide based catalysts operate,<sup>34, 71</sup> these oxygen defects nucleate. Defined intermediate oxides with crystallographic shear planes like  $\text{Mo}_4\text{O}_{11}$  are formed by reduction at temperatures higher than 773 K.<sup>72, 73, 74</sup>

The geometric basis for the shear structures is the structure of  $\text{MoO}_3$ . Orthorhombic  $\text{MoO}_3$  may be interpreted as a layered structure build up by two layers of chains of  $\text{MoO}_4$  tetrahedra running along the c-axis (Figure 1.1).<sup>75</sup> Following Kihlberg's XRD analysis of  $\text{MoO}_3$  (Pbmn,  $a=3.964 \text{ \AA}$ ,  $b=13.863 \text{ \AA}$ ,  $c=3.699 \text{ \AA}$ ,  $\beta=120.9^\circ$ ) five different Mo-O bond distances are observed in  $\text{MoO}_3$ .<sup>75</sup> The terminal  $\text{Mo}=\text{O}$  bonds have bond lengths of  $1.671 \text{ \AA}$  and  $1.734 \text{ \AA}$ , while the Mo-O bond distances of the bridging oxygens in c-direction is  $1.948 \text{ \AA}$ . Within the model of the chains of  $\text{MoO}_4$  tetrahedra in the c-direction, the two remaining oxygen distances of  $2.332 \text{ \AA}$  and  $2.251 \text{ \AA}$  to neighbour tetrahedra chains form a distorted octahedron (Figure 1.1). Thus, the structure may alternatively be described as being build up by heavily distorted octahedra as shown in Figure 1.1. However, it should be noted that both descriptions the sixfold or the fourfold coordination of the Mo cation are each idealised. The Mo-O-Mo angles in  $\text{MoO}_3$  deviate from the values found in a symmetric octahedron ( $180^\circ$  and  $90^\circ$ ) and their values of  $98^\circ$ ,



104° and 143° reflect the transitional stage between the octahedral and tetrahedral coordination. The fourfold coordination of the Mo cations was found to be in good agreement by vibrational spectroscopy data.<sup>30, 76</sup> In contrast but not in contradiction to vibrational spectroscopy, ESR results have led to the assumption of a sixfold coordinated Mo cation.<sup>77, 78</sup> Therefore, both descriptions, the sixfold or the fourfold coordination may be seen as the attempt to describe the structure of MoO<sub>3</sub> from the point of two idealised atom arrangements.

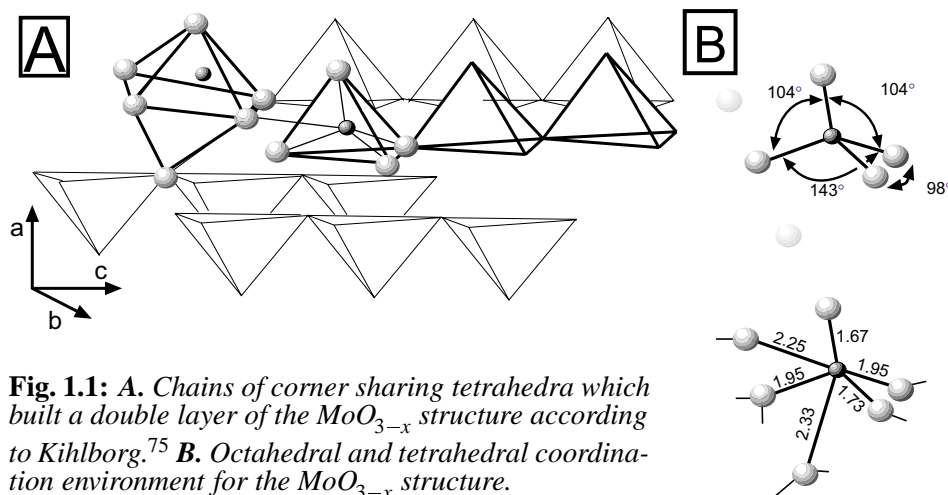


**Fig. 1.1:** **A.** Chains of corner sharing tetrahedra which built a double layer of the MoO<sub>3-x</sub> structure according to Kihlberg.<sup>75</sup> **B.** Octahedral and tetrahedral coordination environment for the MoO<sub>3-x</sub> structure.

The electronic structure is probably as important for the catalytic activity of MoO<sub>3</sub> as the geometric structure. Valence and conduction electrons determine the electronic properties of solids. Transition energies can be precisely determined by optical absorption/reflection spectroscopy between the valence and the conduction band, between defect states, between the valence band and defect states or between defect states and the conduction band, respectively.<sup>79, 80</sup>

The optical properties of molybdenum oxides strongly change as a function of the oxygen vacancy concentration.<sup>81</sup> Even MoO<sub>3-x</sub> prepared at elevated temperatures under atmospheric oxygen pressure always contains some oxygen defects.<sup>3</sup> Deb estimated the oxygen vacancy concentration to be  $3 \times 10^{-19}$ /mol resulting in a formal stoichiometry of 2.999.<sup>82</sup> Therefore, MoO<sub>3</sub> is a n-type semiconductor with indirect band gaps<sup>83</sup> that have reported widths between 2.9 eV and 3.15 eV.<sup>84, 85</sup> The introduction of oxygen vacancies in MoO<sub>3</sub> even gives rise to electric conductivity.<sup>5</sup> Thus, substoichiometric MoO<sub>3-x</sub> is a semiconductor, while MoO<sub>2</sub> has metallic properties. The valence band is generated by oxygen 2p- $\pi$  orbitals, while the conduction band is formed by overlapping metal 4d and 5s bands.<sup>86</sup> Electron hole pairs are formed upon absorption. These electron-hole pairs may form excitons, which have absorptions in the UV regime themselves. MoO<sub>3-x</sub> is reported to have three bands at 3.7 eV, 4.3 eV and 4.5 eV which were at-

tributed to exciton formation.<sup>3</sup> Upon reduction of  $\text{MoO}_3$ ,  $\text{Mo}^{6+}$  ions are reduced to  $\text{Mo}^{5+}$  (e.g. in  $\text{Mo}_4\text{O}_{11}$ ) or  $\text{Mo}^{4+}$  (e.g. in  $\text{MoO}_2$ ).  $\text{Mo}^{5+}\text{--O--Mo}^{6+}$  interactions form additional conduction bands in the reduced material with respect to  $\text{MoO}_3$ .<sup>70, 87-92</sup>

The additional charge carriers formed during the reduction process are injected into these bands and distort the lattice in their surroundings. This coupled electron-lattice distortion is called polaron. Porter et al.<sup>4</sup> observed these polaron or intervalence charge transfer (IVCT) bands at 2.48 eV and at 2.13, 2.42 and 1.3(sh) eV for  $\text{MoO}_2$  and  $\text{Mo}_4\text{O}_{11}$ , respectively. Therefore, the sample colour of  $\text{MoO}_{3-x}$  changes as a function of the degree of reduction e.g. yellow ( $\text{MoO}_{3-x}$ ) or grayish/blue ( $\text{MoO}_{3-y}$ ) with  $x < y$ . The number of charge carriers injected into this additional bands influence the position and intensity of this absorption band. The systematic blue shift of the absorption band between 2-2.5 eV with decreasing metal-oxygen ratio can directly be correlated to the degree of reduction of the molybdenum oxide.<sup>4, 78, 92</sup>

Another characterisation method for reduced Mo oxides is electron spin resonance spectroscopy (ESR). Łabanowska explained ESR results on different types of oxygen defects which were formed in  $\text{MoO}_{3-x}$  depending on the oxygen partial pressure and the temperatures employed using crystal field theory.<sup>77</sup> Pentacoordinated  $\text{Mo}^{5+}$  with an oxygen vacancy and hexacoordinated  $\text{Mo}^{5+}$  were observed upon reduction /oxidation of  $\text{MoO}_{3-x}$ . The crystal field splittings of these centres were calculated to be  $E_1 = E_{z^2} - E_{yz} = 2.65$  eV,  $E_2 = E_{xy} - E_{yz} = 3.83$  eV and  $E_3 = E_{xz} - E_{yz} = 5.08$  eV in case of the hexacoordinated  $\text{Mo}^{5+}$  centre and  $E_1 = E_{z^2} - E_{yz} = 3.4$  eV,  $E_2 = E_{xy} - E_{yz} = 1.5$  eV and  $E_3 = E_{xz} - E_{yz} = 1.0$  eV in case of the pentacoordinated  $\text{Mo}^{5+}$  centre, respectively. However, a quantification of the amount of oxygen vacancies was not possible, due to suggested ESR silent defect centres.

Raman spectroscopy serves as a unique tool to investigate molybdenum oxides, and to obtain structural information about molybdenum oxides.<sup>10, 20, 25, 36, 51</sup> Raman spectroscopy is a sensitive tool to investigate metal ligand distances, coordination and symmetry of metal centres.<sup>26, 93, 94</sup> The choice of the excitation wavelength may dramatically influence the observed Raman cross section especially when characterising strongly absorbing materials as shown in the following Section of this Chapter. Based on a normal mode analysis and a valence force field calculation, the observed Raman spectrum of orthorhombic  $\text{MoO}_3$  is well understood.<sup>30</sup> Julien and Nazri showed that the intensities and positions of IR/Raman spectra of  $\text{MoO}_3 \cdot (\text{H}_2\text{O})_x$  are extremely sensible to small structural changes of the Mo-O polyhedra.<sup>95</sup>

### 1.1.1.1 Theory of Raman Scattering

The Raman process is a *inelastic scattering process* which produces secondary light quanta with different energies different to that of the excitation frequency.<sup>37-39</sup> During the interaction of the primary light quantum with a molecule or crystal, the energy of vibrational states may be exchanged and a secondary light quantum of lower or higher energy is emitted. The energy difference is equal to the generated or destroyed *vibrational energy*  $E_{vib}$ . The inelastic interaction of a primary light quantum with a crystal in its vibrational ground state produces the *Stokes Raman spectrum*, a red-shifted spectrum. If a molecule or crystal are not in their vibrational ground state, the interaction of the primary light may produce a blue-shifted Raman spectrum, the *anti-Stokes Raman spectrum*.

Raman spectra have their origin in the electronic polarisation caused by the incident electromagnetic radiation. Lasers are normally used as *exciting source* in the ultraviolet (UV), visible (VIS; e.g. HeNe (632 nm), frequency doubled NdYag (532 nm)), or near-infrared (NIR, e.g. NdYag (1064 nm)).

Other exciting light quanta are elastically scattered to give the *Rayleigh scattering* (of frequency  $\nu_0$ ) of unscattered energy. The intensity of the Rayleigh line is several orders of magnitude higher than that of the Raman lines and may dominate the Raman spectrum of a weak Raman scatterer at low energies.

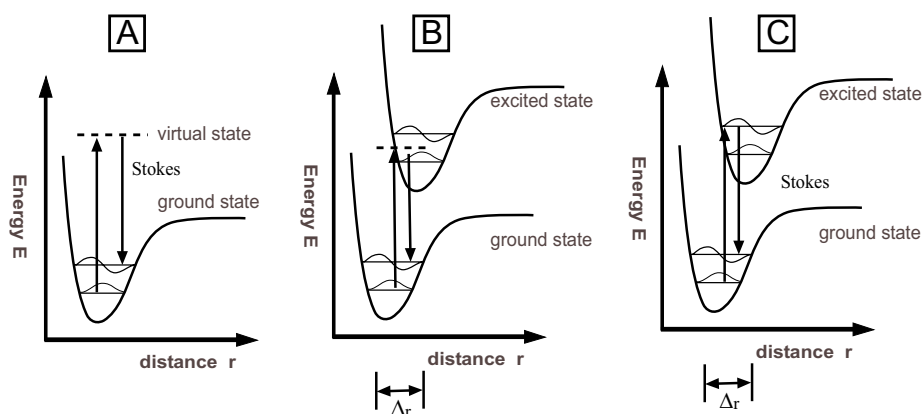


**Fig. 1.2:** Schematic representation of the transition for Raman scattering (A), pre-resonance Raman (B) and resonance Raman (C).

When a molecule or crystal is exposed to an electric field, electrons and nuclei are forced to move in opposite directions. A dipole moment is induced which is proportional to the electric field strength and to the *molecular polarisability*  $\alpha$ . A vibration described by the normal coordi-

nate  $q_k$  can be observed in the Raman spectrum only if it modulates the molecular polarisability.

$$(1.1) \quad \left[ \frac{\partial \alpha}{\partial q} \right] \neq 0$$

If the symmetry of a molecule or a crystal is such that this condition is fulfilled, then the transition is said to be allowed or Raman active; if it is not fulfilled, it is said to be forbidden or Raman inactive.

A normal vibration is described by the normal coordinate  $q_k$  and the normal frequency  $\nu_k$ :

$$(1.2) \quad q_k = q_0^K \cos(2\pi\nu_k t)$$

If a molecule or a crystal interacts with an oscillating of frequency  $\nu_0$  a dipole moment,  $P$ , with alternating polarity of the frequency,  $\nu_0$ , is induced. The components of the vector of the electric field with respect to Cartesian coordinates are described by  $E_x$ ,  $E_y$  and  $E_z$ . The induced dipole moment  $p_i$  can be described by its components:

$$(1.3) \quad \begin{aligned} p_x &= \alpha_{xx}E_x + \alpha_{xy}E_y + \alpha_{xz}E_z \\ p_y &= \alpha_{yx}E_x + \alpha_{yy}E_y + \alpha_{yz}E_z \\ p_z &= \alpha_{zx}E_x + \alpha_{zy}E_y + \alpha_{zz}E_z \end{aligned}$$

where  $\alpha_{ij}$  are components of the polarisability tensor  $\alpha_a$ :

$$(1.4) \quad \alpha_a = \begin{bmatrix} \alpha_{xx} & \alpha_{xy} & \alpha_{xz} \\ \alpha_{yx} & \alpha_{yy} & \alpha_{yz} \\ \alpha_{zx} & \alpha_{zy} & \alpha_{zz} \end{bmatrix}$$

which projects the electric field vector  $\vec{E}$  to the induced dipole moment vector  $\vec{P}$ . This can be

written in matrix notation as:

$$(1.5) \quad \vec{p} = \alpha \vec{E}$$

$$(1.6) \quad \alpha_k = \alpha_0 + \left[ \frac{\partial \alpha}{\partial q_K} \right]_o q_0^K \cos(2\pi \nu t) + \dots$$

Equations 1.5 and 1.6 can be combined to give:

$$(1.7) \quad p_K = \alpha_o E_0 \cos(2\pi \nu_0 t) + \frac{1}{2} \left[ \frac{\partial \alpha}{\partial q_K} \right]_o q_0^K E_0 [\cos(2\pi(\nu_0 - \nu_K)t) + \cos(2\pi(\nu_0 + \nu_K)t)]$$

This oscillating Hertzian dipole  $|\vec{p}_k|$ , produces the scattered electromagnetic radiation. The first term in Eq. 1.7 describes the Rayleigh scattering, the second term Stokes Raman scattering, and the third anti-Stokes Raman scattering. This classical equation, however, is not suitable for the derivation of the intensities of Stokes and anti-Stokes Raman lines. Only a quantum mechanical treatment of the Raman scattering process reveals information about the intensities of the Raman lines.<sup>37-39, 96</sup>

The Raman cross section in general is small due to the small transition probability to the virtual state. Resonance Raman spectroscopy (RRS) or pre-resonance Raman scattering makes use of an excitation source of a frequency close to a molecular electronic absorption frequency as shown in Figure 1.1.1.1. Under these conditions, resonance occurs which may enhance the intensities of the Raman lines by several orders of magnitude, especially those arising from totally symmetric vibrations. Such a resonance Raman effect may be of crucial importance for the detection of strongly absorbing materials and/or materials with a inherent low Raman cross section. An electronic absorption, plus a displaced excited electronic state with respect to the ground state are the prerequisites for a resonance Raman effect.<sup>97</sup> If the excited electronic state is not displaced, one of the involved Franck-Condon factors for the absorption or the emission of the inelastic scattered photon is very small and the resonance Raman effect is very weak or does not occur.<sup>38</sup>

The bonding in  $\text{MoO}_3$  may be described as a mixture of ionic and covalent bonding.<sup>86-99</sup> Perturbations of the  $\text{MoO}_3$  lattice due to oxygen vacancies thus cannot be screened as in the case of metallic bonding.<sup>100</sup> Minor relaxation effects of the lattice are expected. This relaxation affects the local distortion of the M-O polyhedra which in turn is expected to influence the lattice vibrations of the Raman spectra. The effects of minor coordination or symmetry changes of the Mo-O polyhedra on the Raman spectra of  $\text{MoO}_x$  compounds may be used to gain information about the concentration of oxygen vacancies in  $\text{MoO}_{3-x}$ .

When resonant coupling to electronic states occurs during Raman excitation the observed Raman cross section is expected to be altered as a function of the oxygen vacancies concentration, because the resonant Raman cross section is always a superposition of absorption and re-absorption processes. The absorption and the re-absorption efficiencies strongly depend on the exact position of the electronic transition with respect to the excitation wavelength and the detected Raman band as shown in Figure 1.3. Because the position of the electronic transition in  $\text{MoO}_{3-x}$  changes as a function of the oxygen vacancy concentration, the observed Raman cross section should be a function of the oxygen stoichiometry for a given resonant excitation frequency.

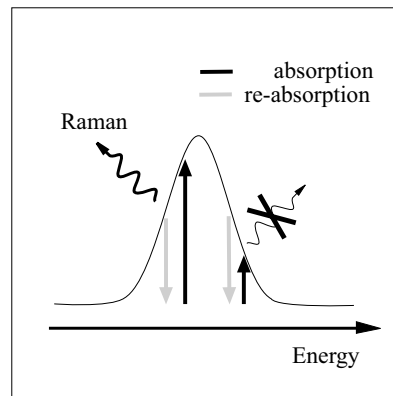


**Fig. 1.3:** The exact position of the excitation wavelength and the wavelength of the emitted Raman light with respect to the electronic absorption determines the overall efficiency of the Raman scattering process. Dark arrows indicate the position of the excitation wavelength, while the grey arrows indicate the re-absorption of the scattered Raman light.

However, the characterisation and quantification of oxygen vacancies in molybdenum oxides is rather difficult. ESR or UV/VIS spectroscopies have been used to characterise point and extended defects in  $\text{MoO}_{3-x}$ .<sup>3, 4, 77, 78</sup> UV/VIS spectroscopy is extremely sensitive to oxygen vacancies in  $\text{MoO}_{3-x}$  and has been used to determine the concentration of oxygen vacancies in  $\text{MoO}_{3-x}$ .<sup>4, 92</sup> However the analysis of the broad, strongly overlapping band positions of the UV/VIS spectrum is complicated and not straightforward. Extended defect structures have been investigated by TEM and EXAFS.<sup>54, 74, 101-104</sup> The influence of different amounts of oxygen vacancies on the Raman spectra of  $\text{MoO}_{3-x}$  samples with  $\text{MoO}_3$  structure has not been investigated yet. The objective of the study reported in this Chapter is to investigate the influence of the concentration of oxygen vacancies on the Raman spectra of  $\text{MoO}_{3-x}$ . A correlation

of the spectroscopic features of the Raman spectra of  $\text{MoO}_{3-x}$  with the oxygen/metal ratio of the samples as determined by UV/VIS spectroscopy would offer a straightforward possibility to determine minor changes of the oxygen/metal ratio by *in situ* Raman characterisation during catalytic action. However, the Raman spectra may also be influenced by the particle size and the morphology of  $\text{MoO}_{3-x}$ . Therefore, particle size and morphology has to be characterised to exclude effects on the observed Raman spectra. Therefore, a method has to be developed to determine the oxygen/metal ratio of  $\text{MoO}_{3-x}$  samples which can be used easily.

Other techniques which were often used for the determination of the oxidation state of the sample under investigation, like XPS or UPS, cannot be used for the characterisation of such low concentration of oxygen defects, because the vacuum conditions and the X-ray irradiation may already induce substoichiometry in molybdenum oxides<sup>70, 105-107</sup> and therefore change the sample properties.

### 1.1.2 Experimental

Polycrystalline greenish, well crystallised  $\text{MoO}_3$  powder was prepared by tempering commercial  $\text{MoO}_3$  (Merck) in synthetic air at 923 K (sample A) for 48 h. The formed big  $\text{MoO}_{3-x}$  crystals still had a light green colour, although stoichiometric  $\text{MoO}_3$  should be colourless. Pale yellow  $\text{MoO}_{3-x}$  powder was obtained by oxidation in pure oxygen at 823 K for 2h (sample B). Yellow  $\text{MoO}_3$  was obtained by oxidising  $\text{MoO}_{3-x}$  (Merck) at 673 K in  $\text{N}_2/\text{O}_2$  (80vol% / 20 vol%) for 20 h (sample C). Sample D had a gray colour and was  $\text{MoO}_{3-x}$  as received (Merck). Deep gray/blue  $\text{MoO}_3$  was prepared from ammonium heptamolybdate by heating in  $\text{N}_2$  and subsequent oxidation at 670 K in synthetic air for 1h (sample E).

Scanning electron micrographs (SEM) of the samples were taken on a Hitachi S-4000 microscope with an accelerating voltage of 5 kV to study the sample morphology.

All XRD measurements were made at RT with a STOE STADI-P (Ge primary monochromator,  $\text{Cu-K}\alpha_1$  radiation) in focussing transmission diffractometer equipped with position sensitive detector (PSD).

Diffuse reflection UV/VIS (DR-UV/VIS) spectra were taken on a Perkin Elmer Lambda 9 spectrometer with a scan speed of 240 nm/min, a slit width of 5.0 nm and a response time of 0.5 s with  $\text{SiO}_2$  as a reflectance standard. Within this  $\text{MoO}_{3-x}$  sample series, the DR-UV/VIS spec-

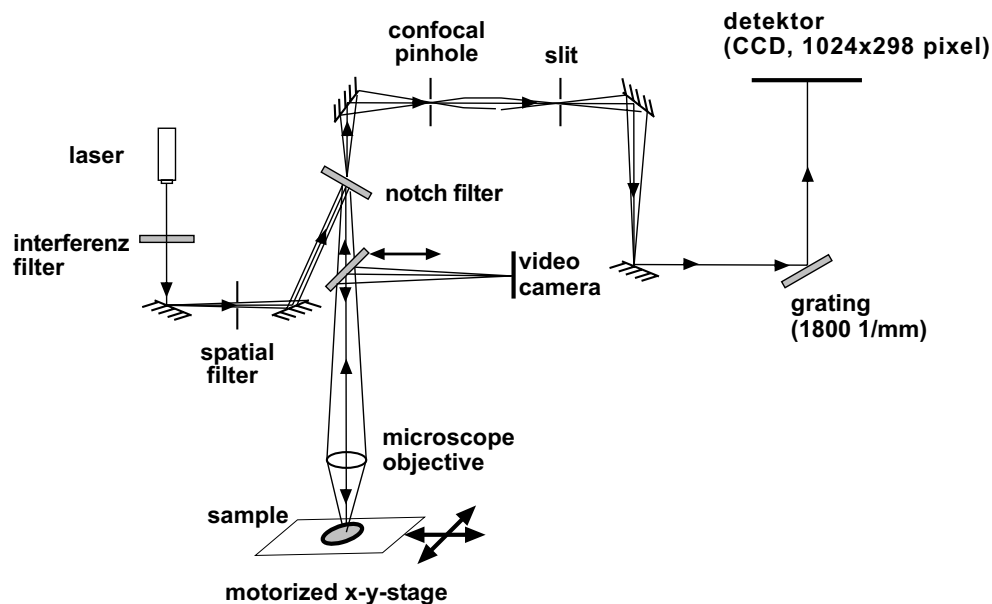


**Fig. 1.4:** Optical setup of the Dilor LABRAM B microscope.

tra were fitted in the energy range between 0.55 eV and 4.8 eV with Gaussian functions and the error function for the band gap to deconvolute the overlapping absorption bands. Such a decomposition step was necessary because the deconvolution cannot be done by visual inspection due to the rather broad superimposed peaks. Furthermore, the strong overlapping, broad absorption bands made it necessary to use a randomised search minimisation method implemented in the spectrahandler software<sup>108</sup> which searches for the global minimum of the fitting parameter function instead of the usually used least-square minimisation method which may find only local minima. The fitting solution strongly depends on the starting parameters employed due to the rather flat global minimum of the fitting parameter function. The iteratively mutual evaluation of the DR-UV/VIS spectra of five different oxygen defective  $\text{MoO}_3$  samples was used to optimise the band positions, intensities and shapes of the Gaussian fitting curves within the set of DR-UV/VIS spectra.

All Raman spectra were recorded with DILOR LABRAM I spectrometer equipped with a confocal microscope (Olympus) and a computerised XY-table. Modern Raman spectrometers equipped with confocal microscopes as shown in Figure 1.4 offer the possibility to obtain Raman images with a submicron lateral resolution. Evaluation of structural inhomogeneities or the analysis of complex mixtures within the micron scale are feasible. The entrance slits were set to  $200 \mu\text{m}$ , giving a spectral resolution of  $2 \text{ cm}^{-1}$ . A notch filter was applied, to cut off the laser line and the Rayleigh scattering up to ca.  $150 \text{ cm}^{-1}$ . The spectrometer is equipped with



a CCD camera (1024\*298 diodes), which is peltier-cooled to 243 K to reduce thermal noise. A He-laser (632.8 nm, Melles Griot, 14 mW) was used for excitation. The laser power is estimated to be 0.12 mW at the sample location. The laser light was focussed onto the sample using a 100x objective lens (Olympus). All Raman spectra were recorded in backscattering geometry on a line of about 40  $\mu\text{m}$  length across the manually pressed powder. Fifty Raman spectra were recorded for each sample with a spatial resolution of ca. 0.7  $\mu\text{m}$  to improve the statistics and to detect even small changes in the  $\text{MoO}_{3-x}$  spectra.

### 1.1.3 Results and Discussion

#### 1.1.3.1 SEM and XRD

sample	a-axis	b-axis	c-axis
A	$396.2 \pm 0.1$	$1385.7 \pm 0.1$	$369.8 \pm 0.1$
B	$396.2 \pm 0.1$	$1385.8 \pm 0.1$	$369.7 \pm 0.1$
C	$396.2 \pm 0.1$	$1386.1 \pm 0.1$	$369.7 \pm 0.1$
D	$396.2 \pm 0.1$	$1386.4 \pm 0.1$	$369.6 \pm 0.1$
E	$396.1 \pm 0.1$	$1386.6 \pm 0.1$	$369.6 \pm 0.1$

**Table 1.1:** Refined lattice parameters [pm] of the  $\text{MoO}_{3-x}$  samples.

sample	110	200	020
A	*	*	*
B	$0.08 \pm 0.02$	$0.07 \pm 0.02$	$0.05 \pm 0.02$
C	$0.05 \pm 0.02$	$0.08 \pm 0.02$	$0.17 \pm 0.02$
D	$0.08 \pm 0.02$	$0.07 \pm 0.02$	$0.22 \pm 0.02$
E	$0.09 \pm 0.02$	$0.05 \pm 0.02$	$0.43 \pm 0.02$

**Table 1.2:** Stress/strain as determined by XRD [%] (\*internal standard).

The SEM micrographs in Figure 1.5 illustrate the influence of the different preparation conditions on the particle size and morphology of the prepared samples. In general, the higher the preparation temperature the more often an oriented and platelet-like morphology is found. Sample A, which has been prepared at 923 K exhibits long, well developed platelets of  $\text{MoO}_3$  crystals. The particle size is in the range of some 100  $\mu\text{m}$ . In contrast to sample A, the particle sizes of sample B, which has been prepared at 823 K, is found to be in the 10 micron range, but the platelet-like orientation of the crystals is still retained.

When the preparation temperature is lower than 773 K (sample C-E), the particle size of the fine powdered samples C and D are in the few micron to submicron range. The morphology of the particles resembles more spherical particles in contrast to samples A and B. The absence of distinct edges (samples C to E) indicates a termination of the crystallites by strongly terraced surfaces.

The X-ray diffraction patterns of the five different samples are shown in Figure 1.6 on page 18. All X-ray diffraction patterns are similar to the pattern of orthorhombic  $\text{MoO}_3$  reported in the JC-PDF2 database (No. 35076).

Sample	-110	-200	-020
A	*	*	*
B	559	202	247
C	41	154	144
D	34	80	119
E	34	60	136

**Table 1.3:** Particle sizes as determined by XRD [nm] (\*internal standard).

The platelet-like shape of the  $\text{MoO}_3$  oxide particles leads to a high intensity of the (0k0) diffraction peaks associated with the basal planes of the  $\text{MoO}_3$  platelets especially in case of sample A due to preferential orientation. The refined crystallographic data<sup>109</sup> of all samples are listed in Table 1.1. A contraction of the c-axis of 0.2 pm combined with a elongation of the b-axis of 0.9 pm is observed from sample A to E according to literature.<sup>110</sup> Therefore, it may be assumed that oxygen vacancies mainly replace bridging oxygen atoms in c-direction.<sup>111</sup> As a consequence of the changing bonding situation due to these oxygen vacancies, the bonds in b-direction are slightly elongated. A stress/strain and particle size analysis further supports this interpretation (Table 1.2 and Table 1.3). Sample A was used as an internal standard for this evaluation.

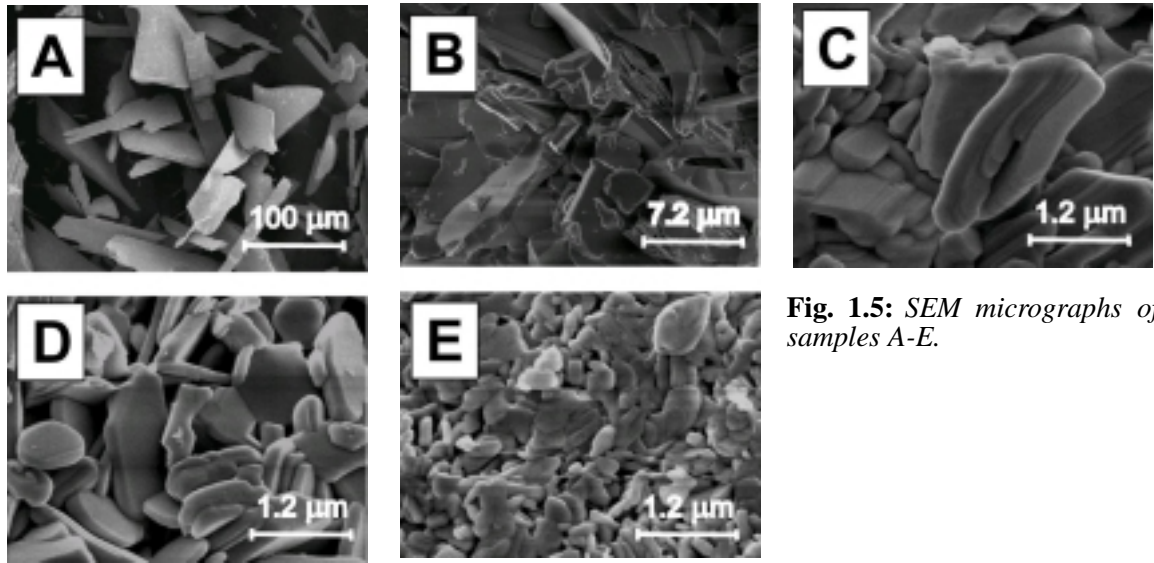


**Fig. 1.5:** SEM micrographs of samples A-E.

A stress/strain and particle size analysis of the 110, 200 and 020 reflections revealed an increase of the stress/strain along the b-direction from 0.05 to 0.43% and a decrease in the particle size in this direction from 247 to 136 nm from sample B to E. A stress/strain and particle size analysis with (00l) reflections was not possible due to preferential orientation of the internal standard (sample A).

The XRD and SEM characterisation, thus, separates the investigated samples into two groups. The samples A and B form the first group, whereas samples C to E having more spherical particles of smaller size form the second group. Particle size effects on vibrational spectra, which cannot be ruled out a priori, should reflect this grouping in their data sets.

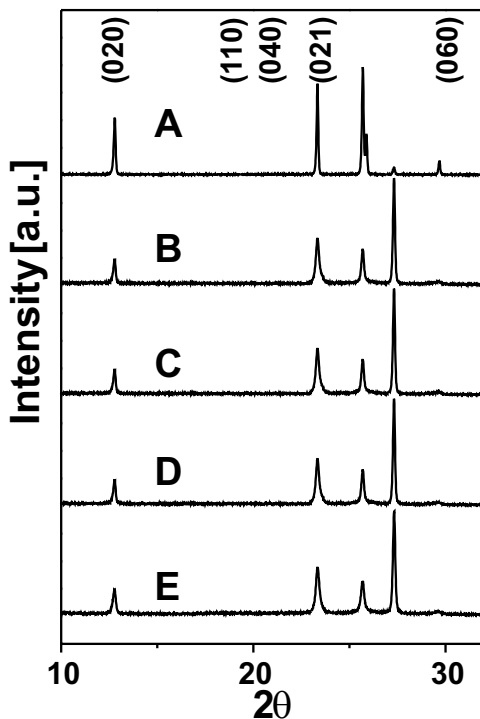


**Fig. 1.6:** XRD patterns of the samples A to E. All samples show the typical  $\text{MoO}_3$  reflections. The XRD patterns are vertically shifted for better visualisation.

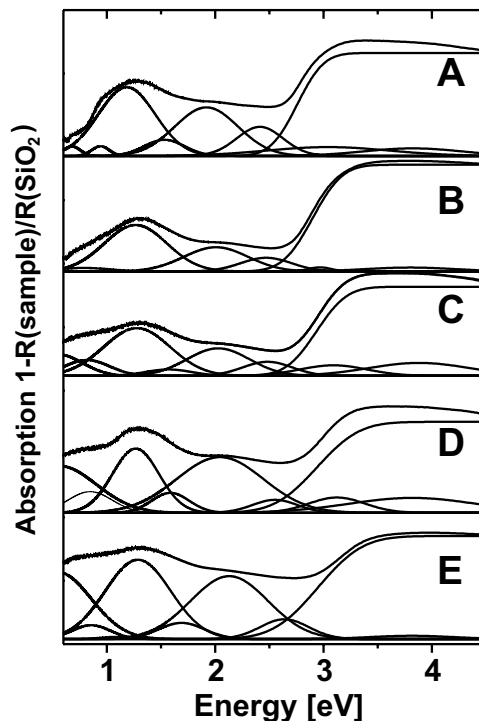


**Fig. 1.7:** DR-UV/VIS spectra and their deconvoluted electronic transitions of the samples A to E. The DR-UV/VIS spectra are vertically shifted for better visualisation.

### 1.1.3.2 UV/VIS Spectroscopy

The UV/VIS spectra of the samples and the fitted Gaussian curves are shown in Figure 1.7. The positions and intensities of the fitted Gaussian absorption bands are listed in Table 1.4 and 1.5. Eight Gaussian functions and the error function were found to be necessary to fit the five observed DR-UV/VIS spectra. As an example, the spectrum of the sample C (Figure 1.8) is discussed in detail. The positions of the fitted absorption bands were determined to be 3.88, 3.09, 2.94 (bandgap), 2.48, 2.03, 1.57, 1.28, 0.82 and 0.55 eV.

For a defect free molybdenum trioxide, only the optical bandgap and excitons should be observed in the UV-VIS spectra. Therefore, all other absorption bands are due to lower valent Mo cations, e.g.  $\text{Mo}^{5+}$  or  $\text{Mo}^{4+}$ . According to Goodenough,<sup>86, 98</sup> there are two limiting descriptions of the valence electrons in  $\text{MoO}_3$ . Crystal field theory applies if the intraatomic interactions are stronger than the interatomic interactions. The electrons can be treated as being localised to an individual atom or a Mo-O polyhedra. Band theory applies if the interatomic interactions are stronger than the intraatomic interactions. In this limit, the electrons are itinerant, occupying a delocalised electron state. However, for  $\text{MoO}_3$  intra- and interatomic interactions are comparably strong.<sup>3, 86</sup>

Collective ordering of electronic states observed in  $\text{MoO}_x$  compounds, like CDW transitions,<sup>112-115</sup> underline the importance of a the band structure description. ESR results accentuate the strong intraatomic forces and the need for crystal field theory to interpret the experimental results.<sup>77</sup> Therefore, band structure and crystal field theory, may be used to interpret the observed properties of  $\text{MoO}_{3-x}$  compounds. The observed DR-UV/VIS spectra are discussed in the following using both models.

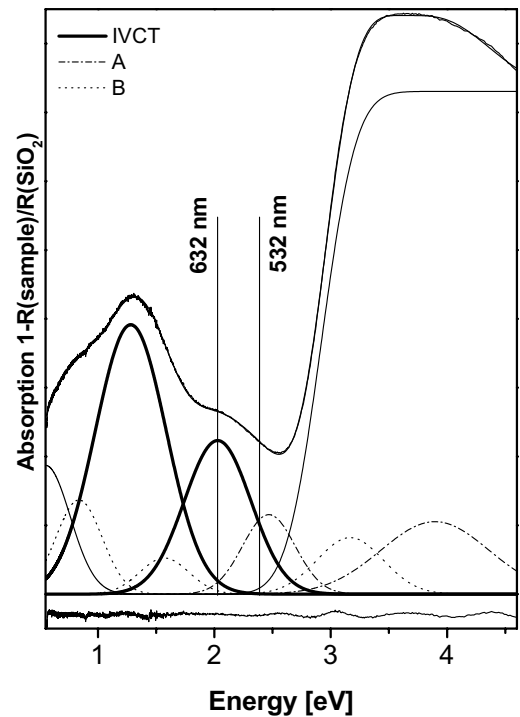


**Fig. 1.8:** DR-UV/VIS spectra of  $\text{MoO}_{3-x}$  and its deconvolution by Gaussian bands. The thick solid lines are assigned to IVCT transitions. Bands denoted with A (dashed lines) are attributed to d-d transitions of the  $[\text{MoO}_6]^{5+}$  defect state, while group of bands denoted with B (dotted lines) are assigned to d-d transitions of the  $[\text{MoO}_5]^{5+}$  defect state.

Within the band structure picture, the two absorption bands at 3.85 and 3.15 eV are attributed according to literature<sup>4, 3</sup> to exciton bands due to  $\text{Mo}^{5+}$  and  $\text{Mo}^{4+}$  cations. The remaining six, low energy absorption bands at 2.47, 2.03, 1.57, 1.28,

0.84 and 0.55 eV are attributed to absorptions from the valence band to three defect states within the band gap and absorptions from the defect states to the conduction band as shown in Figure 1.9. Two  $\text{Mo}^{5+}$  defect states are found at 1.28 and 2.03 eV above the valence band. The energetically less favoured defect state at 2.03 eV may be attributed to a  $\text{Mo}^{5+}$  defect state in the vicinity an

oxygen vacancy while the defect state at 1.28 eV is caused by an additional charge at the Mo centre. All  $\text{Mo}^{4+}$  defect states, if present, are suggested in the vicinity of oxygen vacancies.

The interpretation of the DR-UV/VIS spectra within the assumption of molecular absorptions of weakly interacting Mo-O polyhedra leads to the picture of the crystal field theory. The absorption bands at 3.88, 3.09, 2.48, 1.57 and 0.82 eV are interpreted as  $\text{Mo}^{5+}$  d-d band transitions of a heavily distorted polyhedron in an octahedral crystal field as shown in Figure 1.9 according to ESR results of Łabanowska<sup>77</sup> (vide infra). Absorption bands at 2.03 and 1.28 eV are assigned to IVCT transitions of the type  $\text{Mo}^{5+}\text{-O-Mo}^{6+} \rightarrow \text{Mo}^{6+}\text{-O-Mo}^{5+}$ . The absorption band at 2.03 eV is attributed to an oxygen vacancy defect state, e.g.  $[\text{MoO}_5]^{5+}$ , while the band at 1.28 eV is due to a IVCT transition of a hexacoordinated defect state, e.g.  $[\text{MoO}_6]^{5+}$ . When comparing the energetic positions of the  $[\text{MoO}_5]^{5+}$  and the  $[\text{MoO}_6]^{5+}$  defect state within the band gap, the higher symmetry of the  $[\text{MoO}_6]^{5+}$  state should lead to an energetically more favourable state than that of  $[\text{MoO}_5]^{5+}$  due to a better charge compensation.

sample	polaron	$d_{yz}^1-d_{xz}^1$	IVCT <sup>1</sup>	$d_{yz}^1-d_{xy}^1$	IVCT <sup>2</sup>	$d_{yz}^2-d_{xz}^2$	bg	$d_{yz}^1-d_{xy}^1$	$d_{yz}^2-d_{z^2}^2$
A	0.68	0.94	1.18	1.53	1.920	2.41	2.76	3.04	3.82
B	0.68	0.84	1.23	1.53	1.990	2.46	2.90	2.97	3.80
C	0.55	0.82	1.28	1.57	2.028	2.48	2.94	3.09	3.88
D	0.56	0.85	1.27	1.59	2.045	2.55	2.94	3.12	3.82
E	0.54	0.84	1.26	1.64	2.069	2.61	2.97	3.21	3.89

**Table 1.4:** Band positions in eV of the DR-UV/VIS spectra.

sample	polaron	$d_{yz}^1-d_{xz}^1$	IVCT <sup>1</sup>	$d_{yz}^1-d_{xy}^1$	IVCT <sup>2</sup>	$d_{yz}^2-d_{xz}^2$	bg	$d_{yz}^1-d_{xy}^1$	$d_{yz}^2-d_{z^2}^2$
A	0.01	0.01	0.20	0.03	0.15	0.07	0.45	0.05	0.04
B	0.00	0.05	0.12	0.06	0.10	0.05	0.59	0.01	0.02
C	0.06	0.04	0.18	0.02	0.10	0.04	0.44	0.04	0.07
D	0.14	0.04	0.12	0.03	0.20	0.02	0.33	0.04	0.08
E	0.17	0.02	0.19	0.02	0.18	0.05	0.34	0.01	0.01

**Table 1.5:** Relative integral intensities of the absorption bands  $I_r$  normalised to the sum of intensities.

Łabanowska<sup>77</sup> has explained ESR results, using the crystal field model by different types of oxygen defects which are formed depending on the oxygen partial pressure and the preparation tempera-

tures employed. Accordingly, the Mo-O bonding in  $\text{MoO}_3$  may be described as mainly ionic, which should result in d-d transitions due to an octahedral crystal field splitting. Upon reduction/oxidation of  $\text{MoO}_3$  a pentacoordinated  $\text{Mo}^{5+}$  with an oxygen vacancy and a hexacoordinated  $\text{Mo}^{5+}$  were characterised. The crystal field splittings of these centres were calculated to be  $E_1 = E_{z^2} - E_{yz} = 2.65$  eV,  $E_2 = E_{xy} - E_{yz} = 3.83$  eV and  $E_3 = E_{xz} - E_{yz} = 5.08$  eV in case of the hexacoordinated  $\text{Mo}^{5+}$  centre and  $E_1 = E_{z^2} - E_{yz} = 3.4$  eV,  $E_2 = E_{xy} - E_{yz} = 1.5$  eV and  $E_3 = E_{xz} - E_{yz} = 1.0$  eV in case of the hexacoordinated  $\text{Mo}^{5+}$  centre. The calculated crystal field splittings of Łabanowska support the presented interpretation of the nature of the UV/VIS absorption bands. The differences between the energetic states obtained by Łabanowska and the band positions determined by DR-UV/VIS spectroscopy may be caused by a different degree of reduction of the samples investigated in both studies.

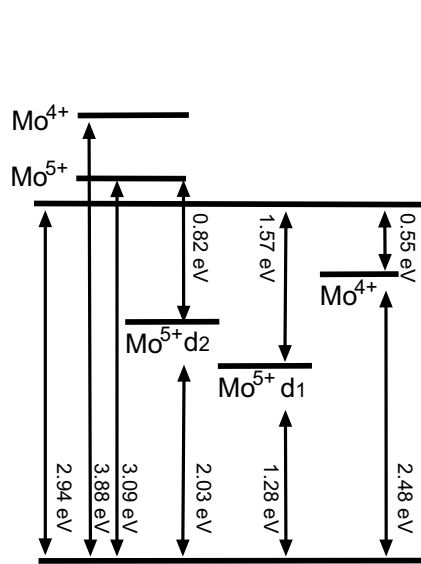


**Fig. 1.9:** Electronic states as obtained by fitting of the DR-UV/VIS spectrum of  $\text{MoO}_{3-x}$  under the assumption of a band theory model to be valid for the description of the electronic structure of  $\text{MoO}_{3-x}$ .

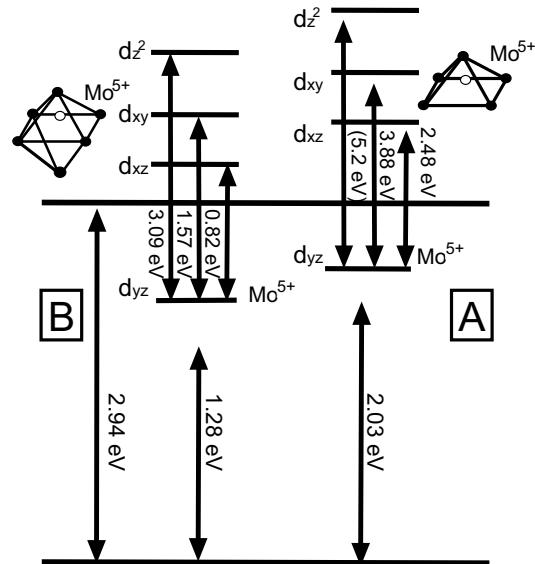


**Fig. 1.10:** Electronic states as obtained by fitting of the DR-UV/VIS spectrum of  $\text{MoO}_{3-x}$  under the assumption of a crystal field model to be valid for the description of the electronic structure of  $\text{MoO}_{3-x}$ .

The relative integral intensities ( $I_r = I_i / \sum I_a$ ) of the absorption bands being 0.08 (3.88 eV) 0.04 (3.09 eV) 0.45 (2.94 eV), 0.04 (2.48 eV), 0.10 (2.03 eV), 0.18 (1.28 eV), 0.02 (1.57 eV), 0.04 (0.82 eV), and 0.06 (0.55 eV), further support this interpretation. Two groups of absorption bands are found (Figure 1.10). The group of absorption bands at 2.94, 2.03 and 1.28 eV have relative integral intensities between 0.10 and 0.45. The second group of bands with positions at 3.88, 3.09, 2.48, 1.57 and 0.55 eV have relative integral intensities smaller than 0.08. The first group is formed

by the bandgap and IVCT transitions, while the second group of absorptions is caused by d-d transitions. However, the low energy absorption band which is observed at 0.55 eV cannot be assigned to a d-d transition according to Łabanowskas results. Because of its low integral intensity it may be assigned to an bipolaron. Such absorptions have been reported for  $\text{WO}_3$  to be located at 0.54 eV.<sup>116</sup> The shift of its position to lower energies with increasing number of oxygen vacancies further support this view, because the difference between the local distortions around the bipolaron and the strain within the lattice decreases as well.

Porter et al.<sup>4</sup> correlated the systematic blue shift of the absorption band between 2-2.5 eV with increasing oxygen/metal ratio to the degree of reduction of the molybdenum oxides.<sup>4, 78</sup> This correlation was established from the UV/VIS spectra of  $\text{Mo}_4\text{O}_{11}$ ,  $\text{Mo}_9\text{O}_{26}$ ,  $\text{MoO}_2$  and  $\text{H}_{0.34}\text{MoO}_3$ <sup>117</sup> by applying Meyer's rule<sup>118</sup> which is valid under the assumption that the band structure and the mobility of the electronic carriers does not change. This correlation of Porter et al.<sup>4</sup> is used to gain information on the electronic properties and, hence, the stoichiometries of the  $\text{MoO}_{3-x}$  samples.

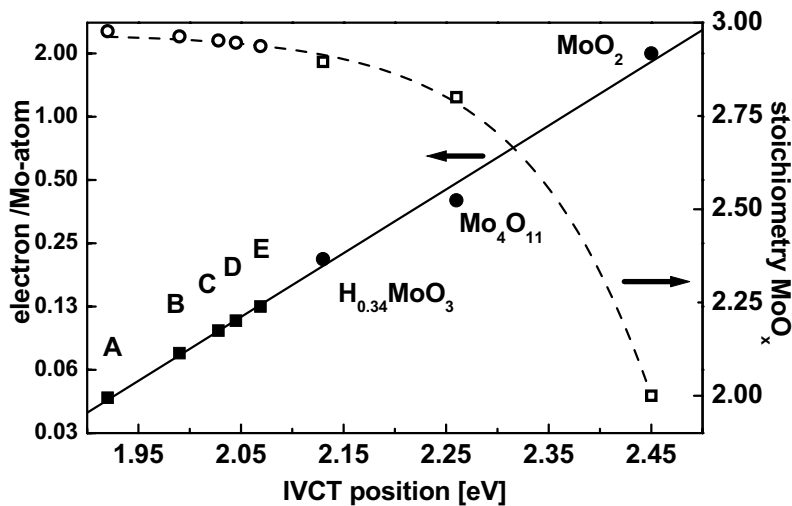


**Fig. 1.11:** The number of electrons per Mo atom as a function of the position of the  $[\text{MoO}_5]^{5+}$ -IVCT transition for the different  $\text{MoO}_{3-x}$  samples (squares). The values of Porter<sup>4</sup> and Tinet<sup>117</sup> are also shown (circles).

When comparing the UV/VIS spectra of samples A to E, a blue shift of the IVCT absorption transition at 2 eV, which has been attributed to a  $[\text{MoO}_5]^{5+}$  defect centre, is observed (see Table 1.4). This blue shift can directly be correlated to an increasing number of electrons per Mo centre or indirectly to a decreasing oxygen/metal ratio of the molybdenum oxide (Figure 1.11).<sup>4</sup> The calculated oxygen/metal ratios decrease from sample A to E, as expected from the preparation method employed. The oxygen/metal ratios of the different  $\text{MoO}_{3-x}$  samples, were determined to be 2.977

(A), 2.963 (B), 2.952 (C), 2.946 (D) and 2.937 (E), respectively. All this obtained oxygen/metal ratios are higher than the corresponding values of reported intermediate oxides like  $\text{Mo}_4\text{O}_{11}$  (2.75),  $\text{Mo}_5\text{O}_{14}$  (2.8) or  $\text{Mo}_9\text{O}_{26}$  (2.89).<sup>28</sup> Due to the low number of oxygen vacancies in the oxygen/metal ratio range between 2.9 and 3, the  $\text{MoO}_3$  crystal structure is retained.

An oxygen vacancy was said to lead to a displacement of the Mo atom in direction of the terminal oxygens.<sup>119</sup> The lattice perturbations which are induced by this displacement of the Mo cation leading to a stronger deformed MoO polyhedra may be screened on a longer scale distance due to coulombic interaction. The strong local distortion of the defective Mo-O polyhedra due to the changed bonding and charge situation thus results in overall small lattice relaxations as detected by XRD. In addition to these strong local distortions, each polyhedron is also affected by the lattice deformation exerted by the other oxygen vacancies. This distortion which is experienced by Mo-O polyhedra determines the energetic position of the defect state with respect to the valence band and the conduction band, while the total number of the lattice defects determines the intensity of the absorption. Therefore, the observed increase of the IVCT absorption band position from 1.92 eV (Sample A) to 2.07 eV (sample E) may be explained by the increase of the additional distortion of the Mo-O polyhedra due to the increasing concentration of additional oxygen vacancies. Under the assumption of a random oxygen vacancy distribution throughout the crystal one oxygen vacancy may be estimated per 43  $\text{MoO}_3$  units in sample A, per 23  $\text{MoO}_3$  units in sample B, per 21  $\text{MoO}_3$  units C, per 19  $\text{MoO}_3$  units in sample D, and one per 16  $\text{MoO}_3$  units in sample E.

In addition to the above described blue shift of the IVCT band from 1.93 to 2.13 eV, a less pronounced blue shift of the second IVCT band is observed from 1.21 to 1.29 eV. The smaller blue shift of this IVCT band is explained by a less pronounced distortional effect of hexacoordinated  $[\text{MoO}_6]^{5+}$  defect centres on the  $\text{MoO}_3$  lattice as compared to pentacoordinated  $[\text{MoO}_5]^{5+}$  defect centres because of their higher coordination number. The observed shift of the  $d_{yz}$ - $d_{xz}$  transition of the pentacoordinated  $[\text{MoO}_5]^{5+}$  centre from 2.40 to 2.64 eV further supports the above described model, because the stronger the repulsive interactions between  $[\text{MoO}_5]^{5+}$  defect centres the more energetically unfavoured the  $d_{xz}$  orbital should be. For the  $d_{yz}$ - $d_{xz}$  transition of the hexacoordinated  $[\text{MoO}_6]^{5+}$  a shift was not observed as expected.



### 1.1.3.3 Raman Micro-Spectroscopy

In Figure 1.12-1.14 the Raman spectra of the five different  $\text{MoO}_{3-x}$  samples are shown normalised with respect to the band at  $823 \text{ cm}^{-1}$ . All samples show the characteristic Raman bands of  $\text{MoO}_3$  (Figure 1.12). Sample A most closely resembles the single crystal Raman spectrum reported by Py and Maschke with characteristic Raman bands at 996 ( $A_g$ ,  $\nu_{as}$  M=O stretch), 822 ( $A_g$ ,  $\nu_s$  M=O stretch), 667 ( $B_{2g}$ ,  $B_{3g}$ ,  $\nu_{as}$  M-O-M stretch), 473 ( $A_g$ ,  $\nu_{as}$  O-M-O stretch and bend), 380 ( $B_{1g}$ ,  $\delta$  O-M-O scissor), 376 ( $B_{1g}$ ), 366 ( $A_{1g}$ ,  $\delta$  O-M-O scissor), 334 ( $A_g$ ,  $B_{1g}$ ,  $\delta$  O-M-O bend), 293 ( $B_{3g}$ ,  $\delta$  O=M=O wagging), 285 ( $B_{2g}$ ,  $\delta$  O=M=O wagging), 247 ( $B_{3g}$ ,  $\tau$  O=Mo=O twist), 216 ( $A_g$ , rotational rigid  $\text{MoO}_4$  chain mode,  $R_c$ ), 197 ( $B_{2g}$ ,  $\tau$  O=Mo=O twist), 159 ( $A_g/B_{1g}$ , translational rigid  $\text{MoO}_4$  chain mode,  $T_b$ ), 129 ( $B_{3g}$ , translational rigid  $\text{MoO}_4$  chain mode,  $T_c$ ), 116 ( $B_{2g}$ , translational rigid  $\text{MoO}_4$  chain mode,  $T_c$ ), 100 ( $B_{2g}$ , translational rigid  $\text{MoO}_4$  chain mode,  $T_a$ ) and  $89 \text{ cm}^{-1}$  ( $A_g$ ,

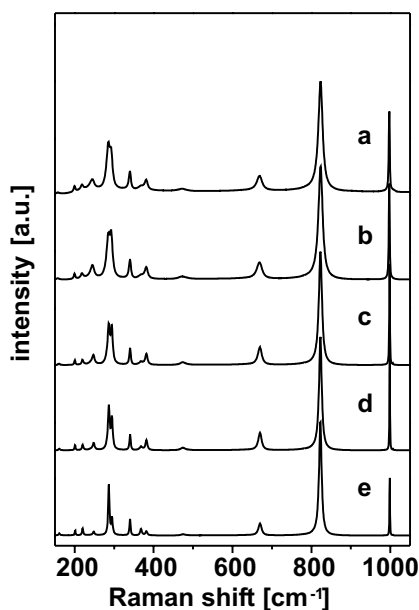


**Fig. 1.12:** Averaged Raman spectra of the data set of 100 Raman spectra of samples A to E in the energy range 150 to 1050  $\text{cm}^{-1}$ . Spectra are vertically shifted for better visualisation.

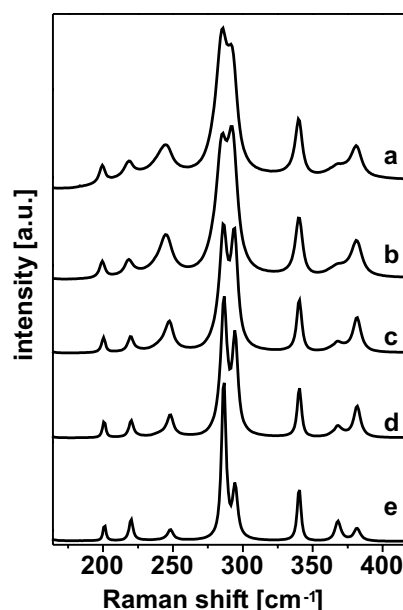


**Fig. 1.13:** Averaged Raman spectra of the data set of 100 Raman spectra of samples A to E in the energy range 150 to 400  $\text{cm}^{-1}$ . Spectra are vertically shifted for better visualisation.

translational rigid  $\text{MoO}_4$  chain mode,  $T_a$ ). The observed bands are assigned according to the single crystal study of Py et al<sup>30, 31</sup> and summarised in Table 1.6.

The  $\text{MoO}_3$ -lattice compensates the distortions exerted by oxygen vacancies via minor structural changes all over the crystal as suggested by UV/VIS and XRD results, i.e. a compression in the

c-direction and a expansion along the b-axis.

The Mo=O bond distances along the a- and b- axis (167 and 173 pm) are shorter than the Mo-O bond distance along the c-axis (195 pm). The Raman bands at  $995\text{ cm}^{-1}$  and  $823\text{ cm}^{-1}$  can be assigned to the stretching vibration of the terminal Mo=O bonds along the a and b axis. The bridging oxygens (longer bond distances) along the c-axis are the most weakly bound oxygens as shown by Mestl et al.<sup>68</sup> The generation of oxygen vacancies should therefore lead to anion vacancies along the c-axis. Therefore, a displacement of the Mo atom toward the terminal oxygen in b-direction can be expected upon loss of bridging oxygen, thus weakening the bond to the terminal O atom along the a-axis.

Because the variation of the stoichiometry within the sample series is rather small, only minor variations of the Raman bands of localised vibrations, e.g. the  $666$ ,  $823$  or  $995\text{ cm}^{-1}$  band are expected. Because of the different degree of crystallisation of the samples and the lower oxygen/metal ratios, a broadening of the intense bands at  $823$  and  $995\text{ cm}^{-1}$  should be expected. The higher the concentration of oxygen vacancies the shorter the lifetime of the excited state should be and should, therefore, lead to a broadening of the Raman bands. Exactly this is experimentally found (Figure 1.14). Moreover, Raman bands are observed at  $1004$  and  $1008\text{ cm}^{-1}$  and identified as the stretching vibrations of newly formed terminal Mo=O bond in b-direction of tetrahedra with an anion deficiency, in accordance with Raman studies of Mestl et al.<sup>68</sup> With increasing oxygen vacancy concentration, these Raman bands broaden and increase in intensities (Figure 1.14). The intense Raman bands at  $995\text{ cm}^{-1}$  are asymmetrically broadened to lower energies, which is explained by a superposition of at least two different Mo=O species present in deeper reduced  $\text{MoO}_{3-x}$ . Further, a loss of the translational symmetry is expected because of the oxygen vacancies in the lattice. The broad background in the lattice phonon region which is most pronounced in sample E can be explained by a multitude of combination modes of acoustic and acoustic plus optical modes due the relaxation of the k-selection rule (Figure 1.13).

Lattice phonons which are polarised in the c-direction should be more sensitive to the structural changes of the lattice which were introduced by the different oxygen vacancy concentrations, because the perturbations which are caused by the oxygen vacancies are expected to be most

Raman	IR		Sym.	calc.	A	B	C	D	E
	TO	LO							
	1002	1002	B <sub>3u</sub>	999					
	962	1010	B <sub>2u</sub>	997	1011	1006	1006	1009 1004	1007
995			A <sub>g</sub>	998	997	998	998	997	997
995			B <sub>1g</sub>	996	985 966				
	818	974	B <sub>3u</sub>	822	956	958	958		
	814	825	B <sub>2u</sub>	822	823	823	823	823	823
819			A <sub>g</sub> , B <sub>1g</sub>	822	747		781		
666			B <sub>2g</sub> , B <sub>3g</sub>	668	669	669	669	668	668
473			A <sub>g</sub> , B <sub>1g</sub>	473	474	473	473	472	472
	545	851	B <sub>1u</sub> , A <sub>u</sub>	671		580 561	581	577	
	500	525	B <sub>3u</sub>	507		533	530	531	531
	441	505	B <sub>2u</sub>	507					
	388		B <sub>2u</sub>	380					
	363	390	B <sub>3u</sub>	358					
379			B <sub>1g</sub>	386	382	382	382	381	380
365			A <sub>g</sub>	365	368	368	368	368	368
	353	363	B <sub>2u</sub>	334					
	348	352	B <sub>3u</sub>	333					
338			B <sub>1g</sub>	329					
337			A <sub>g</sub>	327				340?	
291			B <sub>3g</sub>	290	294	294	294	292	291
283			B <sub>2g</sub>	285	286	287	286	285	285
			A <sub>u</sub>	281					
			B <sub>1g</sub>	270					
	268	343	B <sub>1u</sub>	276					
	260	260	B <sub>2u</sub>	267		241	241		
246			B <sub>3g</sub> , A <sub>u</sub>	257	248	248	248	245	245
217			A <sub>g</sub>	230	220	220	220	218	218
198			B <sub>2g</sub>	200	201	201	200	199	199
	228	228	B <sub>3u</sub>	227					
	192	192	B <sub>1u</sub>	192	183				
158			A <sub>g</sub>	162	161	161	160	157	157
154			B <sub>1g</sub>	155					
129			B <sub>3g</sub>	138	127	132	131	130	127
116			B <sub>2g</sub>	118					
99			B <sub>1g</sub>	102					
83			A <sub>g</sub>	84					
	53	53	B <sub>2u</sub>	53					
			A <sub>u</sub>	49					
	44	44	B <sub>3u</sub>	44					

**Table 1.6:** Raman and IR position as reported by<sup>30, 95</sup> and the positions of the Raman bands of the samples A to E.[cm<sup>-1</sup>]

pronounced in c-direction. Translational or rigid chain Raman modes should be sensitive to the particle sizes of the samples. However, the rigid chain modes along the b direction (band at 159 cm<sup>-1</sup>) are not experimentally resolved and the rigid chain modes along the a direction (A<sub>g</sub>, 82 cm<sup>-1</sup>, B<sub>1g</sub>, 98 cm<sup>-1</sup>) are only weakly observed due to the notch filter employed (not shown). Hence, changes in the band profiles of these rigid chain modes cannot be discussed.

The positions of the rigid chain modes along the c-direction ( $B_{2g}$ , 117,  $B_{3g}$ , 130  $\text{cm}^{-1}$ ) were determined to be 117 and 130  $\text{cm}^{-1}$  (A and B) and 118 and 130  $\text{cm}^{-1}$  (C, D and E) (not shown). For sample A and B the observed intensity ratio  $I_{116}/I_{129}$  is 1.1 and 0.6, while samples C to E show all ratios of 0.3. This change of the  $I_{116}/I_{129}$  ratio resembles the trend found for the crystallite sizes of the samples. Hence, the observed changing intensity ratios are attributed to the altered crystallite sizes as shown in Figure 1.15.

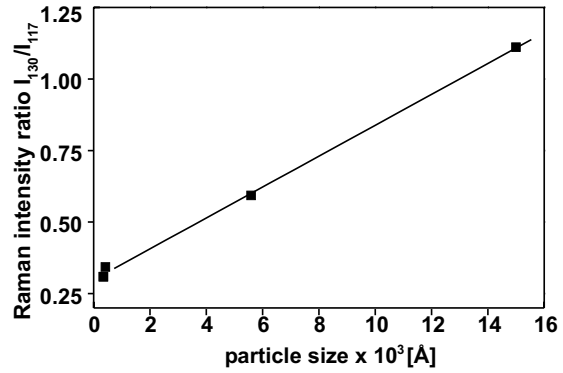
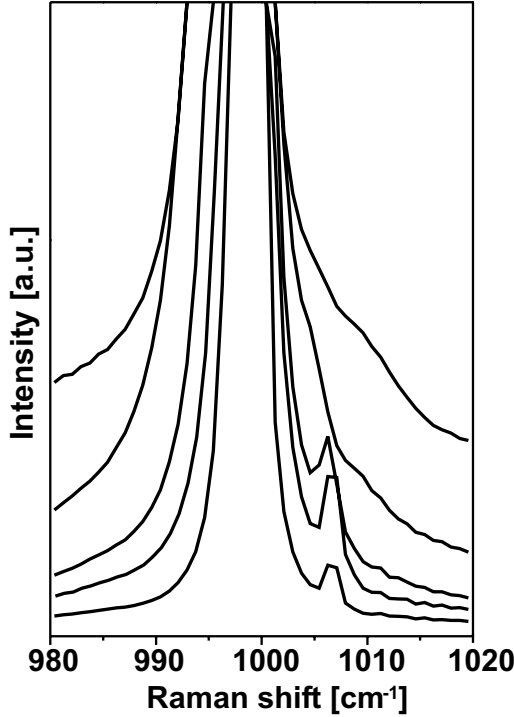


**Fig. 1.14:** (left side) Averaged Raman spectra of the data set of 100 Raman A to E in the energy range 950 to 1050  $\text{cm}^{-1}$ . Spectra are vertically shifted for better visualisation.

**Fig. 1.15:** The intensity ratios of the rigid chain modes at 117 and 130  $\text{cm}^{-1}$  as a function of the normalised particle size as determined by XRD and SEM.

In Figure 1.16, the intensity of the wagging modes of the terminal M=O groups at 283 ( $B_{2g}$ ) and 293  $\text{cm}^{-1}$  ( $B_{3g}$ ) which are polarised parallel to the c-direction are shown as a function of the oxygen/metal ratio. The ratio  $I_{283}/I_{290}$  of sample A resembles the value found in the single crystal spectrum of Py and Maschke, where the  $B_{2g}$  has three times the intensity of the  $B_{3g}$  mode. With increasing oxygen vacancy concentrations, a shift of the  $B_{3g}$  mode position is observed by 3  $\text{cm}^{-1}$  to lower energy. In sample E, these two wagging modes are hardly resolved any more. Because these wagging modes are both polarised parallel to the c-direction but belong to different symmetry races, the intensity ratios reflect symmetry changes due to the distortions along the c-axis introduced by the oxygen vacancies.

The ratio  $I_{283}/I_{290}$  decreases from sample A to E (Figure 1.16) as a function of the sample stoichiometry. The ratio  $I_{283}/I_{290}$  is linearly correlated with the oxygen vacancy concentration of the samples. Therefore, the intensity ratio of the wagging modes at 283 and 290  $\text{cm}^{-1}$  can easily be used to determine the stoichiometry of the sample. However, if the oxygen/metal ratio is smaller than 2.94 these two Raman bands cannot

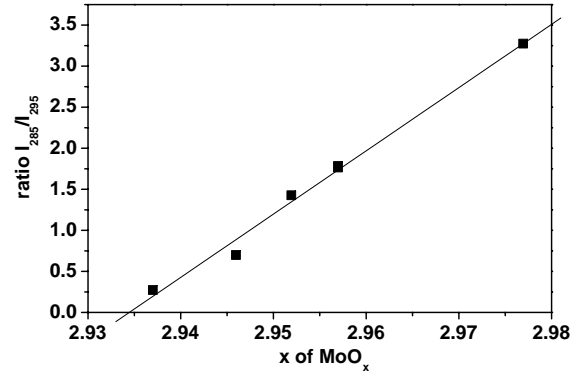


**Fig. 1.16:** Intensity ratio of the Raman bands at 285 and 295  $\text{cm}^{-1}$  ( $I_{285}/I_{295}$ ) as a function of the sample stoichiometry as determined by DR-UV/VIS spectroscopy.

be clearly resolved. Hence for lower oxygen/metal ratio it cannot be used and another measure for the oxygen/metal ratio has to be found.

The observed relative Raman cross section as determined by the integral intensity of the Raman band at 823  $\text{cm}^{-1}$  is shown in Figure 1.17 as function of the stoichiometry of the samples. The observed Raman efficiencies (■, full line) are the product of the absorption efficiency (dotted line) and the efficiency of the Raman scattered light not to be re-absorbed (dashed line).

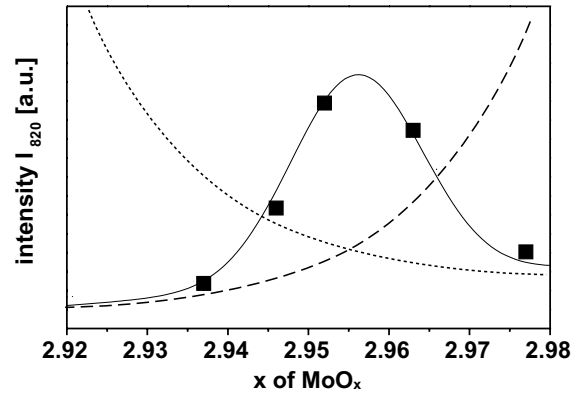


**Fig. 1.17:** Overall Raman efficiency (■, full line) as a function of the sample stoichiometry as determined by DR-UV/VIS spectroscopy. The observed Raman efficiencies are the product of the absorption efficiency (dotted line) and the efficiency of the Raman scattered light not to be re-absorbed (dashed line).

the IVCT transition at 2 eV is expected to satisfy

the required conditions for a resonant coupling of the Raman scattering to the electronic transition, because a large displacement of the normal coordinate with respect to the ground state is expected for the  $[\text{MoO}_5]^{5+}-[\text{MoO}_6]^{6+} \rightarrow [\text{MoO}_5]^{6+}-[\text{MoO}_6]^{5+}$ -IVCT transition at 2 eV in contrast to the  $[\text{MoO}_6]^{5+}-[\text{MoO}_6]^{6+} \rightarrow [\text{MoO}_6]^{6+}-[\text{MoO}_6]^{5+}$ -IVCT transition at 1.28 eV due the change of the coordination number of the involved polyhedra. Under the assumption of a resonant coupling of the Raman scattering to the  $[\text{MoO}_5]^{5+}-[\text{MoO}_6]^{6+} \rightarrow [\text{MoO}_5]^{6+}-[\text{MoO}_6]^{5+}$ -IVCT transition at 2 eV the

observed behaviour of the intensity can be explained by two factors affecting the measured intensity (Figure 1.17). These factors are the absorption of the exciting photons (see Figure 1.17 dashed line) and the re-absorption of the Raman scattered photons within  $\text{MoO}_{3-x}$  (see Figure 1.17 dotted line). The absorption efficiency is directly correlated to the efficiency of the Raman excitation. The re-absorption efficiency is correlated to the overall Raman scattering efficiency, because the Raman scattered light is partly re-absorbed and annihilated. The emitted Stokes Raman light of the band at  $823\text{ cm}^{-1}$  for example is red-shifted by 0.1 eV with respect to the excitation wavelength.

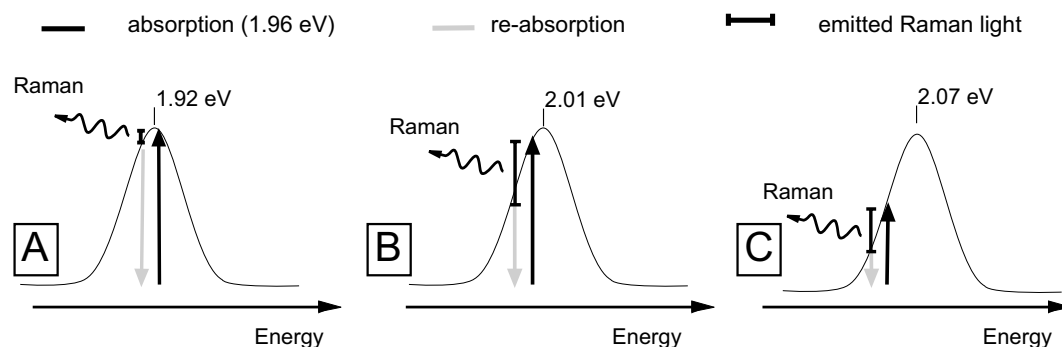


**Fig. 1.18:** The exact position of the excitation wavelength and the wavelength of the emitted Raman light with respect to the electronic absorption determines the overall efficiency of the Raman scattering process. Dark arrows indicate the position of the excitation wavelength, while the grey arrows indicate the re-absorption of the scattered Raman light. A, B and C reflect the situations found for samples A, C and E.

The exact position of the excitation wavelength with respect to the IVCT transition determines the overall yield of Raman scattered light as shown in Figure 1.18. The overall Raman scattering efficiency is in first order the product of both efficiencies, which are described by Gaussian shapes in analogy to the UV/VIS absorption. In Figure 1.18 the three different situations are illustrated. First, the excitation wavelength is blue-shifted by 0.04 eV with respect to the maximum of the IVCT transition (Figure 1.18A). The Raman light of the band at  $823\text{ cm}^{-1}$  then is red-shifted by 0.06 eV with respect to the maximum of the IVCT transition. Therefore, the overall Raman cross section is small because the absorption and re-absorption efficiency are comparably high (sample A). In Figure 1.18B, the excitation wavelength matches the low energy wing of the IVCT transition. The optimum match of the incoming laser light and the electronic transition leads to a resonance Raman enhancement of the laser excitation. The re-absorption efficiency of the red-shifted Raman light, on the other hand is dramatically smaller than the absorption efficiency of the excitation wavelength. The overall Raman scattering cross section thus becomes large (sample C). In Figure 1.18C,

the position of the excitation wavelength with respect to the maximum of the IVCT transition is located on the low energy tail of the IVCT transition (sample E). Therefore, the overall Raman efficiency is again small. Because of the energy mismatch between the incoming laser light and the absorption, only a weak resonance Raman enhancement does occur.

In summary, the blue-shift of the IVCT transition, which is caused by an increasing concentration of oxygen vacancies, is directly correlated to the overall Raman efficiency and may, therefore, be used for in situ Raman investigations to determine the oxygen vacancy concentration of  $\text{MoO}_{3-x}$  samples.

### 1.1.4 Conclusions

In this Chapter, UV/VIS spectroscopy has been used to characterise the electronic structure of molybdenum trioxide samples with different oxygen defect stoichiometries. UV/VIS spectroscopy was further used to quantify the concentration of the oxygen vacancies according to Meyer's rule.<sup>4, 118</sup> The shift of IVCT at 2 eV is explained by minor distortions of the  $\text{MoO}_6$ -polyhedra caused by lattice relaxations which are induced by coulombic interactions due to additional oxygen vacancies. A model which is based on crystal field theory is used to interpret the DR-UV/VIS spectra of the  $\text{MoO}_{3-x}$  compounds. The obtained results are in good agreement with ESR investigations of Łabanowska.<sup>77</sup> This model obtained for  $\text{MoO}_{3-x}$  samples may be extended to the other intermediate molybdenum oxides between  $\text{MoO}_3$  and  $\text{MoO}_2$  because the reported correlation of Porter et al. was established with experimental data of intermediate molybdenum oxides.<sup>4</sup>

The observed Raman intensities indicated a resonant coupling of the Raman scattering to the IVCT transition at 2 eV. The strong influence of the exact position of the excitation wavelength on the observed intensity of the Raman band at  $823\text{ cm}^{-1}$  with respect to the position of the IVCT transition was explained by the interplay of absorption and re-absorption efficiency in case of resonant Raman scattering. The strong IVCT transition at 2 eV which has been related to a oxygen defective  $[\text{MoO}_5]^{5+}$  centre is further expected to play a key role when explaining a resonant Raman scattering of intermediate oxides with a excitation wavelength of 632.8 nm (1.96 eV) as shown in the following Section.

The sample stoichiometry as determined by DR-UV/VIS spectroscopy has been correlated with intensity ratio changes of the wagging modes at 295 and 285  $\text{cm}^{-1}$  observed in the Raman spectra. This correlation may be used to determine the degree of reduction of  $\text{MoO}_{3-x}$  by Raman spectroscopy. Further, it has been shown that the influence of the particle size as determined by SEM and XRD on the obtained Raman spectra was found to be rather small and limited to rigid chain modes. The correlation of the degree of reduction with the Raman spectral changes may be used for *in situ* Raman spectroscopic investigations to determine the influence of oxygen vacancies on the catalytic properties of  $\text{MoO}_3$  samples. This correlation is expected to help to understand *in situ* Raman data of  $\text{MoO}_{3-x}$  during selective oxidation conditions.

## 1.2 Resonance Raman Spectroscopic Characterisation $\text{Mo}_4\text{O}_{11}$ and $\text{MoO}_2$

### 1.2.1 Introduction

Intermediate molybdenum oxides like Magnéli phases,<sup>120</sup> e.g.  $\text{Mo}_4\text{O}_{11}$  or  $\text{Mo}_5\text{O}_{14}$ ,<sup>34</sup> are believed to be catalytically active.<sup>53, 121, 103</sup> With respect to  $\text{MoO}_3$  first ordered crystallographic shear planes,<sup>122</sup> then block or columnar structures are subsequently formed as a function of the oxygen vacancy concentration by the reorganisation of the initially random defects<sup>123</sup> prior to the crystallisation of  $\text{MoO}_2$ . Phase characterisations by X-ray diffraction (XRD)<sup>124, 82</sup> and transmission electron microscopy (TEM)<sup>54, 125</sup> have been reported of the molybdenum oxide system.

Structural properties, like the degree of polymerisation in case of polyoxo molybdenum species<sup>126</sup> or the degree of distortion of  $\text{MoO}_x$ -polyeders can be determined by Raman spectroscopy.<sup>127</sup> Hardcastle and Wachs<sup>93</sup> correlated Raman shifts with the M-O bond order and bond lengths. Furthermore, LRS provides useful information about the degree of crystallisation or about structural defects as shown in the previous section. Hence, Raman spectroscopy is suited for the characterisation of  $\text{MoO}_x$  catalysts. Although, numerous intermediate molybdenum oxide phases exist, mostly Raman or infrared (IR) spectroscopic characterisations of the stoichiometric oxides  $\text{MoO}_3$ <sup>30, 31</sup> and  $\text{MoO}_2$ <sup>32</sup> have been reported.

Olson and Schrader<sup>128</sup> reported the Raman spectrum of a thin film of  $\text{Mo}_4\text{O}_{11}$ . A similar Raman



spectrum of a thin film was obtained by Spevack and McIntyre<sup>32</sup> but not identified as  $\text{Mo}_4\text{O}_{11}$ . Up to now, however, no correlation has been reported of the structure of catalytically important reduced molybdenum oxides as determined by Raman spectroscopy and their catalytic behaviour. One reason for this may be the often reported small Raman scattering efficiency of intermediate molybdenum oxides.<sup>36</sup> Due to this small efficiency a relation of *in situ* Raman spectroscopic results and catalytic activities may not unambiguously deducible because phases or compounds present in the catalyst may escape Raman detection. Especially in case of molybdenum intermediate oxide phases with their estimated small Raman cross sections, *in situ* Raman detection may be limited. Therefore, conditions have to be found for *in situ* Raman spectroscopy to overcome this problem. Due to this small Raman cross sections, the sensitivity of the spectrometer determined by the optical devices and the detector may have to be improved to detect these compounds. In cases of strongly absorbing materials the re-adsorption of the emitted Raman light strongly reduces the observed Raman cross section, a resonant enhancement of the Raman scattering by selecting a proper excitation wavelength, may be of crucial importance to detect the Raman spectra of such materials. The results of the previous section indicated resonant coupling of the Raman scattering to the IVCT transition at 2 eV to be operative in molybdenum trioxide.

The enormous structural variability of molybdenum oxides<sup>103, 129, 130</sup> leads to different electronic and, therefore, optical properties<sup>4, 81</sup> of each intermediate oxide phase. The valence band of such oxides is generated by oxygen 2p- $\pi$  orbitals, while the conduction band is formed by overlapping metal 4d and 5s bands.<sup>3</sup> Low energy absorption bands in substoichiometric  $\text{MoO}_3$  are observed at about 2 eV due to intervalence transfer transitions (IVCT) between  $\text{Mo}^{5+}-\text{O}-\text{Mo}^{6+}$  and  $\text{Mo}^{5+}-\text{Mo}^{6+}$  (see previous section),<sup>78, 91, 88</sup> which form additional conduction bands with respect to  $\text{MoO}_3$ . The additional charge carriers formed during the reduction process are injected into the bands and distort the lattice in their surroundings. This coupled electron-lattice distortion is called polaron. Porter et al.<sup>4</sup> observed these polaron bands at 2.48 eV and at 2.13, 2.42 and 1.3(sh) eV for  $\text{MoO}_2$  and  $\text{Mo}_4\text{O}_{11}$ , respectively. The number of charge carriers injected into this additional bands affect the absorption in the visible regime according to Meyer's rule.<sup>118</sup> Therefore, the systematic blue shift of the absorption band between 2-2.4 eV with decreasing metal-oxygen ratio can directly be correlated to the degree of reduction of the molybdenum oxide as shown in the previous section.<sup>68</sup> These

electronic properties of reduced molybdenum oxides may explain a possible resonance Raman effect operative in molybdenum oxides when using a He-Ne laser (632.8 nm/1.96 eV) in contrast to the often used frequency doubled Nd-YAG (532 nm/2.33 eV) or argon lasers (514 nm/2.41 eV). Resonant absorption due to the observed strong IVCT transition at about 2 to 2.5 eV could lead to an enhanced Raman cross section.

The structure of  $\text{MoO}_3$  and its Raman spectrum has been described in the previous Section. In Figure 1.19 the atomic motions are shown of the Raman vibrations for the Raman bands observed at 285, 666, 823 and  $995\text{ cm}^{-1}$ . The Raman bands in the high energy regime may be understood as strongly localised vibrations. Therefore, the application of the Hardcastle-Wachs approach leads to correct Mo-O bond distances, as calculated from the Raman shifts with the exception of the band at  $823\text{ cm}^{-1}$ .<sup>131</sup>

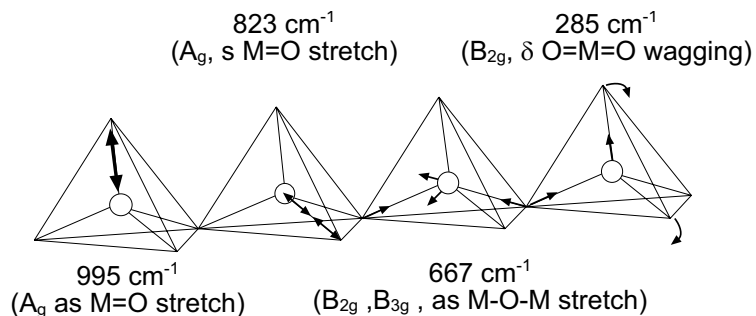


**Fig. 1.19:** Schematic drawing of the atomic motions for the Raman bands at 285, 666, 823 and  $995\text{ cm}^{-1}$ .

The structure of  $\text{MoO}_2$  is of a distorted rutile type. Along the a-axis, the  $\text{MoO}_6$ -octahedra are joined by sharing edges to form strings (Figure 1.20). XRD analysis of monoclinic  $\text{MoO}_2$  (P21/c,  $a = 5.610\text{ \AA}$ ,  $b = 4.857\text{ \AA}$ ,  $c = 5.626\text{ \AA}$ ,  $\beta = 120.9^\circ$ ) gives Mo-O bond distances of 1.968 to 1.970  $\text{\AA}$  (Mo-O(I)) and 2.075 to 2.077  $\text{\AA}$  (Mo-O(II)).<sup>132</sup> Raman bands of monoclinic  $\text{MoO}_2$  were observed at 744, 589, 571, 495, 461, 363, 345, 228 and  $203\text{ cm}^{-1}$  with a broad wing of the Rayleigh scattering, due to the metallic state of  $\text{MoO}_2$ .<sup>132</sup> The Raman bands at 744 and  $589\text{ cm}^{-1}$  may be attributed to the Mo-O(I) and Mo-O(II) stretching vibrations.

Orthorhombic  $\text{Mo}_4\text{O}_{11}$  is built up by  $\text{ReO}_3$ -slabs (layers), which can be described as being formed by three layers of, mutually interconnected by  $\text{MoO}_4$ -tetrahedra (Figure 1.20).<sup>133</sup> The adjacent rows of  $\text{MoO}_6$ -polyhedra are parallel oriented in contrast to the monoclinic form of  $\text{Mo}_4\text{O}_{11}$ . Three quarters of the Mo atoms in the  $\text{Mo}_4\text{O}_{11}$  structure are sixfold coordinated and the remaining quarter is

tetrahedrally coordinated. The different Mo-O bond distances in  $\text{Mo}_4\text{O}_{11}$  have been determined to be 1.743-1.764 Å for the tetrahedrally coordinated Mo. For the three short Mo-O bonds in the sixfold coordinated Mo bond distances were found of 1.742-1.770 Å, 1.775-1.810 Å and 1.866-1.924 Å, respectively. The remaining bond distances in the  $\text{MoO}_6$ -polyhedra were determined to be 2.110-2.15 Å, 2.056-2.097 Å and 1.983-2.023 Å, respectively. Olson and Schrader<sup>128</sup> reported the Raman spectrum of a thin film supported on Si which contained monoclinic and orthorhombic  $\text{Mo}_4\text{O}_{11}$  with Raman bands at 908, 880, 834, 792, 730, 451, 430, 377 and 186  $\text{cm}^{-1}$ .

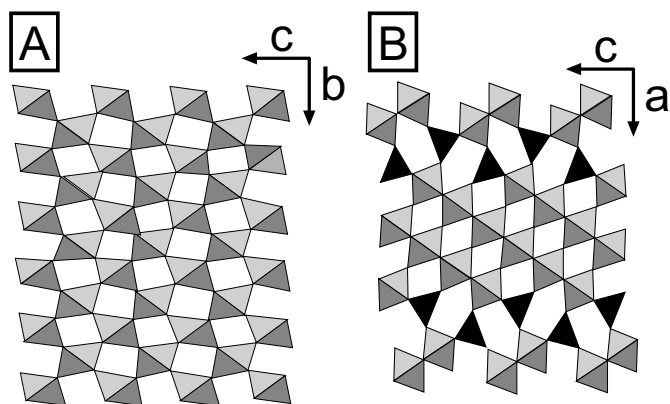


**Fig. 1.20:** *A: Structure of  $\text{MoO}_2$ , the  $\text{MoO}_6$ -octahedra are joined along the  $a$ -axis by sharing edges to form strings B: Structure of orthorhombic  $\text{Mo}_4\text{O}_{11}$  build by  $\text{ReO}_3$ -slabs, which can be described as being formed by three layers of  $\text{MoO}_6$ -polyhedra, mutually interconnected by  $\text{MoO}_4$ -polyhedra.*

In this study, a sample was used containing orthorhombic  $\text{MoO}_3$ , monoclinic  $\text{MoO}_2$  and  $\text{Mo}_4\text{O}_{11}$  as identified by XRD. This multiphasic sample was diluted with hexagonal boron nitride as internal standard to evaluate the relative Raman cross sections of  $\text{MoO}_3$ ,  $\text{MoO}_2$  and  $\text{Mo}_4\text{O}_{11}$ . Boron nitride exhibits only one active Raman mode, the transverse optical mode at  $\nu_{TO}$  at 1367  $\text{cm}^{-1}$  ( $E_{2g}$ ).<sup>134</sup> The BN Raman band does not interfere with  $\text{MoO}_x$ -Raman bands. Boron nitrate as an insulator of white colour does not absorb visible light. Therefore, boron nitrate suits as an optimal diluent and internal standard for proving resonant Raman enhancement as a function of the excitation wavelength in the visible regime. A resonance Raman effect in the reference compound boron nitride can be ruled out. Therefore, a comparison of the Raman spectra and the relative intensities of characteristic Raman bands of different Mo compounds as a function of excitation frequency should reveal a resonance Raman effect operating in oxygen defective molybdenum oxides,<sup>135</sup> e.g.  $\text{Mo}_4\text{O}_{11}$ .

## 1.2.2 Experimental

The sample containing  $\text{MoO}_3$ ,  $\text{MoO}_2$  and  $\text{Mo}_4\text{O}_{11}$  as determined by XRD was prepared by oxidation of commercially available  $\text{MoO}_2$  (Merck) at 673 K for 5h. The black colour of the starting material  $\text{MoO}_2$  was retained after this oxidation treatment. A second sample was prepared by diluting the oxidised sample 1:10 in hexagonal boron nitride (Goodyear). The mixture was homogenised in an agate mortar for 15 minutes.

The experimental conditions of XRD, Raman and DR-UV-VIS spectroscopy have been described on page 14. XRD crystalline phase identification was done with the ICDD-PDF-2 database.

A frequency doubled Nd-YAG laser (532 nm) and a HeNe-laser were used for the excitation of the Raman spectra. Notch filters for 632.8 nm and 532 nm (Kaiser optics) were applied to cut off the laser line and the Rayleigh scattering up to ca.  $150\text{ cm}^{-1}$ . Raman spectra of the undiluted sample were recorded using a HeNe laser with ca. 0.1 mW at the sample location. The laser power at the sample position in case of the diluted sample was about 10 mW for the Nd-YAG and 1.4 mW for the HeNe laser. All Raman spectra were recorded in backscattering geometry and two spectra with an accumulation time of 30 sec. (632 nm) and 200 sec. (532 nm) were averaged. Two sets of Raman images of 100 spectra each were recorded at identical sample positions with different excitation wavelengths. All Raman images were referenced to the internal standard boron nitride. The images were further normalised to maximum intensity of each single image to obtain a comparable contrast in all images.

## 1.2.3 Results and Discussion

### 1.2.3.1 XRD

In Figure 1.21, the XRD pattern of the undiluted, molybdenum oxide sample (A) is shown together with the sum of simulated XRD<sup>109</sup> patterns (B) of orthorhombic  $\text{MoO}_3$  (26%), monoclinic  $\text{MoO}_2$  (8%) and orthorhombic  $\text{Mo}_4\text{O}_{11}$  (66%). For the simulation, the JCCD-PDF2 data of orthorhombic  $\text{MoO}_3$  (Pbnm:  $a=3.963\text{ \AA}$ ,  $b=13.855\text{ \AA}$ ,  $c=3.696\text{ \AA}$ , JCCD-PDF2 No. 35069)<sup>75</sup> monoclinic  $\text{MoO}_2$  (P21/c,  $a=5.610\text{ \AA}$ ,  $b=4.857\text{ \AA}$ ,  $c=5.626\text{ \AA}$ ,  $\beta=120.9^\circ$ , JCCD-PDF2 No. 32671)<sup>132</sup> and orthorhombic

$\text{Mo}_4\text{O}_{11}$  (Pnma,  $a=24.49 \text{ \AA}$ ,  $b=5.457 \text{ \AA}$ ,  $c=6.752 \text{ \AA}$ , JCCD-PDF2 No. 5337)<sup>133</sup> were used. The lattice constants which thus determined to be  $a=3.952 \text{ \AA}$ ,  $b=13.827 \text{ \AA}$ ,  $c=3.688 \text{ \AA}$  ( $\text{MoO}_3$ ),  $a=5.610 \text{ \AA}$ ,  $b=4.804 \text{ \AA}$ ,  $c=5.587 \text{ \AA}$ ,  $\beta=119.7^\circ$  ( $\text{MoO}_2$ ) and  $a=24.418 \text{ \AA}$ ,  $b=5.442 \text{ \AA}$ ,  $c=6.734 \text{ \AA}$  ( $\text{Mo}_4\text{O}_{11}$ ). The observed small deviations of the lattice parameters of the compounds found in the oxidised sample with respect to the JCCD-PDF2 data are explained with the existence of lattice defects in all compounds due to their low preparation temperature.

### 1.2.3.2 Raman Microscopy

#### 1.2.3.2.1 Identification of $\text{Mo}_4\text{O}_{11}$

In Figure 1.22, three selected Raman spectra are shown of an image of 100 spectra recorded over a range of ca.  $400 \mu\text{m}^2$  of the undiluted oxidised sample. Three different Raman spectra were

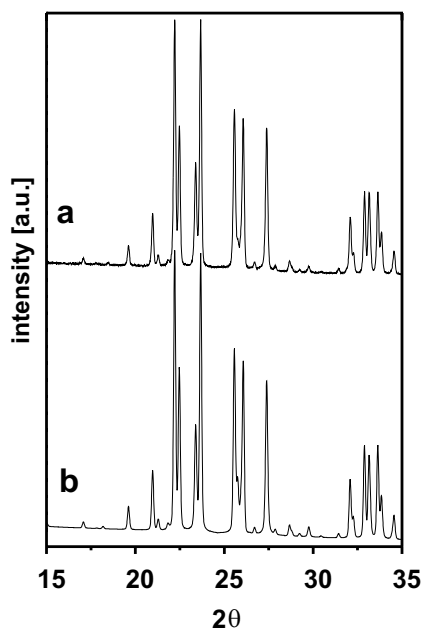


**Fig. 1.21:** *A: XRD pattern of the molybdenum oxide sample and B: Sum of simulated XRD patterns of  $\text{MoO}_3$ ,  $\text{Mo}_4\text{O}_{11}$  and  $\text{MoO}_2$ .*

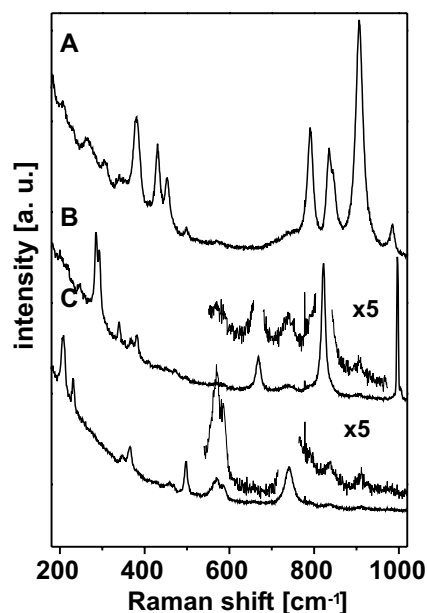


**Fig. 1.22:** *Characteristic Raman spectra of the undiluted sample taken with 632.8 nm excitation: A:  $\text{MoO}_3$ , B:  $\text{MoO}_2$  and C:  $\text{Mo}_4\text{O}_{11}$ . Raman spectra are vertically shifted for better visualisation.*

observed. Orthorhombic  $\text{MoO}_3$  (spectrum B of Figure 1.22) was detected with Raman bands at 247, 284, 292, 339, 352, 367, 380, 469, 667, 823, 996 and  $1004(\text{sh}) \text{ cm}^{-1}$ , while monoclinic  $\text{MoO}_2$  (spectrum C of Figure 1.22) gave Raman bands at 207, 230, 347, 364, 458, 496, 569, 585 and  $740 \text{ cm}^{-1}$ . The observed Raman bands of  $\text{MoO}_3$  and  $\text{MoO}_2$  compare well with the reported litera-

ture values and can be assigned accordingly.<sup>30-32</sup> The third compound was identified as orthorhombic  $\text{Mo}_4\text{O}_{11}$ <sup>128, 136</sup> (spectrum A in Figure 1.22) with Raman bands at 183, 206, 229, 264, 306, 340, 380, 431, 452, 498, 568, 744(sh), 790, 835, 843, 907 and 985  $\text{cm}^{-1}$ .

The Raman bands at 907 and 985 of  $\text{Mo}_4\text{O}_{11}$  are attributed to terminal Mo-O vibrations, while the observed Raman bands at 835 and 843  $\text{cm}^{-1}$  are ascribed to bridging Mo-O<sub>2</sub> vibrations. The Raman bands at 744(sh) and 790  $\text{cm}^{-1}$  are attributed to bridging Mo-O<sub>3</sub> vibrations. Due to the crystal structure of  $\text{Mo}_4\text{O}_{11}$  two sets of independent Raman bands of terminal Mo-O and bridging Mo-O<sub>2</sub> vibrations are expected. Therefore, the Raman bands at 835, 843 and 987  $\text{cm}^{-1}$  are interpreted as the terminal Mo-O and the bridging Mo-O<sub>2</sub> vibration, which is symmetry split, of a distorted tetrahedra similar to those found in  $\text{MoO}_3$ . The

second set of Raman bands at 790 and 907  $\text{cm}^{-1}$  are assigned to Mo-O and Mo-O<sub>2</sub> vibrations of the  $\text{MoO}_4$ -tetrahedra interconnecting the slabs of the more distorted tetrahedra.

The bond distances were calculated with the Hardcastle-Wachs model to be 1.69 Å (987  $\text{cm}^{-1}$ ), 1.73 Å (907  $\text{cm}^{-1}$ ), 1.76 Å (843  $\text{cm}^{-1}$ ), 1.76 Å (835  $\text{cm}^{-1}$ ), 1.79 Å (790  $\text{cm}^{-1}$ ) and 1.83 Å (744  $\text{cm}^{-1}$ ) respectively, and are in agreement with XRD data. However, the calculation is based on the assumption of an isolated Mo-O bond and this may lead to erroneous values especially in cases of symmetry related vibrations.<sup>93</sup>

In Figure 1.24 the calculated bond distances of  $\text{MoO}_3$ ,  $\text{Mo}_4\text{O}_{11}$  and  $\text{MoO}_2$  according to the Hardcastle-Wachs<sup>93</sup> are shown as a function of the bond distances obtained

XRD. For short bond distances the Hardcastle-Wachs model gives a good estimate of the XRD bond

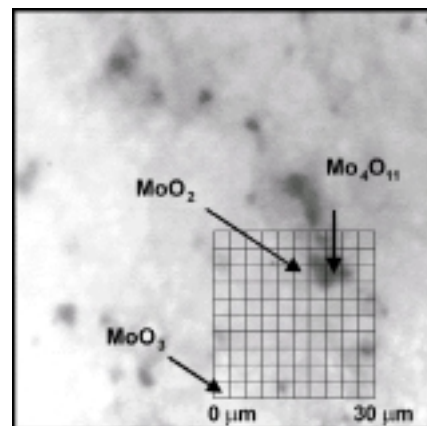


**Fig. 1.23:** Optical image of the diluted sample (sample: BN 1:10). The arrows indicate the positions at which the Raman spectra of  $\text{MoO}_3$ ,  $\text{MoO}_2$  and  $\text{Mo}_4\text{O}_{11}$  (Figure 1.25 and 1.26) were recorded.

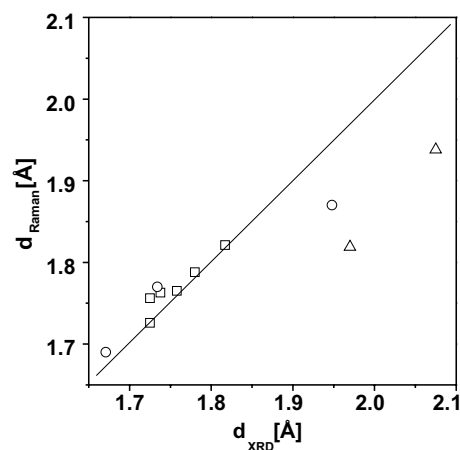


**Fig. 1.24:** Calculated bond distances ( $\text{MoO}_3$  ○,  $\text{Mo}_4\text{O}_{11}$  □ and  $\text{MoO}_2$  △) according to the Hardcastle-Wachs model as a function of bond distances determined by XRD.

distances as expected for the model's assumption of a localised harmonic oscillator. However, for longer bond distances, higher degrees of reduction (like  $\text{MoO}_2$ ) or symmetry related Raman bands (Raman band at  $823\text{ cm}^{-1}$  of  $\text{MoO}_3$ ) the Hardcastle-Wachs models fails to predict correct bond distances. Therefore, the predictions of this approach have to be taken with care, but still offer a first interpretation of observed Raman bands.

#### 1.2.3.2.2 Excitation at the Wavelength of 632.8 nm

In Figure 1.23, the optical image of the oxidised sample diluted in BN is shown as taken by the video camera attached to the microscope. The Raman image area is indicated by the grid in Figure 1.23. The rectangles in the grid indicate the positions on the sample at which the Raman spectra were recorded. Arrows in Figure 1.23 show the lateral positions on the sample at which the Raman

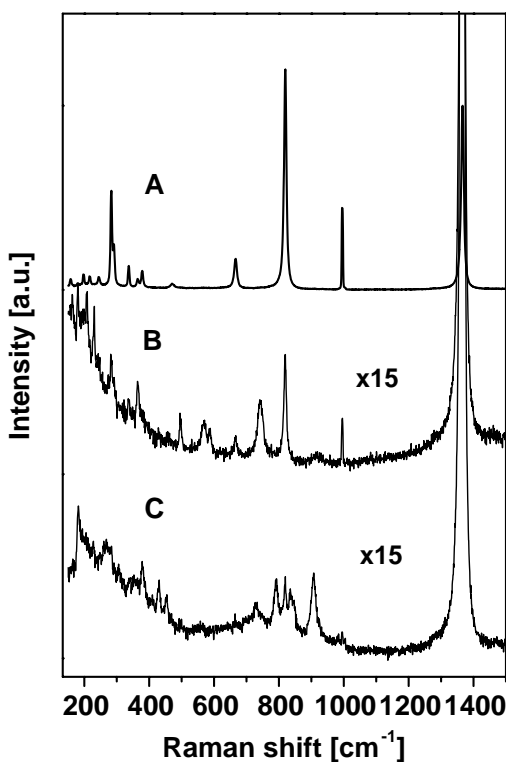


**Fig. 1.25:** Characteristic Raman spectra taken of the diluted sample at 632.8 nm: A:  $\text{MoO}_3$ , B:  $\text{MoO}_2$  and C:  $\text{Mo}_4\text{O}_{11}$ . Raman spectra are referenced to the boron nitride band at  $1367\text{ cm}^{-1}$  and vertically shifted for better visualisation. The Raman spectra were recorded at the positions indicated in Figure 1.23.

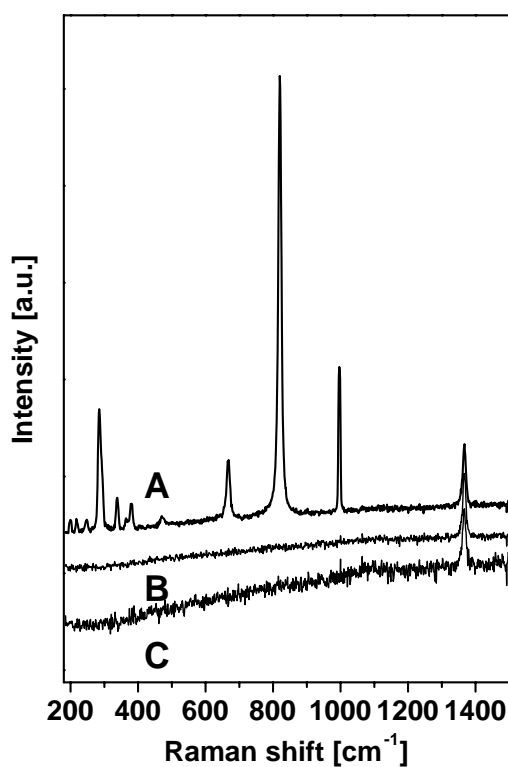


**Fig. 1.26:** Characteristic Raman spectra taken of the diluted sample at 632.8 nm: A:  $\text{MoO}_3$ , b:  $\text{MoO}_2$  and c:  $\text{Mo}_4\text{O}_{11}$ . Raman spectra are referenced to the boron nitride band at  $1367\text{ cm}^{-1}$  and vertically shifted for better visualisation. The Raman spectra were recorded at the positions indicated in Figure 1.23.

spectra of  $\text{MoO}_3$ ,  $\text{MoO}_2$  and  $\text{Mo}_4\text{O}_{11}$  (Figure 1.25) have been recorded. Dark regions are due to large particles consisting of  $\text{MoO}_2$  and  $\text{Mo}_4\text{O}_{11}$  as identified by the Raman spectra shown in Figure

1.25. All Raman spectra shown in Figure 1.25 and 1.26 are referenced to the intensity of the Raman band at  $1367\text{ cm}^{-1}$  of the internal standard boron nitride. All components of the sample *e.g.*  $\text{MoO}_3$ ,  $\text{MoO}_2$  and  $\text{Mo}_4\text{O}_{11}$ , are positively identified in the Raman image by their characteristic vibrations. In Figure 1.27 a to c, Raman images are shown as calculated from the relative intensities of the bands at  $996\text{ cm}^{-1}$  (characteristic of  $\text{MoO}_3$ , Figure 1.27 a),  $740\text{ cm}^{-1}$  (characteristic of  $\text{MoO}_2$ , Figure 1.27b) and  $907\text{ cm}^{-1}$  (characteristic of  $\text{Mo}_4\text{O}_{11}$ , Figure 1.27c ) when excited at  $632\text{ nm}$ . The dark areas in the upper and lower right of Figure 1.27 b and c are indicative for the presence of  $\text{MoO}_2$  and  $\text{Mo}_4\text{O}_{11}$ , whereas the darker area in the lower left corner of Figure 1.27a and d is due to Raman scattering of  $\text{MoO}_3$ .

#### 1.2.3.2.3 Excitation at the Wavelength of $532\text{ nm}$

In Figure 1.25, Raman spectra are shown which were recorded of the same sample area using a frequency doubled Nd-YAG laser with an excitation wavelength of  $532\text{ nm}$ . Only the Raman spectra of  $\text{MoO}_3$  and boron nitride could be detected using this laser excitation wavelength. The confocal Raman image generated from the intensities of the band at  $996\text{ cm}^{-1}$ , characteristic for  $\text{MoO}_3$ , is shown in Figure 1.27 a as referenced to the boron nitride band at  $1367\text{ cm}^{-1}$ . In accordance with literature data<sup>135</sup> both laser excitations,  $532\text{ nm}$  and  $632.8\text{ nm}$  identify  $\text{MoO}_3$  at identical positions in the Raman images 1.27 a and 1.27 d on page 40. Spectral traces of  $\text{Mo}_4\text{O}_{11}$  or  $\text{MoO}_2$ , however, could not be detected using the excitation wavelength of  $532\text{ nm}$  (Figure 1.27 e and 1.27 f).

These results indicate that an additional mechanism operates in oxygen defective molybdenum oxides which influences the absorption process due to their dark colour. It can be assumed that a resonance enhancement leads to the detection of the reduced Mo oxides when excited at  $632.8\text{ nm}$ . This effect may be based on the coupling of the Raman scattering process to electronic transitions due to oxygen vacancies in the lattice.

Since the reduced molybdenum oxides in general are of dark almost black colour, i.e. absorb visible light of any wavelength, a resonance Raman enhancement could be expected for both the  $632.8\text{ nm}$  and  $532\text{ nm}$  excitation wavelengths. However, this is not observed. Therefore, a more detailed analysis of UV/VIS spectra of molybdenum oxides is necessary in order to explain the observed



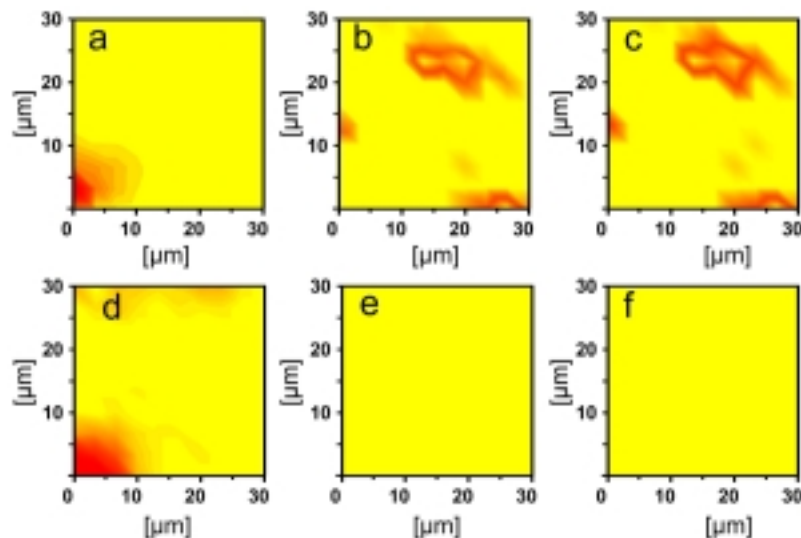


**Fig. 1.27:** Raman images excited at 632 nm: **a:** intensity distribution of the band at  $996\text{ cm}^{-1}$  characteristic for  $\text{MoO}_3$ , **b:** intensity distribution of the band at  $740\text{ cm}^{-1}$  characteristic for  $\text{MoO}_2$  and **c:** intensity distribution of the band at  $907\text{ cm}^{-1}$  characteristic for  $\text{Mo}_4\text{O}_{11}$ . Raman images recorded at 532 nm: **d:** intensity distribution of the band at  $996\text{ cm}^{-1}$  characteristic for  $\text{MoO}_3$ , **e:** intensity distribution of the band at  $740\text{ cm}^{-1}$  characteristic for  $\text{MoO}_2$  and **f:** intensity distribution of the band at  $907\text{ cm}^{-1}$  characteristic for  $\text{Mo}_4\text{O}_{11}$ .

resonance Raman effect. The understanding of the electronic absorption observed in the UV/VIS spectra of molybdenum oxides may be the basis for an understanding of the resonance effects in the Raman spectra.

### 1.2.3.3 UV/VIS Spectroscopy

The oxidised sample, characterised by XRD and Raman, and  $\text{MoO}_2$  are black and very strong absorbing materials. Therefore, the DR-UV/VIS spectra which were obtained of these materials are broad and structureless (Figure 1.28A) as compared to the UV/VIS spectrum of a  $\text{MoO}_{3-x}$  sample (Figure 1.28B). A detailed analysis of these broad and featureless spectra was thus not possible. The dilution of the oxidised sample or  $\text{MoO}_2$  in BN was not feasible either, because of the strong absorption of BN in the UV. Therefore, a series of  $\text{MoO}_{3-x}$  samples of the  $\text{MoO}_3$  structure has been prepared with different concentration of oxygen vacancies (see previous section). In Figure 1.28, the UV/VIS spectrum of one representative, reduced  $\text{MoO}_{3-x}$  sample is shown together with the fitted Gaussian curves. The absorption bands at 2.03 and 1.28 eV have been assigned to IVCT transitions of the type  $\text{Mo}^{5+}\text{-O-Mo}^{6+} \rightarrow \text{Mo}^{6+}\text{-O-Mo}^{5+}$ . The absorption band at 2.03 eV is attributed to an oxygen vacancy defect state, *e.g.*  $[\text{MoO}_5]^{5+}$ , while the band at 1.28 eV is due a IVCT transition

of a hexacoordinated defect state, *e.g.*  $[\text{MoO}_6]^{5+}$ .

The concentration of the oxygen vacancies has been correlated with the systematic blue shift of the absorption band between 2 and 2.5 eV.<sup>4, 70, 135</sup> This correlation was established by Porter et al. from the UV/VIS spectra of  $\text{Mo}_4\text{O}_{11}$ ,  $\text{Mo}_9\text{O}_{26}$  and  $\text{MoO}_2$  by applying Meyer's rule,<sup>118</sup> which is valid under the assumption that the band structure and the mobility of the electronic carriers does not change within the series of molybdenum oxides.

Because this correlation was setup using UV/VIS-data from  $\text{Mo}_4\text{O}_{11}$ ,  $\text{Mo}_9\text{O}_{26}$  and  $\text{MoO}_2$  the model which has been developed in the previous Section on the electronic properties of the  $\text{MoO}_{3-x}$  samples is also valid for intermediate molybdenum oxides like  $\text{Mo}_4\text{O}_{11}$ . Therefore, the attempt is made to explain the observed resonant Raman enhancement of  $\text{Mo}_4\text{O}_{11}$  and  $\text{MoO}_2$  by this model which is based on

crystal field theory. The major difference between the  $\text{MoO}_{3-x}$  samples and  $\text{Mo}_4\text{O}_{11}$  is seen in the number of charge carriers in the conduction bands, which in turn lead to minor changes of the band structure as indicated by the observed blue shift of the IVCT absorption between 1.93 and 2.5 eV.

#### 1.2.4 Discussion of the Resonance Raman Effect

The above described interpretation of the DR-UV/VIS spectra of reduced  $\text{MoO}_{3-x}$  samples can explain the experimental observation of the different Raman signal intensities for different excitation frequencies. The IVCT transition at 2.03 eV between a pentacoordinated  $\text{Mo}^{5+}$  and a hexacoordinated  $\text{MoO}^{6+}$  should lead to a displacement of the potential curve of the excited state with respect to the ground state as compared to the other transitions. This displacement is a prerequisite for the

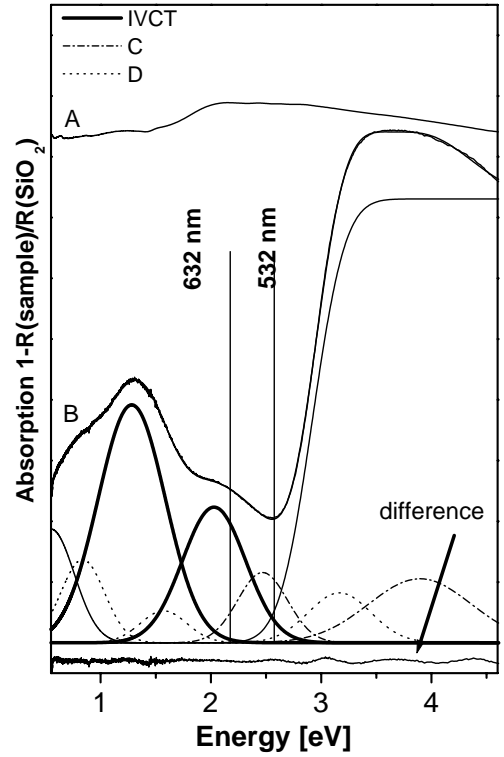


**Fig. 1.28:** DR-UV/VIS spectra of the oxidised  $\text{MoO}_2$  sample (A) and of  $\text{MoO}_{3-x}$  (B). The thick solid lines are assigned to IVCT transitions. Bands denoted with C (dashed lines) are attributed to d-d transitions of the  $[\text{MoO}_6]^{5+}$  defect state, while group of bands denoted with D (dotted lines) are assigned to d-d transitions of the  $[\text{MoO}_5]^{5+}$  defect state.

resonance Raman effect.<sup>38</sup> Therefore, it can be assumed that the observed resonance enhancement of the Raman scattering process is based on the coupling of the Raman scattering process to the electronic IVCT transition at 2 eV in nonstoichiometric  $\text{MoO}_{3-x}$ . Since oxygen vacancies cause this transition, it is assumed that similar IVCT transitions in intermediate molybdenum oxides like  $\text{Mo}_4\text{O}_{11}$  are the origin for the resonant enhancement of the Raman scattering.

Olson and Schrader,<sup>128</sup> as well as Spevack and McIntyre,<sup>32</sup> however, report the Raman spectrum of thin films of  $\text{Mo}_4\text{O}_{11}$  using an excitation wavelength of 514 nm. In the present study, the Raman spectrum of  $\text{Mo}_4\text{O}_{11}$  or  $\text{MoO}_2$  was not observed using an excitation wavelength of 532 nm. This was explained by a resonant coupling of the Raman scattering to the IVCT transition and the higher re-absorption efficiency with respect to the absorption efficiency as compared to the case when excited with 632 nm (Figure 1.3). These at first sight contradicting observations may be explained by different absorption efficiencies of the Raman scattered light in case of the thin films and the powdered material. In case of the thin films of  $\text{Mo}_4\text{O}_{11}$  supported on a reflecting support, the sample thickness may be smaller than the penetration depth of the excitation and Raman scattered light. Therefore, the observed re-absorption efficiency of thin films could be smaller as compared to powder samples. In contrast to thin film samples<sup>32, 128</sup> with a defined thickness on top of reflecting materials like metals or silicon, the absorbing and reflecting properties of solid powders are additionally strongly influenced by the particle size and shape,<sup>79</sup> which may lead as a consequence to a complete annihilation of the emitted Raman light.

This resonant enhancement of Raman scattering may be used to characterise catalytically important partial oxidation catalysts like mixed MoVW oxides by *in situ* Raman spectroscopy.<sup>34</sup>

### 1.2.5 Conclusions

The above described results indicate that a resonance enhancement is operative in molybdenum intermediate oxides based on the coupling of the Raman scattering process to electronic transitions caused by lattice oxygen vacancies. This enhancing resonance Raman effect was demonstrated to be responsible for the detection of the molybdenum oxides  $\text{MoO}_2$  and  $\text{Mo}_4\text{O}_{11}$  in an oxide mixture with  $\text{MoO}_3$  and BN by comparison of the Raman spectra obtained by excitation with 632.8 nm and

532 nm. In addition, a re-absorption process of the Raman scattered light leads to a yet undetermined reduction of the resonant Raman efficiency.

### 1.3 Summary

In this Chapter a resonance Raman effect has been proven to be operative in molybdenum oxides. For a excitation wavelength of 632 nm (1.96 eV) the observed Raman cross section varied as a function of the degree of reduction of  $\text{MoO}_{3-x}$  samples. This was explained by a coupling of Raman scattering to the IVCT transition at 2 eV due to oxygen vacancies present in the materials. The observed Raman cross section are explained by the different absorption and re-absorption efficiencies due a shift of the IVCT transition with increasing concentrations of oxygen vacancies. Further, a electronic model which is based on the crystal field theory has been proposed to explain the observed electronic transitions of  $\text{MoO}_{3-x}$ .

For  $\text{MoO}_2$  and the intermediate oxide  $\text{Mo}_4\text{O}_{11}$  a Resonance Raman effect was proven by comparing Raman images which have been recorded with different excitation wavelengths. The strong IVCT transition at 2 eV which has been related to a oxygen defective  $[\text{MoO}_5]^{5+}$  centre plays a key role when explaining a resonant Raman scattering of intermediate oxides with a excitation wavelength of 632.8 nm (1.96 eV) as shown in the following Sections.

The resonant enhancement of the Raman cross section of reduced transition metal oxides may be very helpful to detect structural changes of molybdenum oxide based catalysts induced by varying oxygen stoichiometries during *in situ* Raman studies of the structure-activity and selectivity relationships of this class of catalyst materials.

This observation is of particular interest for *in situ* Raman studies on molybdenum oxide based catalysts because the experimental setup, *e.g.* the choice of the laser, limits or expands the possibility of *in situ* Raman detection.

## Chapter 2

# Catalytic and Physico-Chemical Characterisation of a Molybdenum Oxide Based Partial Oxidation Catalyst\*

This Chapter is addressed to the study of physicochemical and catalytic properties of a catalyst with a composition and preparation procedure similar to industrial V and W promoted molybdenum oxides based catalysts, which are technically used for the selective oxidation of acrolein to acrylic acid. It is highly important to further develop not only the performance of such industrial catalysts but also the fundamental understanding of such multielement and multiphasic catalysts, *e.g.* the role of each phase and their interaction under catalytic action. This information is prerequisite for future material science tailoring of molecularly defined selective catalysts.

The objective of the first part of this Chapter is the investigation of the degree of reduction and elemental composition of a technical catalyst by means of XRD, Raman and SEM/EDX. Changes in the redox properties, elemental compositions and structure of the catalyst induced by the thermal activation in an inert atmosphere are discussed with respect to the altered catalytic performance of the thermally activated material in the methanol oxidation. The second part is addressed to a deeper understanding of the thermal activation procedure. Therefore, the structures of the different

---

\* Parts of this Chapter are published in G. Mestl, Ch. Linsmeier, R. Gottschall, M. Dieterle, J. Find, D. Herein, J. Jäger, Y. Uchida and R. Schlögl, Molybdenum Oxide based Partial Oxidation Catalysts: 1. Thermally induced Deficiency, Element and Structural Heterogeneity and the Relation to catalytic Performance, *J. Mol. Catal. A.*, **2000**, *162*, 455 and M. Dieterle, G. Mestl, J. Jäger, Y. Uchida, H. Hibst and R. Schlögl, Mixed molybdenum oxide based partial oxidation catalyst: 2. Combined X-ray Diffraction, Electron Microscopy and Raman Investigation of the thermal Stability of (MoVW)<sub>5</sub>O<sub>14</sub>-type Oxides, (submitted, *J. Mol. Catal. A*)

thermally activated catalyst samples were investigated by XRD, TEM and Raman.

## **2.1 Thermally Induced Oxygen Deficiency, Elemental and Structural Heterogeneity and the Relation to Catalytic Performance**

### **2.1.1 Introduction**

Catalysts based on molybdenum oxide are industrially used for partial oxidation of hydrocarbons *e.g.* unsaturated aldehydes to carbon acids<sup>1, 15, 16, 137</sup> and are active in oxidative coupling reactions.<sup>138</sup> For such oxides, the Mars-van Krevelen mechanism is generally accepted for selective partial oxidation reactions and describes the role of the so-called, active "lattice" oxygen for selective partial oxidations.<sup>139</sup> The adsorption of alkenes is suggested to occur at the (100) surface of MoO<sub>3</sub> on coordinatively unsaturated Mo sites under the formation of an allylic intermediate.<sup>140, 141</sup> The second reaction step, the nucleophilic oxygen insertion, is thought to occur on the (010) surface *via* the formation of a  $\sigma$  bond between the "lattice oxygen" and the allylic intermediate. The nucleophilic oxygen species is then inserted into the hydrocarbon to give the oxygenated product, which desorbs, leaving an oxygen vacancy at the catalyst surface.<sup>142</sup> This oxygen vacancy is re-oxidised in the last step of the catalytic cycle and it is suggested that this occurs via oxygen bulk diffusion. However, the actual nature of the "lattice" oxygen is still not fully unravelled, and it is still under debate which of the different possible metal-oxygen species actually take part in the oxygen insertion reaction.<sup>15, 46</sup> From this accepted model, it can be assumed that the surface oxygen defects generated during catalysis may be replenished either by surface oxygen diffusion, by oxygen diffusion through the surface near layer or by oxygen bulk diffusion (Figure 2.1). It may further be anticipated that each of these three layers has a different chemical composition and structure. Moreover this three-layer model may still be too simple and the actual catalyst may exhibit spatial differences in composition and structure. It may be anticipated that oxygen diffusivities are affected by the elemental compositions and the geometric structures of the catalyst phases. The real metal-oxygen stoichiometry and defect structure of molybdenum oxides thus may play an important role in selective partial oxidation reactions. It can be assumed that the degree of reduction, and hence

the presence of reduced surface metal centres, strongly affects the adsorption properties of hydrocarbons, and the C-H bond activation. The electronic properties of reduced molybdenum oxides, *i.e.* high electron density at the surface, may effect the oxygen activation.

X-ray diffraction (XRD) and transmission electron microscopy (TEM) literature provides information about structural changes of molybdenum oxides<sup>34, 43, 44, 73, 110, 120, 122, 124, 133, 143-153</sup> as function of their degree of reduction. The loss of oxygen from the  $\text{MoO}_3$  lattice first was suggested to lead to a Mo-Mo bond across the anion vacancy.<sup>75, 154</sup> These defects are mobile and order to extended shear defect structures upon further reduction.<sup>54, 101, 119, 124</sup> A whole series of oxygen deficient structures was identified between  $\text{MoO}_3$  and  $\text{MoO}_2$ .<sup>124, 129, 147, 145</sup>

The basis of partial oxidation catalysts often is molybdenum oxide mixed with vanadium and tungsten oxides.<sup>155</sup> For example, the best catalytic properties for the selective oxidation of acrolein were reported for a mixture of  $\text{MoO}_3$  with 7 - 15%  $\text{V}_2\text{O}_4$ , which was suggested to exhibit the  $\text{Mo}_3\text{VO}_{11}$ -structure with the formal stoichiometry of  $\text{Mo}_{0.75}\text{V}_{0.25}\text{O}_{2.75}$ .<sup>155-157</sup> These MoVW mixed oxide catalysts have been improved over the years by adding more and more promoters.<sup>9, 33, 158-164</sup> Hence, it has become increasingly more difficult to fully understand the role of each element and each phase present in such multielement partial oxidation catalysts on an atomic level.

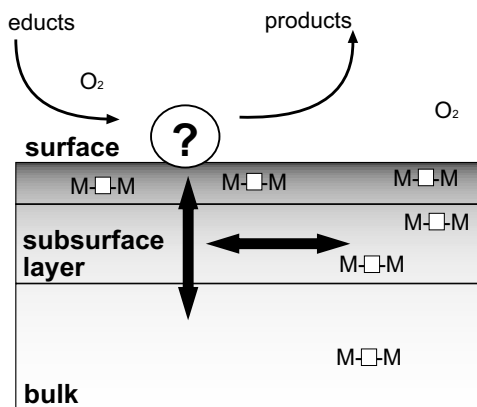


**Fig. 2.1:** Schematic drawing of different possible oxygen diffusion pathways in multicomponent, multiphasic partial oxidation catalysts.

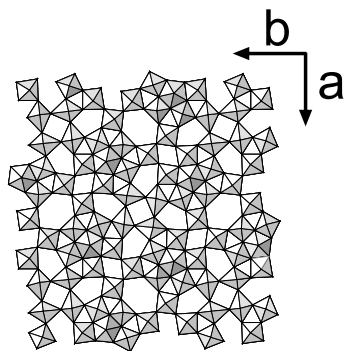


**Fig. 2.2:** Schematic drawing of the  $\text{Mo}_5\text{O}_{14}$  lattice.

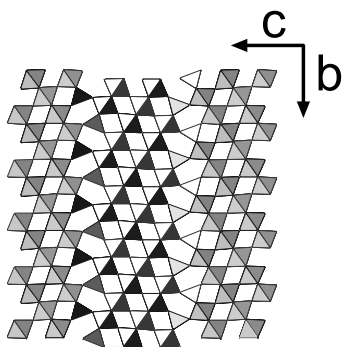


**Fig. 2.3:** Schematic drawing of the  $\text{Mo}_4\text{O}_{11}$  lattice.

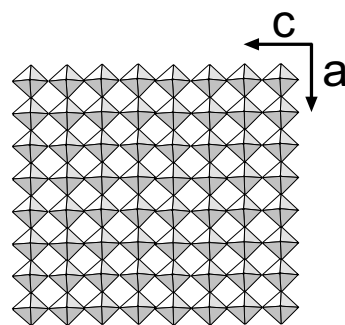


**Fig. 2.4:** Schematic drawing of the  $\text{MoO}_3$  lattice.

Previous XRD and HRTEM results on this MoVW mixed oxide catalyst of a formal stoichiometry of  $\text{Mo}_9\text{V}_3\text{W}_{1.2}\text{O}_x$  revealed an nanocrystalline state being built by  $\text{Mo}_5\text{O}_{14}$  sub-units.<sup>34</sup> The crystallisation of a oxide of  $\text{Mo}_5\text{O}_{14}$  structure was observed after thermal activation in air.<sup>34</sup> Kihlberg described this oxide to crystallise in the space group 4/mmm with an orthorhombic unit cell of the dimensions  $a = b = 4.599$  nm and  $c = 3.937$  pm which is characterised by a superstructure along the  $c$  axis.<sup>149, 48</sup> The structure is built up by distorted four-, six- and sevenfold (pentagonal bipyramids) Mo coordination polyhedra being mutually connected by sharing corners or edges and stacked along  $a$ . The Mo-O distances of the sixfold coordination sphere range between 164 to 173 pm and between 228 to 237 pm, those of the pentagonal bipyramids are 177, 181, 219 and 223 pm (Figure 2.4). The structure is disordered in the  $ab$  plane with the Mo atoms of the pentagonal bipyramid randomly distributed above and below this plane<sup>48</sup>, and crystallises in bundles of small needles.  $\text{Mo}_5\text{O}_{14}$  is metastable with respect to  $\text{MoO}_2$  and  $\text{MoO}_3$  and slowly decomposes at its formation temperature.<sup>149</sup> Each of these crystallographic structures in principle may expose different metal-oxygen groups and types of oxygen vacancies at their surfaces. The possibly different nature and role of these different sites for selective partial oxidation reactions is not understood yet, although often discussed.<sup>15, 46, 139, 140, 141, 165</sup> Due to the discussed relevance of oxygen defects for selective oxidation, the effect of thermal activation was investigated and, hence, the removal of oxygen on the catalytic activity of a MoVW mixed oxide catalyst. Because methanol is very reactive and because the possible reaction products are linked to different reaction channels,<sup>166-169</sup> the conversion of methanol to formaldehyde was used as a test reaction to investigate the catalytic properties of the mixed oxide. Pure molybdenum oxide catalysts exhibit high selectivities to formaldehyde.<sup>170</sup> The rate determining step was identified to be the hydrogen abstraction from the methyl group.  $\text{Mo}=\text{O}$  double bonds were suggested to be active for the formaldehyde formation,<sup>166-169</sup> while bridged Mo-O-Mo sites lead to dimethyl ether.<sup>169</sup> In this respect it is interesting to note that the oxygen exchange capabilities of the different Mo-O bonds in  $\text{MoO}_3$  to depend on the Mo-O bond order.<sup>70, 171</sup>

The objective of this Section is to the investigate the degree of reduction and elemental composition of a technical catalyst by means of XRD, Raman and SEM/EDX. Changes in the redox properties, elemental compositions and structure of the catalyst induced by the thermal activation in an inert atmosphere are discussed with respect to the altered catalytic performance of the methanol



oxidation.

## 2.1.2 Experimental

### 2.1.2.1 Catalyst Preparation

The catalyst was prepared by spray drying aqueous solutions of the respective ammonium salts to give the formal composition of  $\text{Mo}_{0.68}\text{V}_{0.23}\text{W}_{0.09}\text{O}_x$  followed by calcination at 700 K in a 5%/95%  $\text{O}_2/\text{N}_2$  mixture. One part of this batch was modified by heating in an inert gas stream of 150 ml/min at 813 K for 2 h. This activation was characterised by TG-DTA with a SEIKO micro-balance. An ion-molecule-reaction mass spectrometer (IMR-MS 100, Atomika) was used to detect the desorbing gases.  $\text{Xe}^+$  and  $\text{Kr}^+$  ions were used for ionisation. The mass signal intensities were referenced to the intensity of a defined flow of benzene added at the reactor outlet. The error in quantification due to the non-linear behaviour of the ionisation cross sections are considerable for components like  $\text{H}_2\text{O}$  or  $\text{MeOH}$ , which are partly protonated in the octupole of the IMR-MS by secondary reactions. In order to reduce these problems,  $\text{H}_2\text{O}$  had been calibrated in the presence of  $\text{MeOH}$  and *vice versa* but still the error is about 20 relative %.

### 2.1.2.2 Catalytic Characterisation

The catalyst (50 mg, BET surface area  $4 \text{ m}^2/\text{g}$ , average particle size:  $10 \mu\text{m}$ ) was diluted with SiC (Aldrich, 500 mg, particle size  $5 \mu\text{m}$ ) and placed between quartz wool plugs in a glass tubular flow reactor of 6 mm inner diameter and 300 mm length leading to a catalyst bed length of 15 mm. The reactor dead volume was minimised to 1.5 ml by a glass stick inserted downstream of the catalyst bed. A flow of 5 ml/min  $\text{N}_2$  was feed into an evaporator at 298 K to obtain a gas stream saturated with  $8 \mu\text{mol}/\text{ml}$   $\text{CH}_3\text{OH}$ . The default gas flow of  $\text{O}_2$  was 2.5 ml/min to get a reactant ratio of  $\text{MeOH}:\text{O}_2=2.5$ . An additional flow of  $\text{N}_2$  was used to obtain a constant total flow rate of 200 ml/min (space velocity  $28300 \text{ h}^{-1}$ ). Product analysis was performed by IMR-MS (IMRMS 100, Atomika) as stated above.

### 2.1.2.3 SEM/EDX Analysis

Scanning electron microscopy (SEM) was conducted with a S 4000 FEG microscope (Hitachi). The acceleration voltage was set at 10 kV, the objective aperture was 30  $\mu\text{m}$ , and the working distance was 10 mm. The samples were suspended in  $\text{CCl}_4$ , and mounted on Be platelets. Energy dispersive X-ray analysis (EDX) was done with a DX 4 analyser system (EDAX) equipped with a Li-doped Si crystal with an resolution of 140 eV at 5.9 keV, and an acceleration voltage of 15 kV. Adsorption correction was automatically performed, position correction was done by inspection.

### 2.1.2.4 X-Ray Diffraction

XRD patterns were recorded on a theta-theta diffractometer (Stoe) in Bragg-Brentano geometry using a scintillation counter detector. Monochromatic (graphite secondary monochromator)  $\text{Cu K}_\alpha$  (154.18 pm) radiation was used. The measured XRD diffractograms were simulated with the Cerius software package (MSI) using Retrieve single crystal data (ICSD-PDF-2).

### 2.1.2.5 Raman Spectroscopy

Confocal Raman microspectroscopy was conducted with a LabRam B Raman spectrometer, which has been described on page 1.4. The slit width was set to 200  $\mu\text{m}$  giving a resolution of  $2.5 \text{ cm}^{-1}$ . The line at 632 nm of a HeNe ion laser (Melles Griot) was used with laser powers of 0.14 mW and 15 mW at the sample position. Laterally resolved confocal Raman spectra were recorded of an area of  $900 \mu\text{m}^2$  giving a set of 1000 Raman spectra per sample. An objective with a magnification of 100 was used giving a spatial resolution about 700 nm. Each spectrum is the sum of 2 accumulations each integrated for 400 sec. These sets of spectra were statistically evaluated using SIMPLISMA (**S**imple-to-use **i**nteractive **s**elf-modelling **m**ixture **a**nalysis).<sup>172-177</sup> The SIMPLISMA approach allows to resolve the spectral data matrix  $\mathbf{D}$  ( $v \times c$ ) in pure component spectra and a matrix of the concentration coefficients without prior information about the pure spectra or the concentration profiles. The matrix notation is:  $\mathbf{D}^T = \mathbf{CS}$ , and  $\mathbf{D}^T = (c \times v)$  contains mixture spectra in its rows. The matrix  $\mathbf{C}$  ( $c \times n$ ) contains in its columns the fractional contributions of the pure components in the mixture spectra, where  $n$  is the number of pure components.  $\mathbf{S}$  ( $n \times v$ ) contains the pure spectra.

**S** can be resolved by least-squares, when using in **C** the observed intensities of the pure variables in the spectra in **D**. The SIMPLISMA software runs under the MATLAB environment.

## 2.1.3 Results and Discussion

### 2.1.3.1 Thermal Activation of the Untreated Mixed Oxide

Figure 2.5 shows the TG analysis (solid line) of the untreated mixed oxide upon thermal activation (section **A**), during subsequent partial oxidation in methanol : oxygen = 2:1 (section **B**) and methanol : oxygen = 4:3 (section **C**), and reoxidation in pure  $O_2$  (section **D**). The final weight after reoxidation (**D**) to  $MoO_3$  (98% of the original value) evidences that the thermal activation (section **A**) not only led to the loss of  $H_2O$  and  $NH_3$  ( $\approx 2$  wt%), but also to a considerable loss of oxygen ( $\approx 3$  wt%), as  $NO$  and  $NO_2$  which was detected by IMR-MS. The catalytic reaction with methanol (section **B**) led to a further loss of oxygen, while a subsequent increase in the oxygen partial pressure (section **C**) first led to a weight gain within 30 min to decrease again later. This transient behaviour in section **C** may be interpreted as the establishment of a steady state of an average oxide stoichiometry below the nominally fully oxidised composition. From the final weight after complete reoxidation, it may be attempted to estimate the stoichiometry of the active catalyst material. From this estimation it may be suggested that the actual catalyst has a stoichiometry between the only known stable phases in this regime,  $Mo_8O_{23}$  and  $Mo_5O_{14}$ . This estimation of the oxygen/metal ratio of the catalyst can be compared with that determined by RBS.<sup>14</sup>

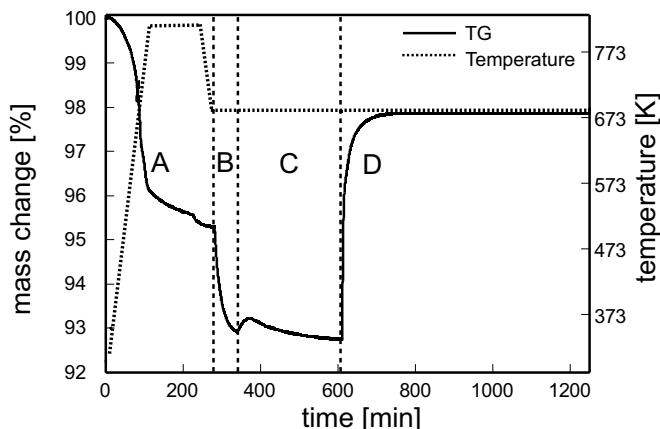


**Fig. 2.5:** Thermogravimetric analysis of the weight changes of the untreated mixed oxide upon thermal activation (section **A**), subsequent partial oxidation in methanol : oxygen = 2:1 (section **B**) and methanol : oxygen = 4:3 (section **C**) and complete reoxidation in pure  $O_2$  (section **D**). Solid line: weight change in %; Dashed line: temperature program during the experiment.

### 2.1.3.2 Temperature Programmed Reaction Spectroscopy (TPRS)

Because the thermal activation in inert gas did not change the BET surface area (it remained constant at 4 m<sup>2</sup>/g), the catalytic activities and selectivities of the untreated and the thermally activated catalyst can be compared for identical reactor loadings. In Fig 2.6, the TPRS is displayed from 298 to 673 K together with the isothermal steady state run for both materials. Beside CO, the main product over the untreated mixed oxide was 0.45 vol% CH<sub>2</sub>O, corresponding to a formaldehyde selectivity of 66% at 31% conversion. Thermal activation increased the CH<sub>2</sub>O steady state yield by a factor of 3 as shown in Figure 2.5 with a CH<sub>2</sub>O selectivity of 80% at 93% conversion. These data may be compared with those of an industrial Fe<sub>2</sub>O<sub>3</sub>/MoO<sub>3</sub> catalyst reaching 95 to 99% methanol conversion with a formaldehyde selectivity between 91 and 94%.<sup>178</sup> The thermal activation changed the byproduct spectrum of this reaction too. The thermally activated catalyst gave only a small amount of (CH<sub>3</sub>)<sub>2</sub>O as the byproduct. Thus according to literature,<sup>166-169</sup> it may be concluded that two reaction paths are active on the catalyst depending on thermal activation.

The activation energies of the formaldehyde formation over both catalysts were determined between 600 and 663 K (inset of Figure 2.6). As CH<sub>2</sub>O was the main product and because CO<sub>2</sub> was not detected, the apparent activation energy for the CH<sub>2</sub>O formation could be determined to be  $E_a = 79$  kJ/mol for the untreated mixed oxide, and  $E_a = 73$  kJ/mol for the thermally activated catalyst.

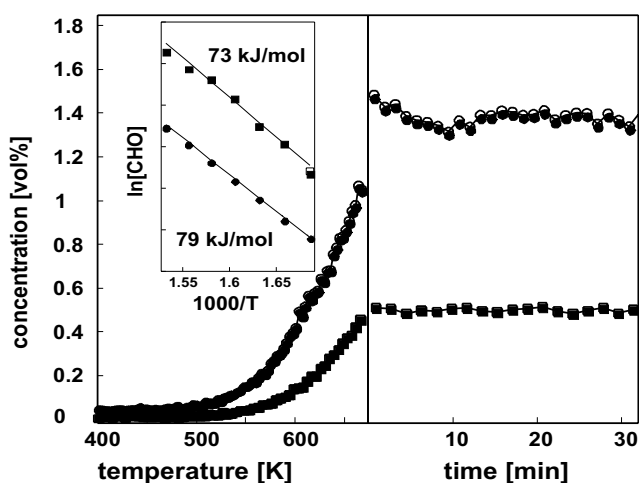


**Fig. 2.6:** TPRS from 298 to 673 K (vol% formaldehyde) together with the isothermal steady state run at 673 K for 50 mg of both, the untreated mixed oxide and the thermally activated catalyst, diluted in 500 mg SiC. The inset shows the activation energies determined over both catalysts: thermally activated mixed oxide ●; untreated mixed oxide ■.

The improved activity of the thermally activated catalyst is not attributed to a decreased activation energy but to an increased preexponential factor, *i.e.* an increased number of active sites on the

catalyst surface. An increase of the O<sub>2</sub> partial pressure in the feed by a factor of 3 at 673 K reactor temperature led to a decrease in the CH<sub>2</sub>O selectivity from 80% to 61% during 3 h on stream. From the three-fold increase of the stoichiometric oxygen partial pressure, one would expect a much more dramatic decrease in selectivity than the observed one quarter and the clear detection of CO<sub>2</sub>. CO<sub>2</sub>, however, was only detected in traces.

### 2.1.3.3 Physicochemical Characterisation

#### 2.1.3.4 SEM/EDX Analysis

The SEM images reveal that large parts of the MoVW mixed oxide precursor consist of about 10  $\mu\text{m}$  large spherical segments (not shown). A higher resolved image (not shown) did not reveal particle shapes which would indicate crystalline material. Secondary electron (SE) imaging and backscattered electron (BSE) imaging modes of operation were used in combination with EDX analysis to investigate the elemental distribution of Mo, V and W. The elemental compositions of different spots in the BSE image were determined by EDX. While the W concentration was comparable (9 and 8 at%), concentration variations were detected for Mo and V with 51 and 43 at%, and 20 and 27 at%, respectively. EDX analysis revealed two phases with differing Mo and V concentrations, while the W content was comparable with 6 and 9 at%, respectively. The bright area in the SE image had a high concentration of 53 at% Mo relative to 18 at% V. Dark areas in the SE image had a Mo concentration of 36 at% but a content of 28 at% V. The dark areas are identified with the outer surface of the spherical-like particles, while the bright ones were due to cleavage faces.

Sample	Global	SEM/EDX*	
	Mo	V	W
untreated oxide	65	24	11
activated catalyst	79	13	8
formal stoichiometry	68	23	9

**Table 2.1:** *Element concentrations of the pristine catalyst and the activated mixed oxide catalyst in at%. (\* normalised to the sum of metals due to uncertainty in oxygen determination).*

EDX mapping was conducted of a 900  $\mu\text{m}^2$  area in order to confirm this result. Figure 2.7 shows the SEM image and the Mo, V, and W distributions are depicted in Figure 2.7 B, C, D, respectively. While the Mo and W concentrations showed a similar distribution (Fig.

2.16B and D), regions of about 5 to 10  $\mu\text{m}$  in size were identified which had a high vanadium

concentration (Fig. 2.7 C) but were depleted in Mo and W (Fig. 2.7 B and D). EDX spectra were recorded of a V rich and V depleted area (marked by arrows in Fig. 2.7 C). Mo, V and W concentrations of 59 at%, 33 at% and 8 at% respectively, were determined for the V-rich area, while Mo, V and W concentrations of 86 at%, 5 at% and 8 at%, respectively, were detected for V depleted areas.

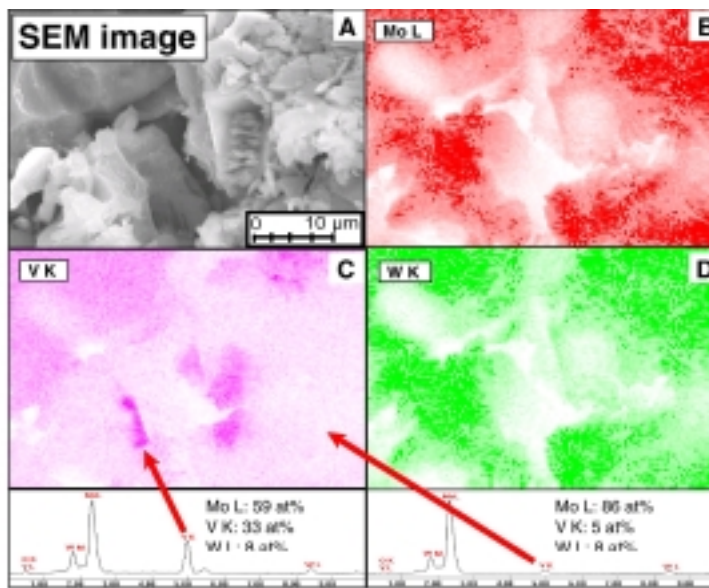


**Fig. 2.7:** SEM-EDX mapping of an area of  $900 \mu\text{m}^2$  of untreated MoVW mixed oxide; **A:** SEM image; **B:** Mo-, **C:** V-, and **D:** W-EDX mapping.

The SEM images of the thermally activated catalyst (Figure 2.8 A) show, that in contrast to the untreated MoVW oxide, the particles were agglomerates of platelet-like crystallites of a few hundredths of nm in size (Figure 2.8B). But there remained parts of the sample which still showed irregular particle shapes (not shown). EDX characterisation of 1 to  $3 \mu\text{m}$  sized platelet-like crystals (not shown) revealed almost the exclusive presence of Mo with 32 at% and only small concentrations of V (3 at%), and W (1 at%). Particles with an irregular habit had higher concentration of V (19 at%) and W (3 at%) relative to Mo (30 at%).

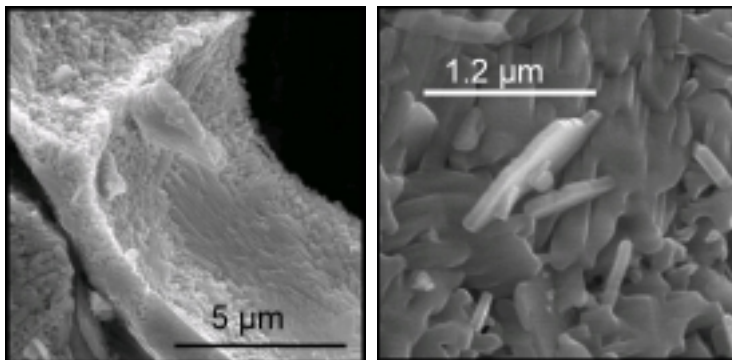


**Fig. 2.8:** SEM images of the thermally activated mixed oxide catalyst.

SEM-EDX mapping of a  $900\ \mu\text{m}^2$  large area was used to probe the elemental heterogeneity after thermal activation (see Table 2.1). While the Mo and W concentration distributions were similar throughout the analysed sample (Mo 71 at%, V 11 at%, W 18 at%), an area of about 5 to  $10\ \mu\text{m}$  size was detected which shows a high V concentration (44 at%) and reduced Mo (48 at%) and W (8 at%) contents. Thermal activation did not lead to homogeneous element distribution on this length scale (see Table 2.1).

TEM-EDX determined the element distribution of the thermally activated catalyst on the submicron scale (not shown). In contrast to the untreated mixed oxide, the thermally activated catalyst exhibited an inhomogeneous element distribution. Thermal activation led to segregation of V on the submicron regime.<sup>14</sup>

In summary, SEM/EDX techniques show that the mixed oxide precursor is characterised by an inhomogeneous elemental distribution on the length scale of a few microns. The element distribution is homogeneous on the submicron scale. The particle shapes do not point to the presence of well crystallised materials. The results may be explained by the preparation procedure. Different isopolyoxometalates, *e.g.* isopolyoxomolybdates or isopolyoxovanadates in solution may lead to elemental inhomogeneities during the drying process (see Chapter 5). Thermal activation led to the formation of regular particle shapes pointing to crystallisation and to vanadium segregation on the submicron scale.

### 2.1.3.5 X-ray diffraction of the MoVW Mixed Oxide

Mo <sub>5</sub> O <sub>14</sub>			MoO <sub>3</sub>	
const.	ICDD [pm]	Calc. [pm]	ICDD [pm]	Calc. [pm]
a	2299.5	2273.2	396.2	395.4
b	2299.5	2273.2	1385.8	1387.2
c	393.7	397.5	369.7	3693.8

**Table 2.2:** *Experimental unit cell parameters and literature data.*

This type of MoVW mixed oxide material was already investigated by H. Werner et al. who used XRD and HRTEM for structural characterisation<sup>34</sup>. The XRD pattern of the present mixed oxide precursor is shown in Figure 2.9 together with simulated XRD patterns

of nanocrystalline Mo<sub>5</sub>O<sub>14</sub> and MoO<sub>3</sub>. The experimentally determined cell parameters as well as

the simulation parameters are given in Tab. 2.2. The experimental XRD pattern fully confirms the results reported by Werner et al.<sup>34</sup>. The MoVW mixed oxide was found almost XRD amorphous (Figure 2.9). The XRD pattern could be simulated as being composed of nanocrystalline oxides of  $\text{Mo}_5\text{O}_{14}$  and  $\text{MoO}_3$  structure. The two very broad reflections at about  $23^\circ$  and  $27^\circ$   $2\theta$  can be attributed, according to the simulated diffraction patterns, to the main metal-metal distances of  $\sim 4 \text{ \AA}$  found in the oxide of  $\text{Mo}_5\text{O}_{14}$  structure and of  $\sim 3 \text{ \AA}$  found in  $\text{MoO}_3$  oxide, respectively. According to the XRD simulations, the presence of nanocrystalline  $\text{V}_2\text{O}_5$  has to be excluded for the untreated mixed oxide. The X-ray coherence lengths between 100 and 1500 pm, which were used for the simulation of the  $\text{Mo}_5\text{O}_{14}$  and  $\text{MoO}_3$  patterns, compare well with the TEM observation of particles smaller than 100 nm.

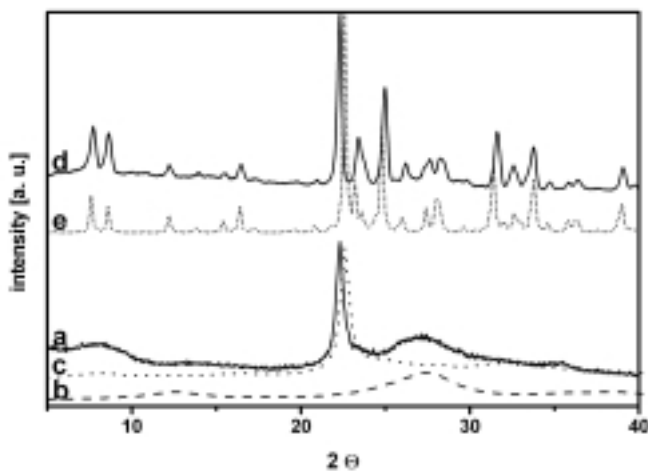


**Fig. 2.9:** XRD pattern of the untreated MoVW mixed oxide (a, dots) together with the simulations of nanocrystalline  $\text{MoO}_3$  (b, short dashed line) and nanocrystalline  $\text{Mo}_5\text{O}_{14}$  (c, long dashed line); XRD pattern of the thermally activated MoVW mixed oxide (d, dots) and the simulated pattern of crystalline  $\text{Mo}_5\text{O}_{14}$  (e, solid line).

The XRD pattern of the thermally activated mixed oxide is also presented in Figure 2.9 together with its simulation. The experimentally observed cell parameters and the simulation parameters are given too in Table 2.2. The crystallinity has increased after thermal activation, in agreement with Werner et al.<sup>34</sup> who also observed crystallisation at 773 K in air. Two phases were positively identified by XRD in the present samples. The main MoVW phase is represented by a structure similar to that of  $\text{Mo}_5\text{O}_{14}$ . The minority phase was identified as being of  $\text{MoO}_3$  structure. In addition, the presence of traces of  $\text{MoO}_2$  and  $\text{VO}_2$  cannot be excluded from the experimental diffractogram. This result was confirmed by a simulation XRD pattern of  $\text{Mo}_5\text{O}_{14}$  and  $\text{MoO}_3$ . The increased crystallinity of  $\text{Mo}_5\text{O}_{14}$  is also reflected in the coherence length parameters of the simulated pattern which are about 30 nm. The incorporation of V or W in both these MoVW phases at Mo positions



is not directly reflected by new reflections. The contraction of the *a* axis and slight expansion of the *c* axis of the  $(\text{MoVW})_5\text{O}_{14}$  unit cell as compared to  $\text{Mo}_5\text{O}_{14}$  indicates the incorporation of V and W into the real structure of this phase. Comparable expansions and contractions of the unit cell parameters were also observed for the real structure of the minority  $(\text{MoVW})\text{O}_3$  phase, also indicating the incorporation of V and W.

### 2.1.3.6 Confocal Raman Microspectroscopy

Raman spectroscopy is suited to characterise the structure of X-ray amorphous materials. The special capabilities of laterally resolved confocal Raman microspectroscopy are combined with the SEM-EDX and XRD results. Raman mapping was done with the lowest possible laser power to avoid irradiation damage.

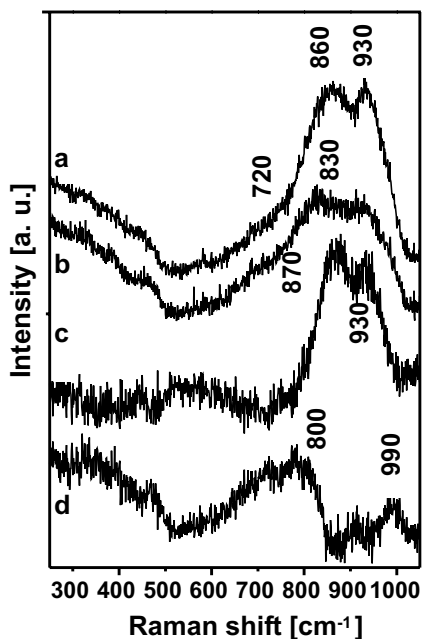


**Fig. 2.10:** *a* and *b*: Two representative confocal Raman spectra of untreated MoVW mixed oxide recorded at two different spots with minimum laser power. *c* and *d*: SIMPLISMA analysis of the set of Raman spectra. Spectrally pure majority *c* and minority *d* components.

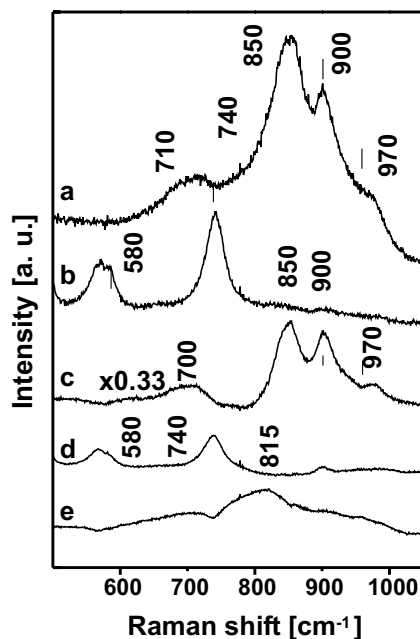


**Fig. 2.11:** *a* and *b*: Two representative confocal Raman spectra of thermally activated MoVW mixed oxide recorded at two different spots with minimum laser power. *c-e*: SIMPLISMA analysis of the set of Raman spectra. Spectrally pure majority *c* and minority *d, e* components.

The Raman spectra of the untreated precursor oxide (Figure 2.10 a,b) showed only a broad ill-defined signal between 600 and 1000  $\text{cm}^{-1}$  and a broad background in the lattice mode regime. The broad feature between 600 and 1000  $\text{cm}^{-1}$  exhibits some structure at about 720(sh), between 830

and  $860\text{ cm}^{-1}$ , and at  $930\text{ cm}^{-1}$ . These bands and shoulders occur in the typical regime of Mo-O vibrations. This observation confirms the XRD result of a nanocrystalline material. SIMPLISMA evaluation (Figure 2.10c, d) gave some additional information on the number of structurally different mixed oxide precursor species. The set of spectra can be calculated by linear combinations of two weighted spectral components. The spectral component 1 shows two features at about  $930$  and  $870\text{ cm}^{-1}$ , while the spectrally pure component 2 shows a weak feature at about  $900\text{ cm}^{-1}$  and a broad band centred at about  $800\text{ cm}^{-1}$ . By comparison with the XRD result of oxides of  $\text{Mo}_5\text{O}_{14}$  and  $\text{MoO}_3$  structure in the precursor material, the spectral component 1 is attributed to the nanocrystalline oxide of  $\text{Mo}_5\text{O}_{14}$  structure, component 2 to the nanocrystalline  $\text{MoO}_3$  oxide.

Two Raman spectra (spectrum a and b of Figure 2.11) recorded at different spots of the thermally activated catalyst confirm that the activated MoVW mixed oxide remained structurally inhomogeneous. Spectrum a of Figure 2.11 shows bands at about  $970(\text{sh})$ ,  $900$ ,  $850$  and  $710\text{ cm}^{-1}$ . Spectrum b exhibits bands at  $740$  and  $580\text{ cm}^{-1}$ . The spectrally pure components of this set of 100 Raman spectra were determined by SIMPLISMA (spectra c, d, and e of Figure 2.11). The spectrally pure major component (spectrum c of Figure 2.11) exhibits bands or shoulders at about  $970$ ,  $900$ ,  $850$ , and  $700\text{ cm}^{-1}$ . This component resembles the experimental Raman spectrum a of Figure 2.11. By comparison with the XRD result, the major component of the Raman spectra is identified with the oxide of  $\text{Mo}_5\text{O}_{14}$  structure present after thermal activation, and therefore may serve as a fingerprint for this oxide. All three transition metal ions, Mo, V, and W, however, have Raman bands due to M-O vibrations in this frequency regime depending on the coordination sphere and symmetry, and probably the degree of reduction. Spectrum d of Figure 2.11 represents one minority component of the thermally activated MoVW mixed oxide. It shows bands at about  $740$  and  $580\text{ cm}^{-1}$  and is comparable to the experimental spectrum b of Figure 2.11. This component can be identified by  $\text{MoO}_2$  by comparison with a reference spectrum of  $\text{MoO}_2$ .<sup>179</sup>  $\text{MoO}_2$  was detected in trace amounts by XRD too. The second spectrally pure minority component identified by SIMPLISMA (spectrum e of Figure 2.11) exhibits only very ill-defined, broad features with a broad maximum at about  $815\text{ cm}^{-1}$ . This component is identified with nanocrystalline oxide of  $\text{MoO}_3$  structure. It is known that  $\text{Mo}_5\text{O}_{14}$  is metastable at its temperature of formation with respect to the disproportionation in  $\text{MoO}_3$  and  $\text{MoO}_2$ ,<sup>34, 149</sup> which explains the detection of oxides of  $\text{MoO}_3$  and  $\text{MoO}_2$  structure.

In summary, Raman and XRD characterisation of the thermally activated material reveals structural heterogeneity of the MoVW mixed oxide with  $\text{Mo}_5\text{O}_{14}$ -type oxides being the major component and  $\text{MoO}_3$ - and  $\text{MoO}_2$ -type oxides being the minority species. Figure 2.12 contains two plots of the laterally resolved Raman spectra recorded of this sample. The Raman image A of Figure 2.12 shows the intensity distribution of the band at  $750\text{ cm}^{-1}$  characteristic of  $\text{MoO}_2$  oxides, while the Raman image B of Figure 2.12 shows the intensity distribution of the band at  $850\text{ cm}^{-1}$  characteristic of oxides of  $\text{Mo}_5\text{O}_{14}$  structure. The different intensity distributions obtained for the two characteristic metal-oxygen vibrations evidence that the sample is structurally heterogeneous. Areas showing a high intensity of the  $\text{Mo}_5\text{O}_{14}$  band at  $850\text{ cm}^{-1}$  exhibits only weak band intensities due to  $\text{MoO}_2$  and *vice versa*. Thus, it may be concluded that the oxides of  $\text{Mo}_5\text{O}_{14}$  and  $\text{MoO}_2$  structure are mutually formed. This result is in agreement with the observation of a spatially heterogeneous element distribution as determined by EDX as shown in the previous Section.

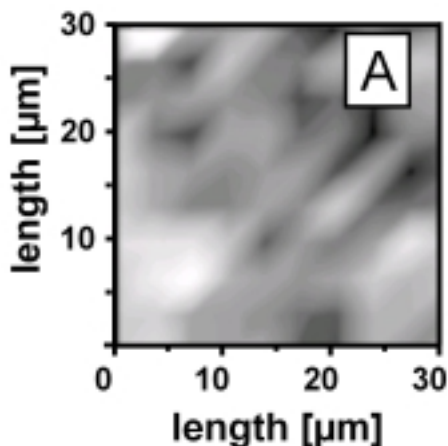


**Fig. 2.12: a:** Raman micro image of the thermally activated MoVW mixed oxide as generated from the intensity of the Raman band at  $740\text{ cm}^{-1}$  (first minority component). Bright areas indicate strong band intensities, dark areas weak intensities.

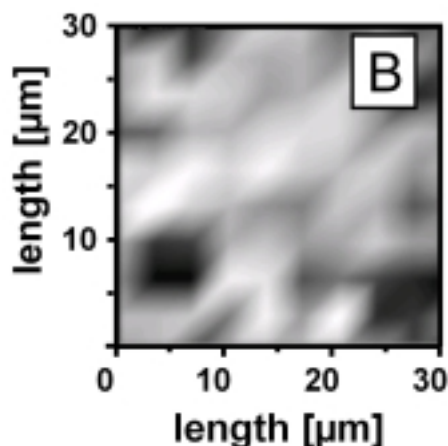


**Fig. 2.12: b:** Raman micro image of the thermally activated MoVW mixed oxide as generated from the intensity of the Raman band at  $850\text{ cm}^{-1}$  (majority component). Bright areas indicate strong band intensities, dark areas weak intensities.

## 2.1.4 Conclusions

Catalytic tests showed that activation at 813 K in inert gas resulted in an increase of the catalytic methanol oxidation and a  $\text{CH}_2\text{O}$  yield by 300%. The activation energies of the formaldehyde formation were found to be similar for both catalysts. Therefore, it can be suggested that the reaction mechanism of the formaldehyde formation was not altered by the thermal activation as compared to

the reaction over the precursor oxide. On the other hand, the pre-exponential factors as determined from the Arrhenius plots differed significantly. This result suggests a higher concentration of sites active for the formaldehyde formation on the thermally activated catalyst as compared to the untreated mixed oxide. Because thermal activation may have caused the formation of surface oxygen defects, there is reason for the assumption that these defects play the key role for the improved catalytic activity as often stated in the literature.<sup>15, 46, 139, 141, 140, 165</sup>

In order to understand this increase of the catalytic reactivity of a MoVW mixed oxide catalyst, the compositional changes were investigated which occur during the activation. SEM-EDX of the untreated catalyst revealed at least two different phases of different V concentrations. According to SEM-EDX, the thermally activated mixed oxide exhibited an inhomogeneous element distribution in the micron and submicron regime.

Additional RBS, XPS, ISS and UPS investigations<sup>14</sup> gave the analytical confirmation that the thermally activated catalyst contained less bulk and surface oxygen and, hence, more oxygen defects relative to the untreated precursor oxide. The combination of these methods was necessary to show that this holds true for both the surface region and the bulk. A picture of the bulk composition and stoichiometry was developed by RFA, global EDX and XRD.

XRD characterisation of the starting material showed the presence of a nanocrystalline material in line with the SEM/TEM investigations. The XRD pattern of the untreated starting material can be simulated and interpreted as being a mixture of nanocrystalline oxides of  $\text{Mo}_5\text{O}_{14}$  and  $\text{MoO}_3$  structure. Confocal Raman microspectroscopy confirmed the presence of two different components in the starting mixed oxide, and the spectra were assigned accordingly. After thermal activation, the mixed oxide consisted of a mixture of a majority of oxides of  $\text{Mo}_5\text{O}_{14}$  structure and a minority of crystalline  $\text{MoO}_3$ -type oxides. The presence of traces of  $\text{MoO}_2$  and  $\text{VO}_2$  oxides cannot be ruled out by XRD. The Raman spectrum of the major oxide phase of  $\text{Mo}_5\text{O}_{14}$  structure could be identified by statistical data evaluation and by comparison with the XRD result. Raman microscopy confirmed the presence of small amounts of oxides of  $\text{MoO}_3$  and  $\text{MoO}_2$  structure. This result may be understood in relation to the metastability of  $\text{Mo}_5\text{O}_{14}$  with respect to  $\text{MoO}_3$  and  $\text{MoO}_2$  at its formation temperature.<sup>34, 149</sup> The combined positive XRD and Raman identification of the oxide of  $\text{Mo}_5\text{O}_{14}$

structure as the majority component may be related to the observed increase of the catalytic activity for formaldehyde formation by a factor of three after thermal activation. These combined observations strongly suggest that the oxide of  $\text{Mo}_5\text{O}_{14}$  structure is one relevant candidate being active and selective for selective partial oxidation reactions.

Andrushkevich reported on a high activity and selectivity of  $\text{Mo}_4\text{O}_{11}$  for the partial oxidation of acrolein.<sup>156</sup> This observation is highly interesting in respect to the presented results.  $\text{Mo}_4\text{O}_{11}$  has an oxygen stoichiometry of 2.75 being very close to the one of  $\text{Mo}_5\text{O}_{14}$ , with 2.8. Despite this close stoichiometry, both crystal structures are very different as shown in Figure 2.3 and 2.2. It is known from experiments to synthesise single phase, well-crystallised Mo oxides that  $\text{Mo}_4\text{O}_{11}$  exhibits a local stability maximum in the phase regime between  $\text{MoO}_2$  and  $\text{MoO}_3$ .<sup>179</sup> The local stability maximum of  $\text{Mo}_4\text{O}_{11}$  and the metastability of  $\text{Mo}_5\text{O}_{14}$  may explain the difference in the reported observations and those of Andrushkevich.<sup>155</sup> Due to the high thermodynamic stability of  $\text{Mo}_4\text{O}_{11}$ , which can coexist with the catalytically inactive  $\text{MoO}_2$ ,  $\text{Mo}_5\text{O}_{14}$  may be regarded as being more active than  $\text{Mo}_4\text{O}_{11}$ . The oxide of  $\text{Mo}_5\text{O}_{14}$  structure remains nanocrystalline under the preparation conditions usually used. This thermodynamically highly unstable oxide and its high instability (high internal energy) is seen to be responsible for a high catalytic activity. Cation ( $\text{V}^{5+/4+}$ ) and anion diffusion may be easy and fast redox changes within the structure may be possible. Hyde and O'Keefe developed a general understanding of a cylindrical shear mechanism which relates  $\text{Mo}_5\text{O}_{14}$ ,  $\text{Mo}_{17}\text{O}_{47}$ ,  $\text{W}_{18}\text{O}_{49}$ ,  $\text{Nb}_{16}\text{W}_{18}\text{O}_{94}$ ,  $\text{Bi}_6\text{Nb}_{34}\text{O}_{94}$ , and tetragonal tungsten bronzes (see Figure 2.13).<sup>180</sup> According to this mechanism, the rotation of a  $\text{Mo}_4\text{O}_{20}$ -subunit within the  $\text{MoO}_3$ -derived oxide planes leads to the formation of 7-fold, and 4-fold coordination beside the 6-fold coordination, primarily without any change in stoichiometry or the oxidation state of the metal centres as shown in Figure 2.13. This rotational shear mechanism can occur at any site within the molybdenum oxide layer, thus, leading to broad varieties of possible defect structures, superstructures, intergrowth and nonstoichiometries. This model explains the structure of the investigated MoVW mixed oxide. It is nanocrystalline and of the  $\text{Mo}_5\text{O}_{14}$  structure. In addition, the metastability of  $\text{Mo}_5\text{O}_{14}$  with respect to its disproportionation into  $\text{MoO}_2$  and  $\text{MoO}_3$  may shed light into the observed long-time instability of these type of industrial catalysts.

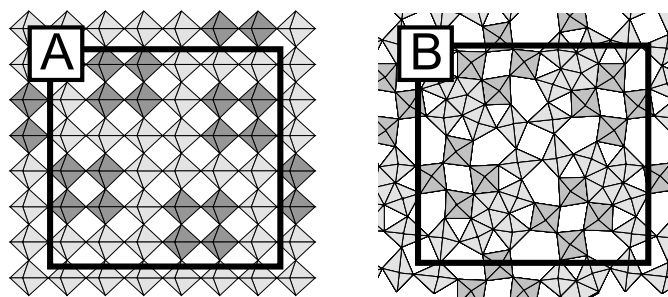


**Fig. 2.13:** *Crystal structures of  $\text{MoO}_3$  and  $\text{Mo}_5\text{O}_{14}$ .*

$\text{Mo}_5\text{O}_{14}$ , as  $\text{Mo}_4\text{O}_{11}$ , tolerates the incorporation of considerable amounts of V and W.<sup>45</sup> Thus, mixed MoVW oxides are formed from  $\text{MoO}_3$ ,  $\text{WO}_3$  and  $\text{V}_2\text{O}_5$  at high temperatures with crystal structures resembling that of  $\text{Mo}_5\text{O}_{14}$ .<sup>42, 47, 181</sup> The stoichiometry of such phases were reported to be  $(\text{Mo}_{0.92}\text{V}_{0.08})\text{O}_{14}$  or  $(\text{Mo}_{0.75}\text{W}_{0.25})\text{O}_{14}$ ,<sup>145</sup> respectively. The incorporation of W, especially, seems to favour the formation of oxide of  $\text{Mo}_5\text{O}_{14}$  structure and can be compared with the results on Ta and Nb incorporation.<sup>45, 48</sup> Hence, it may be concluded that the incorporation of about 8 at% W into the investigated mixed oxide of  $\text{Mo}_5\text{O}_{14}$  structure leads to its stabilisation. This suggestion also seems to be supported by the observation of a homogeneous W distribution throughout the MoVW oxide at all length scales investigated irrespective of the thermal treatment. Vanadium is statistically incorporated into  $\text{Mo}_5\text{O}_{14}$ ,<sup>42, 181</sup> although it seems to prefer octahedral sites close to a metal-metal bond ( $\text{Mo}^{5+}/^{4+}$  centres) in the structurally related  $\text{Mo}_{17}\text{O}_{47}$ .<sup>29</sup> In addition,  $\text{Mo}_5\text{O}_{14}$  seems to tolerate large variations in the V content up to 30 at%. This fact explains why mainly oxides of  $\text{Mo}_5\text{O}_{14}$  structure were detected by XRD and Raman, although SEM/EDX revealed large variations in the V distribution.

In summary,  $(\text{MoVW})_5\text{O}_{14}$  oxides are promising candidates for the active and selective phase in partial oxidation reactions. These  $(\text{MoVW})_5\text{O}_{14}$  oxides are complex systems containing several minority species besides the  $\text{Mo}_5\text{O}_{14}$  phase, which is highly variable in its chemical composition and oxidation state depending on the redox potential of the surrounding gas phase.

## 2.2 Combined X-Ray Diffraction, Electron Microscopy and Raman Investigation of the Phase Stability of Oxides of $\text{Mo}_5\text{O}_{14}$ Structure.

### 2.2.1 Introduction

Transition metal oxides show a broad structural variety due to their ability to form intermediate oxides. These oxides *e.g.* for example molybdenum, tungsten or vanadium oxide, exhibit different crystallographic structures as a function of the oxygen stoichiometry with different physicochemical properties.<sup>5, 86, 114</sup> It can be expected that these intermediate oxides with strong crystallographic anisotropies show different catalytic properties for different exposed crystal faces. One possible reason responsible for surface structure sensitivity may be the differently strong M=O bonds at the different surface planes. The stronger the M=O bond the more basic is its functionality. Other reasons for different activities may be different oxygen species on the different crystal planes, *e.g.* terminal, doubly, or triply bridging oxygens, generating electrophilic or nucleophilic oxidation chemistry on the different crystal planes. In addition to this surface structure sensitivity there may be what one may call "compound sensitivity". Of all possible oxides there may only be one single structurally defined oxide which exhibits the highest catalytic selectivity and activity. This "compound sensitivity" may be due to its special geometric, electronic or diffusion properties providing highly shape selective active sites, optimum match of catalyst and substrate electronic states and fast redox kinetics. Structure and "compound" sensitivity for oxidation reactions serve as guidelines for the development and fundamental understanding of catalysts and their catalytic properties.<sup>15</sup>

It has been shown in the previous Section of this series that a tungsten and vanadium promoted nanocrystalline  $\text{Mo}_5\text{O}_{14}$  oxide is formed at 673 K,<sup>14</sup> far below the temperatures reported by Kihlberg. Therefore, these additional transition metal oxides may be seen as structural or electronic promoters. The promoting role of these additional transition metals (Ta, Nb<sup>121</sup>) may be understood as stabilising these tunnel structures due to their different size ( $\text{Mo}^{6+}$ : 62 pm,  $\text{Ta}^{5+}$ : 68 pm,  $\text{Nb}^{5+}$ : 69 pm<sup>182</sup>) with respect to the Mo cation. Alternatively, different redox properties of cations with sizes comparable to  $\text{Mo}^{6+}$ , *e.g.*  $\text{W}^{6+}$ : 62 pm,  $\text{V}^{4+}$ : 63 pm, or smaller, *e.g.*  $\text{V}^{5+}$ : 59 pm, can also lead to structural promotion by defining an overall oxygen stoichiometry close to

2.8. As a consequence of this stabilisation, these mixed oxide structures are rather stable as selective oxidation catalyst under the oxidative atmospheres and the temperatures needed for high conversions. In this context, it is important to note that the elemental compositions of these mixed oxides  $(\text{Mo}_{0.92}\text{V}_{0.08})_5\text{O}_{14}$  or  $(\text{Mo}_{0.75}\text{W}_{0.25})_5\text{O}_{14}$  are close to that of industrial catalysts.<sup>34, 14</sup>

The catalyst investigated in this study has an overall composition of  $\text{Mo}_{0.64}\text{V}_{0.25}\text{W}_{0.09}\text{O}_x$ .<sup>14</sup> After preparation and calcination of the precursor polyoxometalate at 673 K under nitrogen mainly a nanocrystalline oxide of  $\text{Mo}_5\text{O}_{14}$  structure was observed.<sup>14</sup>

Different activation temperatures have been applied to the quaternary  $(\text{MoVW})_5\text{O}_{14}$  oxide in order to obtain information about the complex and still not well understood thermodynamics and the phase stability of this compound.<sup>149, 14</sup> Therefore, MoVW mixed oxide specimens, which have been thermally treated at different temperatures for different time periods, were investigated by XRD, high resolution transmission electron microscopy (HRTEM), and Raman microspectroscopy.

High resolution transmission electron microscopy is a decisive method to unravel their actual micro- or nano-structure. Especially, because most industrially relevant catalysts are difficult to characterise by the above mentioned techniques due to their high amorphicity. Bulk characterisation methods like XRD or EXAFS, or methods with a low lateral resolution like conventional Raman or IR-spectroscopy are hardly suitable to elucidate the real structures of the different particles within the catalyst material.

## 2.2.2 Experimental

### 2.2.2.1 Preparation of Thermally Activated MoVW Mixed Oxides

The preparation of the starting material of this investigation has been described in the previous Section on page 48. The obtained bluish black compound was used as a solid precursor for the structural investigations,<sup>34, 10</sup> and will be referred to as the starting material.

The thermal activation treatments have been carried out in a quartz tubular flow reactor (see Chapter 4 on page 106) in the temperature range of 673 K to 829 K in a flow of 100 ml/min pure nitrogen for 1 or 2 hours. The accuracy of the indicated temperatures is  $\pm 1^\circ\text{C}$ .



### 2.2.2.2 X-ray Diffraction

All XRD measurements were made with a STOE STADI-P focusing monochromatic transmission diffractometer (Ge primary monochromator, Cu-K $\alpha_1$  radiation), equipped with a position sensitive detector (PSD) at room temperature. The phase analysis was done with the PCW 2.2 software package<sup>109</sup> using Retrieve single crystal data (ICSD-PDF-2).

### 2.2.2.3 Transmission Electron Microscopy

Specimens for electron microscopy have been prepared by the standard powder preparation technique. A small amount of oxide powder was crushed in corundum mortars to a finer powder if necessary. This specimen powder was dispersed in a neutral organic solvent, usually n-pentane, by ultrasonic stimulation. The smallest droplet of such a suspension, typically several  $\mu\text{l}$ , was brought on a copper grid covered by a carbon film.

Such specimens were analysed by a Philips CM 200 FEG electron microscope using a side-entry double-tilt specimen holder. The electron microscopy observations can be classified in different stages. Observations with relatively low magnifications obtain the morphological information of the specimens. Crystallographic information of small particles in the specimen can be obtained by recording their electron diffraction patterns using the selected area electron diffraction technique (SAED). A similar information can directly be obtained by taking the electron micrograph at the highest magnification, if the electron microscope has a sufficient resolution capability and the crystalline specimen is suitably thin and oriented to the incident electron beam. Further possibilities to obtain the crystallographic information by electron microscopy will be discussed below in the different individual cases.

Irradiation damage of the oxide specimens in the electron beam during electron microscopy observation is one of the largest problems of this technique,<sup>53</sup> because MoO<sub>3</sub> crystals and the related intermediate Mo oxides are very sensitive to electron irradiation. Therefore special care has been taken to avoid irradiation damage.

The elemental distribution in the MoVW oxide specimen was obtained by elemental mapping using the EDX equipment (EDAX, Oxford Instruments) or the electron energy loss spectroscopy tech-

nique (EELS) attached to the high resolution electron microscope.

#### **2.2.2.4 Raman Microspectroscopy**

All Raman spectra were recorded with a DILOR LABRAM I spectrometer which as been described on page 15. Experimental conditions are described on page 49. Two scans with an accumulation time of 150 sec. have been averaged for one spectrum.

SIMPLISMA<sup>174, 175, 177</sup> was used to derive the linearly independent Raman spectral components of large data sets. The statistical analysis was applied to a set of 500 Raman spectra in total built by five subsets of 100 laterally resolved Raman spectra recorded of the samples thermally activated at 673, 803, 813, 818 and 829 K, respectively.

### **2.2.3 Results and Discussion**

#### **2.2.3.1 XRD**

The structures of the oxides obtained by thermal activation of the starting material were analysed by XRD (Figure 2.14). The XRD pattern of the XRD nanocrystalline starting material (Figure 2.14a) can be understood as a mixture of a majority of nanocrystalline oxide with  $\text{Mo}_5\text{O}_{14}$  structure and minor amounts of nanocrystalline material with  $\text{MoO}_3$  structure.<sup>14, 34</sup> The thermally activated sample, which showed an enhancement of its catalytic activity by a factor of three consists of a crystalline oxide with  $\text{Mo}_5\text{O}_{14}$  structure and minor amounts of an oxide with  $\text{MoO}_3$  structure.

The crystallisation of mainly the oxide of  $\text{Mo}_5\text{O}_{14}$  structure was observed after thermal activation in the narrow temperature range between 803 K and 818 K (XRD reflections indicated by + in Figure 2.14b, d). The structures of monoclinic  $\text{MoO}_2$  (XRD reflections indicated by # in Figure 2.14) and orthorhombic  $\text{MoO}_3$  (XRD reflections indicated by \* in Figure 2.14) were observed beside the oxide of  $\text{Mo}_5\text{O}_{14}$  structure. In general, the higher the activation temperature the more crystalline oxides of  $\text{MoO}_3$  and  $\text{MoO}_2$  structure were found.

Activation temperatures higher than 823 K led to an almost quantitative decomposition of the  $\text{Mo}_5\text{O}_{14}$  oxide (Figure 2.14e). The main decomposition products were oxides of orthorhombic  $\text{MoO}_3$ ,  $\text{MoO}_2$  structures and X-ray amorphous oxides at activation temperatures above 818 K. The

decomposition of the oxide of  $\text{Mo}_5\text{O}_{14}$  structure may, therefore, be understood as a disproportionation into the thermodynamically stable phases of  $\text{MoO}_2$  and  $\text{MoO}_3$  structure, and a X-ray amorphous mixed oxide. The lattice constants of the oxide of  $\text{MoO}_3$  structure ( $a = 4.217 \text{ \AA}$  ;  $b = 13.458 \text{ \AA}$  ;  $c = 3.951 \text{ \AA}$ ) exhibits contractions of the a- and c-axis, while an elongation of the b-axis is observed in comparison to pure  $\text{MoO}_3$  (Pbmn,  $a = 3.964 \text{ \AA}$ ,  $b = 13.863 \text{ \AA}$ ,  $c = 3.699 \text{ \AA}$ ,  $\beta = 120.9$ ).<sup>75</sup> For the oxide of  $\text{MoO}_2$  structure ( $a = 5.611 \text{ \AA}$  ;  $b = 4.856 \text{ \AA}$  ;  $c = 5.317 \text{ \AA}$ ), the comparison with pure  $\text{MoO}_2$  (P21/c,  $a = 5.610 \text{ \AA}$ ,  $b = 4.857 \text{ \AA}$ ,  $c = 5.626 \text{ \AA}$ ,  $\beta = 120.9$ )<sup>132</sup> reveals a contraction of the a-axis and an elongation of the c-axis. These changes of the lattice parameters are probably due to the incorporated tungsten and vanadium. The lattice parameters of the oxide of  $\text{Mo}_5\text{O}_{14}$  structure ( $a = 22.826 \text{ \AA}$ ,  $c = 3.983 \text{ \AA}$ ) are in good agreement with literature data of V substituted  $\text{Mo}_5\text{O}_{14}$ <sup>47</sup> or calculated data.<sup>14</sup>

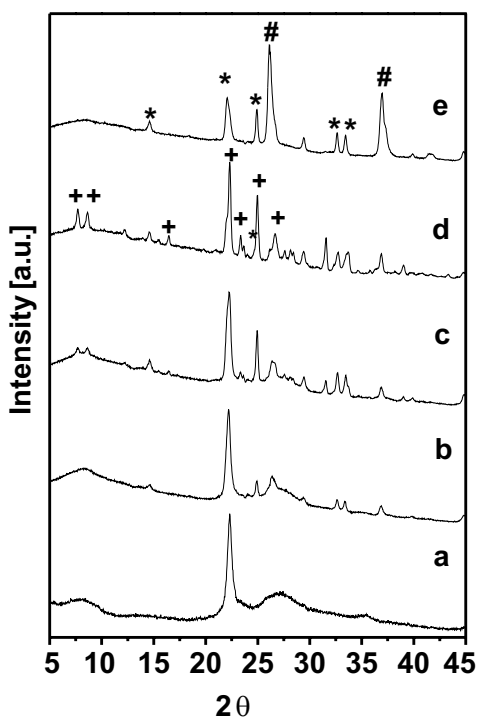


**Fig. 2.14:** XRD pattern of the starting material and catalysts activated at temperatures indicated: a) starting material, b) activated at 803 K, c) activated at 813 K, d) activated at 823 K, e) activated at 829 K. The reflections of  $\text{Mo}_5\text{O}_{14}$  (+),  $\text{MoO}_2$  (#) and  $\text{MoO}_3$  (\*) are indicated.

A quantification of the overall phase compositions of these thermally activated samples was not possible due to the remaining nanocrystalline oxide of  $\text{Mo}_5\text{O}_{14}$  structure in the specimen, which was indicated by the rather high X-ray background (see inset of Figure 2.14). However, in an attempt to further understand the changes in the crystallinity, the integral intensity ratios of the X-ray amorphous background and the observed diffraction peaks both normalised to an internal Si standard were evaluated to gain information about the change in the degree of crystallisation with treatment temperature. About 76 % of the total X-ray intensity was found in the X-ray amorphous background of the X-ray pattern of the starting material. Only 17% of the sample consisted of nanocrystalline oxide of  $\text{Mo}_5\text{O}_{14}$  structure.

Upon thermal treatment, the X-ray amorphous part of the sample diminished. 90% of the total crystalline material within the samples treated at temperatures below 823 K consisted of an crystalline

oxide of  $\text{Mo}_5\text{O}_{14}$  structure. The remaining 10% crystalline oxides comprise mainly of orthorhombic  $\text{MoO}_3$ -type oxides and minor amounts of monoclinic  $\text{MoO}_2$ . After the thermal activation the amount of the crystalline oxide of  $\text{Mo}_5\text{O}_{14}$  structure has strongly decreased on cost of the crystalline oxide of orthorhombic  $\text{MoO}_3$  structure and minor amounts of monoclinic  $\text{MoO}_2$ .

### 2.2.3.2 HRTEM

The MoVW mixed oxides appear as black powders and their particle size distribution is between  $0.1\ \mu\text{m}$  and a few  $\mu\text{m}$  as determined by scanning electron microscopy.<sup>14</sup> These particle aggregates have an inner structure of either small crystallites or are almost amorphous as shown by TEM.<sup>14</sup>

#### 2.2.3.2.1 The Starting MoVW Mixed Oxide Material

The starting material has been thermally treated at 673 K. This temperature leads to complete decomposition of the ammonium oxometalate precursor. Multicomponent systems like these MoVW mixed oxides may show different phases with different elemental compositions depending on their activation history, *e.g.* as a function of treatment temperature, time, atmosphere etc. X-ray diffraction and Raman measurements revealed that the MoVW mixed oxide is mainly nanocrystalline, which has been activated at 723 K. Different molybdenum oxides and bronzes are formed during the complex decomposition process of ammonium molybdates.<sup>183, 184</sup> Additional tungsten or vanadium strongly influence this decomposition process and the phase stability of the oxide of  $\text{Mo}_5\text{O}_{14}$  structure.

Transmission electron microscopy observations, however, unravelled that the specimen contained at least two different types of particles. Electron micrographs and diffraction patterns of the relatively large nanocrystalline particles and the typical aggregates of very small crystalline particles are shown in Figure 2.15 A and B and 2.15 C and D, respectively. The relative amount of the nanocrystalline particles is about four times larger than that of aggregates of crystalline particles. These different types of particles can hardly be distinguished by a simple morphological SEM observation.

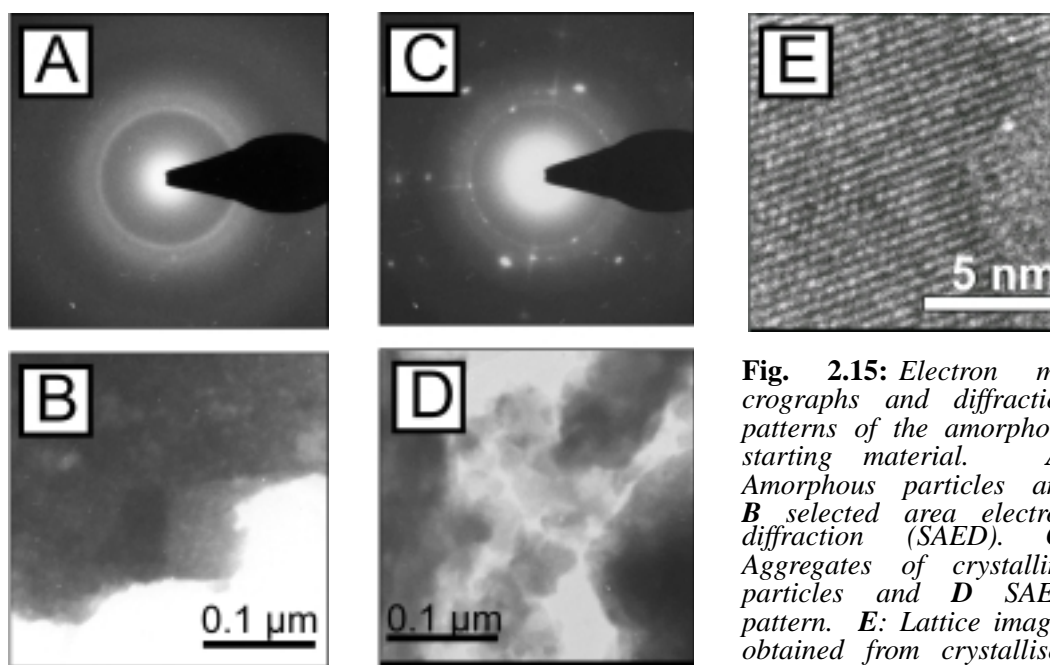


**Fig. 2.15:** *Electron micrographs and diffraction patterns of the amorphous starting material. A: Amorphous particles and B selected area electron diffraction (SAED). C: Aggregates of crystalline particles and D SAED pattern. E: Lattice images obtained from crystallised particles.*

Electron diffraction patterns shown in Figure 2.15 A exhibit relative broad diffraction rings. The first diffraction ring corresponds to a lattice spacing of about 0.42 nm and the mean particle size is estimated to be about 5 nm. Further diffraction rings correspond to the lattice spacings of 0.32 - 0.35, and 0.17 - 0.21 nm, respectively. Therefore, a complete periodic character of the materials in the specimen cannot be deduced from this electron diffraction pattern. Resolved lattice images could not be obtained in high magnification electron micrographs of these type of nanocrystalline particles. The determined lattice constants fit well to the expected regular (0.23 nm) and doubled lattice (0.46 nm) constants in the a and b direction of the tetragonal  $\text{Mo}_5\text{O}_{14}$  oxide.<sup>149</sup> The large mismatch of about 9 % relative to the values reported by Kihlberg may be due to the nanocrystalline state of the material and a contraction along the a and b-axis due to the V and/or W incorporation. The large background seen in the X-ray patterns (Figure 2.14) may in part be caused by this electron microscopy nanocrystalline material. The integral ratio of the nanocrystalline background and the peak areas in the SAED pattern of this material indicates comparable compositions revealed by XRD and electron microscopy.

The electron diffraction patterns recorded of aggregates of crystalline particles exhibit typical diffraction spots, as shown in Figure 2.15 C. The average size of these small crystallite particles was estimated to be about 10 - 15 nm. The individual crystallite particle is, therefore, too small to

be manipulated in the electron microscope in order to determine its crystal structure. An image of resolved lattice planes has been observed at the edge of the small aggregate (Figure 2.15 E). Almost all lattice spacings were determined to be 0.42 nm. Again this value fits well to the expected lattice constants of  $\text{Mo}_5\text{O}_{14}$ . TEM reveals that the decomposition of the ammonium oxometalate precursors at 673 K leads only to a minor crystallisation of about 20 % of the material. This result agrees well with the XRD result of a mainly nanocrystalline starting material (Figure 2.14a).

#### **2.2.3.2.2 Mixed Oxides Activated at 813 K for 1h and 2h.**

After activation at 813 K, crystalline particles of an oxide of orthorhombic  $\text{MoO}_3$  structure are found as shown in Figure 2.16 A and B. Crystals of the oxide of  $\text{Mo}_5\text{O}_{14}$  structure are detected too by TEM in agreement with previous work as shown in Figure 2.16 C and D.<sup>34, 14</sup> The resolution of this electron micrograph is limited due to unfavourable defocusing and a small miss-orientation of the crystal to the incident electron beam. 200 electron diffraction spots can be recognised in the diffraction pattern (Figure 2.16 C) in spite of the forbidden diffraction spots for usual  $\text{Mo}_5\text{O}_{14}$  crystals.

Most importantly, MoVW mixed oxides of another structure have additionally been detected after these temperature treatments. An electron micrograph and the electron diffraction pattern of this structure are shown in Figure 2.16 E and F. It can be deduced from this micrograph and SAED pattern that this peculiar type of an MoVW mixed oxide has a layered or fibrous structure with irregular ordering. This irregular ordering clearly can be recognised in the diffraction pattern. This special MoVW oxide phase was observed after activating the precursor oxide at 813 K for 1 and 2 hours. This peculiar structure is termed "bundle structure", because this structure seems to be formed by bundles of oxide strings as suggested by its electron micrograph (vide infra).

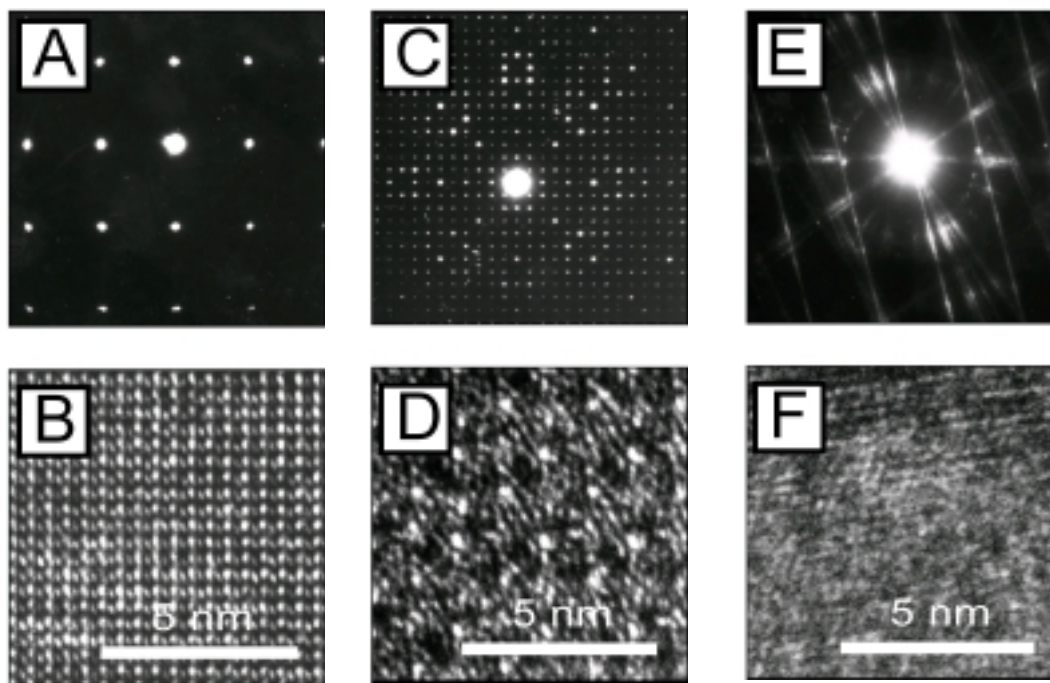


**Fig. 2.16:** *Electron micrographs and SAED patterns of the mixed oxide which was activated at 813 K for 2 hours. A and B: MoO<sub>3</sub>-type particle.*

**Fig. 2.16:** *C and D: Mo<sub>5</sub>O<sub>14</sub>-type particle.*

**Fig. 2.16:** *E and F: Electron micrograph and SAED pattern of "bundle" structure.*

### 2.2.3.2.3 Mixed Oxides Activated at 818 K for 2h

About 80% of the found oxide particles are of Mo<sub>5</sub>O<sub>14</sub> structure with a lattice constant of 0.42 nm after this activation treatment (Figure 2.17 A and B). Their crystallite size has remarkably increased as compared to that of the crystallites in the specimen activated at 813 K for 2h. The average crystallite size after the thermal treatment at 818 K is estimated to be around 1020 nm. Some MoVW mixed oxide crystals are of orthorhombic MoO<sub>3</sub> structure (Figure 2.17 C). The electron microscopic image taken at high magnification (x 750000) and the diffraction pattern of one characteristic MoO<sub>3</sub> crystal are shown in Figure 2.17 C and D. In the electron micrograph, the morphologic structure of the MoO<sub>3</sub> crystallite surface can be seen in addition to the two dimensional lattice image. The crystal surfaces exhibit a lot of atomic steps formed by small islands or intrusions, as recognised by the small difference of the crystal contrast. In the diffraction pattern, streaks are detected in one direction.

The peculiar "bundle" structure again could be found in this specimen (micrograph not shown). This

so-called "bundle" structure cannot be defined as being crystalline due to its lack of a well defined periodicity. The "bundle" structure seems to be built up from bundles of molecular oxide chains.

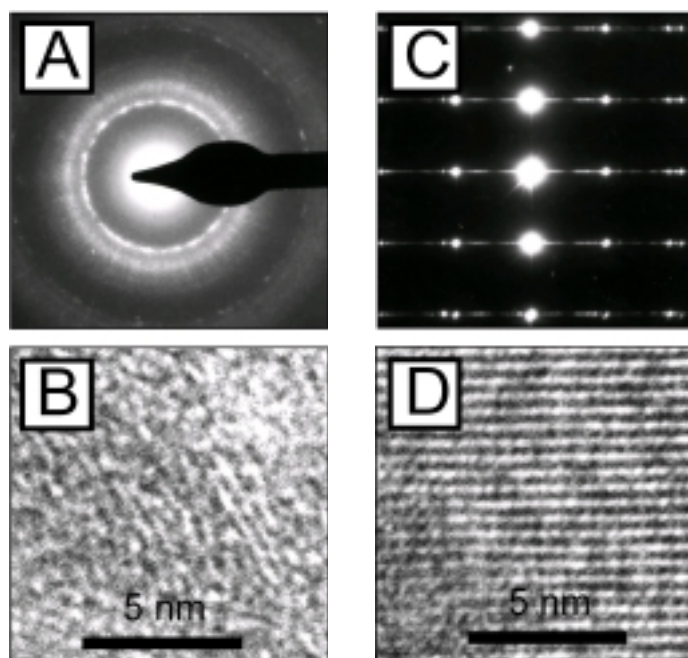


**Fig. 2.17:** *Electron micrographs and SAED patterns of the mixed oxide which was activated at 818 K for 2 hours. A and B: particle of the oxide of  $\text{Mo}_5\text{O}_{14}$  structure. C and D: particle of the oxide of  $\text{MoO}_3$  structure.*

There could be an alternative explanation for the observed streaks in the diffraction pattern (Figure 2.16c). The "bundle" phase may have discontinuous planes perpendicular to these streaks in the diffraction pattern. In this case, the "bundle" phase can be understood as having a layered structure. These layers have to be oriented in this case nearly parallel to the incident electron beam.

However, this alternative explanation for the streaks cannot be accepted as being correct, because the micrographs of the "bundle" structure does not change when the tilting angle between the specimen and the incident electron beam is arbitrarily changed. For any tilting angle, the average distance between the streaks was measured to be 0.35 nm. This distance seems to be slightly shorter than the distance between two transition metal ions placed at the centre of  $\text{MO}_6$  polyhedra. The shorter distance can be understood by the fact that the average distance between quasi net planes formed from randomly bundled oxide chains is usually smaller than the diameter of the individual oxide chain.

Unfortunately, it is almost impossible to deduce the atomic structure of this "bundle" phase from HRTEM observations alone. This intermediate state of the "bundle" structure between an amor-



phous and a crystalline material is the most interesting feature of the MoVW mixed oxide activated at 813 and 818 K.

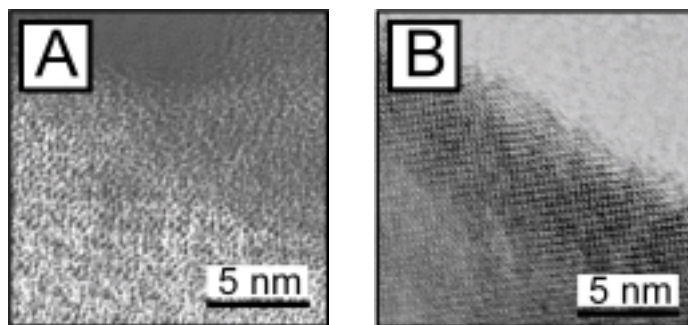


**Fig. 2.18:** High resolution electron micrograph of the fringed edge of a crystalline oxide of  $\text{Mo}_5\text{O}_{14}$  structure **A** and a crystalline oxide of  $\text{MoO}_3$  structure **B** in the sample activated at 818 K.

In Figure 2.18 high resolution TEM images of mixed oxide crystals of  $\text{Mo}_5\text{O}_{14}$  (Figure 2.18A) and of  $\text{MoO}_3$  structure (Figure 2.18B) are shown. Important to note is the fringed appearance of the crystal's edge, which has lost the regular arrangement of the atoms compared to deeper laying zones. In Figure 2.18B a well crystallised oxide of  $\text{MoO}_3$  structure is shown irradiated along the [010] direction. The fringed structure of the  $\text{MoO}_3$  crystal edge is thinner as compared to that of the  $\text{Mo}_5\text{O}_{14}$  crystal but also recognised. These observations point to different compositions of the surface layer and bulk of the catalyst material.

#### 2.2.3.2.4 Mixed Oxides Activated at 829 K for 2h

After this activation treatment, the MoVW mixed oxides are further crystallised (micrographs not shown). Rather small crystals of  $\text{Mo}_5\text{O}_{14}$  structure (510nm) and larger ones of  $\text{MoO}_3$  structure are found. Crystals having the  $\text{MoO}_2$  structure have not been observed, due to a small concentration of rather large, well crystallised  $\text{MoO}_2$  in the sample as proven by XRD (Figure 2.14e) and Raman (vide infra).

Particles or crystallites showing the "bundle" structure could not be detected after this treatment anymore. This result can be explained by the assumption, that the bundle structure is an intermediate in the disproportionation process of the oxide of  $\text{Mo}_5\text{O}_{14}$  structure to  $\text{MoO}_3$  and  $\text{MoO}_2$ , and an amorphous phase as shown by XRD (Figure 2.14) and Raman (vide infra).

It could be argued that the temperature of 818 K is not the phase boundary of this compound because

Raman bands of the oxide  $\text{Mo}_5\text{O}_{14}$  structure are still observed (vide infra). This discrepancy, however, can easily be explained by the observed general elemental inhomogeneity of the MoVW mixed oxide catalyst.<sup>14</sup> The thermally crystallised and the remaining nanocrystalline oxides of  $\text{Mo}_5\text{O}_{14}$  structure may both have different overall elemental compositions. The different concentrations of Mo, V, or W may lead to the observed different thermal behaviour.

A segregation of the different transition metals (Mo, V and W) into clearly separate phases, on the other hand, has not been detected for the precursor oxide and the thermally activated materials within the accuracy of the EDX technique. This observation leads to the conclusion that the elemental phase compositions of the stable nanocrystalline, and the thermally crystallised oxide of  $\text{Mo}_5\text{O}_{14}$  structure only vary by a few atom percent.

### 2.2.3.3 Raman Spectroscopy

XRD and HRTEM analysis revealed that all differently activated MoVW mixed oxides contain some amounts of nanocrystalline, material. Raman spectroscopy was therefore used to hopefully better understand the molecular structure and coordination symmetry of this nanocrystalline material. Characteristic Raman spectra of the thermally activated catalyst are shown in Figure 2.19. The Raman spectrum of the starting material (Figure 2.19a) shows broad Raman bands at about 930, 830, and 705  $\text{cm}^{-1}$ . These very ill-defined Raman bands are attributed to the mixture of nanocrystalline oxides of  $\text{Mo}_5\text{O}_{14}$  and  $\text{MoO}_3$  structure as already discussed in detail in the previous Section.

The Raman spectrum of the sample thermally activated at 803 K (Figure 2.19b) is characterised by Raman bands at 990(br), 908, 860(sh), 850, and

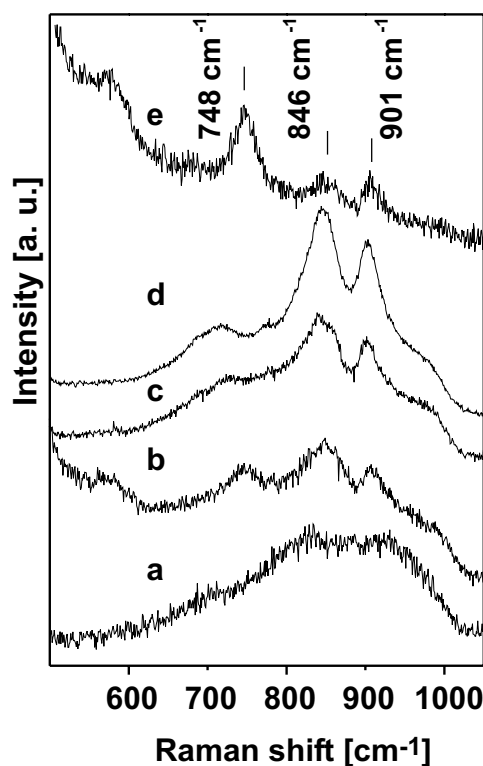


**Fig. 2.19:** Raman spectra of the starting material and thermally activated samples at temperatures indicated: starting material **a**, activated at 803 K **b**, activated at 813 K **c**, activated at 823 K **d**, and activated at 829 K **e**.

745  $\text{cm}^{-1}$ , the sample activated at 813 K exhibits Raman bands at 975(sh), 902, 860(sh), 845, and 718  $\text{cm}^{-1}$  (Figure 2.19c), and the one activated at 818 K shows Raman bands at 975(sh), 902, 845, 775(sh,vw), 718 and at 685(sh,vw)  $\text{cm}^{-1}$  (Figure 2.19d), and at 577, 385, 347, 336, 278, 247  $\text{cm}^{-1}$  (not shown). With increasing activation temperature, the Raman bands become more resolved and shift to lower frequencies due to the higher crystallinity of the oxide of  $\text{Mo}_5\text{O}_{14}$  structure (Figure 4b-4d; compare also the Raman result shown in the previous Section).

After thermal activation at 829 K, above the disproportionation temperature of the oxide of  $\text{Mo}_5\text{O}_{14}$  structure as determined by XRD, the Raman bands of monoclinic  $\text{MoO}_2$  are detected at 748, 596, 575, 498, 461, and 363  $\text{cm}^{-1}$  (Figure 2.19e) in agreement with XRD (Figure 2.14). The Raman signals of the oxide of  $\text{Mo}_5\text{O}_{14}$  structure at 845 and 902  $\text{cm}^{-1}$  have lost most of their intensity but it still can be detected.

In order to account for sample inhomogeneities, Raman images of 100 spectra were recorded of all differently activated samples over an area of 900  $\mu\text{m}^2$  with a lateral resolution of 0.7  $\mu\text{m}$ . Raman spectra resembling the spectrum of well-crystallised oxides of the  $\text{MoO}_3$  structure have not been included in the set of statistically evaluated Raman data. Due to the extremely high Raman cross section of well-crystallised  $\text{MoO}_3$ , the characteristic Raman bands of  $(\text{MoVW})\text{O}_3$  oxides would completely overwhelm all additional Raman information. Therefore, the sample areas which were Raman spectroscopically characterised were selected such not to contain the characteristic  $\text{MoO}_3$  bands. The spectrally pure components of the Raman spectra are shown in Figure 2.20 as determined by statistical analysis of the whole set of 500 Raman spectra using the SIMPLISMA approach. Three different spectral components can be distinguished building up all recorded Raman spectra. The first pure component resembles the typical Raman spectra of monoclinic  $\text{MoO}_2$  with pure spectral features at 746  $\text{cm}^{-1}$  (Figure 2.20a) and 549, 499, 462 and 364  $\text{cm}^{-1}$  (not shown). The second pure spectral component (Figure 2.20b) exhibits features at 960, 910, and 870  $\text{cm}^{-1}$  and resembles typical Raman spectra of oligomeric molybdenum oxide clusters, comparable to hepta or octamolybdates.<sup>10, 20, 36</sup> Hence, it may be concluded that the pure spectral component 2 of the set of Raman spectra of thermally activated MoVW mixed oxides is due to oligomeric MoVW oxide clusters in structural analogy to polyoxometalates. These oligomeric MoVW clusters are identified as the material being responsible for the X-ray amorphous background. The third pure spectral

component (Figure 2.20c) mainly resembles the crystallised oxide of  $\text{Mo}_5\text{O}_{14}$  structure with spectral features at 902, 860, 845 and  $720\text{ cm}^{-1}$  with contributions of an nanocrystalline oxide of  $\text{MoO}_3$  structure with spectral features at 985, and  $815\text{ cm}^{-1}$ . The weak feature at  $785\text{ cm}^{-1}$  is due to traces of  $\text{MoO}_2$ . This finding seems to imply that the oxides of  $\text{Mo}_5\text{O}_{14}$  structure are always accompanied by  $\text{MoO}_3$  and  $\text{MoO}_2$ , in line with the XRD results (Figure 2.14) and literature observations.<sup>14, 149</sup> The broad ill-defined feature at  $815\text{ cm}^{-1}$  and the weak feature at about  $985\text{ cm}^{-1}$  in the SIMPLISMA trace c of Figure 2.20 indicate a very low degree of crystallisation of the oxide of  $\text{MoO}_3$  structure. However, it has to be noted that the Raman image was taken from an area such not to contain the characteristic Raman bands of  $\text{MoO}_3$ , because of there strong overwhelming intensity. This low crystallinity results in a very weak Raman cross section relative to that of the oxide with  $\text{Mo}_5\text{O}_{14}$  structure.

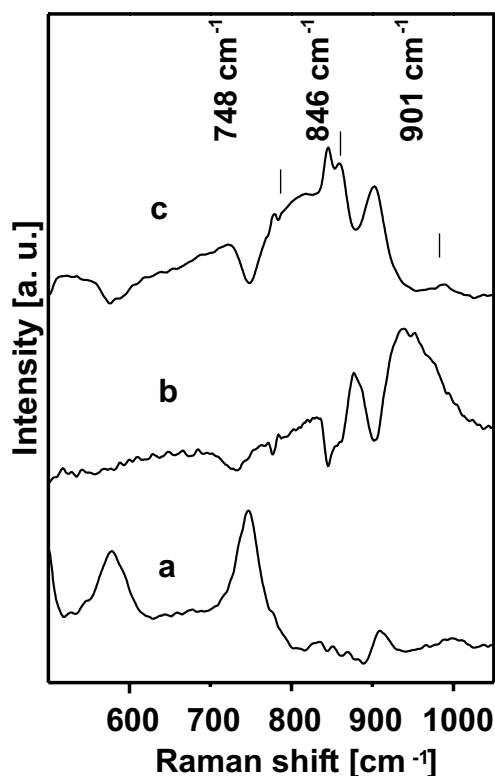


**Fig. 2.20:** Spectral components according to the SIMPLISMA analysis of the set of 500 Raman spectra: oxide of  $\text{MoO}_2$  structure **a**, oligomeric MoVW clusters **b**, and oxide of  $\text{Mo}_5\text{O}_{14}$  structure **c**.

Using the statistical SIMPLISMA approach, information can be obtained too about changes in the composition of the differently activated samples. The mean spectral weight of each component, e.g. the ratio of each spectral component normalised to the sum of all spectral weights, is a measure of the relative changes of the sample composition as a function of the activation temperature (Figure 2.21). The amount of nanocrystalline oxide of  $\text{Mo}_5\text{O}_{14}$  structure in the MoVW mixed oxide samples, presumably present as oligomeric molybdenum oxide clusters, continuously decreases with increasing activation temperature as may be expected. The amount of the oxide of  $\text{MoO}_2$  structure seems to be high after

treatments at intermediate temperatures about 803 K. Its relative concentration decreases at these treatment temperatures at which the crystalline oxide of  $\text{Mo}_5\text{O}_{14}$  structure is formed, and subsequently increases again. The intermediate higher amount of  $\text{MoO}_2$  may be related to the formation process of the crystalline oxide of  $\text{Mo}_5\text{O}_{14}$  structure. Kihlberg reports that  $\text{Mo}_5\text{O}_{14}$  can be generated by tempering the respective amounts of  $\text{MoO}_2$  and  $\text{MoO}_3$ .<sup>149</sup> The amount of crystalline oxide of  $\text{Mo}_5\text{O}_{14}$  structure increases at temperatures up to 818 K. Crystallisation in general, should lead to higher Raman cross sections and a decrease of the FWHM of the Raman bands. Exactly this is observed for the Raman spectra of the oxide of  $\text{Mo}_5\text{O}_{14}$  structure. Its amount decreases again at higher temperatures due its disproportionation into oxide of  $\text{MoO}_2$  and  $\text{MoO}_3$  structure as shown by XRD.

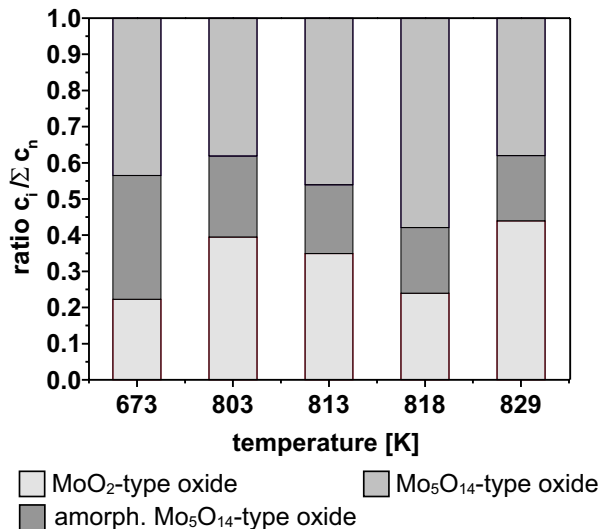


**Fig. 2.21:** Qualitative analysis of the spectral weight of each spectral pure component as a function of the activation temperature.

In the  $\text{Mo}_5\text{O}_{14}$ -structure, one third of the  $\text{MoO}_6$  polyhedra share two triangular channels, i.e. the  $\text{MoO}_6$  polyhedra are strongly deformed. All other  $\text{MoO}_6$  polyhedra share only one triangular channel, i.e. these  $\text{MoO}_6$  polyhedra are less distorted. Following the analysis of Kihlberg,<sup>149</sup> the bond length of the shortest Mo-O bond (in c-direction) in the  $\text{Mo}_5\text{O}_{14}$ -structure is between 1.67 Å and 1.69 Å depending on the distortion of the  $\text{MoO}_6$  polyhedron. The number of triangu-

lar channels to which a  $\text{MoO}_6$  polyhedron is bound, e.g. one or two, determines the second terminal Mo-O bond length (within the ab-plane) to be between 1.85 Å and 1.94 Å, or between 1.71 Å and 1.77 Å, respectively.

Following this XRD analysis, three groups of different bond length's should be expected for the terminal Mo-O vibrations. One group of Mo-O bonds parallel to the c-axis, and two groups of Mo-O bonds in the ab-plane of the different types of  $\text{MoO}_6$  polyhedra with respect to the triangular channels. Exactly these three different Mo-O groups are determined from the experimental Raman spectrum applying the Hardcastle and Wachs model<sup>93</sup> to the Raman bands above  $700\text{ cm}^{-1}$ . The

bond lengths of the terminal Mo-O bond in c-direction of all MoO<sub>6</sub> polyhedra are estimated to be 1.69 Å (broad Raman band at 985 cm<sup>-1</sup>). The bond lengths of the terminal Mo-O bond in the ab-plane of the MoO<sub>6</sub> polyhedra sharing one triangular channel are estimated to be 1.76 Å (Raman band at 860 cm<sup>-1</sup>) and 1.77 Å (Raman band at 845 cm<sup>-1</sup>). The terminal Mo-O bond parallel to the ab-plane of the remaining three MoO<sub>6</sub> polyhedra are estimated to be 1.81 Å (Raman band at 745 cm<sup>-1</sup>), 1.85 Å (band at 720 cm<sup>-1</sup>), and 1.87 Å (band at 688 cm<sup>-1</sup>). The remaining band at 902 cm<sup>-1</sup> not yet being assigned is attributed to the stretching vibration of the terminal Mo-O bond parallel to the c-axis of the MoO<sub>7</sub> pentagonal bipyramids. Although the assignment according to Hardcastle and Wachs is limited because solid vibrations cannot fully be described in a localised model, the above assignment to certain Mo-O bonds may give a first interpretation of the observed Raman bands, as long as detailed Raman data on single crystals are not available.

## 2.2.4 Summary and Conclusion

The combined structural analysis of the MoVW mixed oxide activated at different temperatures, presented in this Section, revealed that the crystallisation of the oxide of Mo<sub>5</sub>O<sub>14</sub> structure occurs only in a rather narrow temperature range between about 800 and 820 K. At activation temperatures above 820 K, the oxide of Mo<sub>5</sub>O<sub>15</sub> structure increasingly disproportionated into oxides of MoO<sub>3</sub> and MoO<sub>2</sub> structure. This disproportionation process seemed to occur via a X-ray amorphous phase, which was termed "bundle" structure according to its appearance in HRTEM images and SEAD. This "bundle structure" is build by chains which are disordered in two dimensions.

The present study on the phase stability of the oxide of Mo<sub>5</sub>O<sub>14</sub> structure revealed that some part of the material remained nanocrystalline during thermal activation. This incongruent crystallisation behaviour of the MoVW mixed oxide most probably is related to the inhomogeneous elemental composition. Mo<sub>5</sub>O<sub>14</sub> tolerates the incorporation of considerable amounts of V and W. Stoichiometries of such phases were reported to be (Mo<sub>0.92</sub>V<sub>0.08</sub>)O<sub>14</sub> or (Mo<sub>0.75</sub>W<sub>0.25</sub>)O<sub>14</sub>, respectively.<sup>45</sup> Especially, the incorporation of W favours the formation of oxides of Mo<sub>5</sub>O<sub>14</sub> structure comparable with the results on Ta and Nb incorporation.<sup>42, 48</sup> Tungsten and vanadium, thus, act as structural promoters enhancing, and stabilising the formation of the Mo<sub>5</sub>O<sub>14</sub> structure. It is known that only 2 to 12%

V lead to a stabilisation of  $\text{Mo}_5\text{O}_{14}$ <sup>46, 101</sup> The MoVW catalyst however contains 28% vanadium<sup>14</sup> more than the structure tolerates according to literature. It is known on the other hand that  $\text{Mo}_5\text{O}_{14}$  tolerates the incorporation of up to 25% W.<sup>46, 45, 101</sup> The 8% W found in the catalyst hence lead to stabilisation of the  $\text{Mo}_5\text{O}_{14}$  structure. Alternatively, the role of W and V may also be discussed in view of lattice oxygen defects. The incorporation of oxygen defects into  $\text{MoO}_3$  leads to a contraction of the c-axis,<sup>129, 101</sup> hence, affect extended regions within the crystal lattice. The promoting effect of V and W may lay in their ability to localise oxygen defects on one side -  $\text{V}^{5+}$  prefers fivefold coordination-, and the confinement of these lattice deformations by the redox stable W on the other. In light of this important role of W and V for the stabilisation of the oxide of  $\text{Mo}_5\text{O}_{14}$  structure it may be understood why W and V are of paramount importance to catalysis. Minor local variations in their concentrations within the specimen already may lead to different local MoVW oxide phases with different stability regimes and most importantly different catalytic behaviour.

The Raman characterisation of the MoVW mixed oxide catalyst may further shed some light on the role of the different metal-oxygen groups for catalytic action. Generally, it can be said that the shorter the M-O distance the more basic is the oxygen. Basic, nucleophilic oxygen groups on the catalyst surface are necessary for C-H bond activation.<sup>15</sup>

The longer and, therefore, weaker the M-O bond the easier this oxygen may be inserted into organic molecules. Selective oxidation catalysts have to discriminate for example between  $\alpha$ -H atoms of aldehydes and vinylic hydrogen atoms. The key to this selective C-H activation may be seen in the strength of the M-O bond of the active site abstracting the hydrogen. Promoters, e.g. V, Nb, Ta, W, stabilise intermediate Mo oxides with the proper M-O bonds for the selective C-H activation. The second step of selective oxidation, the oxygen insertion into the substrate, is facilitated by weaker M-O bonds which are also present in intermediate oxides. Thus, very strongly bound, basic oxygens will unselectively activate C-H bonds, and very labile M-O groups will lead to total oxidation. The optimisation of the catalyst with respect to selectivity and activity may, therefore, be seen as the search for a combination of H-abstracting and oxygen transferring functionalities, e.g. the search of an optimum oxide structure, hence, composition of a MoVW intermediate oxide.

The Raman spectra of the oxide of  $\text{Mo}_5\text{O}_{14}$  structure are highly interesting in this respect. With

the help of the Hardcastle and Wachs model, Mo-O distances were calculated for the  $\text{Mo}_5\text{O}_{14}$  oxide which compared well with the crystallographic data. While the nanocrystalline precursor,<sup>14</sup> and the amorphous part of the activated sample (Figure 2.21b) also showed Raman bands above  $930\text{ cm}^{-1}$ , indicating rather short Mo-O bonds, the oxide of  $\text{Mo}_5\text{O}_{14}$  structure has its main Raman features between  $840$  and  $900\text{ cm}^{-1}$ , due to M-O bond distances between  $1.77\text{ \AA}$  and  $1.73\text{ \AA}$ . Pure  $\text{MoO}_3$ , which is known for total oxidation, has Raman bands in this regime at  $995$ ,  $823$ , and  $666\text{ cm}^{-1}$ , being due to Mo-O distances of  $1.67$  and  $1.95\text{ \AA}$  (according to Hardcastle and Wachs,<sup>93</sup> the bond distance calculated from the band at  $823\text{ cm}^{-1}$  cannot be assigned to any distance in  $\text{MoO}_3$ ).  $\text{MoO}_3$  thus has a much stronger Mo-O bond on one side - good C-H bond activator - and a much weaker one on the other, whose oxygen can easily be released - good oxidator. It must be noted that in situ Raman  $^{18}\text{O}$ -labelling experiments of  $\text{MoO}_3$  have proven that the ease of oxygen exchange increases with increasing bond length or decreasing bond order,<sup>70</sup> supporting the above sketched role of the oxygen transferring M-O groups. A highly active and selective partial oxidation catalyst thus must have optimised oxygen functionalities along with good electron and ion mobilities for fast redox properties.

## 2.3 Summary

In the first Section of this Chapter, it was shown that pretreating the sample at  $813\text{ K}$  in inert atmosphere results in an increase of the  $\text{CH}_2\text{O}$  yield by factor of 3 with a selectivity of 80%. The starting material may be understood as a mixture of nanocrystalline oxide of  $\text{Mo}_5\text{O}_{14}$  and  $\text{MoO}_3$  structure.<sup>34, 14</sup> After thermal activation, the mixed oxide consisted of a mixture of a majority of an oxide of  $\text{Mo}_5\text{O}_{14}$  structure and trace amounts of crystalline oxides of  $\text{MoO}_3$  and  $\text{MoO}_2$  structure.<sup>34, 14</sup> This result was interpreted by the metastability of  $\text{Mo}_5\text{O}_{14}$  with respect to  $\text{MoO}_3$  and  $\text{MoO}_2$ .<sup>149</sup> The combined XRD and Raman identification of the oxide of  $\text{Mo}_5\text{O}_{14}$  structure points to its relevant role for the observed increase of the catalytic activity.

Inhomogeneous element distributions have been proven by SEM-EDX and TEM-EDX suggesting the presence of at least two different phases, one with high V contents, the other with all three metals present.<sup>14</sup> This elemental inhomogeneity was related to structural inhomogeneity by Raman



microspectroscopy.<sup>14</sup>

The combined data can be rationalised in term of a core-shell model of the activated catalyst, as shown in Figure 2.22, the core being mostly of an oxide of  $\text{Mo}_5\text{O}_{14}$  structure, and the shell formed by stoichiometrically ill-defined metal oxide clusters and having a higher degree of reduction (see Figure 2.18). The core and the shell may act differently in the catalytic process. During partial oxidation catalysis, the crystalline core of  $\text{Mo}_5\text{O}_{14}$  structure is suggested to play the role of an electron reservoir for the fast catalytic redox reactions. It also may act as an oxygen buffer due to its open structure of four-, six- and sevenfold coordinated metal ions which allows oxygen and vanadium diffusion as shown by XPS and RBS.<sup>14</sup> The shell provides a high number of active sites and allows fast surface oxygen diffusion, the core may act as the electron accepting reservoir due to its high electronic conductivity. Thus, the catalyst is able to adjust to temporary or spatially changing gas phase compositions within the reactor. The ill-defined shell on top the oxide of  $\text{Mo}_5\text{O}_{14}$  structure also allows fast oxygen exchange to respond to changing gas phase compositions and may provide a high number of active sites for the adsorption of the organic substrate and gas phase oxygen.

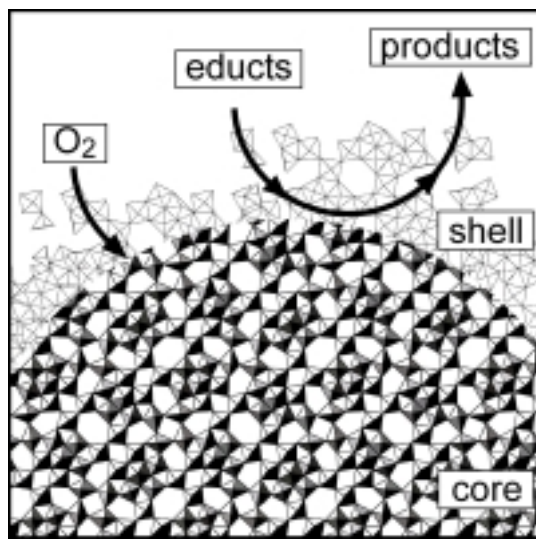


**Fig. 2.22:** Core-shell model: core with the oxide of  $\text{Mo}_5\text{O}_{14}$  structure surrounded by an ill defined amorphous shell.

It can be concluded from physicochemical characterisation that it is of paramount importance to monitor and fully control the elemental composition and the atomic structure of the MoVW oxide in order to fully understand its catalytic activity and selectivity. From the combined information obtained in this study, it may be suggested that vanadium on one hand enhances the catalytic activity of the mixed oxide but on the other destabilises the pre-

sumably active oxide of  $\text{Mo}_5\text{O}_{14}$  structure due to its high reducibility. The tungsten promoter, therefore, may be necessary to counterbalance the V induced instability of the material of  $\text{Mo}_5\text{O}_{14}$  structure.

In order to unravel these suggested different roles of the W and V addition it is necessary to study the influence of added V and W separately. Therefore, samples with only V and W and V/W addition have been prepared. The investigation on the influence of the added promoters on the oxide structure formed upon thermal activation will be presented in the following Chapter.

Precursor preparation and catalyst activation definitely is of importance for the structure of the catalyst, its degree of reduction and its elemental and structural heterogeneity. The question, how to influence the spatial elemental distribution within the ammonium metalate catalyst precursor and, hence, the final catalyst is addressed in the last Chapter of this thesis by the attempt to control the formation of a defined species in solution.

## Chapter 3

# Thermal Activation of Molybdenum Polyoxometalates\*

Most Mo-oxide based catalysts are prepared from aqueous mixed ammonium metalate solutions at given pH values.<sup>185</sup> After drying, these precursors are activated by well-defined thermal procedures under well-defined gas atmospheres. Temperature, heating rates and gas atmospheres are the most important factors for the activation processes. It is possible to control the physicochemical and structural properties of the catalysts *e.g.* crystallinity, thermal stability, redox potential or acid/base properties by these parameters. Therefore, the activation process plays a crucial role for the activity and selectivity of the final catalyst. However, the reproducibility of the activation process of multi-element catalyst systems is difficult and not understood on a molecular level due to the complex multi step activation processes and the numerous factors affecting each single step of the activation process.<sup>1</sup> Therefore, the knowledge of the activation processes is of high importance to understand the generation of active mixed oxide catalysts.

---

\* Parts of this Chapter will be published in M. Dieterle, G. Mestl and R. Schlögl, Thermal Activation of V and W promoted Polyoxometalates (in preparation).

### 3.1 *In situ* Characterisation of the Thermal Activation of Ammonium Heptamolybdate by TG/DTA, XRD and Raman Spectroscopy

#### 3.1.1 Introduction

The objective of the investigation presented in this Chapter is to understand the thermal activation process of  $(\text{NH}_4)_6\text{Mo}_7\text{O}_{24} \cdot 4(\text{H}_2\text{O})$  to molybdenum oxide catalysts using thermoanalytical methods (TG/DTA), *in situ* Raman spectroscopy and *in situ* X-ray diffraction (XRD).

Industrial catalysts contain additionally varying amounts of other transition metals like vanadium and/or tungsten.<sup>35, 186, 187, 188</sup> The presented results are the basis for the evaluation of the influence of V or W promoters on the activation process, which will be presented in the next Section of this Chapter.

Several authors have examined the AHM decomposition by means of TG/DTA<sup>189-193</sup> and XRD.<sup>184-195</sup> It was found, that the AHM decomposition proceeds in three steps.<sup>190, 191, 196</sup> It has been suggested that  $(\text{NH}_4)_6\text{Mo}_7\text{O}_{24} \cdot 4(\text{H}_2\text{O})$  transforms into ammonium pentamolybdate  $(\text{NH}_4)_8\text{Mo}_{10}\text{O}_{34}$  at 383 K, followed by a transformation to ammonium octamolybdate  $(\text{NH}_4)_6\text{Mo}_8\text{O}_{26}$  at 533 K. At 570 K, a hexagonal  $\text{MoO}_3$  phase was found, while  $\text{Mo}_4\text{O}_{11}$  and  $\text{Mo}_9\text{O}_{26}$  are formed at temperatures higher than 650 K.<sup>190, 191</sup> In synthetic air, orthorhombic  $\text{MoO}_3$  is the only observed product above 633 K.

TG/DTA-MS methods provide information about the energetics and the stoichiometry of the observed processes, while *in situ* XRD is suitable to detect the formation of crystallographic ordered structures. In contrast to XRD, *in situ* Raman spectroscopy reflects effects on the more local structure.

#### 3.1.2 Experimental

AHM (p.a.) was used in all experiments as received from Merck.

All TG and DTA measurements were conducted with a SEIKO thermobalance coupled to an ATOM- IKA IMR-MS 100 mass analyser, which was operated with Xe and  $\text{CF}_3\text{I}$  as primary gases to monitor oxygen, water,  $\text{NO}_x$  and ammonia. 20.2 mg AHM were thermally activated at a flow

of 100 ml N<sub>2</sub>/min and a heating rate of 5 K/min. The *in-situ* XRD experiments were conducted in Bragg-Brentano geometry on a STOE diffractometer (Cu-K $\alpha$  radiation) equipped with a secondary monochromator and a Bühler HDS high temperature diffraction chamber. The diffraction data were recorded at isothermal conditions at the corresponding temperatures stated at a flow of 100 ml N<sub>2</sub>/min. Due to the long acquisition time of the XR-diffractometer, the sample was heated in 25 K steps starting at 323 K up to 823 K. Prior to the measurement the temperature was hold constant for 30 minutes to equilibrate the sample.

All *in situ* Raman spectra were recorded with a DILOR LABRAM I spectrometer coupled to a reactor which is described in detail on page 106. 0.5 g AHM was thermally activated at a flow of 100 ml/min N<sub>2</sub>. A HeNe -laser (632 nm, Topag AG) was used for excitation of the Raman spectra in retro geometry. The laser power at the sample position was 50 mW. The sample was heated to 823 K with a heating rate of 5 K/min. Two spectra were averaged with an accumulation time of 30 sec. each.

### 3.1.3 Results and Discussion

#### 3.1.3.1 Thermal Analysis

TG/DTA characterisation of the AHM thermal activation process, which is shown in Figure 3.1, exhibits four endothermic (391, 476, 493 and 581 K) and one weak exothermic weight losses and/or phase transitions (653 K) in the temperature range up to 873 K. The stoichiometry of the starting material has been determined to be (NH<sub>4</sub>)<sub>6</sub>Mo<sub>7</sub>O<sub>24</sub>4.88\*(H<sub>2</sub>O) by TG/DTA under oxygen which leads to a total oxidation to MoO<sub>3</sub> at 873K. The water content of the starting material AHM differed from the formal stoichiometry of (NH<sub>4</sub>)<sub>6</sub>Mo<sub>7</sub>O<sub>24</sub>4\*(H<sub>2</sub>O). The observed weight losses and the estimated stoichiometries of the intermediates of the thermal activation process under inert atmosphere are summarised in Table 3.3.

The gaseous products of the activation process - water and ammonia - are monitored by IMR-MS as shown in Figure 3.1 d and e. NO and N<sub>2</sub>O could not be detected due to their low concentration. In Figure 3.2, the integral values are shown of the water and ammonia MS-signals. The MS-signals

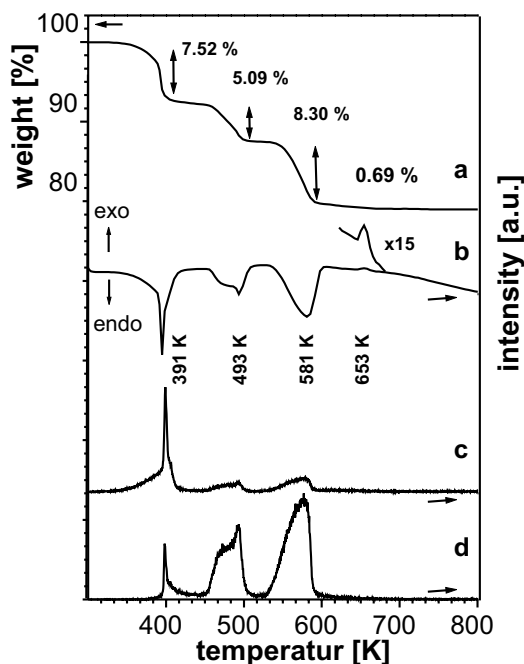


**Fig. 3.1:** TG and DTA signals of the AHM activation at a heating rate of 5 K/min: **a)** TG-signal  
**b)** DTA  
**c)** water-MS-signal  
**d)** ammonia-MS-signal.

have been baseline corrected, normalised and integrated with respect to the determined weight losses in the TG experiments expressed as molecules per Mo formula unit. These data were used to discriminate weight losses due to water and ammonia.

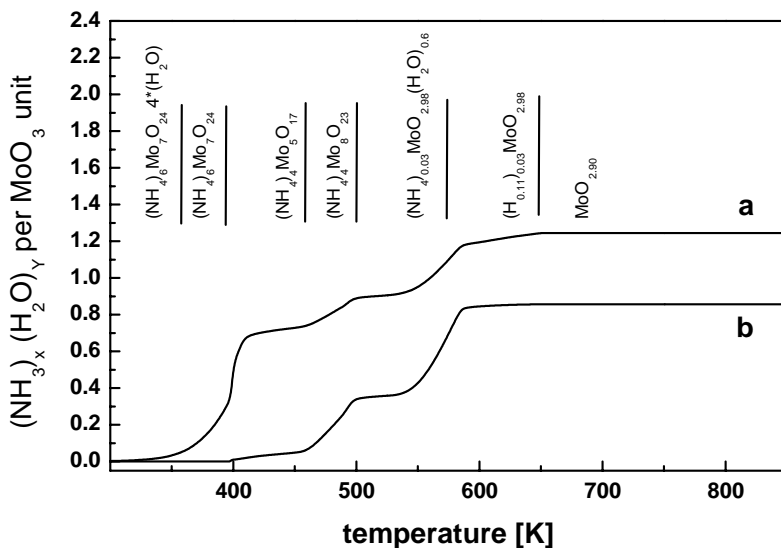


**Fig. 3.2:** Integral ammonia **a** and water **b** IMR-MS signals recorded during the thermal activation process.

The first weight loss is interpreted as being due to three independent processes, which are the loss of physisorbed and interlayer water, and subsequently that of ammonia. The total weight loss for this step of 7.52 wt% is composed of a weight loss of 6.83 wt% due to physisorbed and interlayer water and one of 0.68 wt% due to ammonia. The loss of physisorbed water is already observed at room temperature in absence of water vapour. The loss of interlayer water is assigned to the strong

DTA signal at 391 K. The observed weight loss is equivalent to a loss of 0.68 H<sub>2</sub>O per Mo. The formal stoichiometry of this intermediate stage can be calculated to be MoO<sub>3.43</sub>(NH<sub>4</sub>)<sub>0.86</sub>(H<sub>2</sub>O)<sub>0.02</sub>, which is equivalent to dehydrated ammonium heptamolybdate (NH<sub>4</sub>)<sub>6</sub>Mo<sub>7</sub>O<sub>24</sub>. Subsequent to the dehydration step between 391 K and 420 K the loss of 0.06 NH<sub>3</sub> per Mo (0.57 wt%) leads to a formal stoichiometry of MoO<sub>3.41</sub>(NH<sub>4</sub>)<sub>0.80</sub>(H<sub>2</sub>O)<sub>0.01</sub> which is equivalent to (NH<sub>4</sub>)<sub>8</sub>Mo<sub>10</sub>O<sub>34</sub>. The weak, strongly overlapping DTA signal for this process is observed at 405 K.

process	temperature (5K/min )	total weight loss	NH <sub>3</sub> weight loss	H <sub>2</sub> O weight loss	transformation to	equivalent to	theoretical weight loss	N per Mo	H <sub>2</sub> O per Mo	NO per MO
I	391	6.83	-	6.83	MoO <sub>3.43</sub> (NH <sub>4</sub> ) <sub>0.86</sub> (H <sub>2</sub> O) <sub>0.02</sub>	(NH <sub>4</sub> ) <sub>6</sub> Mo <sub>7</sub> O <sub>24</sub>	6.89	—	0.68	—
Ib	405	0.68	0.57	0.11	MoO <sub>3.41</sub> (NH <sub>4</sub> ) <sub>0.80</sub> (H <sub>2</sub> O) <sub>0.01</sub>	(NH <sub>4</sub> ) <sub>8</sub> Mo <sub>10</sub> O <sub>34</sub>		0.06	0.01	
Ila	475	3.45	2.05	1.40	MoO <sub>3.34</sub> (NH <sub>4</sub> ) <sub>0.59</sub>	(NH <sub>4</sub> ) <sub>2</sub> Mo <sub>3</sub> O <sub>10</sub>		0.21	0.14	~0.01
Ilb	493	1.64	0.99	0.74	MoO <sub>3.26</sub> (NH <sub>4</sub> ) <sub>0.51</sub>	(NH <sub>4</sub> ) <sub>4</sub> Mo <sub>8</sub> O <sub>26</sub>	5.71	0.10	0.07	~0.01
III	581	7.76	4.38	2.79	(NH <sub>4</sub> ) <sub>0.03</sub> MoO <sub>2.98</sub>		7.80	0.46	0.28	~0.02
IV	653	0.69	0.17	0.76	H <sub>0.16</sub> MoO <sub>2.98</sub>		0.58	<0.01	0.06	—
sum		21.05	8.16	12.63	MoO <sub>2.90</sub>		21.03	0.86	1.24	~0.03

**Fig. 3.3:** TG-MS data of the AHM activation process.

The second weight loss between 450 and 525 K is split into two weight losses (DTA signals at 475 and 493 K) which are both accompanied by the release of ammonia. The observed total weight loss for this second process of 5.09 wt% splits up into 3.45 wt% and 1.64 wt% for the first and second process, respectively. 0.23 and 0.38 ammonia per Mo are released within the first and second process, respectively. The formal stoichiometries at these two stages are calculated to be MoO<sub>3.34</sub>(NH<sub>4</sub>)<sub>0.59</sub> and MoO<sub>3.26</sub>(NH<sub>4</sub>)<sub>0.51</sub>. These stoichiometries are equivalent to (NH<sub>4</sub>)<sub>2</sub>Mo<sub>3</sub>O<sub>10</sub> and (NH<sub>4</sub>)<sub>4</sub>Mo<sub>8</sub>O<sub>26</sub> for the first and second stage, respectively.

The formal removal of seven water molecules and six ammonia molecules from (NH<sub>4</sub>)<sub>6</sub>Mo<sub>7</sub>O<sub>24</sub> 4(H<sub>2</sub>O) leads exclusively to MoO<sub>3</sub>. Opposite to that, dark coloured, reduced molybdenum oxide compounds are formed during activation in inert atmosphere.<sup>197</sup> The dark coloured, reduced

molybdenum oxide compounds indicate a reduction of the starting material, AHM, during the thermal activation. The reduction of the sample is coupled to the oxidation of ammonia to  $\text{NO}_x$  or  $\text{N}_2$ , comparable to the results of Valmalette,<sup>197</sup> who found  $\text{N}_2\text{O}$  during the ammonium metavanadat decomposition. By this oxidation of  $\text{NH}_3$  to  $\text{N}_2\text{O}$  or  $\text{NO}$  two or three water molecules are released per  $\text{NH}_3$ , respectively. The amount of the formed  $\text{NO}_x$  for the second step was calculated from the difference of the water and ammonia weight losses to be smaller in total than 0.02  $\text{NO}_x$  per Mo.

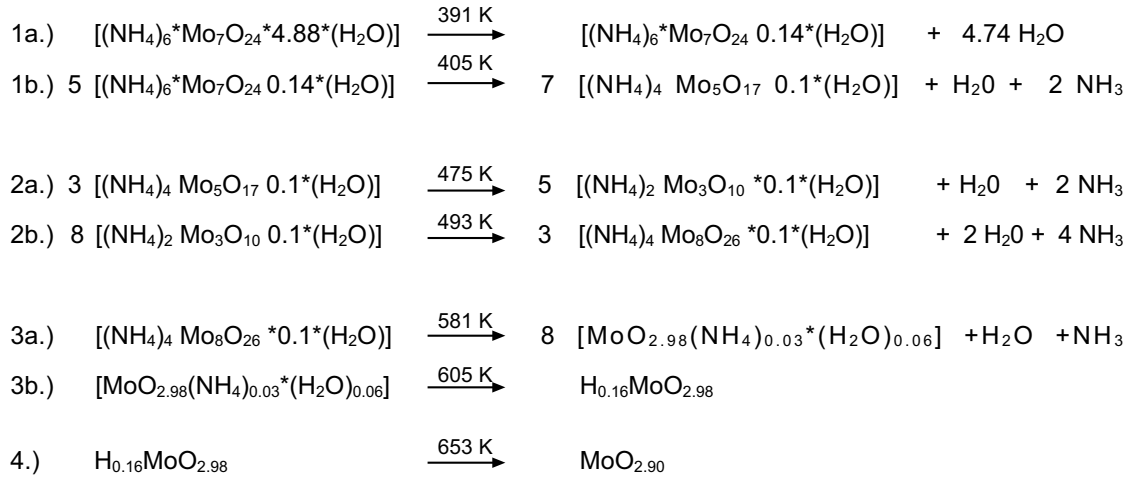


**Fig. 3.4:** Calculated stoichiometries of the AHM activation process in  $\text{N}_2$  with a heating rate of 5 K/min.

A total weight loss of 7.76 wt% is observed for the third process at 581 K (4.38 wt% due to ammonia and 2.79 wt% due to water). 0.46 and 0.28 ammonia and water molecules are released per Mo and a formal stoichiometry is estimated to be  $\text{MoO}_{2.98}(\text{NH}_4)_{0.03}(\text{H}_2\text{O})_{0.06}$  at 591 K. The remaining ammonia molecules are expelled from the structure upon further heating to 605 K.

During the last decomposition step, which is completed at about 660 K, 0.08 water molecules are released per Mo without ammonia being detected. Therefore, it is concluded that this amount of water arises from the decomposition of a molybdenum bronze, also being indicated by the dark colour of the sample. The formal stoichiometry of this bronze is calculated to be  $\text{H}_{0.16}\text{MoO}_{2.98}$ .

The decomposition of this hydrogen bronze results in a compound with the formal stoichiometry of  $\text{MoO}_{2.90}$ . The transformation and the stoichiometries of the products of the different activation processes, as determined by TG/DTA-MS are summarised in the equations given in Figure 3.4.



### 3.1.3.2 XRD

In order to further corroborate the estimated stoichiometries and to obtain further information on the crystallographic structures formed during the AHM activation *in situ* XRD experiments have been performed. The XRD patterns observed during the activation process are shown in Figure 3.5. Five different crystallographic structures could be identified during the activation. Starting from AHM (Figure 3.5a) the loss of water at 391 K leads to a nanocrystalline phase (Figure 3.5b), which is detected up to 498 K. The loss of water seems to induce a loss of the long range order of the metal-oxygen clusters in AHM.

A loss of ammonia at 405 K was observed by TG-MS indicating a transformation to a compound with a formal stoichiometry of  $(\text{NH}_4)_8\text{Mo}_{10}\text{O}_{34}$ . The loss of ammonium heptamolybdate reflections coincides with the release of ammonia, and only broad reflections are observed at  $12\ 2\Theta$  ( $3.3\ \text{\AA}$ ) and  $26\ 2\Theta$  ( $7.2\ \text{\AA}$ ). These broad reflections point to the presence of nanocrystalline material at 373 K with X-ray coherence lengths of maximum  $50\ \text{\AA}$  (Figure 3.5b). TG-MS indicated a transformation of  $(\text{NH}_4)_4\text{Mo}_5\text{O}_{17}$  to  $(\text{NH}_4)_2\text{Mo}_3\text{O}_{10}$  at 475 K and to  $(\text{NH}_4)_4\text{Mo}_8\text{O}_{26}$  at 493 K. Upon further heating to 498 K the centres of these broad diffraction peaks shift to  $3.4$  and  $7.4\ \text{\AA}$  (Figure 3.5c). This two diffraction peaks are both attributed to average inter-Mo-O polyhedra distances. With decreasing charge per Mo in the polyoxometalates  $(\text{NH}_4)_6\text{Mo}_7\text{O}_{24}4(\text{H}_2\text{O})$  (0.86),  $(\text{NH}_4)_4\text{Mo}_5\text{O}_{17}$  (0.8) and  $(\text{NH}_4)_4\text{Mo}_8\text{O}_{26}$  (0.5), a tendency is observed of increasing dislocation of the Mo cation toward the two strongest bound oxygens. The average M-O bond distance of the two shortest and two longest Mo-O bonds are determined to be  $1.73, 1.72, 1.71\ \text{\AA}$  and  $2.25, 2.27, 2.33\ \text{\AA}$  for

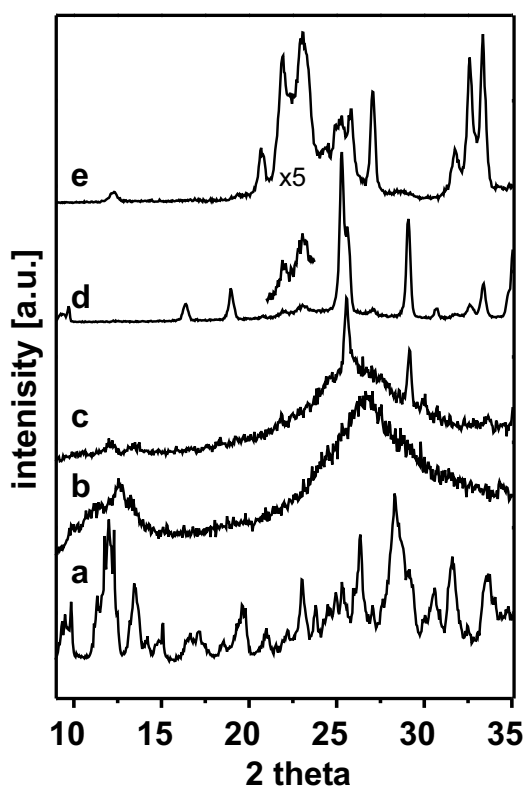


**Fig. 3.5:** *In situ* XRD pattern during the thermal activation of AHM in inert atmosphere. The patterns were recorded at 298 K **a**, 503 K **b**, 573 K **c**, 603 K **d** and 798 K **e**. The patterns were normalised to the maximum intensity and vertically shifted for better visualisation.

With decreasing charge per Mo in the polyoxometalates  $(\text{NH}_4)_6\text{Mo}_7\text{O}_{24}4(\text{H}_2\text{O})$  (0.86),  $(\text{NH}_4)_4\text{Mo}_5\text{O}_{17}$  (0.8) and  $(\text{NH}_4)_4\text{Mo}_8\text{O}_{26}$  (0.5), a tendency is observed of increasing dislocation of the Mo cation toward the two strongest bound oxygens. The average M-O bond distance of the two shortest and two longest Mo-O bonds are determined to be  $1.73, 1.72, 1.71\ \text{\AA}$  and  $2.25, 2.27, 2.33\ \text{\AA}$  for

$(\text{NH}_4)_6\text{Mo}_7\text{O}_{24} \cdot 4(\text{H}_2\text{O})$ ,  $(\text{NH}_4)_4\text{Mo}_5\text{O}_{17}$ , and  $(\text{NH}_4)_4\text{Mo}_8\text{O}_{26}$ , respectively. Therefore, the shift of the diffraction peaks at  $12\ 2\Theta$  and  $26\ 2\Theta$  reflects the transformation of the nanocrystalline pentamolybdate to octamolybdate.

Ammonia and water intercalated compounds are formed with the loss of ammonia starting at 535 K of the final formal stoichiometry of  $(\text{NH}_4)_{0.03}\text{MoO}_{2.98}(\text{H}_2\text{O})_{0.06}$  at 581 K. The formation of a hexagonal  $\text{MoO}_3$  structure intercalated with water and ammonia (Figure 3.5c) is observed by intense XRD reflections at  $24\ 2\Theta$  and  $27\ 2\Theta$  already at 498 K. This phase is observed up to 673 K. The reflections of this compound are in good agreement with single crystal data of  $\text{MoO}_3(\text{NH}_3)_{0.33}$  (ICSD-67116). The detection of the hexagonal  $(\text{NH}_4)_{0.03}\text{MoO}_{2.98}(\text{H}_2\text{O})_{0.6}$  phase is accompanied by weak reflections of orthorhombic  $\text{MoO}_3$ , which gain in intensity with increasing temperature.

TG-MS results indicated the loss of residual ammonia to be completed at 605 K. This is in good agreement with the observation that the hexagonal  $(\text{NH}_4)_{0.03}\text{MoO}_{2.98}(\text{H}_2\text{O})_{0.6}$  phase transforms to a mixture of mainly orthorhombic  $\text{Mo}_4\text{O}_{11}$ ,  $\text{Mo}_9\text{O}_{26}$ ,  $\text{H}_{0.16}\text{MoO}_{2.98}$ , and orthorhombic  $\text{MoO}_3$  at 623 K (Figure 3.5e). This transformation temperature is also in good agreement with literature data for the phase transition of the hexagonal  $\text{MoO}_3$  modification to orthorhombic  $\text{MoO}_3$ , which are reported in the temperature range 623 - 643 K.<sup>94, 198, 199</sup> Further, TG-MS results revealed an exothermic process which was attributed to the decomposition of a bronze. This decomposition is revealed in the XRD patterns by a decline of the intensity of the reflection at  $27\ 2\Theta$  by 25 % between 648 K and 673 K (not shown). This reflection is seen as a superposition of the (021) reflections of orthorhombic  $\text{MoO}_3$  and orthorhombic  $\text{H}_{0.31}\text{MoO}_3$  (ICSD No. 1366). Several authors<sup>200-201</sup> reported the decomposition temperature of  $\text{H}_{0.21}\text{MoO}_{2.69}$  at 648 K, which is in good agreement with the present results.

Mainly  $\text{Mo}_4\text{O}_{11}$  and minor amounts of  $\text{MoO}_3$  and  $\text{Mo}_9\text{O}_{25}$  are the only observed decomposition products of AHM at temperatures higher than 673 K (XRD pattern not shown).

### 3.1.3.3 Raman spectroscopy

Characteristic *in situ* Raman spectra of AHM are shown in Figure 3.6 heated with 5 K/min from 323 K to 773 K. Four different stages of the activation process could be observed within the tem-

perature range from 323 K to 510 K. The Raman bands of the starting material (Figure 3.6a)  $(\text{NH}_4)_6\text{Mo}_7\text{O}_{24} \cdot 4.88(\text{H}_2\text{O})$  are located at 223, 246, 310, 340, 367, 449, 554, 572, 633, 845, 864, 885, 893, 908, 919 and  $938 \text{ cm}^{-1}$ , which are in good agreement with literature values.<sup>203</sup>

As shown by TG-MS the first decomposition step is a combined desorption of physisorbed and loosely bound interlayer water and the subsequent release of ammonia. The desorption of water leads to the formation of dehydrated  $(\text{NH}_4)_6\text{Mo}_7\text{O}_{24}$ , while the ammonia loss is accompanied by the transformation to  $(\text{NH}_4)_4\text{Mo}_5\text{O}_{17}$ . Up to 454 K, the Raman spectra of ammonium heptamolybdate are observed. At 454 K the Raman bands of the dehydrated  $(\text{NH}_4)_6\text{Mo}_7\text{O}_{24}$  are observed at 222, 246, 310, 340, 366, 449, 554, 572, 633, 845, 863, 884, 892, 908,  $937 \text{ cm}^{-1}$  (Figure 3.6 b). The continuous small shift by one wavenumber between 323 K and 454 K of the bands at 223, 367, 864, 885, 893,  $938 \text{ cm}^{-1}$  is attributed to an altered electrostatic field around the metal oxygen clusters.

At 432 K the intensities of the Raman bands of the

$(\text{NH}_4)_6\text{Mo}_7\text{O}_{24} \cdot 4(\text{H}_2\text{O})$  decrease and new Raman bands arise which are observed up to 495 K. At 460 K, these new Raman bands are observed at 190, 209, 242, 343, 360, 444, 476, 497, 602, 664, 692, 753, 785, 840, 870, 886, 909, 923, 934, 947 and  $969 \text{ cm}^{-1}$  (Figure 3.6 c). Hunnius<sup>193</sup> reported the Raman bands of  $(\text{NH}_4)_4\text{Mo}_5\text{O}_{17}$  to be located at 195, 211, 240, 275, 312, 328, 342, 355, 381, 409, 426, 445, 476, 500, 599, 661, 691, 751, 785, 834, 841, 864, 881, 893, 922, 935, 930 and  $948 \text{ cm}^{-1}$ . The structure of  $(\text{NH}_4)_4\text{Mo}_5\text{O}_{17}$  was determined by Fuchs<sup>204</sup> to consist of two  $[\text{Mo}_5\text{O}_{17}]^{4-}$  units. Therefore, the appropriate formula is  $(\text{NH}_4)_8\text{Mo}_{10}\text{O}_{34}$ . The positions of the Raman bands of the decamolybdate are in good agreement with ours except the very weak Raman bands at 909 and  $969 \text{ cm}^{-1}$ .

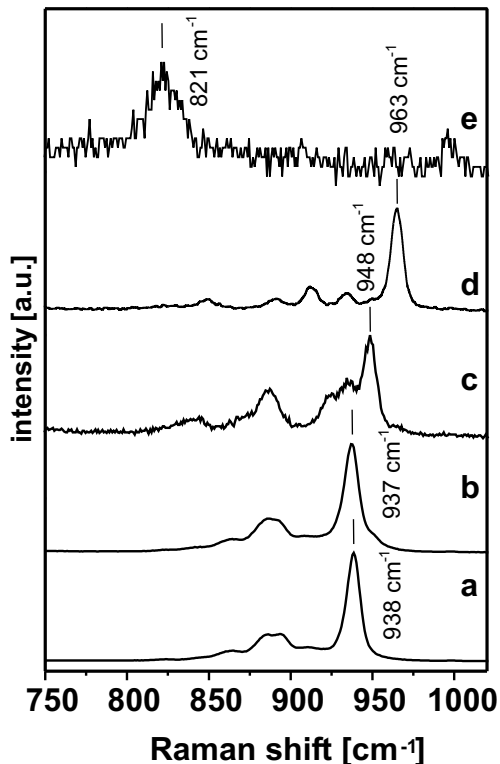


**Fig. 3.6:** *In situ* Raman spectra in the range 600 to  $1050 \text{ cm}^{-1}$  during the thermal activation of AHM in inert atmosphere. Spectra were recorded at 298 K **a**, 383 K **b**, 440 K **c**, 475 K **d** and 523 K **e**. Spectra are normalised with respect to the most intense band in the range 800 to  $1000 \text{ cm}^{-1}$  and vertically shifted for better visualisation.

At 488 K, new Raman bands arise, which are observed up to 539 K. These are located at 203, 224, 238, 286, 340, 373, 448, 502, 622, 726, 848, 889, 911, 933, 949, 952 and 963  $\text{cm}^{-1}$  (Figure 3.6 d). Hunnius<sup>193</sup> reported the Raman bands of  $(\text{NH}_4)_4 \text{Mo}_8\text{O}_{26}$  to be located at 202, 225, 243, 268, 286, 300, 338, 363, 374, 389, 409, 439, 453, 480, 507, 542, 631, 608, 675, 727, 755, 848, 889, 911, 932, 951 and 965  $\text{cm}^{-1}$ . Therefore, the Raman spectrum which is observed between 488 K and 539 K is attributed to  $(\text{NH}_4)_4 \text{Mo}_8\text{O}_{26}$ .

The second activation step was shown by TG-MS to be split into two processes. The first resulted in a formal stoichiometry of  $\text{MoO}_{3.34}(\text{NH}_4)_{0.59}$  which is equivalent to  $(\text{NH}_4)_2\text{Mo}_3\text{O}_{10}$  in line with results of Kiss et al.<sup>195</sup>. Therefore,  $(\text{NH}_4)_2\text{Mo}_3\text{O}_{10}$  is expected to be an intermediate between  $(\text{NH}_4)_8\text{Mo}_{10}\text{O}_{34}$  and  $(\text{NH}_4)_4 \text{Mo}_8\text{O}_{26}$ . It may be argued, that the additional Raman bands at 909 and 963  $\text{cm}^{-1}$  which have been detected in all Raman spectra of  $(\text{NH}_4)_8\text{Mo}_{10}\text{O}_{34}$  may point to the existence of such an intermediate compound. However, the Raman bands of  $\text{NaNH}_4\text{Mo}_3\text{O}_{10} \cdot \text{H}_2\text{O}$  have been reported by Himeno to be located at 874, 901, 918 and 950  $\text{cm}^{-1}$  and cannot explain these additional bands. Further, the intensity at 951  $\text{cm}^{-1}$  of the Raman spectra recorded between 450 and 520 K is almost constant as expected for an isobestic point. This indicates the absence of an intermediate in the transformation of  $(\text{NH}_4)_8\text{Mo}_{10}\text{O}_{34}$  to  $(\text{NH}_4)_4 \text{Mo}_8\text{O}_{26}$ . Hunnius explained the results of Kiss et al.<sup>195</sup> of an intermediate between  $(\text{NH}_4)_8\text{Mo}_{10}\text{O}_{34}$  and  $(\text{NH}_4)_4 \text{Mo}_8\text{O}_{26}$  by a mixture of  $(\text{NH}_4)_6\text{Mo}_7\text{O}_{24} \cdot 4(\text{H}_2\text{O})$  and a polymeric ammonium dimolybdate, which is regularly present in commercial  $(\text{NH}_4)_6\text{Mo}_7\text{O}_{24} \cdot 4(\text{H}_2\text{O})$ .<sup>193</sup> The decomposition of this ammonium dimolybdate also leads to  $(\text{NH}_4)_4 \text{Mo}_8\text{O}_{26}$  at 453 K. However, the Raman bands of the dimolybdate are located at 850, 920 and 940  $\text{cm}^{-1}$  and cannot explain the observed band at 963  $\text{cm}^{-1}$ .<sup>49</sup> The structures of the polyoxoanions of  $(\text{NH}_4)_6\text{Mo}_7\text{O}_{24} \cdot 4(\text{H}_2\text{O})$ ,  $(\text{NH}_4)_8 \text{Mo}_{10}\text{O}_{34}$  and  $(\text{NH}_4)_4 \text{Mo}_8\text{O}_{26}$  are shown in Figure 3.7. Seven  $\text{MoO}_6$  octahedra built up the  $[\text{Mo}_7\text{O}_{24}]^{6-}$  anion by sharing edges and vertices. The  $[\text{Mo}_8\text{O}_{26}]^{4-}$  anion consists of four sets of two edge sharing octahedra. Two of this sets are interconnected by sharing vertices. This larger units of four octahedra form the  $[\text{Mo}_8\text{O}_{26}]^{4-}$  by sharing edges. The  $[\text{Mo}_{10}\text{O}_{34}]^{8-}$  anion resembles the  $[\text{Mo}_8\text{O}_{26}]^{4-}$  anion except for the two tetrahedra which share vertices with octahedra on opposite sides of the  $[\text{Mo}_8\text{O}_{26}]^{4-}$  anion. The stoichiometry of the solid state transformation between  $(\text{NH}_4)_6\text{Mo}_7\text{O}_{24} \cdot 4(\text{H}_2\text{O})$  and  $(\text{NH}_4)_8 \text{Mo}_{10}\text{O}_{34}$  suggests a concerted reaction of ten  $[\text{Mo}_7\text{O}_{24}]^{6-}$  anions to seven  $[\text{Mo}_{10}\text{O}_{34}]^{8-}$  anions which seems rather unlikely

due to the complexity. A simpler reactions mechanism would consist of four  $[\text{Mo}_7\text{O}_{24}]^{6-}$  anions reacting to two  $[\text{Mo}_{10}\text{O}_{34}]^{8-}$  anions and one structurally very similar  $[\text{Mo}_8\text{O}_{26}]^{4-}$  anion. This reactions mechanism could explain the additional Raman bands at 918 and 963  $\text{cm}^{-1}$ , by the presence of minor amounts of octamolybdate as the byproduct of  $(\text{NH}_4)_8\text{Mo}_{10}\text{O}_{34}$ .

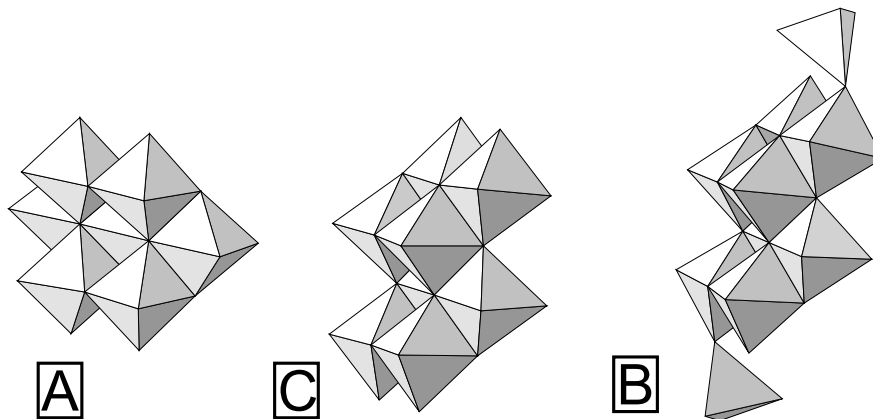


**Fig. 3.7:** Schematic representation of the  $[\text{Mo}_7\text{O}_{24}]^{6-}$  (A),  $[\text{Mo}_8\text{O}_{26}]^{4-}$  (B) and the  $[\text{Mo}_{10}\text{O}_{34}]^{8-}$  (C) anions.

Upon further heating, the sample colour changes to dark blue, indicating the formation of reduced molybdenum oxides. The Raman cross section sharply decreases upon reduction and, thus, precisely indicates the onset of the deep reduction of the sample at 539 K. Above 539 K, the Raman spectra of orthorhombic  $\text{MoO}_3$  are observed with weak and broad bands at 244, 287, 338, 377, 462, 667, 821, 996  $\text{cm}^{-1}$  (Figure 3.6 e). Furthermore, additional weak and broad Raman bands are observed at 690 and 900  $\text{cm}^{-1}$  at 555 K. Seguin et al.<sup>94</sup> observed the Raman bands of monoclinic  $\text{MoO}_3 \cdot (\text{H}_2\text{O})_{0.5}$  (with hexagonal stacking along the (010) direction) and orthorhombic  $\text{MoO}_3 \cdot (\text{H}_2\text{O})_{0.33}$  at 194, 276, 395, 409, 473, 673, 699, 908, 925, 981 and 986  $\text{cm}^{-1}$  and 207, 254, 345, 441, 671, 710, 822, 905, 922 and 968  $\text{cm}^{-1}$ , respectively. Therefore, the weak Raman bands located at 690 and 900  $\text{cm}^{-1}$  are assigned to a water and ammonia intercalated hexagonal  $\text{MoO}_3$  phase. XRD results indicated the well crystallised hexagonal  $\text{MoO}_3$  phase to be predominant in the temperature range from 535 to 673 K beside minor amounts of orthorhombic  $\text{MoO}_3$ . The *in situ* Raman results point to a predominance of orthorhombic  $\text{MoO}_3$  minor amounts of an ill defined hexagonal  $\text{MoO}_3$  phase in contrast to XRD. This discrepancy is explained by the different Raman cross sections of the orthorhombic and hexagonal  $\text{MoO}_3$  phases and/or different degrees of reduction of both oxides.

### 3.1.4 Summary

It could be shown by TG, XRD and Raman spectroscopy, that the activation process of AHM proceeds by consecutive transformations of ammonium heptamolybdate to decamolybdate and octamolybdate, before water and ammonia containing hexagonal phases are formed. At temperatures above 603 K, a mixture of oxides is formed mainly consisting of  $\text{Mo}_4\text{O}_{11}$ .

According to the XRD analysis, nanocrystalline intermediate compounds are found in the temperature range between 403 K to 548 K with an estimated particle size of 50 Å. The obtained Raman spectra, however, do not show considerable broadening which could be expected from the nanocrystalline state. This can be explained by the assumption that the solid state Raman spectra are due vibrations of molecular metal-oxygen clusters separated by the ammonia counter ions with weak or no interactions. Raman spectra of these anions in aqueous solutions, which resemble those obtained from solid state samples, further support this view. During the transformations between the different polyoxometalates, the long range ordering of these molecular metal-oxygen clusters is only retained on a nanoscale, as shown by the broad diffraction peaks as seen in the XRD. But the molecular structure of the metal oxygen clusters remain defined, which indicates that the transformation is not mediated by a step of total disruption of the metal-oxygen clusters.

It has to be noted, that the obtained results strongly depend on the experimental parameters due to the predominantly kinetic control of the thermal activation processes under the chosen experimental conditions.

## 3.2 Thermal Activation of V and W Promoted Mo-Oxide Based Catalysts

### 3.2.1 Introduction

Catalyst optimisation for a special reaction often leads to complex mixtures of a series of elements within one catalyst as discussed in the previous Section. A deeper understanding of the role of each element in catalysis and its effects on the geometric structure of the catalyst and its physical-chemical properties is difficult to develop. Moreover, the influence of the added element on the catalyst activation or on its catalytic performance are usually unknown on an atomic

scale.<sup>1, 9, 16, 34, 71, 205-209</sup> However, the activity and/or selectivity may be improved by variation of the elemental composition of a such a multielement oxide catalyst. Such a improvement may in principle arise from the formation of new mixed oxide phases or mixtures of different phases.<sup>210</sup> Two types of new phases may be formed in principle in the former case. First, phases may exist with a geometric arrangement of the atoms which is not found in that of the pure oxides, *e.g.* for example the formation of the  $\text{Bi}_3\text{FeMo}_2\text{O}_{12}$  phase, which is used as for the propene oxidation to acrylic acid.<sup>1</sup> Second mixed oxide phases may be created with a structural chemistry similar to the pure oxides. The chemistry of molybdenum oxide based catalysts which are promoted by minor amounts of V or W is dominated by the structural motif of the parent molybdenum oxide.<sup>33, 44-42, 43, 211</sup> This may be understood by the similar structural oxide chemistry of pure V-, W-oxides and Mo-oxides.<sup>50, 40</sup> The preference for highest oxidation state and the similar radii of these cations ( $\text{V}^{5+}$  (0.59 Å),  $\text{Mo}^{6+}$  (0.59 Å) and  $\text{W}^{6+}$  (0.60 Å))<sup>212</sup> are responsible for the similar solid state chemistry of these transition metal oxides.

The physicochemical properties of the new mixed oxides, *e.g.* redox properties, thermal stability, oxygen mobility, crystallinity or morphology are a function of the amount and type of added promoter.<sup>43, 213</sup> The change of physicochemical properties of molybdenum oxides by V and W promoters may be caused by the ability to localise oxygen defects at V-sites -  $\text{V}^{5+}$  prefers fivefold coordination-, and the confinement of these lattice deformations by the redox stable  $\text{W}^{6+}$ . The change of physicochemical properties of mixed oxides may be explained by the d-wave expansion, different site preferences, redox energies of the different cations.<sup>214</sup>

However, beside of this thermodynamic influence of V and W promoters on the formed structure, they may affect physicochemical properties by changed kinetics of the thermal activation process. Thus, transient intermediate phases which occur during the activation process may influence the final state of the catalyst. For example, the stability of intermediate phases during the activation process may be in- or decreased. Therefore, phases may result from the activation process, which cannot be formed in case of the pure precursors. The objective of this investigation is to elucidate the influence of tungsten and/or vanadium on the thermal activation process under inert atmosphere ( $\text{N}_2$ ) as compared to that of ammonium heptamolybdate. Therefore, a series of ammonium molybdates have been prepared which contain additionally 10 % V and /or W.

## 3.2.2 Experimental

### 3.2.2.1 Preparation of the Catalyst Precursors

Three samples were prepared by dissolving appropriate amounts of ammonium heptamolybdate (AHM, Merck, p.a.), ammonium metavanadate (AMV, Merck, p.a.) and ammonium metatungstate (AMW, Goodfellow) in water. The solutions were kept for 1 h at 368 K, before the solvent was evaporated. The obtained powders were dried at 383 K for 24 h. Samples with the following metal compositions were prepared: a) 90 mol% Mo and 10 mol% V (Mo9V1), b) 90 mol% Mo and 10 mol% W (Mo9W1) and c) 80 mol% Mo, 10 mol% V and 10 mol% W (Mo8V1W1). Experimental details about TG-MS, Raman spectroscopy and XRD have been given in the previous Section on page 83. 35.6 mg (Mo9V1), 33.2 mg (MoV1W1) and 46.5 mg (Mo9W1) of the polyoxometalate precursors were used in the TG-MS experiments which were performed at 5 K/min at a flow of 100 ml/min N<sub>2</sub>.

## 3.2.3 Results and Discussion

### 3.2.3.1 TG/DTA-MS

The TG/DTA-MS data of the thermal activation processes of the AHM and the V, W and V/W promoted samples are presented in Figure 3.8. In general, less structured TG profiles of the promoted samples are observed compared to AHM. The number of activation steps of the promoted catalyst precursors compare with those of the AHM activation. The determined formal stoichiometries are also comparable with those of the AHM activation process and are therefore not discussed in detail.

### 3.2.3.2 XRD

Only nanocrystalline polyoxometalates are present at low activation temperature comparable to the AHM activation. At elevated temperatures, these transform into H<sub>2</sub>O and NH<sub>3</sub> intercalated hexagonal MoO<sub>3-x</sub> and mainly Mo<sub>4</sub>O<sub>11</sub> in case of AHM. The *in situ* XRD patterns recorded during the activation processes of the V, W and VW promoted samples are shown in Fig. 3.9-3.12. The thermal stability ranges of the different phases are summarised in Table 3.1 and visualised in Fig. 3.13.



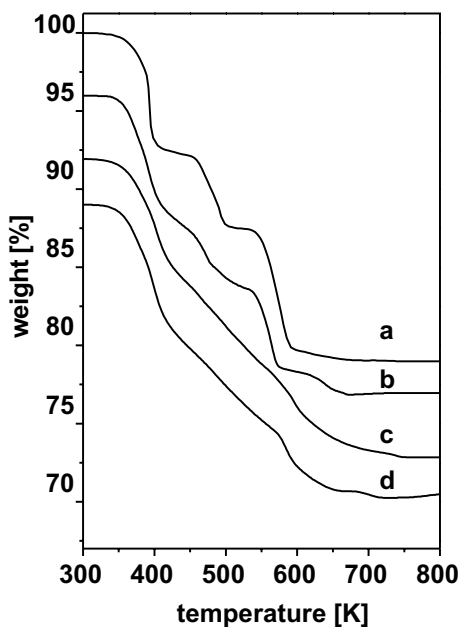


**Fig. 3.8:** Weight loss of the promoted catalyst samples upon heating under  $N_2$  with 5 K/min: (A) AHM; (B) AH(MV); (C) AH(MVW) and (D) AH(MW). TG curves are vertically shifted for better visualisation.

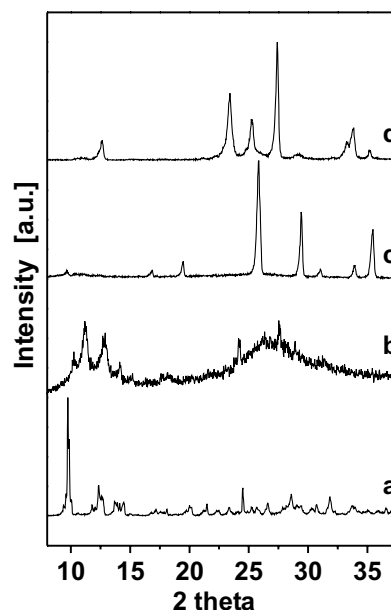


**Fig. 3.9:** In situ XRD patterns of the thermal activation of the Mo9VI catalyst precursor in inert atmosphere. The patterns were recorded at 298 K **a**, 423 K **b**, 523 K **c** and 773 K **d**. The patterns were normalised to the maximum intensity and vertically shifted for better visualisation.

### 3.2.3.2.1 Thermal Activation of the V-Promoted AH(MV)

The XRD patterns of the thermal activation shown in Figure 3.9 indicate the presence of AH(MV) from room temperature to 348 K (Figure 3.9 a). The loss of water and ammonia leads to the formation of nanocrystalline  $(NH_4)_8(MoV)_{10}O_{34}$  and  $(NH_4)_4(MoV)_8O_{26}$  which are observed from 348 to 498 K (Figure 3.9 pattern b). From 523 to 623 K, water and ammonia intercalated hexagonal  $MoO_{3-x}$  is observed (Figure 3.9 pattern c), which transforms to an ill defined orthorhombic  $MoO_3$  (Figure 3.9 pattern d) at temperatures above 648 K. Interestingly, the formation of intermediate oxides like  $Mo_4O_{11}$  could not be detected as observed for AHM. This points to a lower thermal stability of V promoted intermediate oxides as compared to pure molybdenum oxides.

The overall minor influence of added V on the structures of the parent molybdenum oxide may be explained by the similarity between the  $V_2O_5$  and  $MoO_3$  structure. The coordination of V in  $V_2O_5$  may be described as square pyramidal, or since there is a sixth oxygen in a much greater distance, as a highly distorted octahedron. Although the sixth oxygen is at a distance nearly twice as great as that of the nearest oxygen in  $V_2O_5$  a relation may be seen between the idealised structures of  $V_2O_5$

and  $\text{MoO}_3$  as shown in Figure 3.10. This similarity of the structures may explain the mutual solubility of minor amounts of one oxide in the other and, thus, the minor influence of the V promoter on the structures formed during the activation process.

temperatures for the occurrence of (in [K])					
sample	$(\text{NH}_4)_6\text{Mo}_7\text{O}_{24} \cdot 4(\text{H}_2\text{O})$	nanocrystalline material	hexagonal $\text{MoO}_3$ phases	intermediate oxides	$\text{MoO}_3$
Mo	323-348	348-523	548-648	648-773	
Mo9V1	323-348	348-498	523-623		648-823
Mo9W1	323-448	398-623		648-823	
Mo8V1W1	323-423	373-648		673-823	

**Table 3.1:** Temperature dependence for the occurrence of crystalline phases as determined by XRD.

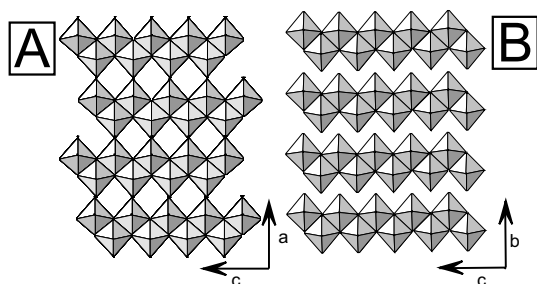


**Fig. 3.10:** Structural representation of the idealised  $\text{V}_2\text{O}_5$  (A) and the  $\text{MoO}_3$  (B) structure.

### 3.2.3.2.2 Thermal Activation of the W-Promoted AH(MW)

The X-ray patterns of the W promoted sample shown in Figure 3.11 indicate in general a lower degree of crystallisation as compared to AHM or the V promoted sample. From 323 K to 448 K,  $(\text{NH}_4)_6(\text{MoW})_7\text{O}_{24} \cdot 4(\text{H}_2\text{O})$  is observed (Figure 3.11 pattern a).  $(\text{NH}_4)_6(\text{MoW})_7\text{O}_{24} \cdot 4(\text{H}_2\text{O})$  transforms to a nanocrystalline material in the temperature range from 403 to 623 K (Figure 3.11 pattern b-d). This nanocrystalline material transforms to an ill defined  $(\text{MoW})_4\text{O}_{11}$  oxide (Figure 3.11 pattern e) at 648 K. At 773 K, additionally weak reflections of orthorhombic  $(\text{MoW})\text{O}_3$  are observed. Interestingly, the hexagonal  $\text{MoO}_{3-x}$  phase could not be detected in contrast to the pure Mo and V promoted samples.

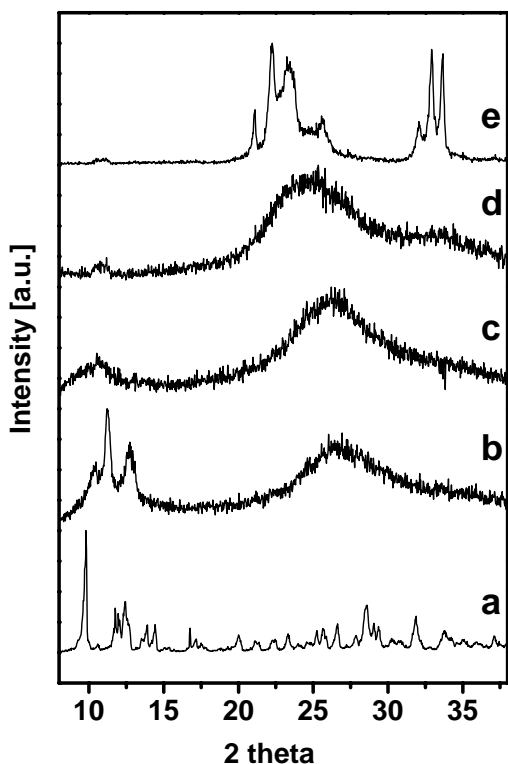


**Fig. 3.11:** *In situ XRD patterns of the thermal activation of the Mo9W1 catalyst precursor in inert atmosphere. The pattern were recorded at 323 K a, 423 K b, 523 K c, 623 K d and 773 K e. The pattern were normalised to the maximum intensity and vertically shifted for better visualisation.*

The diffraction patterns of the nanocrystalline material below 623 K point to a strong influence of the added tungsten on structural reorganisation processes. The thermal stability of the polyoxometalates seems to be extended such that the polymerisation to the hexagonal phase does not occur and that a direct transformation is observed to the shear structures above 648 K. Hence, the influence of the added W may be described as an inhibitor of structural reordering processes within the molybdenum oxide matrix. Such an influence may be explained by the structural chemistry of pure molybdenum or tungsten and their mixed intermediate oxides. The intermediate oxides of tungsten and molybdenum may be seen as being derived from the  $\text{ReO}_3$ -structure. In the  $\text{ReO}_3$  or  $\text{WO}_3$  structures,  $\text{MO}_6$  octahedra are connected through vertices only.

Series of related structures arise when octahedra share edges in regular intervals. These structures with formal stoichiometries of  $\text{M}_n\text{O}_{3n-1}$  and  $\text{M}_n\text{O}_{3n-2}$  may be regarded as built of slices of the  $\text{ReO}_3$  structure (see the  $\text{Mo}_4\text{O}_{11}$  structure in Figure 2.3 on page 46). Examples of the structural series of such binary oxides are  $\text{Mo}_8\text{O}_{23}$  and  $\text{Mo}_9\text{O}_{26}$  and  $\text{W}_{20}\text{O}_{58}$ ,  $\text{W}_{24}\text{O}_{70}$ ,  $\text{W}_{25}\text{O}_{72}$ ,  $\text{W}_{40}\text{O}_{118}$ . Higher members of the  $\text{M}_n\text{O}_{3n-1}$  series are represented by mixed (MW) oxides, in which the proportion of W is of fundamental importance for the width of  $\text{ReO}_3$  slices (see Table 3.2).

The increasing value  $n$  with increasing W content stems from  $\text{WO}_6$  octahedra with preferential sharing vertices only.<sup>120</sup> This may explain the dynamic influence of tungsten on the structural reor-

percent W	structure known
0	$\text{Mo}_8\text{O}_{23}$ , $\text{Mo}_9\text{O}_{26}$
14-24	$(\text{M},\text{W})_{10}\text{O}_{29}$ , $(\text{MW})_{11}\text{O}_{32}$
32-44	$(\text{M},\text{W})_{12}\text{O}_{35}$
48	$(\text{MW})_{14}\text{O}_{41}$

**Table 3.2:** *Structures of mixed tungsten molybdenum oxides as a function of the W content according to Ref. 120*

ganisations during the activation of the parent molybdenum oxide. Structural reorganisation require mobility of the oxygen anions (or oxygen vacancies) and/or the metal cations. The redox stable W with its octahedral coordination and only sharing vertices does not participate in oxygen vacancy diffusion through the material which is mediated by a change of edge to vertex connection. Therefore, the oxygen mobility in W promoted samples is lowered. Hence, the structural reorganisation to ordered three dimensional lattices is inhibited.

### 3.2.3.2.3 Thermal Activation of the V and W-Promoted AH(MVW)

The diffraction patterns of the sample promoted by V and W, shown in Figure 3.12, resemble those of the sample with W only. The X-ray patterns indicate  $(\text{NH}_4)_6(\text{MoVW})_7\text{O}_{24} \cdot 4(\text{H}_2\text{O})$  (Figure 3.12 pattern a) from 323 to 423 K. It transforms to a nanocrystalline material (Figure 3.12 pattern b-d) which is observed from 373 to 648 K. The X-ray patterns of the polyoxometalates point to a higher degree of crystallinity as compared to the sample promoted only by W, which may stem from different kinetics of the thermal activation processes. At temperatures above 673 K, ill-defined  $(\text{MoVW})_4\text{O}_{11}$  oxide is observed (Figure 3.12 pattern e) comparable to the W promoted sample. It may be concluded that W promotion has a much stronger influence on the structures formed during the activation process than V addition. The degree

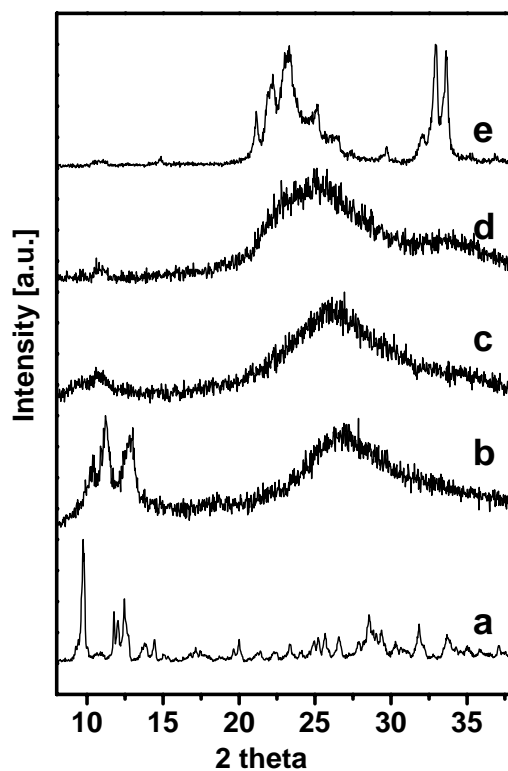


**Fig. 3.12:** *In situ* XRD pattern of the thermal activation of a V and W promoted catalyst precursor in inert atmosphere. The pattern were recorded at 423 K (A), 523 K (B), 573 K (C), 623 K (D) and 773 K (E). The pattern were normalised to the maximum intensity and vertically shifted for better visualisation.

of crystallinity of W promoted samples is lower than that of the sample promoted by V. For the combined V and W promoted sample V addition counterbalances the structural effects of W.

The Tammann temperature,<sup>215</sup> which is defined as  $0.5 T_M$  ( $T_M$  melting point in K) provides a quali-

tative measurement of the oxygen mobility. The Tammann temperature increases in the order  $V_2O_5$  (482 K),  $MoO_3$  (534 K) to  $WO_3$  (873 K).<sup>216</sup> An increased oxygen mobility may be expected for V promoted Mo-Oxide, whereas W addition should lead to a decrease. Therefore, the influence of W on the formed molybdenum oxides may be rationalised by the inhibition of structural reordering due to lowered oxygen mobility, *i.e.* the mobility of oxygen vacancies. The minor influence of V may be explained by the structural similarity between  $MoO_3$  and  $V_2O_5$ . V promotion in addition leads to a higher concentration of oxygen vacancies and, hence, a higher oxygen mobility. The influence of the redox stable W on the structures formed and their degree of crystallinity is reflected in the onset temperatures for the reduction by  $H_2$  (determined by temperature programmed reduction ( $H_2$ -TPR) experiments, not shown). The W-promoted sample shows the lowest onset temperature for reduction as compared to pure Mo or V, V and W promoted samples.

### 3.2.3.3 *in situ* Raman Spectroscopy

At low temperatures, the activation process of AHM is dominated by the transformation between different structures built by discrete polyoxometalate anions. It could be shown in the previous Section that *in situ* Raman spectroscopy is especially suited for the characterisation of the ammonium polyoxometalate structures. The analysis of the observed Raman bands of the promoted samples revealed that V or W addition had no influence on the formed polyoxometalate structures. The observed Raman spectra resemble those during the AHM activation process (Raman spectra not shown). However, the formation and decomposition temperatures of the different polyoxometalates as detected by *in situ* Raman spectroscopy were affected by the V and W addition. These data are summarised in Table 3.3 and visualised in Figure 3.13 on page 102.

#### 3.2.3.3.1 Thermal Activation of the V-Promoted AH(MV)

Only a minor influence was proven of the V on the thermal stability of the polyoxometalates.  $(NH_4)_6(MoV)_7O_{24} \cdot 4(H_2O)$ ,  $(NH_4)_8(MV)_{10}O_{34}$  and  $(NH_4)_4(MoV)_8O_{26}$  are positively identified in the temperature range from 323 to 448 K, from 430 to 544 K, and from 496 to 556 K, respectively. Only the thermal stability of  $(NH_4)_8(MV)_{10}O_{34}$  seems to be affected by the V addition. This higher stability of  $(NH_4)_8(MoV)_{10}O_{34}$  may be explained by a preferential occupation of the two tetrahe-

drally coordinated cation sites by V which prefers such a fivefold coordination (see Figure 3.7 on page 92). In summary, the *in situ* Raman spectroscopy confirms the XRD results. The V addition has only a minor influence on the formed polyoxometalates and their thermal stability.

### 3.2.3.3.2 Thermal Activation of the W-Promoted AH(MW)

W addition leads to more pronounced changes of the thermal stability of the different polyoxometalates as V promotion. The  $(\text{NH}_4)_6(\text{MoW})_7\text{O}_{24} \cdot 4(\text{H}_2\text{O})$ ,  $(\text{NH}_4)_8(\text{MoW})_{10}\text{O}_{34}$ , and  $(\text{NH}_4)_4(\text{MoW})_8\text{O}_{26}$  are observed in the temperature ranges from 323 to 472 K, from 442 to 562 K and from 562 to 580 K, respectively. The upper thermal stability boundary is shifted to higher temperatures for all W promoted polyoxometalates. W addition inhibits the structural reorganisations during the activation process as shown by XRD. These higher transformation temperatures support the discussed role of W as an inhibitor of the structural reorganisations.

temperatures for the occurrence of (in [K])			
sample	$(\text{NH}_4)_6\text{Mo}_7\text{O}_{24} \cdot 4(\text{H}_2\text{O})$	$(\text{NH}_4)_8\text{Mo}_{10}\text{O}_{34}$	$(\text{NH}_4)_4\text{Mo}_8\text{O}_{26}$
Mo	323-454	432-495	488-539
Mo9V1	323-448	430-544	496-556
Mo9W1	323-472	442-562	562-580
Mo8V1W1	323-442	432-524	498-603

**Table 3.3:** Temperature dependence for the occurrence of polyoxometalates as determined by Raman spectroscopy.

### 3.2.3.3.3 Thermal Activation of the V-and W-Promoted AH(MVW)

For this sample  $(\text{NH}_4)_6(\text{MoVW})_7\text{O}_{24} \cdot 4(\text{H}_2\text{O})$ ,  $(\text{NH}_4)_8(\text{MoVW})_{10}\text{O}_{34}$ , and  $(\text{NH}_4)_4(\text{MoVW})_8\text{O}_{26}$  phases are observed by *in situ* Raman spectroscopy in the temperature ranges from 323 to 442 K, 432 to 524 K and from 498 to 603 K, respectively. By comparison with the W promoted sample it may be suggested that the additional V counterbalances the structural promoting W effect.

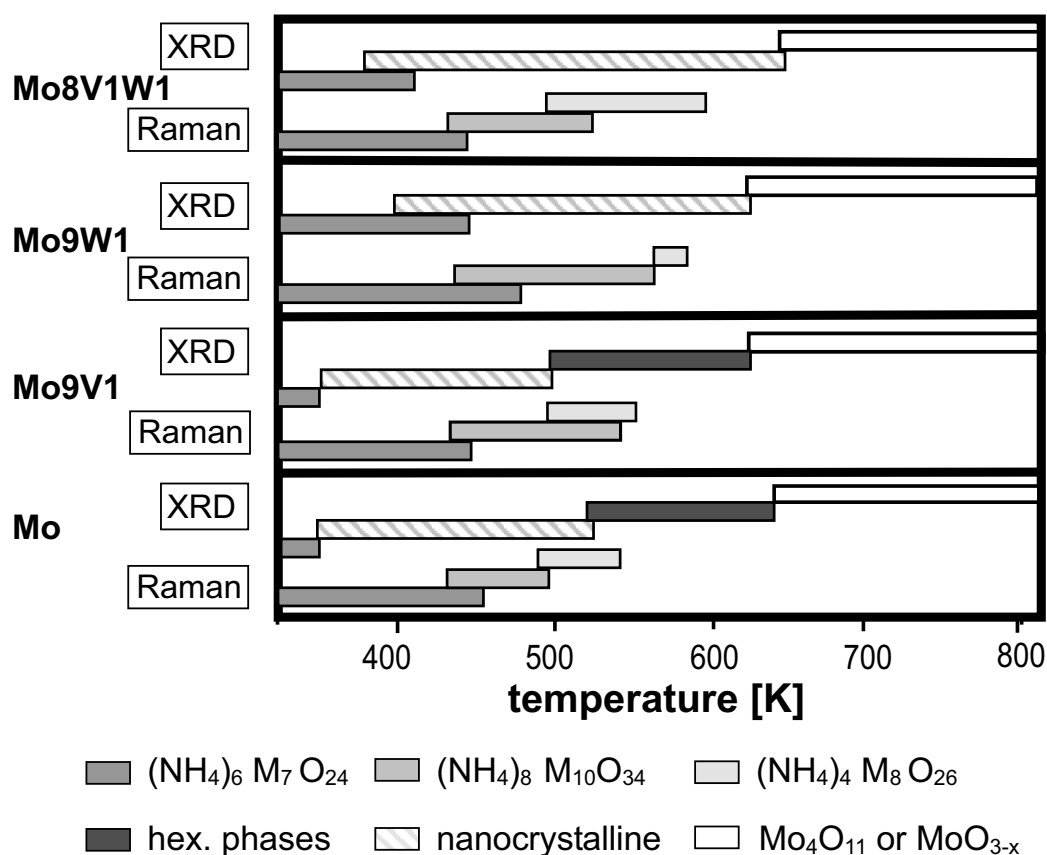


**Fig. 3.13:** Temperature dependence of the observed phases during the activation processes of the pure Mo and the V, W and V/W promoted catalyst precursors.

In summary, the obtained *in situ* Raman spectra of the activation processes of V, W and V/W promoted ammonium heptamolybdates indicate only a minor effect on the formed structures. The observed thermal stability ranges for the differently promoted samples point to a minor influence of the added V or W on polyoxometalate structures below 600 K. W inhibits structural reorganisation processes which is confirmed by the *in situ* Raman spectroscopic results. This is further supported by the onset temperatures of reduction, which were determined by the loss of the Raman signal at 539 K (Mo), 556 K (Mo9V1), 580 (Mo9W1) and 603 K (Mo8V1W1), respectively. It is important to note that the W inhibition of the structural reorganisation does not affect the local structure of the polyoxometalates as proven by similar Raman spectra recorded during the activation processes of the differently promoted samples.

### 3.3 Conclusions

Thermal activation of ammonium heptamolybdate (AHM) in inert  $N_2$  atmosphere has been studied by *in situ* -XRD, TG/DTA coupled to IMR-MS and *ex situ* Raman spectroscopy. The stoichiometries and structures of the different intermediates during the complex activation process have been characterised. AHM loses weakly bound water up to 393 K, before X-ray amorphous ammonium deca- and octamolybdates are formed. At higher temperatures, the ammonium octamolybdate decomposes into water and ammonia intercalated  $MoO_3$  and hydrogen bronzes. At 623 K, the  $Mo_4O_{11}$  and minor amounts of  $MoO_3$  and  $Mo_9O_{26}$  are found.

The influence of V and W additions were investigated on the structures formed during the activation processes. Only a minor influence of V could be observed on the structures formed during the activation process as compared to the AHM activation process. This mutual solubility of minor amounts of one oxide in the other oxide is explained by the similarity of the structures. W addition leads to more pronounced structural changes during the activation process as compared to the AHM case. Minor amounts of tungsten in the molybdenum oxides matrix inhibit structural reorganisation processes. Such an inhibition is explained by the octahedral coordination of the redox stable W which shares only vertices. This is believed to strongly affect the oxygen vacancy mobility in the material, and therefore the evolution of its long range order. The V addition on the other hand leads to a higher oxygen mobility and, therefore, the formation of stable  $MoO_{3-x}$  at elevated temperatures.

The promoter effects on mixed molybdenum oxides may shed a first light on the role of these promoters for the mixed MoVW oxide catalyst. The changed kinetics upon thermal activation and thermodynamics<sup>179</sup> of W promoted phases as compared to pure Mo phases due to a lower oxygen mobility in such materials points to a mainly structural influence of W.



## Chapter 4

# ***In situ* Raman investigations on molybdenum oxide based catalysts**

*In situ* characterisation of catalysts gained remarkable interest in the last decade.<sup>20-25</sup> Photon in/out techniques are particularly suitable for *in situ* characterisations.<sup>36, 217</sup> *In situ* Raman spectroscopy provides many advantages (many catalytically active transition oxides are Raman active, extreme pressure or high temperature *in situ* conditions are possible and a simple *in situ* cell setup can be used).<sup>36, 217</sup> Such *in situ* studies assure that the observed time dependent, structural changes are related to simultaneous changes of the catalytic activity. The direct correlations can be established between the structural and chemical features and the performances of catalysts under different process conditions. However, several disadvantages of the *in situ* Raman spectroscopy like sensitivity limitations due to possible small Raman cross section of the materials under investigation, impossibility of quantification due to unknown Raman cross sections, and fluorescence problems may limit the application of *in situ* Raman spectroscopy.<sup>10, 27</sup>

For *in situ* studies, at least two different experiments - catalytic tests and spectroscopy - have to be combined. These two experiments intersect at the design of the *in situ* cell, which is of crucial importance for the generalisation of the obtained catalytic and spectroscopic results. Several different *in situ* Raman cells have been reported.<sup>25, 218-221</sup> The design of most of these *in situ* cells, however, are focussed on the optimisation of Raman spectroscopy. They are not catalytic reactors. In order to minimise local heating effects, *in situ* cells were developed with rotating sample wavers or rotating laser beams.<sup>221, 222</sup> Other cells were developed for the use under Raman microscopes with a high lateral resolution.<sup>25</sup> But most of the arrangements employed so far, do not result in plug-flow

reactor conditions and, hence, catalytic data have to be considered with care. Mass and temperature gradients are expected in the reactor and above the catalyst powder, due to the large cell volumes, pressed sample wafers or large optical windows. Additionally, the laser spot in these *in situ* cells probes the sample surface always being in contact with fresh gases, thus, structural information is not representative for the catalyst at higher contact times.

In order to ensure that the obtained *in situ* structural information is representative of the active state of the catalyst, it is of utmost importance that catalyst activation and catalysis are carried out under conditions as closely related to those in regular catalytic test reactors. The realisation of an *in situ* Raman cell, comparable to actual catalytic reactors in which the entire gas is flowing through the catalyst bed is not trivial because one also has to consider the requirements of the *in situ* spectroscopy used. These difficulties can of course be overcome to a large extent by adopting an *in situ* cell geometry similar to tubular plug-flow reactors.

In Figure 4.1 A, the setup of the *in situ* Raman spectrometer/reactor is shown which was designed at the Fritz Haber Institute and built by Analyzer Systems (Netherlands). The *in situ* cell is a quartz tubular flow reactor with an inner diameter of 10 mm and a length of 310 mm. The cell is designed as a double-bed reactor. An optical window is attached to the centre of the reactor at an angle of 45° to monitor structural changes of the second catalyst bed (see Figure 4.1 B). Thus, the laser spot probes the structure of the operating catalyst as a function of space velocity, *e.g.* catalyst loading of the first bed and linear gas velocity. Temperature gradients are minimised by completely enclosing the quartz window inside the reactor furnace. The oven temperature is controlled by four separated heating zones operated by four coupled Eurotherm controllers. *In situ* reactor temperatures above 800 K and pressures of a few atm can be achieved with this design. The temperature uniformity is typically better than 2 K along the radial profile and over a distance of 10 cm along the reactor axis. The gaseous products are analysed by an attached GC-MS (Hewlett Packard GC1079) equipped with an DB-WAX 58 column (Varian). The educt gas composition and flow are controlled by mass flow controllers (Bronkhorst). Liquids are introduced to the reactant gases by a vaporiser which is fed by metering pumps. The catalytic activities obtained in the *in situ* reactor are similar to those measured in separate plug-flow reactors. This important fact renders possible the development of meaningful relationships between structural and catalytic properties.

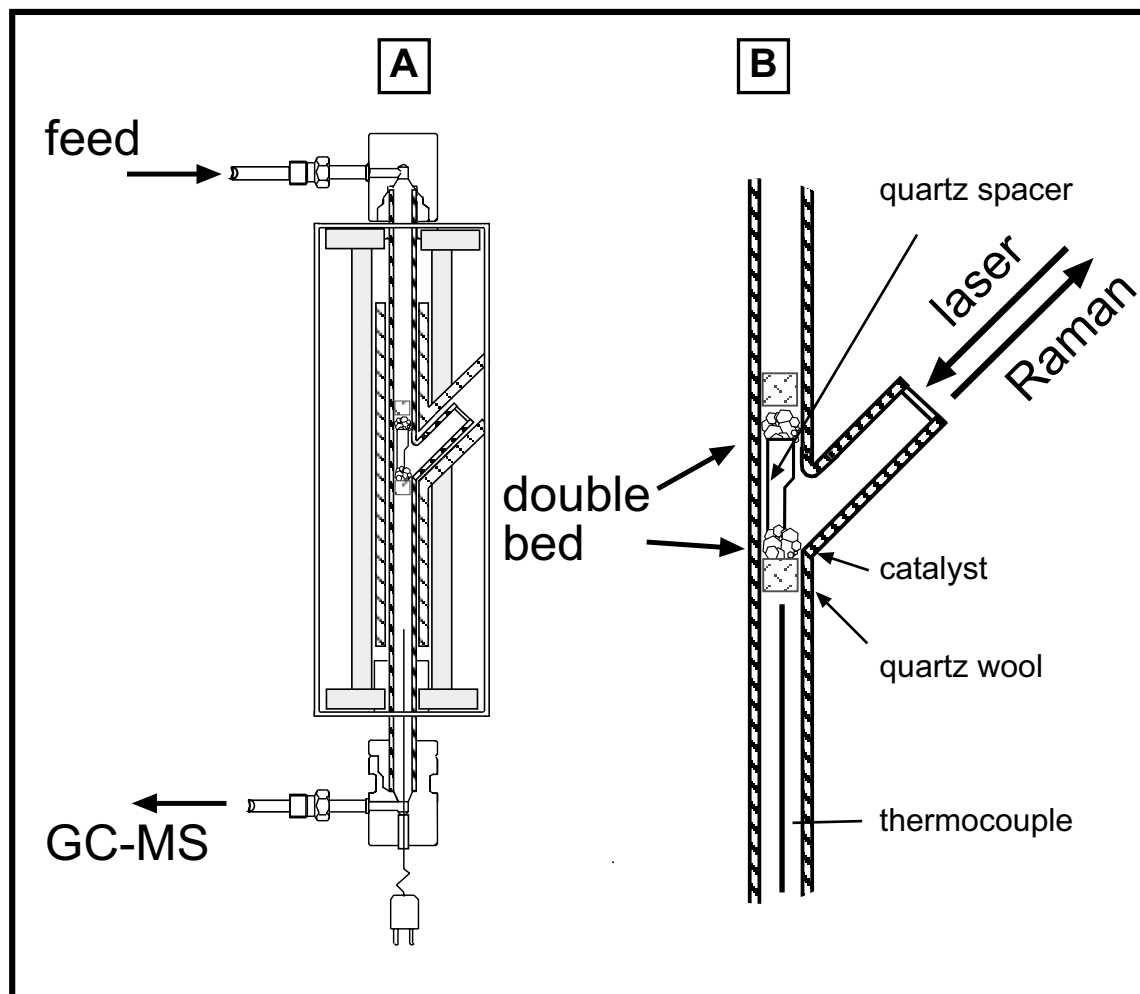


**Fig. 4.1:** A: Furnace and double bed *in situ* Raman reactor; B: Quartz reactor with the attached quartz glass window.

A HeNe laser is used for all *in situ* experiments in order to exploit the resonance Raman effect which was proven for molybdenum oxides (see Chapter 1). However, due to the strong absorption of reduced molybdenum oxides, a relation of *in situ* Raman spectroscopic results and catalytic activities may still be ambiguous because phases or compounds present in the catalyst may escape Raman detection. In the first part of this Chapter, the reduction of  $\text{MoO}_3$  by hydrogen is used as a test reaction for the sensitivity of the *in situ* Raman setup because reduced molybdenum oxides are formed and, hence, a very low Raman cross section is expected. In the second part, a combined *in situ* Raman and temperature programmed reaction spectroscopic (TPRS) study will be presented of the propene oxidation over mixed MoVW oxide catalysts. The objective is to unravel the role of V and W promoters on the catalytic and structural properties of the molybdenum oxide catalysts.

## 4.1 *In situ* Raman Studies on the Reduction of MoO<sub>3</sub>

### 4.1.1 Introduction\*

The reduction of MoO<sub>3</sub> at low temperatures is of particular interest because of the formation of a MoO<sub>x</sub>H<sub>y</sub> phase. In presence of hydrocarbons, MoO<sub>x</sub>H<sub>y</sub> further transforms into a FCC-MoO<sub>x</sub>C<sub>y</sub>H<sub>z</sub> phase, which shows remarkable catalytic activities in selective isomerisation reactions of n-alkanes into branched isomers with low aromatisation or cracking activity.<sup>223, 224</sup>

Matsuda et al. investigated the influence of the reduction period on the catalytic activity of reduced MoO<sub>3</sub>.<sup>225</sup> Under pure hydrogen atmosphere the maximum isomerisation activity was reached after a reduction period of about 24 h at 623 K. The BET surface increased during the reduction by about two orders of magnitude.<sup>223-226</sup> Vuurman et al.<sup>226</sup> explained this large increase of BET area by an inhibition of the structural collapse to crystalline MoO<sub>2</sub>, while bridging oxygens along the [010] direction are substituted by hydrogen during reduction. As a result of the lattice contraction due to the removal of bridging oxygens, the crystals fracture and develop a large surface area. Such a preferential loss of bridging oxygens has experimentally and theoretically been confirmed by Raman spectroscopy and by DFT calculations, respectively.<sup>70, 111</sup>

The characterisation of the formed MoO<sub>x</sub>H<sub>y</sub> by X-ray diffraction techniques is difficult due to a poor degree of crystallisation of this material. Moreover, because of the pyrophoric properties of MoO<sub>x</sub>H<sub>y</sub> passivation at room temperature in oxygen atmosphere is necessary prior to *ex situ* characterisations. *In situ* Raman spectroscopy offers a direct way to characterise the formation of MoO<sub>x</sub>H<sub>y</sub>. For a structural description of MoO<sub>3</sub> see Chapter 1 on page 8.

### 4.1.2 Experimental

The reduction of MoO<sub>3</sub> was carried out over a time period of 24 h in a flow of 100 ml/min of pure hydrogen at 623 K in the above described *in situ* Raman reactor. The Dilor Labram B spectrometer (see page 15) is used for all experiments. A He-laser (632.8 nm, Topag AG, 100 mW) was used for excitation of the Raman spectra. The laser power was 50 mW at the sample location. The laser light

---

\* Parts of this Chapter will be published in M. Dieterle, G. Mestl, C. Bouchy, E. Derouane and R. Schlögl, *In situ* Raman Investigations on reduced Molybdenum Oxides (in preparation).

was focussed onto the sample using a 250 mm objective lens which resulted in a focal spot of about 1.5 mm diameter. Due to the large focal area, laser heating effects have not been observed so far for all laser powers used. All Raman spectra were recorded in backscattering geometry. Acquisition times were adjusted to experimental needs, *e.g.* acquisition times between 5 sec. and 2 h were necessary for a single Raman spectrum.

### 4.1.3 Results and Discussion

After 24 h of reduction the sample was passivated at room temperature under oxygen atmosphere prior to XRD characterisation.  $\text{MoO}_2$  and  $\text{MoO}_x\text{H}_y$  phases were identified in accordance with reported data of Ledoux and coworkers.<sup>223, 224</sup>

Due to the generally low Raman scattering intensity of reduced molybdenum oxides, only the intense Raman bands in the high energy regime are discussed in the following. The *in situ* Raman spectra recorded during the reduction of  $\text{MoO}_3$  are shown in Figure 4.2. The Raman spectrum of orthorhombic  $\text{MoO}_3$  with bands at 666, 823 and 995  $\text{cm}^{-1}$  in the external frequency region has already been described (page 24).

The positions of the Raman bands of  $\text{MoO}_3$  at 666, 823 and 995  $\text{cm}^{-1}$  remain unchanged for the first 240 min of reduction. However, the signal to noise ratio continuously decreases after a subsequent reduction period of 8 min. After 240 min of reduction new Raman bands arise at 591  $\text{cm}^{-1}$  and 1040  $\text{cm}^{-1}$  which replace the Raman bands at 666  $\text{cm}^{-1}$  and 995  $\text{cm}^{-1}$ . It is known that during interaction with  $\text{MoO}_3$  the hydrogen atoms ionise to give protons and electrons.<sup>227-229</sup> The former become attached to bridging oxygen atoms, the latter are trapped at molybdenum sites producing  $\text{Mo}^V$  centres. Formation of a strong  $\sigma$ -bond between the proton and the bridging oxygen leads to the removal of the distortion along the O-Mo-O chain, resulting in the equalisation of the Mo-O distances in the equatorial plane of the octahedra.<sup>227-230</sup> The bonding of the bridging oxygen atoms is weakened due to the  $\sigma$ -O-H bond. The consecutive loss of bridging oxygens induces a further reorganisation of the  $[\text{MoO}_6]$  polyhedron, such that the most strongly bound, *cis* arranged oxygen atoms of the  $[\text{MoO}_6]$  polyhedron assume a higher bond strength as compared to the situation without an oxygen vacancy.<sup>111</sup>

The observed new Raman bands indicate the preferential loss of the bridging oxygens in line with results of Mestl et al.<sup>70</sup>. These new Raman bands are attributed to the terminal Mo=O and the remaining bridging O-Mo-O vibrations of the reduced molybdenum oxide. The observation that for reduced molybdenum oxide the terminal Mo-O vibration is shifted to  $1040\text{ cm}^{-1}$  to higher energies and that the bridging O-Mo-O vibration is found at  $591\text{ cm}^{-1}$  at lower energies as compared to  $\text{MoO}_3$  reflects a change in the deformation of the Mo-O polyhedra. Such an interpretation is in agreement with experimental ESR results and theoretical DFT calculations.<sup>77, 111, 230</sup> A similar shift of the energy of the terminal Mo=O vibration was observed by Sotani et al.<sup>112</sup>. Upon the formation of the molybdenum bronze  $\text{H}_{0.3}\text{MoO}_3$ , the energy of the terminal IR band increased from  $992$  to  $1001\text{ cm}^{-1}$  in  $\text{H}_{0.3}\text{MoO}_3$  as compared to  $\text{MoO}_3$ .

After 333 min of reduction, the Raman bands at  $995\text{ cm}^{-1}$  and  $666\text{ cm}^{-1}$  of  $\text{MoO}_3$  vanish. The introduced oxygen vacancies change the absorbing properties of the reduced  $\text{MoO}_{3-x}$  as proven by the dark sample colour. The increased oxygen vacancy concentration causes a dramatic decrease of the observed Raman cross section, which is lowered by factor of about  $10^4$  after 24 h of reduction as compared to the starting material. Because the reduction induces structural changes of the material, the Raman tensor of the reduced material may be different as compared to the starting material. Therefore, a decision about the number of removed bridging oxygens is not possible due to the unknown evolution of the Raman tensor upon the induced structural changes.

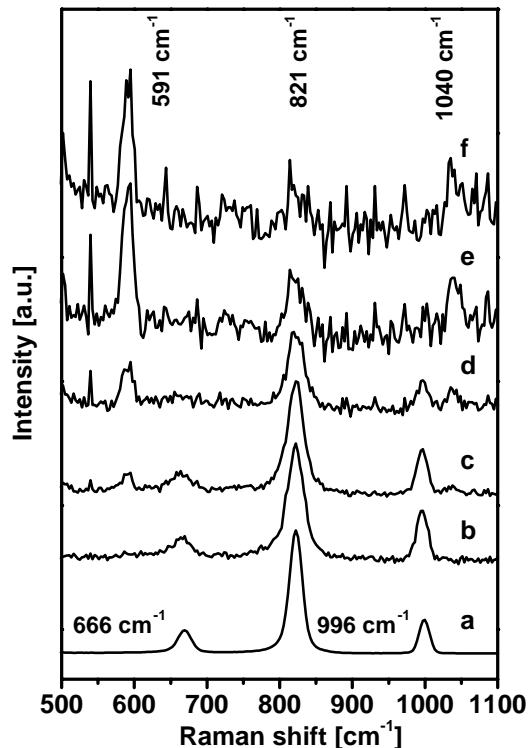


**Fig. 4.2:** *In situ* Raman spectra of the reduction of  $\text{MoO}_3$  at  $623\text{ K}$  under hydrogen atmosphere. The spectra were recorded after 0 (A), 8 (B), 147 (C), 248 (D), 333 (E) and 1530 min (F) of reduction. All Raman spectra are normalised with respect to the most intense band.

The decrease of the Raman cross section stems mainly from the shift of the  $[\text{MoO}_5]^{5+}-[\text{MoO}_6]^{6+} \rightarrow [\text{MoO}_5]^{6+}-[\text{MoO}_6]^{5+}$  IVCT transition to higher energies due to the reduction of the sample. This shift induces a higher re-absorption of the Raman scattered light and, hence, a lower overall Raman

scattering efficiency.

Basic nucleophilic oxygen groups on the catalyst surface are necessary for the first step of alkane isomerisation reaction *e.g.* for the C-H activation. According to the Hardcastle-Wachs model, the bond length of the terminal Mo=O bond in the reduced MoO<sub>x</sub>H<sub>y</sub> phases is calculated from the bond at 1040 cm<sup>-1</sup> to be 1.67 Å as compared to 1.69 Å for the vibration at 995 cm<sup>-1</sup> of MoO<sub>3</sub>.<sup>93</sup> The stronger, *e.g.* more basic, terminal Mo=O bond of the reduced MoO<sub>x</sub>H<sub>y</sub> as compared to MoO<sub>3</sub> may explain the reported increased alkane isomerisation activity of MoO<sub>x</sub>H<sub>y</sub>.<sup>223-225</sup>

#### 4.1.4 Conclusions

The *in situ* Raman characterisation of the formation of MoO<sub>x</sub>H<sub>y</sub> proved the newly designed *in situ* setup to be suited for the investigation of structural changes from MoO<sub>3</sub> to a deeply reduced MoO<sub>x</sub>H<sub>y</sub>. The acquisition times for the deeply reduced samples are about 3000 seconds in contrast to 5 sec. for MoO<sub>3</sub>. When considering the different signal to noise ratios, the observed Raman cross sections of MoO<sub>3</sub> and MoO<sub>x</sub>H<sub>y</sub> vary by a factor of 10<sup>4</sup>. Although, the degree of reduction of the MoO<sub>x</sub>H<sub>y</sub> phase has not been determined yet, it is expected to be higher than the degree of reduction of intermediate oxides like Mo<sub>4</sub>O<sub>11</sub>. Because the observed Raman cross section is mainly a function of the degree of reduction of the sample, the sensitivity of the optics of the newly designed reactor is assumed to be sufficient to detect intermediate oxides in the course of combined *in situ* Raman and TPRS experiments.

The observed higher energy of the terminal Mo=O vibration as compared to MoO<sub>3</sub> may be seen as one important factor which contributes to the higher isomerisation reactivity of reduced molybdenum oxides with respect to MoO<sub>3</sub>. Although, a strict relation of the Raman spectroscopic properties of MoO<sub>x</sub>H<sub>y</sub> and its catalytic activity was not attempted in this experiment, the observed changes of the Raman spectra may help to further understand the catalytic isomerisation processes of such reduced molybdenum oxides.

## 4.2 *In situ* Raman Spectroscopy Studies Combined with Temperature Programmed Reaction Spectroscopy (TPRS) of V and W Promoted Molybdenum Oxide Catalysts\*

Compounds of molybdenum are used as catalysts for a great number of different reactions, especially redox reactions, such as oxidation of hydrocarbons.<sup>1, 231</sup> The catalytic activity and selectivities of molybdenum oxide based catalysts for propene oxidation has been investigated by numerous authors.<sup>1, 15, 121, 205, 231</sup>

The surface of stoichiometric MoO<sub>3</sub> contains active centres according to Haber,<sup>231</sup> which are able to perform the insertion of oxygen into the organic material, but centres for the generation of allyl species are not available. MoO<sub>3</sub> is thus inactive in propene oxidation.<sup>15, 121, 231, 232</sup> The hypothesis, that the MoO<sub>3</sub> surface is not able to generate the allylic species was confirmed by comparing the activity in the oxidation of propene molecules and free allyl radicals generated by the decomposition of allylic compounds. In the temperature range of negligible activity for propene oxidation almost 100% conversion of allylic species to acrolein was observed.<sup>231</sup>

There is general agreement on the mechanism of the oxidation of propene to acrolein and acrylic acid on mixed metal oxide catalysts.<sup>1, 9, 15, 187, 205, 208, 209, 231</sup> The first step is the adsorption of the propene molecule on the catalyst surface followed by the abstraction of a hydrogen atom to form an allylic species. It has been suggested that the allylic species is formed by a surface acid-base pair, or a surface lattice oxide ion with basic properties and a transition metal cation with empty d-orbitals playing the role of the Lewis acid.<sup>1, 233, 234</sup> A second hydrogen abstraction and the addition of an oxygen atom from the oxide lattice then occurs followed by the acrolein desorption. The formed oxygen vacancies are replenished by gaseous oxygen. It was stated that both processes - activation and oxidation of propene - engage different active sites at the surface of the catalyst. Hence, the efficient catalyst for the oxidation of propene to acrolein should be characterised by two functions: the ability to activate propene by formation and bonding of allylic species and the capacity to insert lattice oxygen into such species.<sup>9, 205, 231</sup> Vogel et al.<sup>209</sup> and Fehlings<sup>235</sup> suggested two independent

---

\* Parts of this Chapter will be published in M. Dieterle, G. Mestl, R. Schlögl, *In situ* Raman Spectroscopy Studies Combined with Temperature Programmed Reaction Spectroscopy of V and W Promoted Molybdenum Oxide Catalysts (in preparation).



active centres to be present on the catalyst surface of a mixed MoV-oxide, which are responsible for the selective and total oxidation of acrolein to acrylic acid. Böhnke<sup>236</sup> could show for similar catalysts that the activation energy of the catalyst re-oxidation is a function of its degree of reduction. Estenfelder and Lintz<sup>237</sup> suggested that the degree of reduction of a MoVW mixed oxide catalyst and its kinetic behaviour (selectivity and activity) are closely linked.

The mechanism for the total oxidation is rather less well established. Complete oxidation to CO or CO<sub>2</sub> may occur by sequential oxidation of acrolein or by oxidation of propene by a parallel route, employing either lattice oxygen or surface adsorbed activated oxygen.<sup>1, 15, 33, 205, 231, 238</sup> In summary, the material will be the most efficient catalyst, which possesses the largest number of active and selective sites - which is a function of its composition and structure - and which is capable of reconstituting these surface sites rapidly. Such fast redox properties of the catalyst may be invoked by the addition of lower valent cations. (Bi or V in Mo oxides).<sup>107</sup>

The catalytic properties of transition metal oxides may be discussed in terms of surface structure sensitivity and compound selectivity. Surface structure sensitivity of catalytic reactions stems from the existence of different active sites on different crystal surfaces. Molybdenum oxides exhibit a pronounced crystallographic anisotropy. Surface structure sensitivity of catalytic reactions on MoO<sub>3</sub> has been discussed frequently.<sup>56-66,231</sup> However, varying degrees of reduction due to different preparation methods of samples with different ratios of the (010) and (100) surfaces were not taken into account in attempts to deduce structure-activity relations for catalytic reactions over MoO<sub>3</sub>.

Compound activity relationships for catalytic reactions have been proposed for several mixed molybdenum oxides, *e.g.*, the dependency of the catalytic properties of a given structure as a function of the chemical composition.<sup>1, 33, 59, 64, 231, 238</sup> Pure intermediate molybdenum oxides are readily oxidised to MoO<sub>3</sub> under the conditions of propene oxidation.<sup>121, 130, 232</sup> Therefore, additional transition metals improve the stability and activity of the parent oxide under catalytic conditions. The addition yields phases which persists over a significant range of composition and non-stoichiometric compounds are formed by the addition of lower valent cations like V<sup>5+</sup>. The catalytic properties of such mixed transition metal oxide catalysts are a function of its structure and the compositional range tolerated by that structure. Andrushkevich et al. investigated the catalytic properties of Mo/V

oxides for the oxidation of acrolein to acrylic acid.<sup>33</sup> They concluded that the presence of an oxide with  $\text{Mo}_4\text{O}_{11}$  structure and a stoichiometry of  $\text{V}\text{Mo}_3\text{O}_{11}$  is related to high catalytic activities and selectivities. It was suggested that the catalytic activity of such V promoted catalysts is related to the  $\text{V}^{4+}$  concentration in the catalyst material as determined by ESR.<sup>35</sup> A mixed  $(\text{Mo},\text{V},\text{W})_5\text{O}_{14}$  oxide on the other hand was proposed in Chapter 2 as one candidate for a active and selective catalyst for methanol and acrolein oxidation.<sup>14, 239</sup> However, a clear distinction between surface structure sensitivity and compound sensitivity for mixed MoVW oxides is difficult, because compositional variations of a given structure may have an effect on both, the ratio of the exposed different surface plane areas, and the catalytic properties due to promoters effects.

The metal- oxygen bond energy of the active oxygen groups under reaction conditions has to be in a regime of rapid detachment (hydrocarbon oxidation) and re-generation by gaseous oxygen. Intermediate oxides like  $\text{Mo}_5\text{O}_{14}$  or  $\text{Mo}_4\text{O}_{11}$ ,<sup>149, 151</sup> fulfill this condition because they possess weaker terminal  $\text{M}=\text{O}$  bonds and stronger  $\text{O}-\text{Mo}-\text{O}$  bond as compared to the catalytically less active and less selective  $\text{MoO}_3$ .<sup>58, 231, 240, 241</sup>

The selective oxidation of propene to acrylic acid is industrially carried out as a two step reaction. In the first reaction step propene is selectively oxidised over Mo-Bi catalysts. The produced acrolein is subsequently oxidised over a mixed Mo-V-W oxide to acrylic acid. However for economic reasons, catalysts for the direct selective oxidation of propene to acrylic acid are desired. Therefore, selective oxidation of propene has been chosen as the test reaction. Furthermore, propene oxidation over Mo-V-W catalysts requires in general higher reaction temperatures (573-723 K) as compared to the acrolein oxidation (543 to 593 K). Gai-Boys<sup>54, 101</sup> showed that for  $\text{MoO}_3$  the diffusion of oxygen vacancies and their ordering in larger clusters requires temperatures above 653 K. Therefore, structural reorganisations under catalytic propene oxidation conditions may occur in the temperature range from 523 to 723 K on the time scale of *in situ* Raman spectroscopy.

A deeper understanding of the principal role and effects of each added element on the geometric structure, the physical-chemical properties or on the catalytic performance are usually unknown. In order to elucidate V- and W-promoter effects on the catalytic properties of molybdenum oxide catalysts, a pure Mo oxide catalyst and four V- and/or W-promoted Mo-oxide catalysts have been

tested.

### 4.2.1 Experimental

The *in situ* Raman setup and the experimental conditions have been described on page 106. Two scans with an acquisition time of 450 seconds each were averaged for a single spectrum.

The preparation of the V and W promoted samples has been described in Chapter 3 on page 95. Samples with the following metal compositions were used for catalytic tests: a) pure Mo b) 90 mol% Mo 10 mol% V (Mo9V1), c) 90 mol% Mo and 10 mol% W (Mo9W1), d) 80 mol% Mo, 10 mol% V and 10 mol% W (Mo8V1W1) and e) 60 mol% Mo, 30 mol% V and 10 mol% W (Mo6V3W1).

Temperature programmed reaction spectroscopy (TPRS) is used for the catalyst tests. The catalysts were heated from 523 to 723 K and cooled down to 523 K under catalytic conditions in one TPRS cycle with a constant heating/cooling rate of 0.2 K/min. This slow heating rate has been chosen to assure steady state conversions and selectivities to be measured. For each catalyst 2 or 3 of such TPRS cycles have been carried out. Prior to the first TPRS cycle, the ammonium metalates precursors were thermally activated *in situ* by heating to 673 K with 5 K/min in N<sub>2</sub> and a subsequent oxidation at 673 K in synthetic air for 1h.

1.39 mmol of catalyst as referenced to the metal cations and the assumption of a MO<sub>3</sub> stoichiometry (*e.g.* 200 mg MoO<sub>3</sub>) was used in all experiments. Propene (Linde, 99.95%) and oxygen (Linde, 99.999%) were used as reactants and N<sub>2</sub> (Linde, 99.999%) as an inert diluent. Reactants and products were analysed by a HP 6890 GC-MS gas chromatograph (DB-Wax 58 column, Varian). The total flow of reactants was 50 ml/min consisting of 5 vol% propene, 10 vol% O<sub>2</sub>, the balance was N<sub>2</sub>. All catalysts have been diluted in 2 g quartz powder ( $\varnothing \sim 5\mu$ ) in order to reduce the optical absorption of the catalysts and the reaction exothermicity. Preliminary experiments proved quartz powder to be a poor Raman scatterer which does not interfere with the Raman spectra of the mixed oxides. However, it was not possible to achieve a defined catalyst mesh size from catalyst/quartz mixtures by pressing, crunching and sieving. A fine catalyst powder was always obtained. Therefore, the use of boron nitride (BN) was tested as a diluent for the *in situ* Raman studies. Although

the preparation of a diluted catalyst with a defined mesh size was possible, strong fluorescence due to BN rendered it impossible to record *in situ* Raman spectra above 523 K. Therefore, the quartz powder diluent was used. Blind tests proved the quartz reactor and the diluent SiO<sub>2</sub> to be inactive for propene oxidation below 723 K. The total catalyst bed height summed up to 4 cm of the two beds (see Figure 4.1) giving a space velocity of 1200 h<sup>-1</sup>. Because the BET surface areas of the activated catalysts were in general small (~2 m<sup>2</sup>/g) and did not change during the reaction, the catalytic activities and selectivities of all catalyst samples can directly be compared for the chosen identical reactor loadings and conversions.

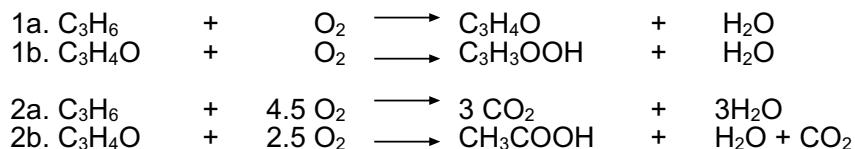


**Fig. 4.3:** Reaction pathways for the propene oxidation over Mo-oxide based catalysts.

Figure 4.3 shows the expected reaction channels for the selective oxidation of propene over Mo-oxide based catalysts. Acrolein and acrylic acid, the desired selective oxidation products (1a and b in Figure 4.3) and the total oxidation products CO<sub>2</sub> and acetic acid (2a and b in Figure 4.3) are expected to be formed. The catalytic properties are expressed in terms of propene conversion and selectivities to the different products as calculated according to equation 4.1 and 4.2. The CO<sub>2</sub> signal was corrected for the amount of CO<sub>2</sub> due to acetic acid formation.

$$(4.1) \quad C = \frac{C_{\text{Propen,out}}}{C_{\text{Propen,in}}} * 100$$

$$(4.2) \quad S_i = \frac{c_i}{C_{\text{Propen,out}} - C_{\text{Propen,in}}} * 100$$

Inner and outer mass transport limitations have been estimated for similar catalysts by Petzold.<sup>242</sup> According to Petzold, mass transport limitations should not be expected for the investigated mixed oxide catalysts even for high conversions.

## 4.2.2 Results and Discussion

### 4.2.2.1 Pure Molybdenum Catalyst

#### 4.2.2.1.1 TPRS Results

The propene conversion and the selectivities to acrolein, CO<sub>2</sub> and acetic acid of the first TPRS run are shown in Figure 4.4 as a function of the reaction temperature. The total activity of the Mo catalyst increases from conversions <1% at 523 K to a maximum conversion of 20% at 716 K. Up to 640 K, the propene conversion increases exponentially with increasing reaction temperature (see Figure 4.4). At temperatures above 640 K, the increase in activity changes and is a linear function

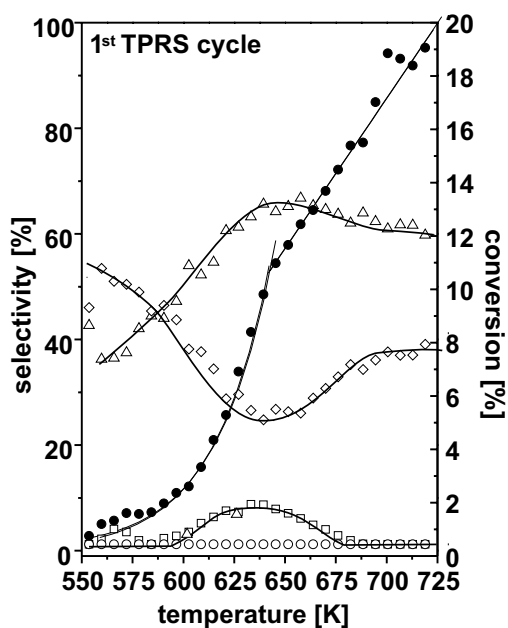


**Fig. 4.4:** Propene conversion ●, selectivities to acrolein ◇, acetic acid □, and CO<sub>2</sub> △ during the first TPRS cycle of the pure Mo catalyst as a function of the reaction temperature.

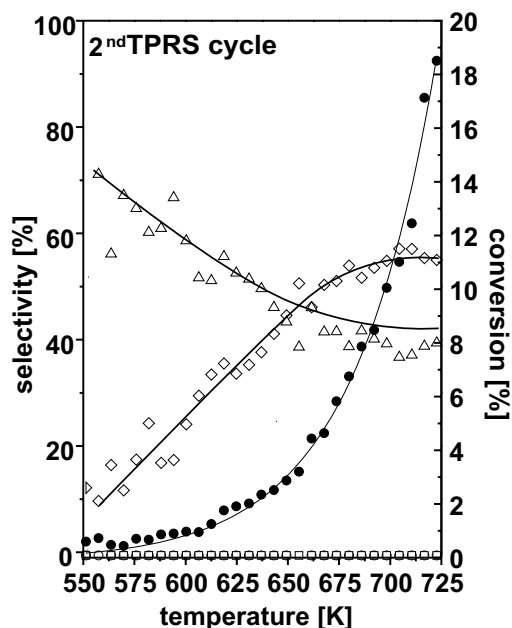


**Fig. 4.5:** Propene conversion ●, selectivities to acrolein ◇, acetic acid □, and CO<sub>2</sub> △ during the second TPRS cycle of the pure Mo catalyst as a function of the reaction temperature.

of the reaction temperature. In Figure 4.6, the Arrhenius plot is shown for the propene oxidation over the Mo catalyst. The data are based on the propene conversion and not on the actual rates of reaction. In case of the first TPRS cycle, an inflection point separates the Arrhenius curve into two linear segments, which indicate a change of the reaction mechanism, catalyst properties or diffusion limitation around 640 K and will be discussed below. The apparent activation energies  $E_A$  of the first TPRS cycle were determined to be 108 and 30 kJ/mol for reaction temperatures up to 640 K and above, respectively.

The formation of acrolein, carbon dioxide and acetic acid is observed over this catalyst. The decision about primary and consecutive products requires variations of the contact time at constant temperatures. However, in absence of a change of the structure or the reaction mechanism and in absence of diffusion limitation the observed selectivities may be used to gain information about the reaction mechanism. These conditions are fulfilled at low reaction temperatures and low conversions (see Arrhenius plot). The initially high selectivity to acrolein of 55% at 542 K ( at 1% conversion) identifies acrolein as the first oxidation product. Above 640 K, the selectivity to acrolein decreases to a constant value of almost 40% at conversions higher than 15%. The selectivity to CO<sub>2</sub> does not tend to zero for quasi zero propene conversion and suggests CO<sub>2</sub> to be formed by a parallel reaction path. At higher reaction temperatures, the selectivity to CO<sub>2</sub> follows an opposite trend as compared to the selectivity to acrolein (see Figure 4.4) and increases to a constant selectivity of 60% above 640 K. This suggests that two independent reaction channels exist for CO<sub>2</sub> formation. CO<sub>2</sub> may be formed directly from propene or by the consecutive oxidation of acrolein.

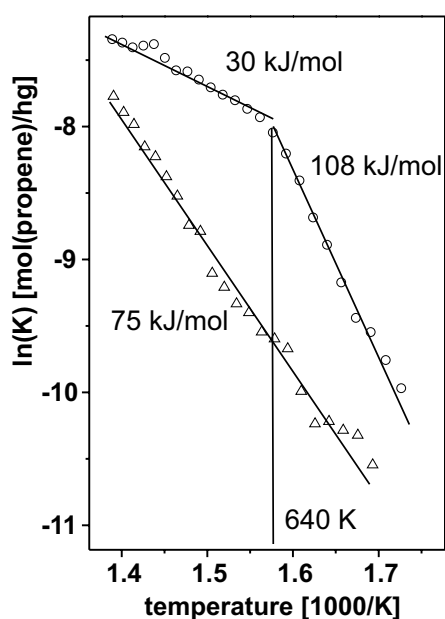


**Fig. 4.6:** Arrhenius plot for propene oxidation of the first  $\Delta$  and second  $\circ$  TPRS cycle over the pure Mo catalyst.

The formation of acetic acid is detected with a maximum selectivity of 9% at 603 K (at 8% propene conversion) during the first TPRS cycle. The decrease of the selectivity to acetic acid above 640 K coincides with an increase of the selectivity to acrolein while the selectivity to CO<sub>2</sub> remains almost unchanged. This points to consecutive oxidation of acrolein to acetic acid.

The propene conversion and the selectivities to acrolein, CO<sub>2</sub> and acetic acid of the second TPRS run are shown in Figure 4.5 as a function of the reaction temperature. Only an exponential increase of the propene conversion with increasing reaction

temperature is observed as expected for a constant number of active sites. The comparison of the Arrhenius plot for the first and second TPRS cycle indicates a change in the catalyst structure during the first TPRS cycle (see Figure 4.6). This points to the presence of different active sites during the

two TPRS cycles. The apparent activation energy for the second TPRS cycle was determined to be 75 kJ/mol. The propene conversion at 716 K of the second TPRS cycle (20%) compares to that of the first cycle (19%). Higher propene conversions are observed at lower reaction temperatures during the first TPRS cycle (see Figure 4.8)

#### 4.2.2.1.2 *In situ* Raman Spectroscopy Results

Selected Raman spectra recorded at 523, 638 and 716 K during the first TPRS cycle are shown in Figure 4.7. Only Raman bands of  $\text{MoO}_3$  (see page 26) are detected during the TPRS cycles indicating the absence of a crystallographic structural change.

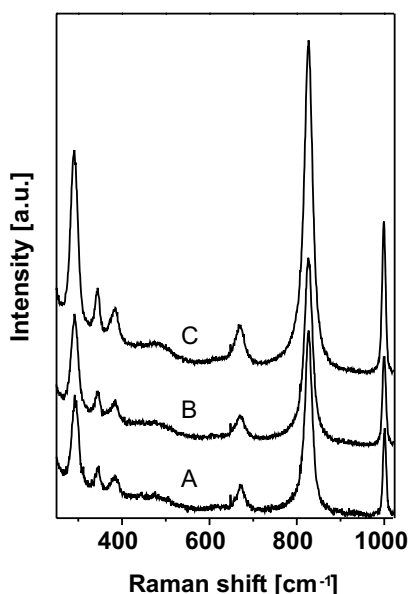


**Fig. 4.7:** Selected *in situ* Raman spectra recorded during the first TPRS cycle of the Mo catalyst at 523 K (A), 638 K (B), 716 K (C).

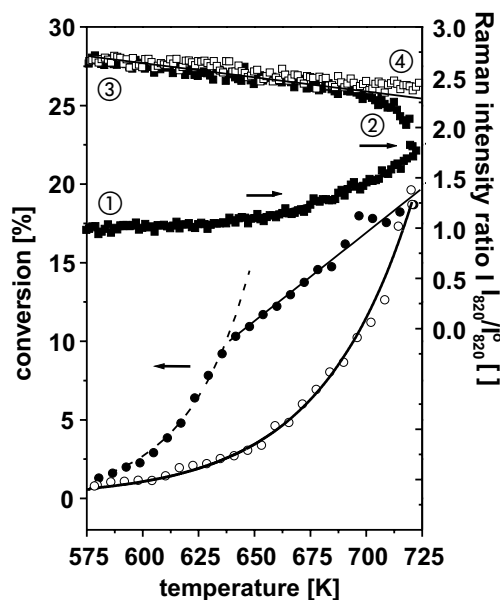


**Fig. 4.8:** Propene conversion (first TPRS cycle: ●; second TPRS cycle: ○) and the intensity ratio of the Raman band at  $823 \text{ cm}^{-1}$  (first TPRS cycle: ■; second TPRS cycle: □), as a function of reaction temperature.

The observed Raman cross section of  $\text{MoO}_{3-x}$  is a function of the degree of the reduction as proven in Chapter 1. The integral intensity of the Raman band at  $823 \text{ cm}^{-1}$ , hence, bears information about the change of the degree of reduction during the TPRS experiment. Integral intensities are used instead of the band intensities at  $823 \text{ cm}^{-1}$  in order to account for possible Raman band broadening at elevated temperatures. Prior to integration, background correction has been conducted with respect to the baseline. These intensities,  $I_{823}$ , were referenced to the initial integral Raman intensity,  $I_{823}^0$ , at the beginning of the TPRS experiment giving the integral intensity ratio  $I_{823}/I_{823}^0$ .

For the first and second TPRS cycle, the intensity ratios of the intense Raman band of  $\text{MoO}_3$  at  $823\text{ cm}^{-1}$  are shown in Figure 4.8 together with the propene conversions as a function of the reaction temperature. The observed increase of the ratio  $I_{823}/I_{823}^0$  during the first TPRS cycle at temperatures above 640 K is explained by a oxidation of the catalyst (see Figure 4.8; 1 to 2 ■). While the sample is cooled down during the first TPRS cycle, the  $\text{MoO}_{3-x}$  is further oxidised (see Figure 4.8; 2 to 3 ■). During the second run, only a minor decrease of the overall higher intensity ratio  $I_{823}/I_{823}^0$  is observed (see Figure 4.8; 3 to 4 □). This indicates that the degree of reduction of the sample is considerably lower and almost constant during the second TPRS cycle, which is confirmed by the linear Arrhenius curve (see Figure 4.6; △).

The increase of the ratio  $I_{823}/I_{823}^0$  during the first TPRS cycle coincides with the maximum selectivity to acetic acid at 640 K. The lower the degree of reduction, the lower is the amount of acetic acid formed. Therefore, it is concluded that a higher degree of reduction is necessary for the formation of acetic acid.

In order to further corroborate the influence of the degree of reduction on the catalytic properties of  $\text{MoO}_{3-x}$ , isothermal propene oxidation were carried out at 673 K over commercial  $\text{MoO}_3$  (Merck) (2 g, undiluted) under the same catalytic conditions as stated above. The characterisation of this commercial  $\text{MoO}_3$  has been described in the Section 1.1. In Figure 4.9, the selectivities to acetic acid and carbon dioxide and the intensity ratio of the Raman band at  $823\text{ cm}^{-1}$ ,  $I_{823}$ , referenced to the initial intensity,  $I_{823}^0$ , are shown as a function of the time on stream. All recorded Raman spectra show only the characteristic Raman bands of  $\text{MoO}_3$  (spectra not shown).

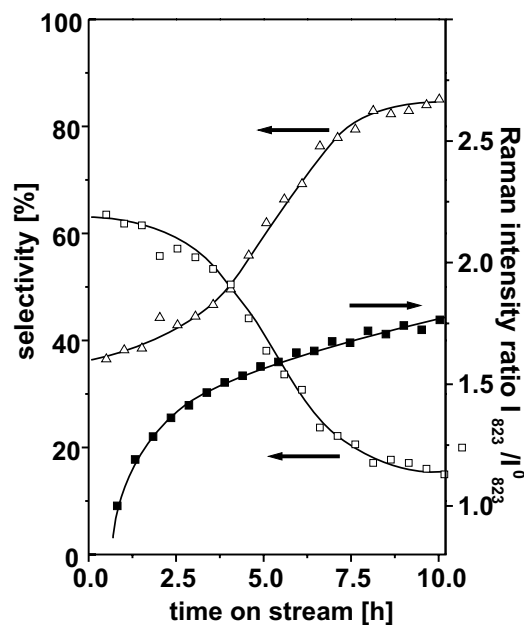


**Fig. 4.9:** Propene oxidation at 673 K over a commercial  $\text{MoO}_3$ : selectivities to acetic acid □, and  $\text{CO}_2$  △ and the evolution of the Raman intensity ratio  $I_{823}/I_{823}^0$  ■ as a function of time on stream.

Acetic acid and carbon dioxide are the main products. Additionally, traces of acrylic acid and



acrolein are detected. However, the total selectivity to these products is less than 5% and, therefore, not discussed.

The propene conversion decreases during 10 h time on stream from initially 3% to less than 1% (not shown). During this period the selectivity to acetic acid decreases from 60% to 20%, while the selectivity to CO<sub>2</sub> raises from 35% to 80%. This change in selectivity is accompanied by an increasing intensity ratio  $I_{823}/I_{823}^0$ . This indicates that the changes in selectivity again are related to the degree of reduction of the catalyst. The higher the degree of reduction, the higher is the selectivity to acetic acid.

Gai-Boys<sup>54</sup> showed by TEM investigations that clusters of oxygen vacancies are formed at the surface of the MoO<sub>3-x</sub> crystals from isolated oxygen vacancies under catalytic conditions of propene oxidation at 653 K. Similar results were obtained by Rohrer by STM investigations on the surface properties of a MoO<sub>3</sub> crystal in methanol oxidation.<sup>243, 244</sup> Gai-Boys<sup>54</sup> suggested that the formed clusters are secondary and detrimental to catalytic reactivity and only accommodate the supersaturation of anion vacancies in the oxide. Anion point defects or small defect clusters were suggested to be the catalytically active sites, which facilitate the fast diffusion of oxygen.<sup>54</sup>

The results of Gai-Boys and Rohrer may explain the above described catalysis and Raman data. In case of the TPRS experiment, the thermal activation of the ammonium metalate precursor under inert atmosphere induces a high concentration of oxygen vacancies (see Chapter 3). The temperature of the subsequent oxidative pretreatment was high enough for the nucleation of these oxygen vacancies, but too low to rapidly oxidise all oxygen vacancies. These oxygen deficiency leads to the low Raman cross section of the starting oxide. The increasing intensity ratio  $I_{823}/I_{823}^0$  suggests that the oxygen vacancies clusters are oxidised during the first TPRS cycle at temperatures above 640 K. The formation of acetic acid seems to be due to the presence of oxygen vacancies clusters, which are readily oxidised within the first TPRS cycle. During the second TPRS cycle the concentration of isolated oxygen vacancies is too small in order to favour a nucleation. Therefore, the formation of acetic acid is not observed during the second TPRS cycle. This interpretation is supported by the constant ratio  $I_{823}/I_{823}^0$  and the absence of an inflection point in the Arrhenius plot during the second TPRS cycle indicating the absence of a second reaction mechanism.

In case of the isothermal propene oxidation over commercial  $\text{MoO}_3$ , the intensity ratio  $I_{823}/I_{823}^0$  is a linear function of the propene conversion at low propene conversions as shown in Figure 4.10. Under isothermal conditions the Raman intensity is merely a function of the degree of reduction of the sample. The lower the defect concentration is the lower is the conversion. This further supports the paramount role of oxygen vacancies for the catalytic properties of  $\text{MoO}_{3-x}$ . The deviation at higher propene conversions from the linear relationship points to the presence of different active centres at higher degrees of reduction. Larger oxygen vacancies clusters influence the Raman cross section in a different manner as compared to isolated oxygen vacancies due to their IVCT transition at higher energies (2.4 eV),<sup>4</sup>. Therefore it is concluded, that two independent active centres exist, which above were suggested to be isolated oxygen vacancies and larger oxygen vacancies clusters, being responsible for the selective or total oxidation, respectively.

In summary, it is concluded that the consecutive oxidation of acrolein to acetic acid is strongly linked to the presence of larger oxygen vacancies clusters, while the formation of acrolein and its consecutive total oxidation over the  $\text{MoO}_{3-x}$  catalyst are strongly related to the presence of isolated oxygen vacancies.

Haber suggested that the degree of reduction of the  $\text{MoO}_{3-x}$  determines the observed selectivities to different products.<sup>231</sup> He concluded that the reduction of the  $\text{MoO}_3$  surface generates new active sites which accelerate the first step of the catalytic reaction, *e.g.* the activation of propene. This sug-

gestion is confirmed by the above *in situ* Raman-catalysis data of  $\text{MoO}_{3-x}$ . Reported different activities and selectivities of catalytic reactions over  $\text{MoO}_{3-x}$  may, thus, stem from different concentrations and types of oxygen vacancies present in the material due to different preparation conditions (temperature, oxygen partial pressure).<sup>59, 64, 231, 245, 240</sup> The relation presented in Chapter 1 of the intensity ratio of the Raman bands of  $\text{MoO}_{3-x}$  at 285 and 295  $\text{cm}^{-1}$  and the concentration of

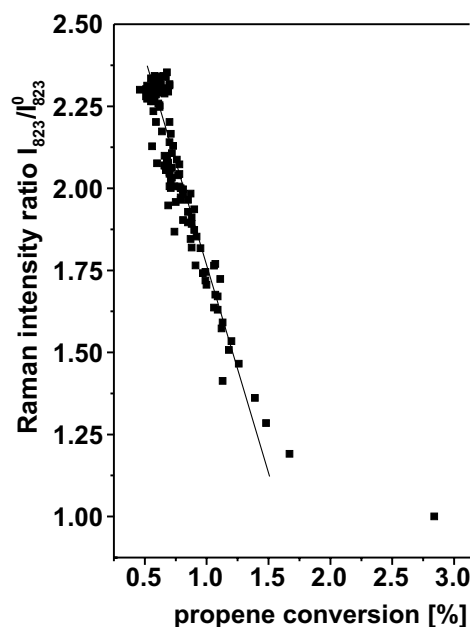


**Fig. 4.10:** Propene oxidation at 673 K over a commercial  $\text{MoO}_3$ : intensity ratio  $I_{823}/I_{823}^0$  ■ as a function of propene conversion.

oxygen vacancies may be used in further investigations to bridge this gap of information.

#### 4.2.2.2 W-promoted Mo-Oxide Catalyst (90% Mo, 10% W, M9W1)

##### 4.2.2.2.1 TPRS Results

The propene conversion and the selectivity patterns of the M9W1 catalyst are shown in Figure 4.11 as a function of the reaction temperature. Below 675 K, the propene conversion exponentially increases with increasing temperature and compares well with that of the pure Mo catalyst in the second TPRS cycle (see Figure 4.14  $\Delta$ ). Above 675 K, the propene conversion levels off to a

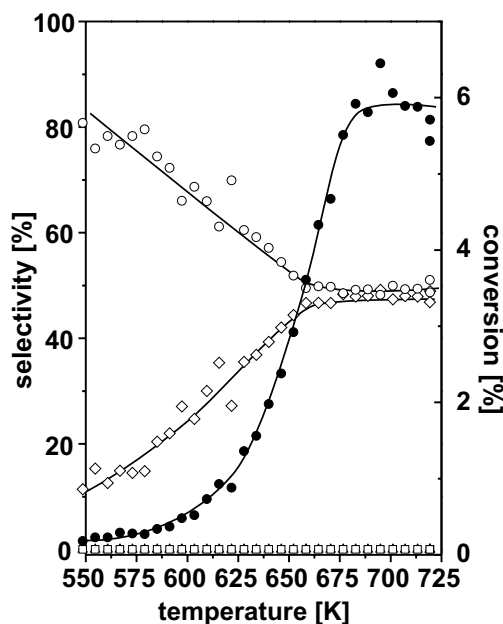


**Fig. 4.11:** Propene conversion  $\bullet$  and selectivities to acrolein  $\diamond$ , acetic acid  $\square$  and  $\text{CO}_2$   $\triangle$  of the first TPRS cycle of the Mo9W1 catalyst as a function of the reaction temperature.

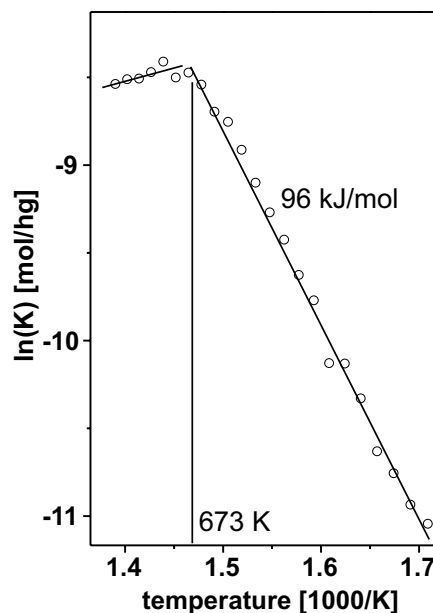


**Fig. 4.12:** Arrhenius plot for propene oxidation of the first TPRS cycle over the MoW catalyst.

constant value of about 6%, which indicates a change of the reaction mechanism and/or catalyst structure or the presence of diffusion limitation (see also the inflection point of the Arrhenius plot in Figure 4.12). The apparent activation energy is calculated to be 96 kJ/mol below the inflection point.

At 716 K, the propene conversion is only one third of that of the Mo catalyst (19%). Acrolein and  $\text{CO}_2$  are the only observed products in contrast to the first TPRS cycle of the pure Mo catalyst.

The initially high selectivity to acrolein of 80% at 550 K decreases to a constant value of 50% at 650 K at propene conversions higher than 3%. The selectivity to CO<sub>2</sub> increases from 11% at 550 K at propene conversions smaller 1% to a constant selectivity of 47% above 650 K at propene conversions higher than 3%. The ratio of selective oxidation products (acrolein) to total oxidations products (CO<sub>2</sub>) increased at 5% conversion from 0.66 to 1.06 by the W-promotion.

#### 4.2.2.3 *in situ* Raman Spectroscopy Results

Selected Raman spectra recorded at 523, 638 and 716 K are shown in Figure 4.13. The Raman spectrum recorded at 523 K (Figure 4.13 A) shows Raman bands at 244, 286, 340, 370, 469, 667, 774, 817, 847, 902 and 995 cm<sup>-1</sup>. The intense Raman bands at 780, 823 and 853 cm<sup>-1</sup> may be interpreted as symmetry split Raman bands of the Raman band 823 cm<sup>-1</sup> of MoO<sub>3</sub>.<sup>93</sup> Such a symmetry split may have its origin in a lower symmetry of the coordination polyhedra around the Mo cation which is caused by the incorporation of W into MoO<sub>3</sub> as shown Purans.<sup>246</sup> Purans et al. investigated the structural influence of W-promotion on

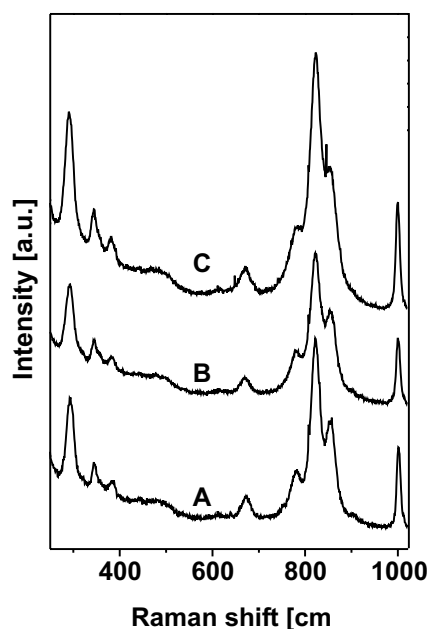


**Fig. 4.13:** Selected *in situ* Raman spectra of the Mo9W catalyst recorded during the first TPRS cycle at 523 K (A), 638 K (B), 716 K (C).

Mo oxides using EXAFS.<sup>246</sup> They observed an elongation of the short Mo=O bonds and a shortening of the longer, bridging Mo-O bonds as a function of the added amount of tungsten, which probably disfavours the *cis*-arrangement of the two strongest Mo-O bonds and, hence, leads to a symmetry lowering.

Apart of the observed symmetry split the observed Raman pattern resembles especially in the low energy regime the Raman spectrum of MoO<sub>3</sub>. Raman bands which would indicate the presence of tungsten oxides were not detected.

Changes of Raman band positions, band intensity ratios or additional bands were not observed rela-

tive to the spectrum recorded at 523 K during the TPRS experiment (see spectrum B and C of Figure 4.13). Thus, the crystalline structure does not change during catalysis. Therefore, the integral intensity ratio  $I_X/I_X^0$  of the most intense Raman bands at  $X=774, 817, 847$  and  $902\text{ cm}^{-1}$ ,  $I_X$ , referenced to the initial intensity,  $I_X^0$ , has been evaluated. The intensity ratio  $I_X/I_X^0$  is constant in the temperature range from 523 to 573 K and increases above 675 K as shown in Figure 4.14. The observed constant ratio  $I_X/I_X^0$  in the low temperature regime is explained by a constant reduction degree of the catalyst at low conversion. The increase of the ratio  $I_X/I_X^0$  coincides with the intersection point of the exponential increasing and the constant propene conversion as already observed for the pure molybdenum catalyst (see Figure 4.8). This overall smaller increase of the intensity ratio  $I_X/I_X^0$  as compared to the Mo catalyst indicates a lower degree of reduction of the W-promoted sample after the oxidative pretreatment.

Interestingly, the formation of acetic acid was not observed over the W-promoted catalyst. It was suggested that acetic acid formation is linked to the presence of larger oxygen vacancies clusters over the pure Mo catalyst. The absence of acetic acid may have its origin in the preferential occupation of these sites by the redox stable W. However, W prefers a corner linked octahedral coordination in its highly stable  $W^{VI}$  state.<sup>126</sup> Therefore, it is unlikely that the W cations are predominantly situated at the larger oxygen vacancies clusters.

In Section 3.1.3.2 on page 88, it has been suggested that the inhibition of structural reorganisations during the thermal activation process of this sample

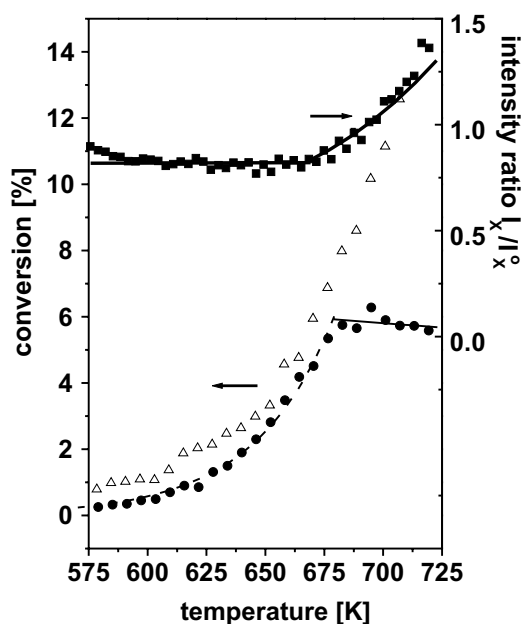


**Fig. 4.14:** Propene conversion of the Mo9W1 ● and pure Mo △ catalyst and the Raman intensity ratio  $I_X/I_X^0$  ■ of the Raman bands at  $X=780, 823$  and  $853\text{ cm}^{-1}$   $I_X$  referenced to their initial intensity  $I_X^0$  as a function of reaction temperature.

stems from a lower mobility of the oxygen vacancies. Such a lower oxygen vacancy mobility inhibits a nucleation of the oxygen vacancies. A W-induced inhibition of the nucleation seems to reasonably explain the absence of acetic acid over the W promoted catalyst. The lower conversions and comparable selectivities as compared to the second TPRS run of the pure Mo catalyst, point to

the absence of a direct participation of the W-promoter in the catalytic cycle. This is confirmed by reports of Barber,<sup>121</sup> who showed for the propene oxidation over mixed Mo/W oxides that molybdenum plays the major catalytic role while tungsten acts as a diluent.

The formation of larger oxygen vacancy clusters is, as shown by quantum chemical calculations, energetically more favourable than the formation of isolated oxygen vacancies.<sup>247</sup> Therefore, isolated oxygen vacancies or small defect clusters are easier to be oxidised for a given oxygen pressure as compared to larger oxygen vacancies clusters. The presence of isolated oxygen vacancies or small defect clusters in the W-promoted catalyst as compared to ordered oxygen vacancies in the pure Mo oxide may be the reason for the different re-oxidation kinetics of these defects and, hence, a lower degree of reduction of the W promoted catalyst after the oxidation pretreatment and during the TPRS cycles. The inhibition of structural reorganisation by W is seen as the reason for this lower degree of reduction of the W-promoted sample. Due to low degree of reduction a reordering of the isolated oxygen vacancies in oxygen vacancies clusters does not occur. This is confirmed by the smaller increase of the intensity ratio  $I_X/I_X^0$  as compared to the Mo catalyst. Because the catalytic activity is strongly related to the presence of oxygen vacancies, the lower reduction degree of the W-promoted catalyst causes a lower overall propene conversion as compared to the pure Mo catalyst above 675 K.

#### **4.2.2.4 V-promoted Mo-Oxide Catalyst (90% Mo, 10% V, Mo9V1)**

##### **4.2.2.4.1 TPRS Results**

The propene conversion and the selectivities to acrolein, CO<sub>2</sub>, acetic and acrylic acid over the M9V1 catalyst are shown in Figure 4.14 as a function of the reaction temperature. Interestingly, a higher propene conversion of 50% is observed at 716 K as compared that of the pure Mo (19%) or the Mo9W1 (7%) catalysts at 716 K. Below 673 K, the apparent activation energy is determined to be 136 kJ/mol and 118 kJ/mol for the first and second TPRS cycles, respectively (see Figure 4.17). Above 673 K, during the first TPRS cycle a considerably lower activation energy of 54 kJ/mol is found. Inflection points observed for the Arrhenius plots of the second and third TPRS cycle at 673 K indicate a reversible structural change, a mechanistic change or the beginning of diffusion limitation.

Acrolein,  $\text{CO}_2$ , acetic and acrylic acid are the main products over the Mo9V1 catalyst. The initially high selectivity to acrolein of 80% at 550 K at propene conversions smaller 1% decreases and follows an opposite trend as compared to the selectivities to acetic and acrylic acid. The initially higher selectivities to  $\text{CO}_2$  as compared to the selectivity to acetic or propenic acid points to an independent reaction path for the total oxidation of acrolein to  $\text{CO}_2$  in line with results of Vogel et al.<sup>209</sup>. The selectivities to carbon dioxide, acetic and acrylic acid tend to zero for a quasi zero propene conversion. This indicates that these products are formed by a consecutive oxidation of acrolein.

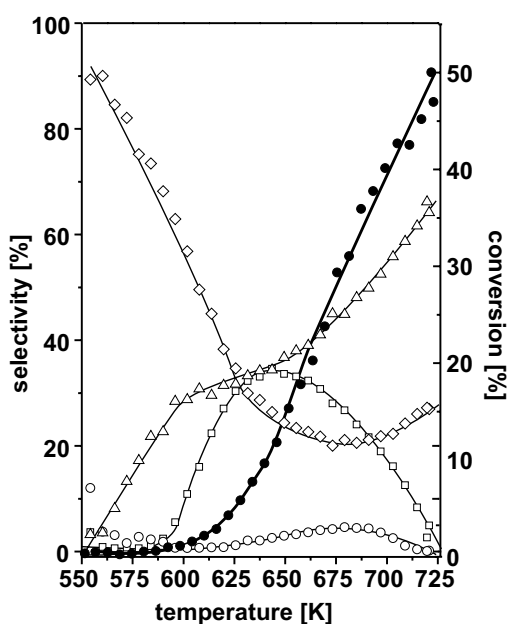


**Fig. 4.16:** Propene conversion • and selectivities to acrolein  $\diamond$ , acetic acid  $\square$ , acrylic acid  $\circ$  and  $\text{CO}_2$   $\triangle$  of the first TPRS cycle of the Mo9V1 catalyst as a function of the catalyst activity.

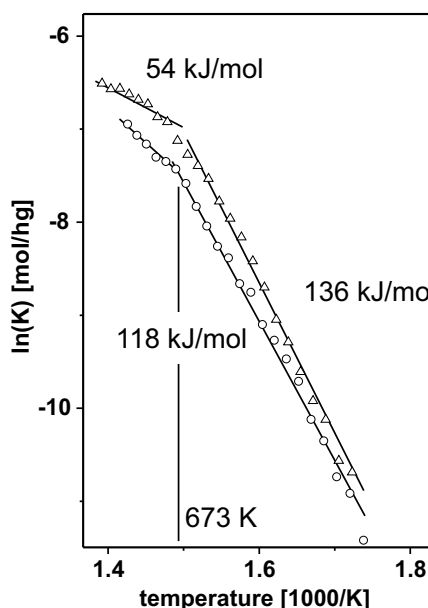


**Fig. 4.17:** Arrhenius plot for propene oxidation of the first  $\circ$  and second  $\triangle$  TPRS cycle over the pure Mo9V1 catalyst.

The selectivities to acetic acid and acrylic acid show maxima of 35% and 5% at 643 and 685 K at propene conversions of 12% and 31%, respectively. An increase of the selectivity to  $\text{CO}_2$  occurs with decreasing selectivities to acetic and acrylic acid, which indicates a consecutive oxidation of the carbon acids to  $\text{CO}_2$  and water at higher conversions. For propene conversions above 40%, the selectivities to acetic and acrylic acid tend to zero.  $\text{CO}_2$  is the major observed product. The maximum selectivities to acetic and acrylic acid are observed at different propene conversions which points to the existence of two independent active centres for each of these acids in line with results

of Stein et al.<sup>71</sup>.

Between 575 and 725 K, acetic and acrylic acid are formed. The formation of acrylic acid was not observed for the pure Mo or W promoted catalysts. In processes of hydrocarbon oxidation, thermodynamics favours the ultimate formation of carbon dioxide and water. Therefore, all partial oxidation products are intermediates derived from kinetic reaction control. Due to the generally lower propene conversions over the Mo and the Mo9W1 catalysts acrylic acid should also be observed if V is not an active part in the catalytic cycle of acrylic acid formation. The opposite is observed. Therefore it is concluded, that V takes actively part in the selective oxidation of acrolein to acrylic acid. V-promotion leads to the generation of active centres which are not present on the surface of pure Mo or W-promoted catalysts. This is further supported by the 2.5 times higher propene conversion of Mo9V1 as compared to the pure Mo catalyst. This higher conversion points to a crucial role of V in the catalytic cycle as proposed by several authors.<sup>35, 163, 248-251</sup> Andrushkevich suggested for the acrolein oxidation to acrylic acid a Mo/V ratio of 3/1 to lead to optimum activity and selectivity.<sup>33</sup> A (MoV)<sub>4</sub>O<sub>11</sub> structure was suggested to be as responsible for the optimum catalytic performance. It was further suggested that the presence of V<sup>4+</sup> is responsible for high conversions and selectivities.<sup>33, 35</sup>

A clear decision about the V-promoter effect cannot easily be drawn because the influence of V is twofold. On one hand, the preferred fivefold coordination of V<sup>5+</sup> leads to oxygen vacancies within the molybdenum oxide matrix. This effect should be even more pronounced for V<sup>4+</sup> cations. It was suggested above for the pure Mo catalyst that isolated oxygen vacancies or small defect clusters are positively linked to high propene conversions. Hence, an increase of oxygen vacancies leads to an increase of the number of active sites and further to an increase of the oxygen mobility as suggested by Levy and DeGroot.<sup>252, 253</sup> The strong increase of the propene conversion by V may thus be described by a lower valent promoter induced defect generation.<sup>107</sup> On the other hand, the redox couple V<sup>5+</sup>/V<sup>4+</sup> may directly take part in the catalytic cycle. In this case, the Mo oxide matrix may be seen as diluent of the active V sites according to the site isolation theory of Grasselli.<sup>17, 254</sup> Because the catalytic cycle of the propene oxidation is rather complex and involves more than one active site,<sup>9, 71, 187, 255, 236</sup> both, the promoter induced defect generation and the direct active role of V in the catalytic cycle may be relevant factors which both contribute to the observed overall



increase of catalytic activity.

#### 4.2.2.4.2 *In situ* Raman Spectroscopy Results

Selected *in situ* Raman spectra which were recorded at 523, 638 and 716 K are shown in Figure 4.18. After the oxidation pretreatment of the V promoted catalyst, *e.g.* at the beginning of the TPRS experiment, the observed Raman spectrum (Figure 4.18 A) shows Raman bands at 223, 246, 293, 344, 383, 473, 666, 823 and 995  $\text{cm}^{-1}$ . Raman bands indicating presence of pure V oxides could not be detected.

Interestingly, additional Raman bands due to a symmetry split of the Raman band at 823  $\text{cm}^{-1}$  are not detected for the V promoted sample. This finding may be interpreted with the assumption that the V in the  $\text{MoO}_3$  structure does not disturb the coordination sphere of the molybdenum cations as it already has been observed for the thermal activation of this catalyst (see Section 3.2.3.2.1 on page 96).

The Raman bands of the spectrum which has been recorded at 638 K (Figure 4.18 B) are located at 291, 343, 383, 409, 444, 606, 668, 794, 826, 858, 918, and 995  $\text{cm}^{-1}$ . The Raman bands at 291, 343, 383, 668, 826 and 995  $\text{cm}^{-1}$  are attributed to  $(\text{Mo,V})\text{O}_3$  oxide. The new additional Raman bands at 409, 444, 794, 858 and 918  $\text{cm}^{-1}$  (spectrum C) gain intensity with increasing reaction temperature while those of the  $(\text{Mo,V})\text{O}_3$  oxide loose intensity.

By comparison of the positions of these new Raman bands with those observed for crystalline reference samples of orthorhombic  $\text{Mo}_4\text{O}_{11}$ <sup>179</sup> (Raman bands in the high energy regime at 755, 818, 844, 862, 871 and 934  $\text{cm}^{-1}$ ), monoclinic  $\text{Mo}_4\text{O}_{11}$ <sup>128</sup> (Raman bands in high energy regime at 729, 791, 835, 912 and 960  $\text{cm}^{-1}$ ) or  $\text{Mo}_8\text{O}_{23}$ <sup>179</sup> (Raman bands in the high energy regime at 636, 682, 761, 842, 908, 930, 951, 990 and 1000  $\text{cm}^{-1}$ ) these compounds can be ruled out to be present. These new Raman bands may be attributed to a oxide of  $\text{Mo}_5\text{O}_{14}$  structure by comparison with the Raman spectra which have been obtained from the industrial catalyst on page 56. Further, the observed Raman band positions are in agreement with those of a crystalline  $(\text{MoW})_5\text{O}_{14}$  reference sample.<sup>256</sup> With the *in situ* formation of this  $(\text{MoV})_5\text{O}_{14}$  oxide, a strong increase of the Rayleigh scattering background and a low signal to noise ratio of the Raman spectra is observed. This in-

indicates a low Raman cross section of the formed  $(\text{MoV})_5\text{O}_{14}$  oxide. The strong increase of the background at  $500\text{ cm}^{-1}$  is attributed to weak and broad Raman background due to the  $\text{SiO}_2$  diluent which becomes viable due to the low  $(\text{MoW})_5\text{O}_{14}$  scattering efficiency.

At 716 K, Raman bands are observed at 291, 613, 716, 811, 835, 853, 920 and  $998\text{ cm}^{-1}$  (see Figure 4.18). The Raman bands of  $(\text{MoV})\text{O}_3$  (291, 823 and  $998\text{ cm}^{-1}$ ) decreased in intensity, but still prove  $(\text{MoV})\text{O}_3$  to be present.

The observation of the Raman bands of the  $(\text{MoV})_5\text{O}_{14}$  oxide coincide with the formation of acrylic acid, while the decrease of the Raman bands of the  $(\text{MoV})\text{O}_3$  oxide coincide with the decrease of the formation of acetic acid. Therefore, it may be concluded that the consecutive oxidation of acrolein to acetic acid is mainly related to the  $(\text{MoV})\text{O}_3$  oxide, while the consecutive selective oxidation of acrolein to acrylic acid is related to the  $(\text{MoV})_5\text{O}_{14}$  oxide.

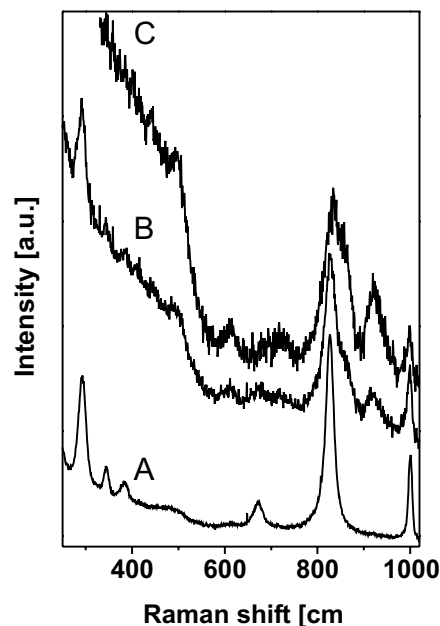


**Fig. 4.18:** Selected *in situ* Raman spectra recorded during the first TPRS cycle of the Mo9V1 catalyst at 523 K (A), 638 K (B), 716 K (C).

#### 4.2.2.5 V,W-promoted Mo-Oxide Catalyst (80% Mo, 10% V, 10% W, Mo8V1W1)

##### 4.2.2.5.1 TPRS Results

The propene conversion and the selectivities to acrolein,  $\text{CO}_2$ , acetic and acrylic acid are presented in Figure 4.19 as a function of the reaction temperature. The propene conversion of 48% at 716 K is comparable to the propene conversion of Mo9V1. Below 660 K, the apparent activation energies were calculated to be 103 and 114 kJ/mol for the first and second TPRS cycle (not shown). Above 660 K, considerable lower activation energies of 60 and 44 kJ/mol are calculated. This finding again indicates structural or mechanistic changes and/or the beginning of diffusion limitation at this temperature. Interestingly, the activation energy of the second TPRS cycle increased as compared to the first cycle.

The maximum selectivity to acrylic acid of 13% at 659 K (18% conversion) increased as compared to the Mo9V1 catalyst. The selectivity to acrylic acid is found to be 11% at 31% conversion, which is 2.3 times higher as compared to the Mo9V1 catalyst, while the selectivities to  $\text{CO}_2$  are comparable. The maximum selectivity to acetic acid of 39% is observed at 626 K at 10% propene conversion which is comparable to the Mo9V1 catalyst. The W-promoter, hence, results in higher selectivities to partial oxidation products at comparable conversions as already observed for the Mo9W1 catalyst.

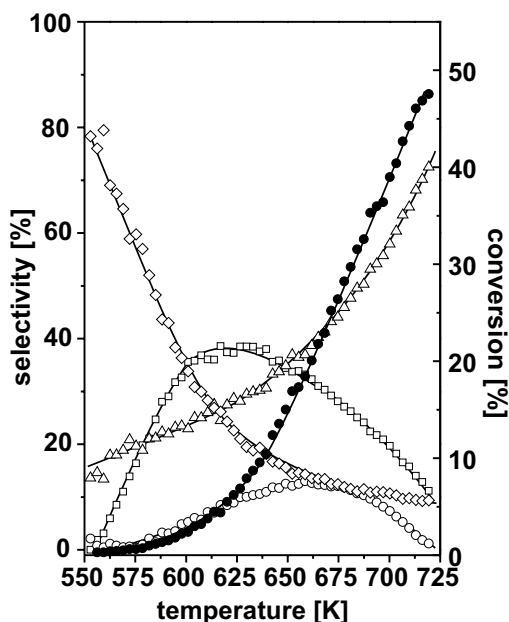


**Fig. 4.19:** Propene conversion  $\bullet$ , selectivities to acrolein  $\diamond$ , acetic acid  $\square$ , acrylic acid  $\circ$  and  $\text{CO}_2$   $\triangle$  of the first TPRS cycle of the Mo8V1W1 catalyst as a function of the reaction temperature.

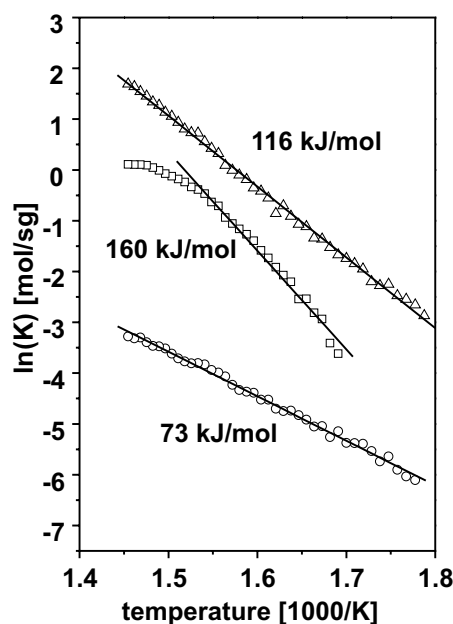


**Fig. 4.20:** Arrhenius plot for acrolein, acrylic acid and  $\text{CO}_2$  of the first TPRS cycle over the Mo8V1W1 catalyst.

In Figure 4.20 the Arrhenius plot and the calculated activation energies of the Mo8V1W1 catalyst are shown for the formation of acrolein, acrylic acid and  $\text{CO}_2$ . The activation energies for the formation of acrolein, acrylic acid and  $\text{CO}_2$  were calculated to be 73, 160 and 116 kJ/mol, respectively. The different activation energies for the formation of the partial and total oxidation products further supports the suggested existence of different active sites being responsible for the formation of each of these products.

#### 4.2.2.5.2 *In situ* Raman Spectroscopy Results

Selected Raman spectra recorded at 523, 673 and 716 K during the TPRS experiment of the M8V1W1 catalyst are shown in Figure 4.21. After the oxidation pretreatment, the signal to noise ratio and the Rayleigh background of the Raman spectra of Mo8V1W1 are considerably higher as compared to the Raman spectra of the pure Mo or the Mo9V1 catalyst. The Raman bands of the spectrum recorded at 523 K (Figure 4.21 spectrum A) are situated at 285, 434, 485, 605, 763, 820, 845, 870 and 995  $\text{cm}^{-1}$ . The Raman bands at 285, 485, 820 and 995  $\text{cm}^{-1}$  are attributed to minor amounts of a  $(\text{MoVW})\text{O}_3$  oxide. The remaining

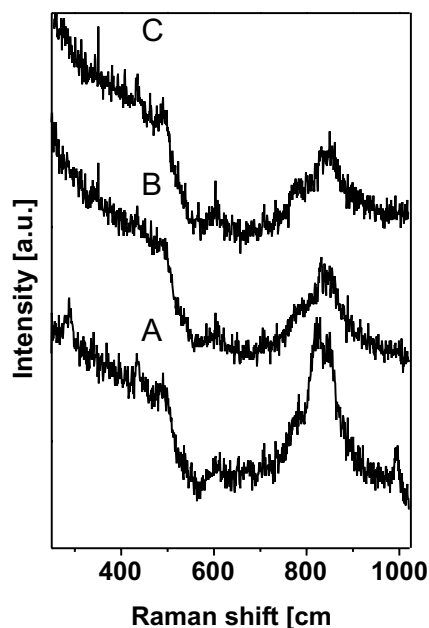


**Fig. 4.21:** Selected *in situ* Raman spectra recorded during the first TPRS cycle of the Mo8V1W1 catalyst at 523 K (A), 623 K (B), 716 K (C).

Raman bands at 434, 605, 763, 845, 870 and 917  $\text{cm}^{-1}$  are attributed to a  $(\text{MoVW})_5\text{O}_{14}$  oxide. The Raman bands of  $(\text{MoVW})\text{O}_3$  vanish with increasing reaction temperatures and the Raman spectrum which has been recorded at 674 K (Figure 4.21 spectrum B) shows Raman bands at 601, 788, 840, 878 and 920  $\text{cm}^{-1}$ . For higher reaction temperatures or consecutive TPRS cycles additional Raman bands or changes of the band positions were not observed (Figure 4.21 spectrum C). The catalytic properties (*e.g.* higher selectivity to selective oxidation products) can only be explained by different degrees of reduction for the different temperatures or TPRS runs. W acts as a structural promoter and stabilises the structure on a high degree of reduction, whereas V enhances the catalytic activity.

#### 4.2.2.6 V,W-promoted Mo-Oxide Catalyst (60% Mo, 30% V, 10% W, Mo6V3W1)

##### 4.2.2.6.1 TPRS Results

This catalyst composition has been prepared because of its relevance for industrially used catalysts. The propene conversion and the selectivities to acrolein,  $\text{CO}_2$ , acetic and acrylic acid are presented in Figure 4.22 as a function of the reaction temperature. The selectivity patterns are comparable to

those of the M8V1W1 catalyst.

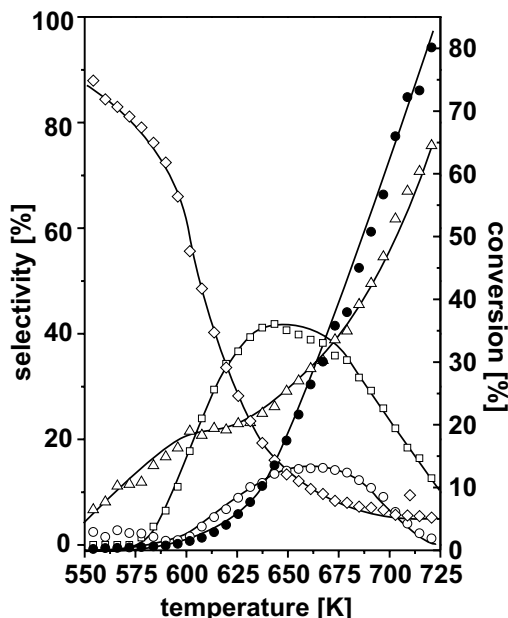


**Fig. 4.21:** Propene conversion ●, selectivities to acrolein ◇, acetic acid □, acrylic acid ○ and  $\text{CO}_2$  △ of the first TPRS cycle of the Mo6V3W1 catalyst sample as a function of the reaction temperature.

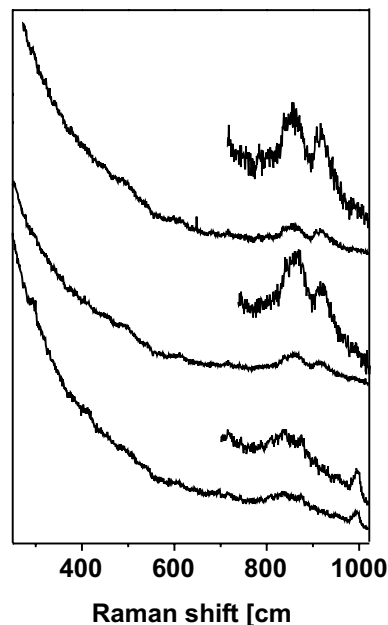


**Fig. 4.22:** Selected in situ Raman spectra recorded during the first TPRS cycle of the Mo6V3W1 catalyst at 523 K (A), 638 K (B), 716 K (C).

The three times higher vanadium content of the Mo6V3W1 catalyst as compared to the Mo8V1W1 catalyst sample leads to an increase in propene conversion. For the Mo6V3W1 catalyst, the propene conversion is 76% at 716 K as compared to 45% for the Mo8V1W1 catalyst which is an increase by a factor of 1.7. Again V is essential for high propene conversions. However, this increasing propene conversion is lower as would be expected from the three times higher V concentration. The apparent activation energies of the first and second TPRS cycle are calculated to be 171 and 165 kJ/mol below 655 K. At higher temperatures the activation energies decrease to 75 and 105 kJ/mol for the first and second TPRS cycle, respectively. Therefore, a limitation of the rate of re-oxidation of the catalyst at high propene conversions may explain the too low increase of propene conversion. Alternatively, the contact time and oxygen/propene ratio employed may be beyond the optimum of this most active catalyst.

The maximum selectivity to acetic and acrylic acid formation are 42% and 15% at 642 and 660 K at 14% and at 30% propene conversion, respectively. At 30% propene conversion, the selectivities

to acetic and acrylic acid are 39% and 15%, which are 2.0 and 2.3 times higher as compared to the Mo8V1W1 catalyst at comparable conversion, respectively. The selectivities to CO<sub>2</sub> are comparable for both catalysts.

#### 4.2.2.6.2 *In situ* Raman Spectroscopy Results

Selected *in situ* Raman spectra recorded at 523, 638 and 716 K are shown in Figure 4.22. The Raman spectrum recorded at 523 K (Figure 4.22 spectrum A) shows Raman bands at 289, 609, 701, 823, 874, 919 and 995 cm<sup>-1</sup>. The signal to noise ratio is low and the Raman bands are situated on top of a very intense Rayleigh background. Again the oxidation pretreatment at 673 K leads to the formation of minor amounts of a (MoVW)O<sub>3</sub> oxide which is identified by the Raman bands at 289, 823 and 995 cm<sup>-1</sup>. The remaining Raman bands at 609, 701, 874 and 919 cm<sup>-1</sup> are attributed to a oxide of Mo<sub>5</sub>O<sub>14</sub> structure. With increasing reaction temperature to 660 K, the Raman bands of the (MoVW)O<sub>3</sub> oxide vanish while those of the Mo<sub>5</sub>O<sub>14</sub> oxide are more resolved (see Figure 4.22 spectrum B). The broad Raman bands of the spectrum recorded at 638 K are situated at 451, 490, 609, 714, 860 and 915 cm<sup>-1</sup>. The observed Raman bands indicate only the presence of a oxide of Mo<sub>5</sub>O<sub>14</sub> structure at temperatures above 638 K. The very intense Rayleigh background points to pronounced semiconducting properties due to a higher concentration of oxygen vacancies, which is explained by the three times higher V concentration.

#### 4.2.2.7 Comparison of the Catalytic Performances of the V-Promoted Catalysts and *in situ* Raman Results

Selected data of the catalytic properties of the V-promoted sample are summarised in Table 4.1. For the second and third TPRS cycle the maximum propene conversion over the Mo9V1 catalyst decreases from initially 50% to 41% and 38% (see Table 4.1). During this deactivation, the selectivities for oxidation products of acrolein (propenic and acetic acid) decrease while the selectivities for the formation of acrolein and CO<sub>2</sub> increase (see Table 4.1). For the Mo8V1W1 a deactivation is observed (see Table 4.1) comparable that of Mo9V1. The Mo6W3W1 catalyst shows higher selectivities to acrolein and acrylic acid (see Table 4.1) at lower propene conversions during the second and third TPRS cycle.

The Raman spectra recorded during the consecutive TPRS cycles of these catalysts did not reveal any structural change which could account for the deactivation behaviour of the different catalysts.

The generally low Raman cross section of intermediate molybdenum oxides may be explained by their semiconducting properties.<sup>5</sup> Due to high electron density at the surface of conducting or semiconducting materials the excitation radiation is elastically scattered at the surface of the material and a strong Rayleigh wing is observed. The penetration depth of the excitation radiation tends to zero for metals and only a strong Rayleigh line superimposed on a high background is observed. Therefore, a strong Rayleigh background is seen as indicative for semiconducting or conducting properties of the catalyst. For  $\text{MoO}_{3-x}$  samples the concentration of oxygen vacancies affects their electronic properties as shown in Section 1.1. The concentration of oxygen vacancies present in an intermediate oxide like  $(\text{MoVW})_5\text{O}_{14}$  affects its Raman cross sections and the observed Rayleigh background due to changed electronic properties. Therefore, the scattering background of the Raman spectra bears information about the conducting properties, *i.e.* nonstoichiometry.

Therefore, the attempt was made to distinguish between the evolution of the Raman signal due to presence of crystalline material and the evolution of the Raman background. The Raman spectra recorded during the TPRS cycles of the Mo9V1 and Mo6V3W1 catalysts were normalised with respect to the most intense Raman band between 850 to 950  $\text{cm}^{-1}$ . The evolution of the crystalline parts contributing to the Raman spectra was estimated by the integral intensity of the Raman bands in the energy range between 750 to 950  $\text{cm}^{-1}$ ,  $I_{\text{cryst}}$ , after these have been baseline corrected. The evolution of the changes of the Raman background was estimated by the total integral Raman

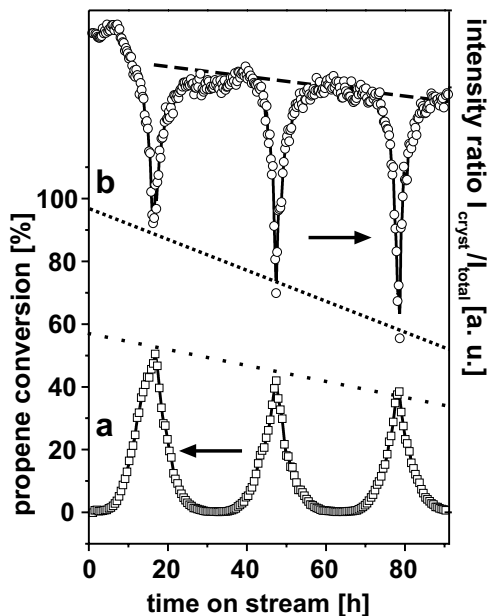


**Fig. 4.23:** Propene conversion (a;  $\square$ ) of the Mo9V1 catalyst and the Raman intensity ratio  $I_{\text{cryst}}/I_{\text{total}}$  (b;  $\circ$ ) as a function of the time on stream.

max propene conversion (716 K)	M9V1 [%]	M8V1W1 [%]	M6V3W1 [%]
1. TPRS cycle	45	47	73
2. TPRS cycle	41	37	68
3. TPRS cycle	37	-	66
selectivity to acetic acid <sup>a</sup>			
1. TPRS cycle	30.3 (673 K)	19.3 (684 K)	38 (667 K)
2. TPRS cycle	33 (693 K)	14 (708 K)	33 (674 K)
3. TPRS cycle	23 (692 K)	—	32 (690 K)
selectivity to acrylic acid <sup>a</sup>			
1. TPRS cycle	8	26	15
2. TPRS cycle	7	20	18
3. TPRS cycle	4	—	18
selectivity to CO <sub>2</sub> <sup>a</sup>			
1. TPRS cycle	45	48	35
2. TPRS cycle	58	54	34
3. TPRS cycle	60	—	38
selectivity to acrolein <sup>a</sup>			
1. TPRS cycle	20	12	10
2. TPRS cycle	36	14	11
3. TPRS cycle	32	—	9

<sup>a</sup> selectivities determined at 30 % propene conversion

**Table 4.1:** Selectivities and propene conversions for the three V promoted catalysts (Mo9V1, Mo8V1W1 and Mo6V3W1).

intensity,  $I_{total}$ . The evolution of the intensity ratio,  $I_{cryst}/I_{total}$ , may directly be addressed to changes of the semiconducting properties *i.e.* the nonstoichiometry during the TPRS cycles. The absolute degree of reduction, of course, cannot be determined by this method.

In Figure 4.23 and 4.24, the intensity ratio  $I_{cryst}/I_{total}$  and the propene conversions of the Mo9V1 and the Mo6V3W1 catalyst are compared as a function of the time on stream. Both catalyst show lower propene conversions during the second and third TPRS cycle. The evolution of the selectivities to partial oxidation and total oxidation products show an opposite trend for these two catalysts (see Table 4.1). Over the Mo9V1 catalyst, the formation of total oxidation products increases during the subsequent TPRS cycles. The evolution of the intensity ratio  $I_{cryst}/I_{total}$  of the Mo9V1 catalyst indicates that the Raman background is found to be more intense at high propene conversions. This points to a higher degree of reduction of the Mo9V1 catalyst at high propene conversions and may explain the changes of the activation energies over these catalysts. At lower conversions and reac-



tion temperatures, the catalyst is reoxidised as seen in the increase of the ratio  $I_{cryst}/I_{total}$  after the maxima of propene conversion, *e.g.* at lower reaction temperatures. The re-oxidation of the catalyst is not completely reversible as indicated by the decreasing baseline of the intensity ratio  $I_{cryst}/I_{total}$  curve (see dashed line in Figure 4.23). At high propene conversions, during the second and third TPRS cycle the degree of reduction of the catalyst increases as compared to the first TPRS cycle (see dotted line in Figure 4.23). This indicates that the catalyst is not stable with respect to its degree of reduction at high propene conversions. The observed changes in selectivity as a function of the propene conversion, hence, may be derived from the different degrees of reduction of the catalyst as a function of the propene conversion.

For the Mo6V3W1 catalyst, the evolution of the intensity ratio  $I_{cryst}/I_{total}$  indicates that this catalyst is not completely reversibly reduced at high propene conversions (see dotted line in Figure 4.23). In contrast to the Mo9V1 catalyst, the baseline of the intensity ratio  $I_{cryst}/I_{total}$  increases (see dashed line in Figure 4.24) which indicates that the degree of reduction of this catalyst decreases with time on stream. The observed deactivation during the TPRS cycles may be explained by the lower degree of reduction of the catalyst due to the irreversible oxidation. In Figure 4.24 the selectivity to acrylic acid is additionally shown as a function of the time on stream. The maxima of the selectivity to acrylic acid coincide with the decrease of the intensity ratio  $I_{cryst}/I_{total}$  (see vertical arrows in Figure 4.24). The observed deactivation and the changes in selectivity may be explained by the lower degree of reduction of the catalyst in subsequent TPRS cycles. At high propene conversions the selectivity strongly decreases due to the increasing degree of reduction.

In summary, the deactivation of both catalyst may be explained by irreversible changes of the degree of reduction of the catalysts during the TPRS experiment (as seen in the evolution of the baseline of the intensity ratio  $I_{cryst}/I_{total}$ ). The selectivities to the observed products are suggested to be a function of the degree of reduction of the catalysts. The overall degree of reduction of the Mo9V1 catalyst is lower than that of the Mo6V3W1 catalyst as seen by the more intense Raman background in the Raman spectra of the Mo6V3W1. During the TPRS experiments, the degree of reduction of the Mo9V1 catalyst increased, while that of Mo6V3W1 decreased. The irreversible changes of the degree of reduction may be explained by changes of the spatial elemental distribution during the TPRS cycles, while the structure of the  $(\text{MoV})_5\text{O}_{14}$  oxide is retained. In Chapter 2.1,

the presence of spatial elemental inhomogeneities was proven by SEM/EDX for a V and W promoted catalyst with a oxide of  $\text{Mo}_5\text{O}_{14}$  structure. Upon thermal activation at 818 K, it was found that the surface of the catalyst depletes of V. The  $\text{Mo}_5\text{O}_{14}$  structure tolerates different amounts of V and W.<sup>42, 48, 45, 181, 47</sup> Although the maximum temperatures of the TPRS experiment were about 100 K below those of the thermal activation of the catalyst described in Chapter 2, the reaction temperatures of the TPRS experiment are still high enough for a V mobility.<sup>239</sup> Therefore, the observed changes between the subsequent TPRS cycles of the catalytic properties of the Mo9V1, Mo8V1W1 and Mo6V3W1 catalysts may be attributed to diffusion of V into the bulk of the material and, hence, lower V concentrations at the surface of the catalyst material, while the  $\text{Mo}_5\text{O}_{14}$  structure is retained as observed by *in situ* Raman spectroscopy. Only minor surface V diffusion into the bulk occurs due to the high bulk V concentration of the Mo6V3W1 catalyst. The increasing selectivities to partial oxidation products over this catalyst during the subsequent TPRS cycles may point to a initial surface V-concentration which is already beyond the optimum for the selective oxidation reactions.

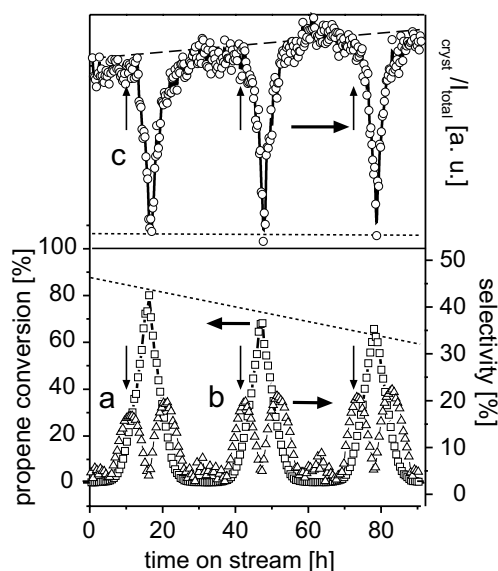


**Fig. 4.24:** Propene conversion (a;  $\square$ ) and selectivity to acrylic acid (b;  $\triangle$ ) of the Mo6V3W1 catalyst and the Raman intensity ratio  $I_{\text{cryst}}/I_{\text{total}}$  (c;  $\circ$ ) as a function of the time on stream.

The formation of the oxide of  $\text{Mo}_5\text{O}_{14}$  structure is observed under the conditions of high conversion for all catalysts containing V. In spite of the paramount importance of oxygen vacancies for the catalytic properties of the catalysts this structure with its intrinsic disorder<sup>42, 149</sup> is rather interesting.

The observation that at high propene conversions the Raman bands of the oxide of  $\text{Mo}_5\text{O}_{14}$  structure are situated always on top of generally high background supports the in Chapter 2 developed core-shell model.

These results, which are valid for the propene oxidation at high conversions are also important for the selective catalytic oxidation reactions at lower temperatures. For example, the selective oxidation of acrolein to acrylic acid is industrially carried out over MoVW mixed oxide catalyst at temperatures below 573 K.<sup>209, 242, 257-260</sup> For this reaction

the formation of the catalytically active structure by the thermal activation process is of paramount importance, because catalysis induced solid state transformation should be much slower at such temperatures. Due to the low reaction temperature long time periods are usually necessary to obtain steady state conversions *e.g.* the optimum degree of reduction of the catalyst. Such long activation periods may be considerably shortened by the *in situ* activation of the catalyst under propene oxidation conditions at higher temperatures.

### 4.2.3 Summary

#### 4.2.3.1 The role of the V and W promoters

In Figure 4.25 and 4.26 the total propene conversions at 716 K and selectivities to acrolein, acrylic and acetic acid and CO<sub>2</sub> at 6 % conversion are shown for all tested catalysts. Upon 10 % and 30 % V addition the propene conversion at 716 K increases from 20 % of the pure Mo catalyst to 47 and 74 %, respectively. Therefore, the propene conversion appears to be a function of the V addition. In contrast to V addition, W addition causes a lower maximum propene conversion as compared to the unpromoted catalyst. Therefore, it has been concluded above, that W acts mainly as a structural promoter which is not directly incorporated into the catalytic cycle. The effect of this structural promoter on the selectivities at 6 % conversion is shown in Figure 4.26.

The W addition increases the selectivity to selective partial oxidation products as can be seen by comparing the selectivities to acrolein and CO<sub>2</sub> of the pure Mo and the Mo9W1 catalysts. The addition of V reduces the formation of CO<sub>2</sub> as compared to the pure Mo and the Mo9W1 catalyst. The V addition leads to the formation of acrylic acid, which could not be observed for the pure Mo or the W promoted catalyst. Therefore, it is concluded above, that V addition causes the formation of new active centres, which are capable of the selective oxidation of acrolein to acrylic acid. V acts as well structural promoter as it destabilises the found structures and lowers the temperature of defect formation. Additional W induces higher selectivities to acrylic acid of the Mo8V1W1 catalyst as compared to the Mo9V1 catalyst. With increasing V content from 10 % to 30 % (Mo6V3W1 and Mo8V1W1 catalysts) the selectivity to CO<sub>2</sub> again is reduced. However, the main effect of the higher V content is the 1.7 times higher maximum propene conversion at comparable selectivities. In summary, the role of the V promoter is a twofold. V addition increases the propene and induces active

sites for the formation of acrylic acid. W addition mainly reduces the formation of total oxidation products.

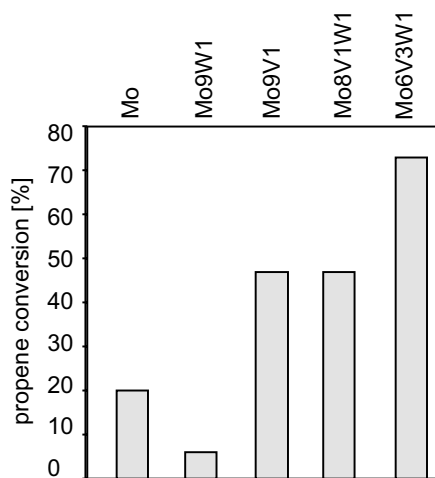


**Fig. 4.25:** Propene conversion at 716 K of all catalysts.

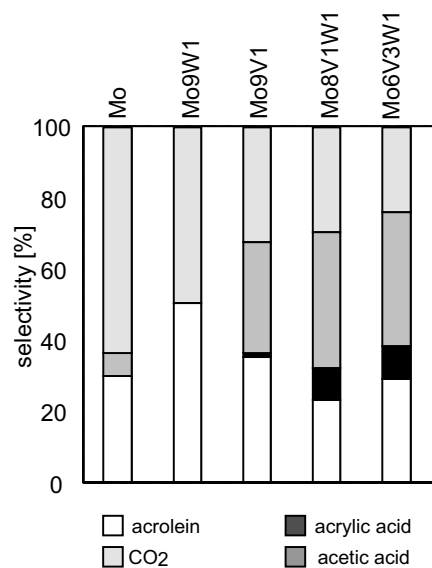
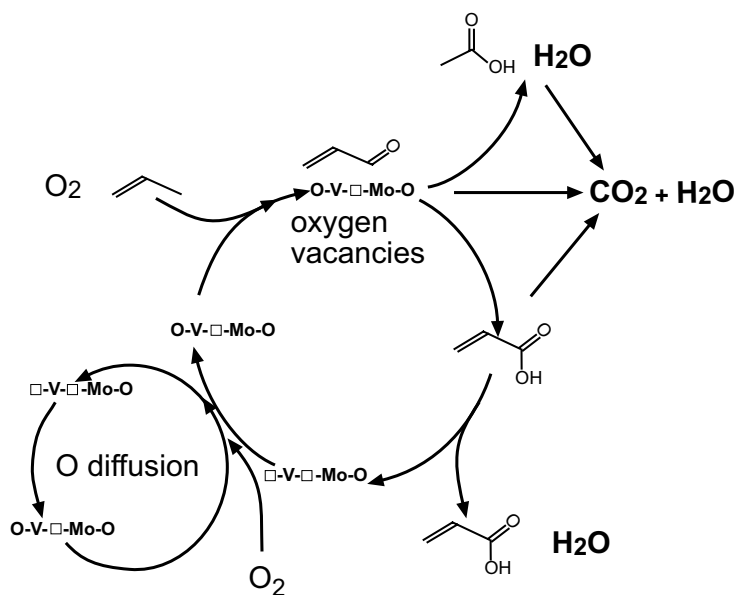


**Fig. 4.26:** Selectivities to acrolein, acrylic and acetic acid and CO<sub>2</sub> over all tested catalysts at 6 % conversion.

#### 4.2.3.2 Model for the Propene Oxidation over MoVW Oxide Catalysts

On the basis of the obtained catalytic performances of the differently promoted catalysts the propene oxidation may be described by the Scheme presented in Fig. 4.27. The primary reaction product over all catalyst samples is acrolein as proven by the high selectivity to acrolein for low propene conversions. The different propene conversions for maximum selectivities to acetic and acrylic acid indicate different active centres for the consecutive oxidation of acrolein in agreement with literature.<sup>209, 71</sup> The presence of larger oxygen vacancies clusters are seen as being strongly related to the formation of acetic acid, while the presence of the V promoter favours the formation of acrylic acid. CO<sub>2</sub> may be formed by oxidation of acrolein or the total oxidation of acetic and acrylic acid. Under the condition of high propene conversions (> 45%) *i.e.* catalysts containing V, the oxide of Mo<sub>5</sub>O<sub>14</sub> structure is formed irrespectively of the overall catalyst composition. Such high conversion are only observed for V promoted samples.

**Fig. 4.27:** Proposed schematic representation of the assumed processes over molybdenum oxide based catalysts for the propene oxidation.



The V incorporation induces a supersaturation of oxygen vacancies at the surface, which do not nucleate due to the added W. Such a stabilisation by tungsten may explain the observed increase in selectivity for the acrylic acid formation. A clear picture of the role of V, however can not be drawn. It may have a twofold influence, *e.g.* promoter induced defect generation or direct participation in the catalytic cycle.

## Chapter 5

# ***In situ* Raman Studies on Mixed Metal-Oxygen-Clusters (Mo, V, W) and Carboxylates in Aqueous Solution\***

### **5.0.4 Introduction**

Mixed transition Mo/V/W-oxide catalysts are prepared by aqueous chemistry methods such as precipitation, coprecipitation, hydro thermal synthesis or sol gel processes, which all are suited for industrial applications.<sup>261</sup> The catalyst precursor is formed via hydrolysis and/or condensation of molecular precursors, *e.g.* ammonium metalates in case of Mo, V or W oxide based catalysts. Appropriate amounts of the ammonium metalates are dissolved in water and the catalyst precursor is obtained by removal of the solvent. Subsequently the precipitate is dried, pelletised (form giving) and calcined.<sup>262</sup> Thermal activation of such a precursor as discussed in previous Sections leads to the active catalyst.

The spatial elemental distribution of mixed multielement catalysts is difficult to control<sup>1, 14, 34</sup> as already shown by SEM/EDX mapping in Section 2.1 on page 52. Spatial inhomogeneity leads to uncontrolled catalyst stoichiometry and, hence, loss in activity and selectivity. Therefore, the spatial elemental homogeneity of such mixed Mo/V/W-oxide catalysts has to be controlled more precisely. It can be assumed that already the precursor solutions (pH, metalate concentration, concentration of counter- or complexing ions) may affect the spatial elemental distribution in the solid catalyst

---

\* Parts of this Chapter will be published in M. Dieterle, G. Mestl, R. Schlögl, *In situ* Raman Studies on Mixed Metal-Oxygen-Clusters (Mo, V, W) and Carboxylates in Aqueous Solution (in preparation).

precursors due to the formation of molecularly defined polyoxometalates.

Especially group IV, V, VI transition cations exhibit a unique and complex aqueous polyoxometalate chemistry due to their similar ionic radii, their preferred high oxidation state (+V and +VI) and their comparable coordination environment.<sup>41-50</sup> The aqueous chemistry of high valent cations such as  $V^{V+}$ ,  $Mo^{VI+}$  and  $W^{VI+}$  is dominated by the formation of polyoxometalates that exhibit compact, highly symmetric molecular structures. The formation of polyoxoanions of Mo, V and W in aqueous solutions with different pH and metalate concentrations have been studied by numerous methods for the pure Mo, V and W systems.<sup>49, 50, 127, 203, 263-268</sup>



**Fig. 5.1: a.**  $[Mo_7O_{24}]^{6-}$  polyeder.

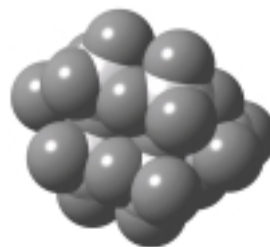


**Fig. 5.1: b.**  $[Mo_7O_{24}]^{6-}$  in a space filling representation.

The spatial homogeneity of the catalyst polyoxometalate precursors could be controlled by the stabilisation of defined mixed polyoxometalates in solution. These dissolved mixed polyoxometalate anions may be seen as preformed fragments of the metal oxide catalyst precursor.<sup>269-274</sup> The space filling representation of the heptamolybdate ion  $[Mo_7O_{24}]^{6-}$  as shown in Figure 5.1 resembles a close packed oxygen lattice. This underlines the idea of influencing the atomic arrangement of the precursor polyoxometalate and the final catalyst by defined molecularly clusters. Several authors reported NMR investigations of mixed [Mo,V,W] polyoxometalates in solution.<sup>275-277</sup>

Another concept to achieve homogeneous elemental distributions in the catalyst precursors is the stabilisation of monomeric oxometalates in order to inhibit the formation of larger isopolyoxometalates already in solution. For mixed metalate solutions with only monomeric metalate ions present in solution a statistical distribution of the different transition metals in the catalyst precursor is expected.

Either way, the different formation kinetics and stabilities of pure and mixed oxo- and polyoxometalates, which all are expected to be present in mixed metalate solutions,<sup>249, 275-277</sup>, need to be controlled in order to favour one defined species in solution. Additional complexing anions like ac-

etate, oxalate or tartrate may be useful to achieve defined species in aqueous solutions and, hence, to obtain catalysts with a well defined spatial distributions of their constituting elements.

The objective of this investigation is to study the chemistry of pure and mixed polyoxometalates in aqueous solutions by *in situ* Raman spectroscopy as a function of the solution pH. First, this investigation is focussed on the evaluation of reference data of pure metalate solutions with high  $[M^{n+}]$  concentrations, which are relevant for catalyst preparation. Further, mixed metalate solutions are investigated, to address the question, if Raman spectroscopy is suited to identify mixed polyoxometalate anions in solution. The second part of the investigation is restricted to the control of the formed polyoxometalates in pure and mixed metalate solutions by addition of complexing agents like acetate, oxalate or tartrate as a function of the solution pH.

#### 5.0.4.1 Raman spectroscopy of Polyoxometalates in Aqueous Solutions

Water is a poor Raman scatterer. Therefore, Raman spectra of polyoxometalates in solution can easily be recorded in contrast to IR spectroscopy. Many solid polyoxometalates contain discrete  $[M_xO_y]^{n-}$  units in their crystal framework.<sup>50, 278</sup> Such discrete metal oxygen clusters are observed in solution too. Hence, Raman spectra of solids may be used to identify dissolved polyoxometalates. The different electrostatic field of the counter ions in solutions and in solids and, hence, slightly different site symmetries of the metal centres lead to minor splits and shifts or changed intensity ratios of the Raman bands.

#### 5.0.4.2 Isopolyoxomolybdates in Aqueous Solution

Several authors characterised polyoxomolybdates in aqueous solutions by Raman spectroscopy.<sup>49, 126 127, 203, 243, 265, 263, 279</sup> Himeno<sup>126</sup> identified six and Griffith<sup>203</sup> four different isopolyoxomolybdates in aqueous solutions. The results of Himeno are summarised in Table 5.1 and illustrated in the predominance diagram in Figure 5.2 as taken from Ref. 280 and modified with respect to  $[Mo_8O_{26}]^{4-}$  and  $[Mo_{36}O_{112}]^{8-}$ . At pH values  $> 6.3$ , the monomeric  $MoO_4^{2-}$  exists. The Raman bands of  $MoO_4^{2-}$  are observed at 318 ( $\nu(F_2)$ ), 841 ( $\nu(F_2)$ ) and 897  $cm^{-1}$  ( $\nu(A_1)$ ). In a concerted reaction the coordination sphere is expanded from four to six and  $[Mo_7O_{24}]^{6-}$  is formed from seven  $MoO_4^{2-}$



anions. No intermediate forms exist between  $[\text{Mo}_7\text{O}_{24}]^{6-}$  and  $[\text{MoO}_4]^{2-}$ .<sup>126, 264, 281</sup>

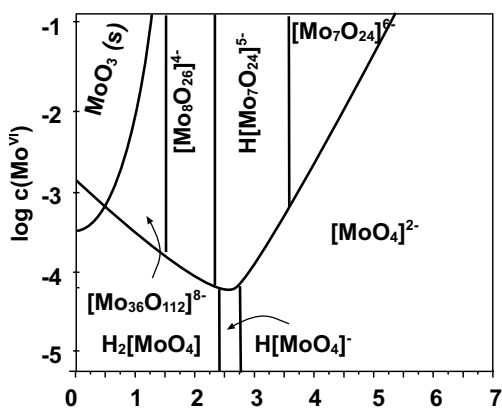


**Fig. 5.2:** Predominance diagram of the molybdate species in aqueous solutions.

$[\text{Mo}_7\text{O}_{24}]^{6-}$  is observed at pH values from 5.8 to 3.5. The Raman bands of the  $[\text{Mo}_7\text{O}_{24}]^{6-}$  anion are observed at 170, 219, 362, 422, 560, 790, 840, 903 and  $943\text{ cm}^{-1}$ .<sup>49, 193, 203, 282</sup> Himeno identified the trimolybdate  $[\text{Mo}_3\text{O}_{10}]^{2-}$  by its Raman band at  $950\text{ cm}^{-1}$  in the pH range from 4.4 to 2.9.<sup>126</sup> At lower pH values between 2.8 to 1.9 two forms of octamolybdates, *e.g.*  $\alpha$ - $[\text{Mo}_8\text{O}_{26}]^{4-}$  and  $\beta$ - $[\text{Mo}_8\text{O}_{26}]^{4-}$ , exist with Raman bands at 959 and  $971\text{ cm}^{-1}$ , respectively.

At pH values from 1.6 to 0.6 the  $[\text{Mo}_{36}\text{O}_{112}]^{8-}$  anion is the dominant species with Raman bands at 901, 955 and  $982\text{ cm}^{-1}$ . At pH values  $< 0.4$   $[\text{Mo}_2\text{O}_5]^{2+}$  is formed which shows Raman bands at 953 and  $920\text{ cm}^{-1}$ .<sup>283</sup> Finally, condensation to  $\text{MoO}_3 \cdot x\text{H}_2\text{O}$ , molybdenum acid, occurs at pH values  $< 1$ .<sup>284</sup>

polyoxomolybdate	pH range	Raman bands assigned according to Ref. 126
$[\text{MoO}_4]^{2-}$	14 - 6.5	897, 841, 318
$[\text{Mo}_7\text{O}_{24}]^{6-}$	5.8 - 3.5	943, 903, 840, 790, 560, 422, 362, 219, 170
$[\text{Mo}_3\text{O}_{10}]^{2-}$	4.4 - 2.9	950
$[\text{Mo}_8\text{O}_{26}]^{4-}$	2.8 - 1.9	971, 959
$[\text{Mo}_{36}\text{O}_{112}]^{8-}$	1.6 - 0.6	982, 955, 901

**Table 5.1:** Raman bands position for various isopolyoxomolybdates in aqueous solution (note that not all Raman bands were listed in Ref 128)

#### 5.0.4.3 Isopolyoxovanadates in Aqueous Solution

Griffith investigated the Raman spectra of aqueous vanadate solutions as a function of pH. The observed polyoxovanadate species and the positions of their Raman bands<sup>203</sup> are listed in Table 5.2. In Figure 5.3 the pH dependency of the different isopolyoxovanadates is shown as taken from

Ref. 203. Monomeric  $[\text{VO}_4]^{2-}$  exists at pH values larger than 11 with Raman bands at 827, 780 and  $340\text{ cm}^{-1}$ .<sup>44</sup> The pyrovanadate  $[\text{V}_2\text{O}_7]^{4-}$  is formed from the protonated  $[\text{HVO}_4]^-$  anion via oxolation in the pH range 14 - 11.9 and shows Raman bands at 228, 351, 503, 545, 810, 877 and  $915\text{ cm}^{-1}$ . For solutions with pH values between 9.5 to 7 the polymeric  $[\text{VO}_3]_n^{n-}$  is identified by its Raman bands at 350, 490 and  $945\text{ cm}^{-1}$ . The  $\text{V}^{\text{V}}$  cation remains tetrahedrally coordinated in all these polyoxometalates.

Coordination expansion from four to six occurs around  $\text{H}^+/\text{V} \sim 2.5$  ( $\text{pH} \sim 6$ ) as seen by the colour change to orange due to a charge transfer transition in  $\text{H}_x[\text{V}_{10}\text{O}_{28}]^{x-5}$  anions in the pH range 5 - 3. The Raman bands of the decavanadate  $[\text{V}_{10}\text{O}_{28}]^{6-}$  are located at 550, 960 and  $988\text{ cm}^{-1}$ . The decavanadate is protonated at lower pH values and the positions of the terminal  $\text{V}=\text{O}$  stretching vibrations at 960 and  $988\text{ cm}^{-1}$

of  $[\text{V}_{10}\text{O}_{28}]^{6-}$  shift by  $15\text{ cm}^{-1}$  to higher energies and are observed at 970, 995  $\text{cm}^{-1}$  and 981, 1005  $\text{cm}^{-1}$  for the protonated species  $\text{H}[\text{V}_{10}\text{O}_{28}]^{5-}$  or  $\text{H}_2[\text{V}_{10}\text{O}_{28}]^{4-}$ , respectively. The decavanadate and its protonated form are the dominant species in solutions with pH values between 8.5 to 1.5. For solutions with  $\text{pH} < 1.5$ , the  $[\text{VO}_2]^+$  exists which shows Raman bands at 380, 429, 714 and  $934\text{ cm}^{-1}$ .

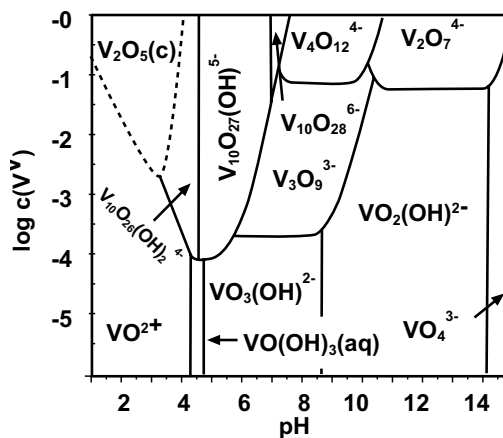


**Fig. 5.3:** Predominance diagram of the vanadate species in aqueous solutions.

polyoxovanadate	pH range	Raman bands [ $\text{cm}^{-1}$ ]
$[\text{VO}_4]^{3-}$	14	827, 780, 340
$\text{H}[\text{V}_2\text{O}_7]^{3-}$	11.9 - 8.5	915, 877, 828, 810, 545, 503, 351, 228
$[\text{VO}_3]_n^{n-}$	8.4 - 7.3	945, 490, 350
$[\text{V}_{10}\text{O}_{28}]^{6-}$	8.5 - 5.5	988, 860, 955, 920, 910, 840, 600, 543, 460, 322, 251, 210, 184
$\text{H}[\text{V}_{10}\text{O}_{28}]^{5-}$	5.5 - 1.5	994, 970, 960, 920, 840
$\text{H}_2[\text{V}_{10}\text{O}_{28}]^{4-}$	5.5 - 1.5	1005, 980, 935, 860,
$[\text{VO}_2]^+$	< 1.5	940, 920

**Table 5.2:** Raman bands for various aqueous polyoxovanadates according to Ref. 203.

#### 5.0.4.4 Isopolyoxotungstates in Aqueous Solution

The various isopolyoxotungstates in aqueous solutions and their corresponding Raman bands are listed in Table 5.3. Ostromecki et al. approximated the positions of the Raman bands from Raman spectra presented in Ref. 285 and 286 by Tytko. These have an error of approximately  $5\text{ cm}^{-1}$  because the exact Raman band positions were not reported by Tytko. The  $\text{WO}_4^{2-}$  exists at pH values larger than 7.5 and shows Raman bands at 330, 834 and  $932\text{ cm}^{-1}$ . The paratungstate-A,  $\text{HW}_6\text{O}_{21}^{5-}$ , and paratungstate-B,  $\text{HW}_{12}\text{O}_{40}^{10-}$ , ions exist at pH values between 4.5 and 2 with Raman bands at 300, 360, 650, 901, 962 and 300, 360, 650, 830, 880, and  $955\text{ cm}^{-1}$ , respectively. The metatungstate U ion of unknown stoichiometry exists at pH values between 3 and 4 with Raman bands at 360, 650, 900 and  $969\text{ cm}^{-1}$ . The metatungstate,  $\text{HW}_{12}\text{O}_{42}^{10-}$ , and polytungstate-Y,  $\text{W}_{10}\text{O}_{32}^{4-}$ , ions exist at pH values from 3 to 1 with Raman bands at 650, 900, 961,  $978\text{ cm}^{-1}$  and 400, 600, 830, 900, 972,  $988\text{ cm}^{-1}$ , respectively.

isopolyoxotungstate ions	pH range	Raman bands [ $\text{cm}^{-1}$ ]
$\text{WO}_4^{2-}$	>7.5	932, 834, 330
$\text{HW}_6\text{O}_{21}^{5-}$	4.5 - 2	962, 901, 650, 360, 300
$\text{HW}_{12}\text{O}_{42}^{10-}$	4.5 - 2	955, 880, 830, 650, 360, 300
(no formula)	3 - 4	969, 900, 650, 360
$\text{H}_2\text{W}_{12}\text{O}_{40}^{6-}$	3 - 1	978, 961, 900, 650
$\text{W}_{10}\text{O}_{32}^{4-}$	3 - 1	988, 972, 900, 830, 600, 400

**Table 5.3:** Raman bands position for various isopolyoxotungstates in aqueous solution (note that not all Raman bands were listed in Ref. 126)

Reports do not agree on the exact pH values at which each of the isopolyoxometalate ions exist in solution, which may be explained by different experimental conditions.<sup>126, 287</sup> However, there is a general agreement on the existence and pH dependence of most species found in Mo, V or W metalate solutions.<sup>126, 203, 280, 288</sup>

#### 5.0.4.5 Assignment of Raman Bands

There is general agreement on the basic assignment of the observed Raman bands of polyoxometalates  $\text{M}=(\text{Mo}, \text{V}, \text{W})$  of certain vibrations.<sup>203, 287</sup> The assignments is based on the structure of the

isopolyoxometalates built by of  $\text{MO}_6$  octahedra, while the monomeric  $\text{MO}_4^{n-}$  ions are tetrahedrally coordinated.<sup>279, 289</sup> The  $\text{MO}_4^{n-}$  anion of  $T_d$  symmetry is expected to show four Raman active vibrations ( $A_1$ , 2  $F_2$  and E). Only three vibrations are observed, which is explained by an unresolved doublet.<sup>290</sup> These vibrations are due to the symmetric stretch ( $A_1$ ), antisymmetric stretch ( $F_2$ ), and two bending modes (E, $F_2$ ).<sup>287</sup>

For the polyoxometalate with  $\text{MO}_6$  building units, the Raman bands above  $900\text{ cm}^{-1}$  are attributed to M=O stretches of the  $\text{MO}_6$  units, bands near  $300\text{--}400\text{ cm}^{-1}$  are the corresponding bending modes of these M=O groups. Bands in the  $800\text{--}900\text{ cm}^{-1}$  regime are due to symmetric O-M-O stretches, bands in the  $600\text{--}400\text{ cm}^{-1}$  range are assigned to M-O-M symmetric stretches, and bands near  $200\text{ cm}^{-1}$  are due to M-O-M bending modes.<sup>287, 291</sup>

For all polyoxometalates in aqueous solutions the Raman bands due to the symmetric stretching vibration of the terminal M=O groups systematically increase in frequency with higher pH values. The stretching frequency of the terminal M=O groups of polyoxometalates is a linear function of the negative charge per  $[\text{MO}_6]^{x-}$  unit with  $M=[\text{V}, \text{Mo}, \text{W}]$  as shown in Figure 5.4. This linear relationship is explained by the influence of the negative charges on the displacement of the cation from the centre of symmetry and, therefore, on the bond strength of the terminal M=O bond. The negative charge of a polyoxometalate are preferably located at the terminal oxygen atoms as shown by X-ray structure investigations.<sup>214, 292-294</sup> A

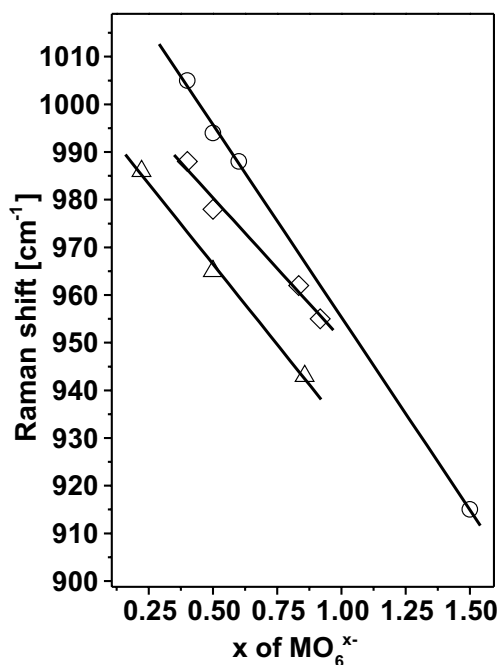


**Fig. 5.4:** Frequency of the terminal M=O stretching vibration as a function of the charge per metal cation for different isopolyoxometalates ( $M=\text{Mo } \triangle, \text{V } \circ$  and  $\text{W } \diamond$ ).

higher negative charge per  $[\text{MO}]^{n-}$  of a given polyoxometalate, hence, leads to a higher symmetric metal coordination. Hence, the terminal M=O bond is weakened and its Raman band is shifted to lower energies as experimentally observed (Figure 5.4). Therefore, this relation may be used for *in situ* Raman studies to distinguish between structural changes (new Raman bands arise) and gradual protonation of already existing polyoxoanions (continuous shift of the M=O stretching frequency

to higher energies). In contrast to the Hardcastle-Wachs model<sup>93</sup> this linear relationship is based on data from solids with molecularly defined units and explained by changes of physico-chemical properties of these units. The estimated energy of the M=O stretching vibration for a neutral polyoxo Mo complex - like  $\text{MoO}_3$  - is calculated to be  $1000\text{ cm}^{-1}$ , which compares well with the experimental value of  $995\text{ cm}^{-1}$ .<sup>30</sup> This points to a general validity of such a relation for polyoxometalates.<sup>30</sup>

## 5.1 Experimental

All Raman spectra were recorded with a DILOR LABRAM I spectrometer equipped with a confocal microscope (Olympus) as shown in Figure 5.5. The entrance slits were usually set to  $200\text{ }\mu\text{m}$ , giving a spectral resolution of  $2\text{ cm}^{-1}$ . A He-laser ( $632.8\text{ nm}$ , Melles Griot) was used for excitation of the Raman spectra. The laser power was  $14\text{ mW}$ . The laser was focused on a point about  $1\text{ mm}$  below the surface of the solution by a  $10\times$  objective lens (Olympus).

All Raman spectra were recorded in backscattering geometry. Two spectra were averaged with acquisition times of usually 40 seconds per spectrum. In order to compare the obtained Raman spectra as a function of the solution pH, all Raman spectra have been normalised to unity with respect to the strongest and weakest intensity in the energy range  $800 - 1020\text{ cm}^{-1}$ . For better visualisation of the Raman spectra and their pH dependency, the spectra have been vertically shifted by a amount similar to the pH value corrected for the found intensity at  $1020\text{ cm}^{-1}$  of the corresponding solution. In such Figures the intensity of the vertically shifted Raman spectra at  $1020\text{ cm}^{-1}$  corresponds to the pH values at data acquisition time.

For each experiment,  $250\text{ ml}$  of ammonium metalate solutions were titrated in a  $500\text{ ml}$  vessel. The solutions were continuously pumped into a second vessel ( $30\text{ ml}$ ), which was placed into third vessel ( $150\text{ ml}$ ) under the microscope. The liquid surface and, thus, the focus of the microscope was kept constant by the continuous overflow from the second into the third vessel. The solutions were then pumped back to the first vessel. This setup was favoured over a setup using an commercial UV/VIS spectroscopy quartz cell. Small gas bubbles, in the UV/VIS cell rendered it impossible to continuously obtain Raman spectra over long time periods.

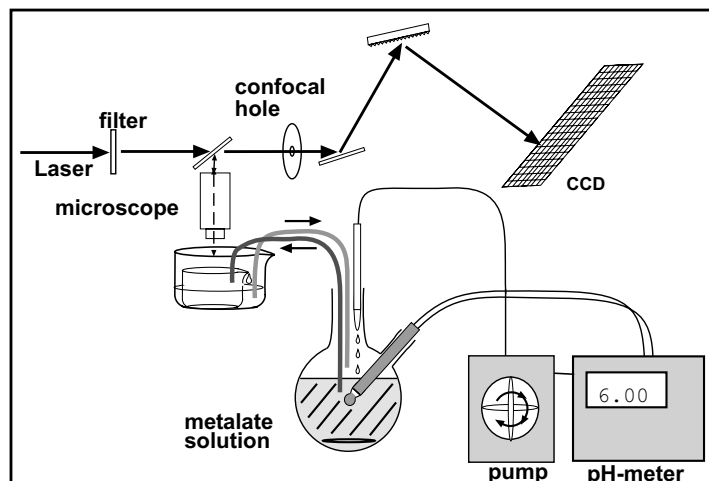


**Fig. 5.5:** *In situ Raman setup for the detection of the aqueous poly-oxometalate species.*

Commercial ammonium heptamolybdate (AHM, Merck, p.a.) and ammonium metatungstate (AMW, Merck, p.a.) and ammonium metavanadate (AMV, Merck, p.a.) and de-ionised water were used to prepare the solutions. The pH of the solutions was determined with a Metrohm 686 titrator during the titration with conc.  $\text{HNO}_3$ . Prior to each titration experiment the pH-electrode was calibrated with commercial pH 7 and pH 3 buffer solutions (Merck). The rate of  $\text{HNO}_3$  addition was 0.05 ML/min for all experiments on pure metalate solutions and 0.02 ml/min for mixed metalate/carboxylate solutions. The titration speed was reduced in order to follow changes of the C=O stretching vibration region and the Raman spectral range had to be extended to  $1800\text{ cm}^{-1}$ . The total metalate concentration was 0.5 M for all experiments. Stoichiometric amounts (*e.g.* 0.5 M solution) of ammonium acetate, oxalate or tartrate were added in case of the mixed metalate/carboxylate solutions (concentrations are referenced to monomeric species).

Table 5.0 lists the five experiment series:

- |                        |                        |                       |
|------------------------|------------------------|-----------------------|
| 1. molybdate solutions | 2. tungstate solutions | 3. vanadate solutions |
| a. pure Mo solution    | a. pure W solution     | a. pure V solution    |
| b. Mo/acetate          | b. W/acetate           | b. V/acetate          |
| c. Mo/oxalate          | c. W/oxalate           | c. V/oxalate          |
| d. Mo/tartrate         | d. W/tartrate          | d. V/tartrate         |

- |  |  |
|--|--|
| <p>4. mixed Mo/V and Mo/W solutions</p> <p>a. Mo9V1 (90%Mo, 10% V)</p> <p>b. Mo9W1 (90% Mo, 10% W)</p> | <p>5. mixed Mo/V/W solutions</p> <p>a. Mo6V3W1(60% Mo, 30%V, 10% W )</p> <p>b. Mo6V3W1/acetate</p> <p>c. Mo6V3W1/oxalate</p> <p>d. Mo6V3W1/tartrate.</p> |
|--|--|

**Table 5.0:** *List of the five experimental series.*

## 5.2 Results and Discussion

### 5.2.1 Pure Molybdate Solutions

The Raman spectra of 0.5 M ammonium molybdate solution are shown in Figure 5.6. The Raman bands at 317, 382, 829 and 896  $\text{cm}^{-1}$  indicate  $[\text{MoO}_4]^{2-}$  in solutions with pH values  $> 6$ . At pH 7.0, the Raman bands of  $[\text{Mo}_7\text{O}_{24}]^{6-}$  show up at 940  $\text{cm}^{-1}$  and replace those of the  $[\text{MoO}_4]^{2-}$ . Upon further acidification the Raman band at 940  $\text{cm}^{-1}$  shifts to higher energies by 9  $\text{cm}^{-1}$  and is located at 949  $\text{cm}^{-1}$  at pH 4.7. The Raman spectrum of the solution with pH 4.7 shows Raman bands at 367, 386, 833, 909 and 949  $\text{cm}^{-1}$  and is attributed to  $\text{H}[\text{Mo}_7\text{O}_{24}]^{5-}$ . This spectrum is observed for solutions with pH values between 4.7 and 3.6. The shift of the terminal M=O vibration is attributed to the protonation of the  $[\text{Mo}_7\text{O}_{24}]^{6-}$  anion. The position for the  $\text{H}[\text{Mo}_7\text{O}_{24}]^{5-}$  anion is calculated to be 952  $\text{cm}^{-1}$  from the linear relationship between the negative charge per Mo and the energy of the M=O stretching vibration as shown in Figure 5.4. However, a band at 952  $\text{cm}^{-1}$  is not observed. This has its reason in the fast consecutive transformation of  $\text{H}[\text{Mo}_7\text{O}_{24}]^{5-}$  to  $[\text{Mo}_8\text{O}_{26}]^{4-}$  which is more stable at high  $[\text{H}^+]$  concentrations due to its lower negative charge per Mo as compared to  $\text{H}[\text{Mo}_7\text{O}_{24}]^{5-}$ . At pH 3.6 new Raman bands arise which replace those of the  $\text{H}[\text{Mo}_7\text{O}_{24}]^{5-}$ . The Raman spectra of the solutions in the pH range 3.6 - 1.9 show bands at 368, 386, 714, 843, 918, 935, 950, 958 and 970  $\text{cm}^{-1}$ . These bands are attributed to the  $\alpha$ - and  $\beta$ - $[\text{Mo}_8\text{O}_{26}]^{4-}$  anions.<sup>126</sup> The Raman band at 958  $\text{cm}^{-1}$  identifies the  $\alpha$ - $[\text{Mo}_8\text{O}_{26}]^{4-}$  while the Raman band at 970  $\text{cm}^{-1}$  proves the  $\beta$ - $[\text{Mo}_8\text{O}_{26}]^{4-}$  anion to be present.<sup>126</sup> The Raman bands observed for solutions with pH values between 1.7 and 0.8 Raman are located at 367, 382, 828, 846, 900, 918, 955 and 981  $\text{cm}^{-1}$ . These new bands have their origin in the formation of the  $[\text{Mo}_{36}\text{O}_{112}]^{8-}$  anion.<sup>295</sup> At pH values  $<$

0.9 the Raman band at  $981\text{ cm}^{-1}$  vanishes and Raman bands are found at  $381$ ,  $718$ ,  $820$ ,  $922$  and  $952\text{ cm}^{-1}$ . The Raman bands at  $922$  and  $955\text{ cm}^{-1}$  identify the  $[\text{Mo}_2\text{O}_5]^{2+}$  cation and these bands are attributed to the asymmetric and symmetric stretching modes of the  $[\text{Mo}_2\text{O}_5]^{2+}$ .<sup>296</sup> The above data are in good agreement with data from Himeno or Griffith. However, the  $[\text{Mo}_3\text{O}_{10}]^{2-}$  anion which was proposed by Himeno could not be identified. Moreover, the observed Raman band at  $949\text{ cm}^{-1}$ , which Himeno interpreted as characteristic for the  $[\text{Mo}_3\text{O}_{10}]^{2-}$  anion is attributed to the  $\text{H}[\text{Mo}_7\text{O}_{24}]^{5-}$  anion because of the continuous shift of the  $\text{Mo}=\text{O}$  stretching vibration between  $939$  and  $949\text{ cm}^{-1}$  due to the increasing protonation of the  $[\text{Mo}_7\text{O}_{24}]^{6-}$  anion.

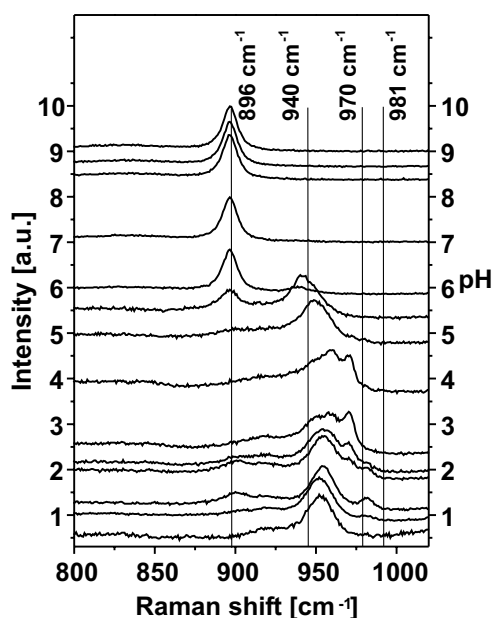


**Fig. 5.6:** Selected Raman spectra recorded during the titration of a  $0.5\text{ M}$  AHM solution. Spectra are normalised and vertically shifted for better visualisation. The intensity at  $1020\text{ cm}^{-1}$  corresponds to the pH value of the solution.

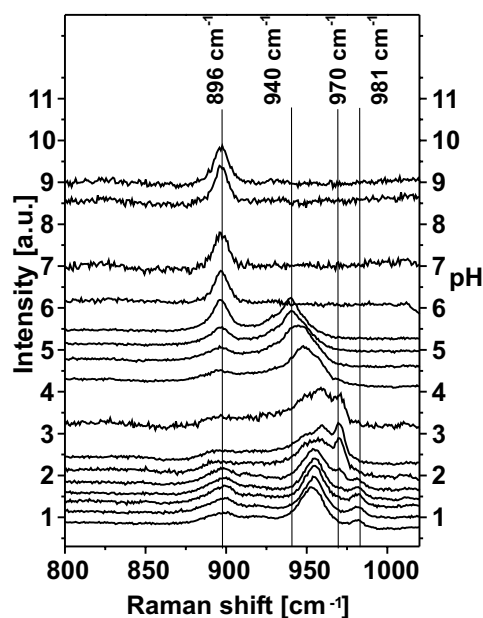


**Fig. 5.7:** Selected Raman spectra recorded during the titration of a mixed solution of AHM ( $0.5\text{ M}$ ) and ammonium acetate ( $0.5\text{ M}$ ). Spectra are normalised and vertically shifted for better visualisation. The intensity at  $1020\text{ cm}^{-1}$  corresponds to the pH value of the solution.

## 5.2.2 Mixed Mo/Carboxylate Solutions

For the mixed metalate/carboxylate solutions, the Raman spectra have been recorded in the spectral range from  $250$  to  $1800\text{ cm}^{-1}$ . The Raman band positions and the intensity ratios of the Raman bands of the acetate, oxalate or tartrate remain unchanged throughout the experiments. Therefore, a description or discussion of their Raman spectra is omitted.



### 5.2.2.1 Mo/Ammonium Acetate Solution

The Raman spectra of the mixed molybdate/acetate solution are shown in Figure 5.7 in the energy range from 800 to 1020  $\text{cm}^{-1}$ . The obtained Raman spectra resemble those of the pure solution. The Raman bands of the  $[\text{MoO}_4]^{2-}$ ,  $[\text{Mo}_8\text{O}_{26}]^{4-}$ ,  $[\text{Mo}_{36}\text{O}_{112}]^{8-}$

point group	$\nu_1$	$\nu_2$	$\nu_3$	$\nu_4$
$T_d$	$A_1$	E	$F_2$	$F_2$
$C_{3v}$	$A_1$	E	$A_1 + E$	$A_1 + E$
$C_{2v}$	$A_1$	$A_1 + A_2$	$A_1 + B_1 + B_2$	$A_1 + B_1 + B_2$
$C_1$	A	2A	3A	3A

**Table 5.1:** Correlation Table for  $T_d$ ,  $C_{3v}$ ,  $C_{2v}$  and  $C_1$ .<sup>37</sup>

and  $[\text{Mo}_7\text{O}_{24}]^{6-}$  anions are located at the same positions as compared to the pure AHM solution. However, minor changes are observed of the pH dependency of the different species. For pH values  $> 3.8$ ,  $\text{MoO}_4^{2-}$  is observed, while in the pH regime from 5.68 to 2.31, from 4.13 to 1.43, and at pH  $< 1.65$  the  $[\text{Mo}_7\text{O}_{24}]^{6-}$ ,  $[\text{Mo}_8\text{O}_{26}]^{4-}$  and  $[\text{Mo}_{36}\text{O}_{112}]^{8-}$  are positively identified, respectively. A weak additional Raman band at is observed 930  $\text{cm}^{-1}$  in the pH range from 9 to 4.2, which was not observed for the pure molybdate solution. This Raman band may tentatively be assigned to a  $[\text{MoO}_x\text{Ac}_y]^{n-}$  species. However, this assignment is ambiguous at this point because this Raman band gains intensity with the occurrence of the  $[\text{Mo}_7\text{O}_{24}]^{6-}$  anion. Therefore, it may be assigned to a new symmetry split Raman band of the  $[\text{Mo}_7\text{O}_{23}(\text{ac})]^{5-}$  complex too. However, a comparison with mixed Mo/oxalate or Mo/tartrate solutions (vide infra) revealed that this new band may be assigned to a monomeric molybdate-acetate complex.

### 5.2.2.2 Mo/Ammonium Oxalate Solution

The Raman spectra of the mixed molybdate/oxalate solution are presented in Figure 5.8. The Raman spectra obtained from the molybdate/oxalate solution differ remarkably from those of the pure molybdate and molybdate/acetate solutions. Because of a overlap between the Raman band at 897  $\text{cm}^{-1}$  and a new band at 905  $\text{cm}^{-1}$  (vide infra), an ambiguous assignment of the former Raman band to the  $[\text{MoO}_4]^{2-}$  is not possible. But the weak Raman band at 830  $\text{cm}^{-1}$  proves the  $[\text{MoO}_4]^{2-}$  anion to be present in solutions with a pH  $> 2.43$ . At a pH of 6.36, new intense Raman bands arise at 860, 905 and 914  $\text{cm}^{-1}$ . These Raman bands are observed for solutions in the pH regime from 6.36 to 2.43. At pH 3.98, Raman bands are observed at 308, 381, 830, 860, 897(sh), 905 and

914 cm<sup>-1</sup>. Raman bands at 308, 860, 905 and 914 cm<sup>-1</sup> have not been observed for pure molybdate solutions.

A comparison of these band positions with those of the [MoO<sub>4</sub>]<sup>2-</sup> suggests a [MoO<sub>4</sub>]<sup>2-</sup> structure of lower symmetry, and, hence, symmetry split Raman bands. The substitution of one oxo ligand by one carboxylate leads to a symmetry reduction from T<sub>d</sub> to C<sub>3v</sub>. Due to this symmetry reduction, only the ν<sub>3</sub>(F<sub>2</sub>) and ν<sub>4</sub>(F<sub>2</sub>) vibrations are expected to split into two Raman active modes of A<sub>1</sub> and E symmetry (see Table 5.1). Therefore, a split is expected for the [MoO<sub>3</sub>(ox)]<sup>-</sup> complex of the two ν<sub>1</sub> and ν<sub>3</sub> Raman bands of the [MoO<sub>4</sub>]<sup>2-</sup> into three Raman bands in the high energy range.

For the monodentate *cis* [MoO<sub>2</sub>(ox)<sub>2</sub>] and bidentate [MoO<sub>2</sub>(ox)]<sup>-</sup> complexes symmetry splits are

expected into four Raman bands (2A<sub>1</sub>, B<sub>1</sub> and B<sub>2</sub>) in the high energy range due to the symmetry reduction from T<sub>d</sub> to C<sub>2v</sub>. Therefore, the three new Raman bands at 860, 905 and 914 cm<sup>-1</sup> are assigned to an [MoO<sub>3</sub>(ox)]<sup>-</sup> complex. At pH < 3.17, Raman bands arise at 378, 541, 719, 828, 912 and 947 cm<sup>-1</sup>, which replace the Raman bands at 308, 381, 830, 860, 905 and 914 cm<sup>-1</sup>. This observed Raman band at 947 cm<sup>-1</sup> points to the presence of the H[Mo<sub>7</sub>O<sub>24</sub>]<sup>5-</sup>. However, the H[Mo<sub>7</sub>O<sub>24</sub>]<sup>5-</sup> should not be stable at high [H<sup>+</sup>] concentrations. A neutral H[MoO<sub>3</sub>(ox)] complex could as well be the origin of the observed Raman spectra at these pH values and seems to be more reasonable than the negatively charged H[Mo<sub>7</sub>O<sub>24</sub>]<sup>5-</sup> anion.

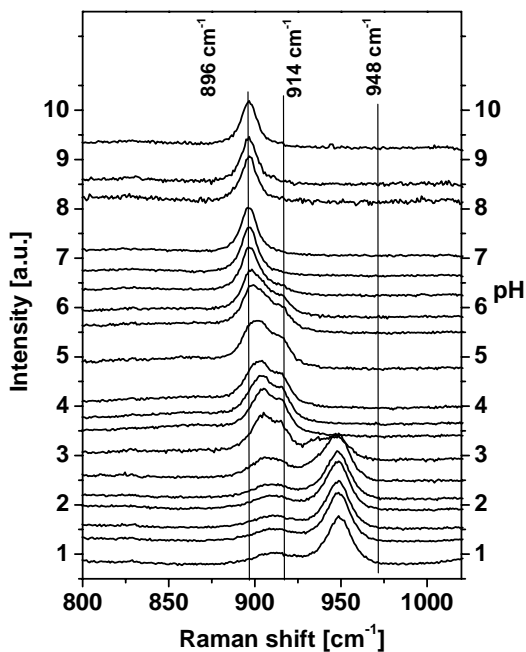


**Fig. 5.8:** Selected Raman spectra recorded during the titration of a mixed solution of AHM (0.5 M) and ammonium oxalate (0.5 M). Spectra are normalised and vertically shifted for better visualisation. The intensity at 1020 cm<sup>-1</sup> corresponds to the pH value of the solution.

### 5.2.2.3 Mo/Ammonium Tartrate Solution

The Raman spectra of the mixed molybdate/tartrate solution are shown in Figure 5.9. The Raman bands of the [MoO<sub>4</sub>]<sup>2-</sup> anion are observed in solution with pH > 5.1. At pH 6.66, new Raman

bands arise at 308, 385, 557, 716, 826, 896 and 934  $\text{cm}^{-1}$  and gradually replace the Raman bands of the  $[\text{MoO}_4]^{2-}$  anion. These Raman bands are observed in the pH range from 6.66 to 1.53 and a gradual shift by 6  $\text{cm}^{-1}$  of the Raman band at 934 to 940  $\text{cm}^{-1}$  is observed in this pH regime. At  $\text{pH} < 1.53$ , an additional shift of the band at 940  $\text{cm}^{-1}$  by 6  $\text{cm}^{-1}$  is observed and the Raman bands are located at 307, 380, 556, 716, 902 and 946  $\text{cm}^{-1}$  at  $\text{pH}$  0.73.

The observed Raman bands between 934 and 946  $\text{cm}^{-1}$  may be attributed to the  $[\text{Mo}_7\text{O}_{24}]^{6-}$  (lower frequencies) and  $\text{H}[\text{Mo}_7\text{O}_{24}]^{5-}$  (higher frequencies) anion. However, all the reported Raman band positions of the stretching  $\text{M}=\text{O}$  vibration of the  $[\text{Mo}_7\text{O}_{24}]^{6-}$  anion in aqueous solutions are in the energy range from 939 to 944  $\text{cm}^{-1}$ .<sup>127, 281, 287, 288</sup> The Raman bands of the  $\text{H}[\text{Mo}_7\text{O}_{24}]^{5-}$  have not been reported in the literature but the energy of the terminal  $\text{Mo}=\text{O}$  vibration is expected to be 952  $\text{cm}^{-1}$  (see Figure 5.4 on page 147). For a given polyoxometalate  $[\text{MoO}_{x-y}(\text{tart})_y]^{y-n}$ , the positions of the terminal  $\text{M}=\text{O}$  vibration are expected to be located at higher energies as compared to the tartrate free compound due to the lower negative charge per Mo of the tartrate free complex. Therefore, the observed vibration at 934  $\text{cm}^{-1}$  cannot be explained by a  $[\text{Mo}_7\text{O}_{24-y}(\text{tart})_y]^{y-6}$  complex.

However, a monodentate  $[\text{MoO}_3(\text{tart})_2]$  complex or a bidentate  $[\text{MoO}_2(\text{tart})]$  complex could reasonably explain the observed solution Raman spectra in the pH range from 6.66 to 1.53. Because of the symmetry reduction from  $T_d$  to  $C_{2v}$  upon exchange of two oxo ligands of the  $[\text{MoO}_4]^{2-}$  anion by tartrate a symmetry split of the four Raman lines of  $[\text{MoO}_4]^{2-}$  into nine of the  $[\text{MoO}_2(\text{tart})_2]^-$  or  $[\text{MoO}_2(\text{tart})]$  is expected. In the high energy range the  $\nu_3$  mode splits into three modes ( $A_1$ ,  $B_1$  and  $B_2$ ) and a total of four Raman lines is expected for the 600 - 1000  $\text{cm}^{-1}$  energy range. Therefore the observed Raman bands at 716 ( $\nu_3$ ), 826 ( $\nu_3$ ), 896 ( $\nu_3$ ) and 934 ( $\nu_1$ )  $\text{cm}^{-1}$  may be interpreted as one

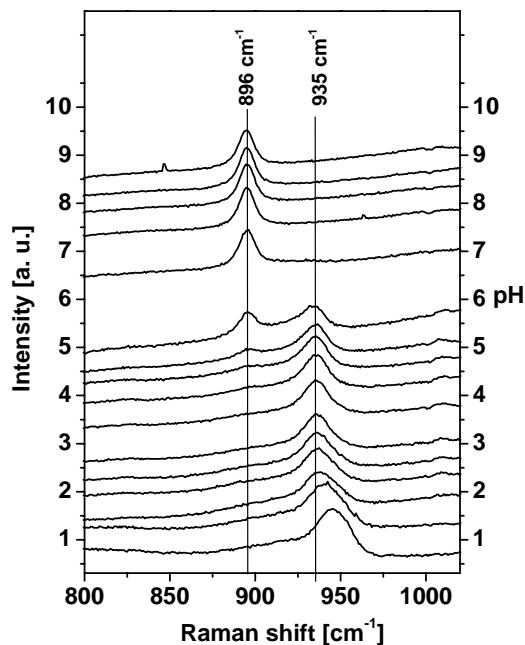


**Fig. 5.9:** Selected Raman spectra recorded during the titration of a mixed solution of AHM (0.5 M) and ammonium tartrate (0.5 M). Spectra are normalised and vertically shifted for better visualisation. The intensity at 1020  $\text{cm}^{-1}$  corresponds to the pH value of the solution.

$\nu_1$  and three symmetry split  $\nu_3$  modes of a tartrate complex. The observation that the total number of observed Raman bands is smaller than the expected nine, is explained by unresolved splittings or weak intensities.

A distinction between monodentate and bidentate tartrate complexes is not possible merely due to observed number of Raman bands and the assumption of a *cis* arrangement of the different ligands. However, the observation that additional polyoxomolybdates are not formed strongly suggests the presence of the neutral, bidentate tartrate complex  $[\text{MoO}_2(\text{tart})]$ . Under the assumption of a monodentate  $[\text{MoO}_2(\text{tart})_2]$  complex, the added stoichiometric amount of ammonium tartrate could only complexate one half of the Mo cations. Therefore, additional Raman bands due the formation of polyoxomolybdates should be expected. Because this is not observed, it is concluded that the tartrate complex  $[\text{MoO}_2(\text{tart})]$  exists in solution in the pH range from 6.6 to 1.5 with Raman bands at 308, 385, 557, 716, 826, 896 and  $934\text{ cm}^{-1}$ . This is further supported by the observation, that Raman bands characteristic for polymeric polyoxomolybdates around  $250\text{ cm}^{-1}$  due to the bending vibrations of Mo-O-Mo bridges are not observed. The good agreement of the positions of the low energy Raman bands obtained from solutions with pH values smaller 1.5 with those of  $[\text{MoO}_2(\text{tart})]$  points to the protonation of the tartrate complex. Therefore, it is concluded that at pH values below 1.5 the protonated tartrate complex  $\text{H}[\text{MoO}_2(\text{tart})]^+$  is formed with Raman bands at 307, 380, 556, 716, 902 and  $946\text{ cm}^{-1}$ .

In very acidic solutions with  $\text{pH} < 1.53$ , a shift of the high energy bands at 896 and  $940\text{ cm}^{-1}$  is observed, while the positions of the other Raman bands at 307, 380, 556, 716 and  $826\text{ cm}^{-1}$  remain unchanged. This points to further protonation of the tartrate complex under very acidic conditions.

The formation of carboxylate complexes has a strong impact on the formation of larger polyoxoanions. For the Mo/oxalate and Mo/tartrate solutions the high stability of the monomeric complexes suppresses the condensation to larger polyoxometalates. Even in presence of acetate where a Mo-acetate complex could not be unambiguously be identified, the condensation to larger polyoxometalates appears to be less favoured.

### 5.2.3 Pure Vanadate Solutions

The Raman spectra of the pure vanadate solutions are shown in Figure 5.10. The observed Raman bands at 352, 826, 870, 916, and 944  $\text{cm}^{-1}$  of solutions with pH values  $> 9.0$  are attributed to  $[\text{VO}_4]^{3-}$  (Raman band at 827  $\text{cm}^{-1}$ ) and  $\text{H}[\text{V}_2\text{O}_5]^{3-}$  (Raman bands at 870 and 916  $\text{cm}^{-1}$ ) and  $[\text{VO}_3]_n^{n-}$  (Raman band at 945  $\text{cm}^{-1}$ ). At pH 9.66, new Raman bands arise at 318, 377, 601, 716, 827, 948, 960 and 988  $\text{cm}^{-1}$  which gradually replace the former Raman bands.

These new Raman bands are attributed to the  $[\text{V}_{10}\text{O}_{28}]^{6-}$  anion, which is observed in the pH range from 9.66 to 7.79 pH. In the pH regime from 7.79 to 6.11, a shift is observed of the bands at 960 and 988  $\text{cm}^{-1}$  by 12 and 13  $\text{cm}^{-1}$  to 971  $\text{cm}^{-1}$  and 999  $\text{cm}^{-1}$ , which is due to the protonation of the decavanadate to  $\text{H}[\text{V}_{10}\text{O}_{28}]^{5-}$ . At pH 6.11, Raman bands are observed at 315, 369, 381, 395, 591, 715, 829, 971 and 999  $\text{cm}^{-1}$ . A shift of the bands at 971 and 999  $\text{cm}^{-1}$  to 977 and 1002  $\text{cm}^{-1}$  between pH 6.1 to 1.3 indicates a lower formal charge of the polyoxovanadate due a further protonation. At pH 4.0, Raman bands are observed at 312, 587, 830, 977 and 1002  $\text{cm}^{-1}$ , which are interpreted as the Raman bands of  $\text{H}_2[\text{V}_{10}\text{O}_{28}]^{4-}$ . New Raman bands arise at 382, 430, 717, 914 and

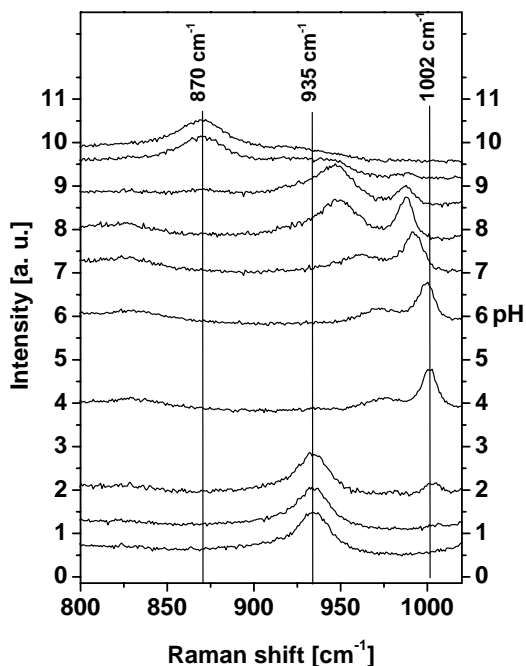


**Fig. 5.10:** Selected Raman spectra recorded during the titration of a MV solution (0.5 M). Spectra are normalised and vertically shifted for better visualisation. The intensity at 1020  $\text{cm}^{-1}$  corresponds to the pH value of the solution.

935  $\text{cm}^{-1}$  at a pH value of 2.6, which replace those of the  $\text{H}_2[\text{V}_{10}\text{O}_{28}]^{4-}$ . These Raman bands are interpreted as being due to  $\text{cis}[\text{VO}_2(\text{NO}_3)_4]^{3-}$ . The corresponding bands of the  $\text{cis}[\text{VO}_2]^{+}$  group in  $\text{cis}(\text{NH}_4)_3[\text{VO}_2\text{Cl}_4]$  and  $\text{cis}(\text{NH}_4)_3[\text{VO}_2\text{F}_4]$  are located at 914, 940  $\text{cm}^{-1}$  and 890, 928  $\text{cm}^{-1}$ , respectively.<sup>287</sup> The positions of the Raman bands of the terminal V=O vibrations increase from 928, 935 to 940  $\text{cm}^{-1}$  for  $\text{cis}(\text{NH}_4)_3[\text{VO}_2\text{F}_4]$ ,  $\text{cis}[\text{VO}_2(\text{NO}_3)_4]^{3-}$  to  $\text{cis}(\text{NH}_4)_3[\text{VO}_2\text{Cl}_4]$ , respectively. The hard acids and soft bases (HSAB)<sup>40</sup> concept may explain the observed order and underline the assignment of the Raman bands at 914 and 935  $\text{cm}^{-1}$  to the  $\text{cis}[\text{VO}_2(\text{NO}_3)_4]^{3-}$ . The small, high

valent  $V^{5+}$  cation is a hard Lewis acid.<sup>40</sup> The hardness of the corresponding Lewis bases decreases in the order  $F^-$ ,  $NO_3^-$  and  $Cl^-$  and accordingly decreases the interaction with  $V^{V+}$ . The smaller this interaction is the stronger are the remaining V-O bonds. This is experimentally seen by the shift of the Raman band positions to higher energies.

## 5.2.4 Mixed V/Carboxylate Solutions

### 5.2.4.1 Vanadate/Ammonium Acetate Solution

Characteristic Raman spectra of the mixed vanadate/ammonium acetate solution are shown in Figure 5.11. As compared to the pure vanadate solution remarkable differences are observed over the whole pH range. Weak Raman bands of  $[VO_3]_n^{n-}$  and  $H[V_2O_7]^{3-}$  are observed for solutions with pH values  $> 9.81$ . The Raman bands at 986, 996 and 1005  $cm^{-1}$  positively identify  $[V_{10}O_{28}]^{6-}$ ,  $H[V_{10}O_{28}]^{5-}$  and  $H_2[V_{10}O_{28}]^{4-}$  anions comparable to pure vanadate solutions. These anions are observed in the pH regimes from 9.81 to 5.37, from 5.37 to 1.65, and from 1.65 to 0.99, respectively. In the pH range from 10 to 1.2, Raman bands are observed at 375, 433, 494, 648, 829, 869, 896, 915, and 927  $cm^{-1}$  of a new species, which was not detected in pure solutions.

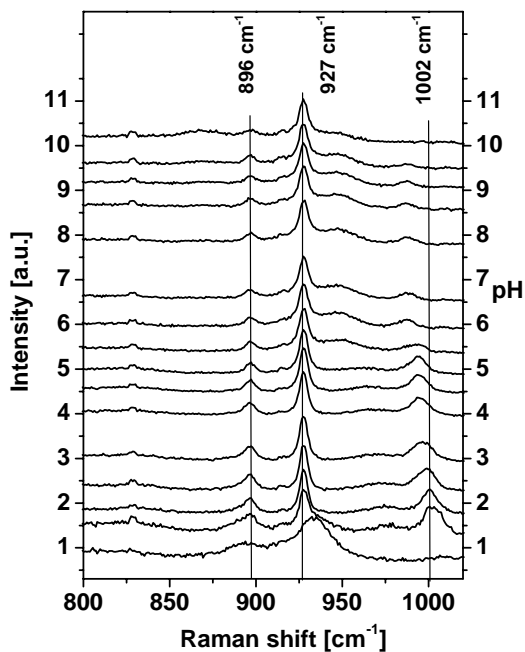


**Fig. 5.11:** Selected Raman spectra recorded during the titration of a mixed solution of AMV (0.5 M) and ammonium acetate (0.5 M). Spectra are normalised and vertically shifted for better visualisation. The intensity at 1020  $cm^{-1}$  corresponds to the pH value of the solution.

The absence of these bands in pure solutions suggest a vanadate-acetate complex to be present. Due to symmetry splittings caused by ligand exchange, as shown above a total of six and nine Raman lines should be expected for the  $[VO_3(ac)]^{2-}$  and  $[VO_2(ac)_2]^-$  complexes. Therefore, the observed nine Raman bands are attributed to the  $[VO_2(ac)_2]^-$  complex.

The observation of these Raman bands over a wide pH range points to a high stability. This high stability and the coexistence of polyoxo vanadates further support the assignment of the observed

Raman bands to the acetate complex  $[\text{VO}_2(\text{ac})_2]^-$ . Because the added stoichiometric amount of ammonium acetate complexates only one half of the metal cations additional polyoxovanadates should be formed if a  $[\text{VO}_2(\text{ac})_2]^{2-}$  complex is assumed to be present. This is experimentally observed. At  $\text{pH} < 1.2$ , a shift is observed of the Raman band at  $927 \text{ cm}^{-1}$  by  $8 \text{ cm}^{-1}$  to  $935 \text{ cm}^{-1}$ . The Raman spectrum of the solution with a pH value of 1.0 exhibits signals at  $376, 718, 894, 915 \text{ cm}^{-1}$  and  $935 \text{ cm}^{-1}$ . The Raman bands at  $935$  and  $915 \text{ cm}^{-1}$  have already been observed for pure solutions and are attributed to  $\text{cis-}[\text{VO}_2(\text{NO}_3)_4]^{3-}$ . However, the Raman band at  $894 \text{ cm}^{-1}$  cannot be attributed to the nitrate complex (see pure V solution). Therefore, it is concluded that a mixture of  $\text{cis-}[\text{VO}_2(\text{NO}_3)_4]^{3-}$  and protonated  $[\text{VO}_2(\text{ac})_2]^-$  complex is present in solution.

#### 5.2.4.2 Vanadate/Ammonium Oxalate Solution

The Raman spectra of the vanadium/ammonium oxalate solution are shown in Figure 5.12. Again remarkable changes are observed as compared to the pure vanadate solutions. However, in contrast to the mixed vanadate/acetate solution the mixed vanadate/oxalate solution is not dominated by a single species. The Raman bands of the monomeric  $[\text{VO}_4]^{3-}$  could not be observed. At pH 9, Raman bands are observed at  $822, 869, 911, 946$  and  $987 \text{ cm}^{-1}$ . The observed Raman band positions indicate the presence of the polymeric  $[\text{VO}_3]_n^{n-}$  (Raman band at  $946 \text{ cm}^{-1}$ ) and of  $[\text{V}_{10}\text{O}_{28}]^{6-}$  (Raman bands at  $869$  and  $987 \text{ cm}^{-1}$ ) within the pH range from 9.0 to 6.2. The Raman bands at  $822, 869$  and  $911 \text{ cm}^{-1}$  are attributed to the  $\text{H}[\text{V}_2\text{O}_7]^{3-}$  anion and vanish for

pH values lower than 8.8. In the pH range from 5 to 2, the Raman band of the  $[\text{V}_{10}\text{O}_{28}]^{6-}$  anion at  $987 \text{ cm}^{-1}$  continuously shifts to  $1005 \text{ cm}^{-1}$  due to its protonation and vanishes at a pH of 2. All this species could be detected in pure solutions too.

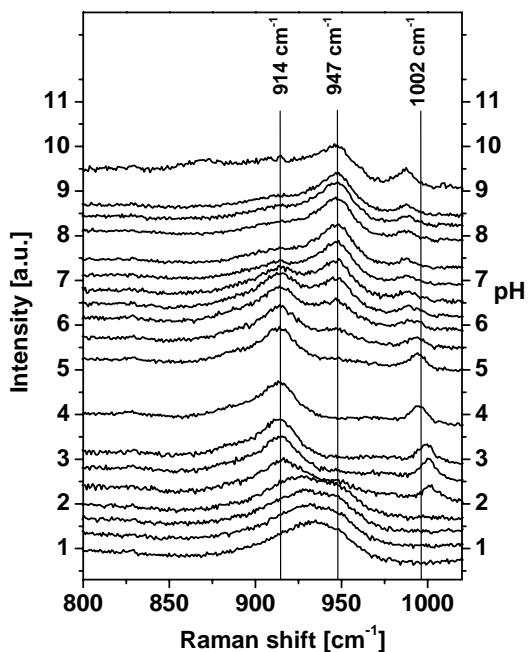


**Fig. 5.12:** Selected Raman spectra recorded during the titration of a mixed solution of AMV (0.5 M) and ammonium oxalate (0.5 M). Spectra are normalised and vertically shifted for better visualisation. The intensity at  $1020 \text{ cm}^{-1}$  corresponds to the pH value of the solution.

In solutions with pH values from 7.9 to 2.0 new Raman bands arise at 303, 431, 526, 829, 889 and 913  $\text{cm}^{-1}$ , and replace the band at 945  $\text{cm}^{-1}$ . At a pH of 5.0, Raman bands are observed at 303, 431, 526, 829, 889, 913, 945 and 995  $\text{cm}^{-1}$ . The observed Raman bands in the low energy regime cannot unambiguously be assigned to this new species, because the Raman bands at 987, 995 and 1005  $\text{cm}^{-1}$  prove the presence of a mixture. Tentatively, the new Raman bands at 526, 829, 889 and 913  $\text{cm}^{-1}$  are assigned to the monodentate oxalate complex  $[\text{VO}_3(\text{ox})]^{2-}$ , because four Raman bands are expected in the high energy range for such a complex with  $C_{3v}$  symmetry. The obvious lower stability of this complex as compared to the acetate  $[\text{VO}_2(\text{ac})_2]^{2-}$  complex may be explained by steric reasons due to the close second carboxy group of the oxalate anion. This lower stability of the oxalate complex also explains the occurrence of polyoxovanadates. From pH 2.0 to 0.8, the Raman band at 913  $\text{cm}^{-1}$  is partially replaced by the Raman band at 935  $\text{cm}^{-1}$  of the *cis*- $[\text{VO}_2(\text{NO}_3)_4]^{3-}$ .

#### 5.2.4.3 Mixed Vanadate/Ammonium Tartrate Solution

Selected Raman spectra of the vanadium/ ammonium tartrate solutions are presented in Figure 5.13. The Raman spectra of the vanadate/ammonium tartrate solution resemble those of the vanadate/acetate solution. They are dominated by one species with Raman bands at 340, 434, 497, 580, 648, 915 and 927  $\text{cm}^{-1}$ . This Raman bands are attributed to a tartrate complex. The total number of observed Raman bands point to the exchange of two oxo ligands by tartrate anions. However, between bidentate  $[\text{VO}_2(\text{tart})]^-$  and monodentate  $[\text{VO}_2(\text{tart})_2]^{2-}$  cannot be distinguished by Raman spectroscopy.

The similarity of the Raman spectra of  $[\text{VO}_2(\text{ac})_2]^-$  and the tartrate complex and the additional observation of polyoxovanadates in solution point to the formation of a monodentate  $[\text{VO}_2(\text{tart})_2]^-$  complex. The Raman bands of this tartrate complex are observed for solutions with pH values between 9.5 and 2. In the pH range from 9.1 to 6.6 a weak additional Raman band at 945  $\text{cm}^{-1}$  points to the formation of  $[\text{VO}_3]_n^{n-}$ . In the pH regime from 6.9 to 0.8, the Raman band at 994  $\text{cm}^{-1}$  indicates the presence of  $\text{H}[\text{V}_{10}\text{O}_{28}]^{5-}$ . At pH values  $< 2$ , the Raman band at 935  $\text{cm}^{-1}$  indicates the presence of *cis*- $[\text{VO}_2(\text{NO}_3)_4]^{3-}$  and of the protonated tartrate complex.



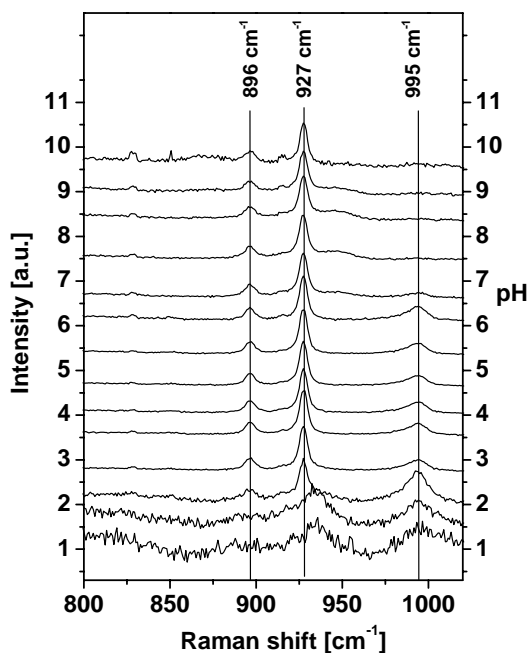


**Fig. 5.13:** Selected Raman spectra recorded during the titration of a mixed solution of AMV (0.5 M) and ammonium tartrate (0.5 M). Spectra are normalised and vertically shifted for better visualisation. The intensity at 1020 cm<sup>-1</sup> corresponds to the pH value of the solution.

The addition of acetate, oxalate or tartrate has a strong impact on the vanadate species formed in aqueous solutions. All carboxylates seem to inhibit the formation of larger polyoxometalates by the formation of carboxylate complexes. The formation of vanadate oxalate complex seems to be hindered probably due to steric reasons. Therefore, the strength of the formed carboxylate complexes does not increase in the order acetate, oxalate and tartrate in contrast to mixed molybdate/carboxylate solutions.

### 5.2.5 Tungstate Solutions

Selected Raman spectra of the tungstate solution are shown in Figure 5.14. Three different Raman spectra could be detected for the tungstate solution in the pH range 9 to 0.8. From pH 9 to 1, Raman bands are observed at 381, 643, 873, 894, 932, 960 and 975 cm<sup>-1</sup>, which are attributed to a mixture of monomeric [WO<sub>4</sub>]<sup>2-</sup> (Raman band at 932 cm<sup>-1</sup>) and oligomeric H[W<sub>12</sub>O<sub>42</sub>]<sup>9-</sup> (Raman bands at 643, 894, 960 and 975). The presence of [W<sub>6</sub>O<sub>21</sub>]<sup>5-</sup> cannot be excluded due to the coincident positions of its Raman bands with those of [W<sub>12</sub>O<sub>42</sub>]<sup>10-</sup>. The Raman band of [WO<sub>4</sub>]<sup>2-</sup> at 932 cm<sup>-1</sup> is observed in the pH range 9 to 5.3. The observed shift of the Raman band at 975 to 979 cm<sup>-1</sup> is attributed to the formation of H<sub>2</sub>[W<sub>12</sub>O<sub>42</sub>]<sup>8-</sup>. For the remaining Raman bands of H<sub>x</sub>[W<sub>12</sub>O<sub>42</sub>]<sup>(10-x)-</sup> spectral changes were not observed in the pH range 9 to 1. At pH 1, Raman bands are observed at 383, 717, 897, 945, 969 and 979 cm<sup>-1</sup>, which remain unchanged to pH 0.8 and indicate H<sub>x</sub>[W<sub>12</sub>O<sub>42</sub>]<sup>x-10</sup>.

### 5.2.5.1 W/Ammonium Carboxylate Solutions

The Raman spectra of the tungsten/ammonium acetate solution are shown in Figure 5.15. The Raman spectra of the mixed tungstate/acetate solution resemble strongly the Raman spectra, which were obtained from the pure tungstate solution. These spectra are not discussed in detail. The Raman spectra of the mixed tungstate/oxalate and tungstate/tartrate solutions resemble the Raman spectra of the pure tungstate solution too. Therefore, these Raman spectra are not shown or discussed in detail, because no interaction between the complexing anions acetate, oxalate or tartrate with the polyoxotungstates in solution could be observed.

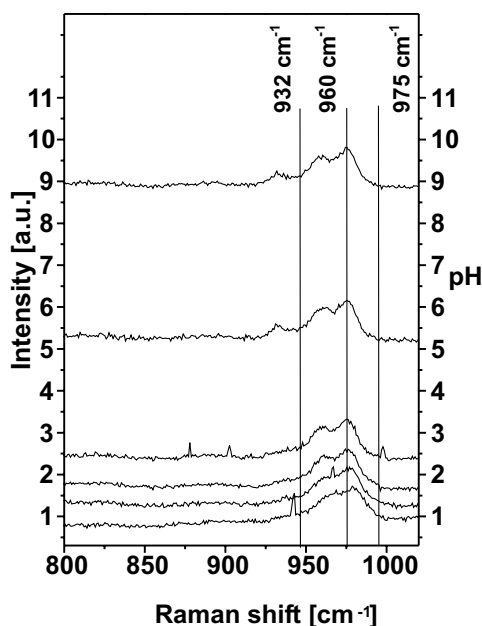


**Fig. 5.14:** Selected Raman spectra recorded during the titration of a AMW solution (0.5 M). Spectra are normalised and vertically shifted for better visualisation. The intensity at 1020 cm<sup>-1</sup> corresponds to the pH value of the solution.

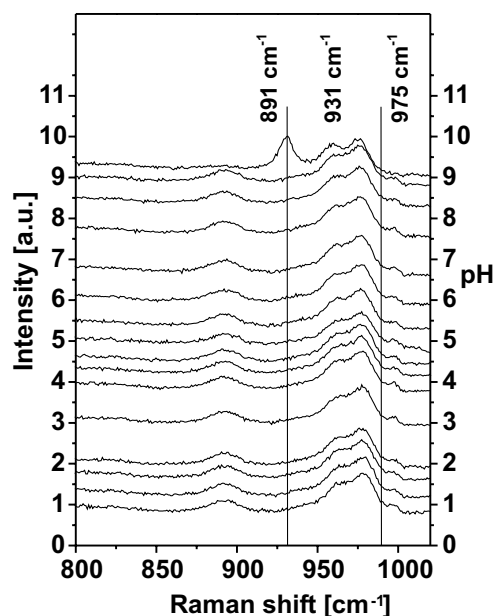


**Fig. 5.15:** Selected Raman spectra recorded during the titration of a mixed solution of AMW (0.5 M) and ammonium acetate (0.5 M). Spectra are normalised and vertically shifted for better visualisation. The intensity at 1020 cm<sup>-1</sup> corresponds to the pH value of the solution.

## 5.2.6 Mixed Binary metalate Solutions

### 5.2.6.1 Mo(90%)/V(10%) and Mo(90%)/W(10%) Solutions

Selected Raman spectra of the Mo/V solutions are shown in Figure 5.16. The Raman spectra of the mixed molybdate/vanadate solution resemble the Raman spectra of a superposition of the pure

solutions. The Raman spectra of the observed molybdate and vanadate species and the pH dependence of the different polyoxoanions are in good agreement with those of the pure solutions. Minor differences are observed for the pH dependency of the heptamolybdate, which may point to an incorporation of minor amounts of V into the polyoxomolybdates. However, most of the V cations present in solution are found in isopolyoxovanadate anions. Therefore, it may be concluded, that the preparation of a polyoxometalate catalyst precursor with a homogeneous elemental distribution is not possible from simply mixed molybdate/vanadate solutions. This is in agreement with experimental findings.<sup>297</sup>

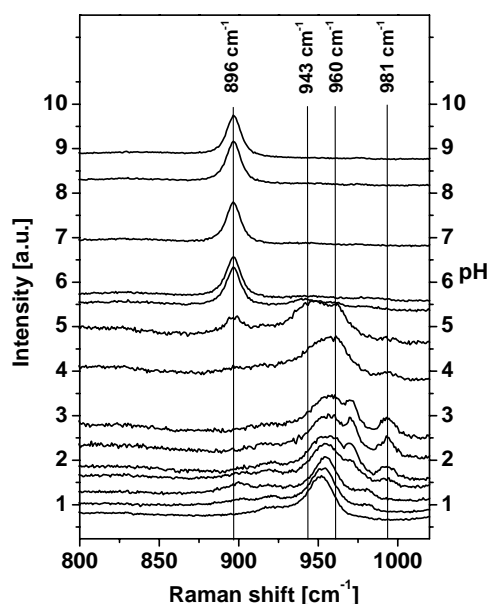


**Fig. 5.16:** Selected Raman spectra recorded during the titration of a mixed solution of AHM (0.45 M) and AMV (0.05 M). Spectra are normalised and vertically shifted for better visualisation. The intensity at 1020 cm<sup>-1</sup> corresponds to the pH value of the solution.

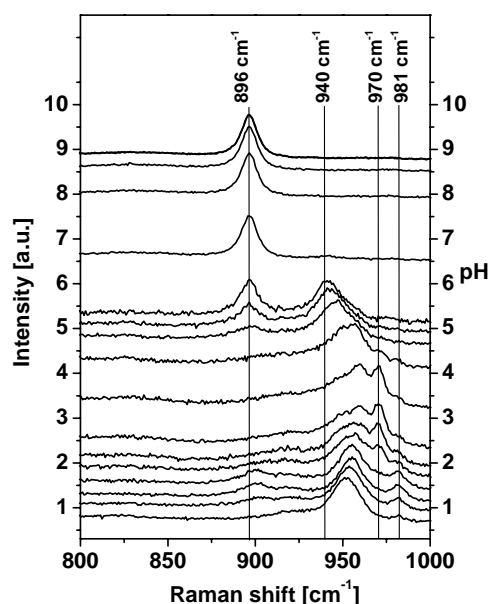


**Fig. 5.17:** Selected Raman spectra recorded during the titration of a mixed solution of AHM (0.45 M) and AMW (0.05 M). Spectra are normalised and vertically shifted for better visualisation. The intensity at 1020 cm<sup>-1</sup> corresponds to the pH value of the solution.

The Raman spectra of the Mo/W solution are shown in Figure 5.17. The observed Raman spectra resemble those of the pure molybdate solution. On basis of the Raman spectra of the mixed molybdate/tungstate solutions evidence cannot be found for the formation of mixed Mo/W polyoxoanions. However, Howarth et al. identified by NMR different mixed Mo/V and Mo/W species in aqueous solutions.<sup>249, 275-277</sup> They observed the formation of mixed polyoxometalates for M/W mixed solutions where preferentially one or two cations were substituted by the minor component present in solution. The substitution of one or two Mo atoms in [Mo<sub>7</sub>O<sub>24</sub>]<sup>6-</sup> by V or W should lead due

to a different symmetry of the mixed anion and to changes in the Raman spectra. However these changes may not be resolved by Raman spectroscopy due to the rather broad and often overlapping Raman bands of polyoxometalates in aqueous solutions. Only broader less resolved Raman bands were found which indicate a mixture of different anions to be present in solution. A molecular defined mixed polyoxo anion in mixed metalate solutions is a prerequisite for a defined, elemental distribution of the ammonium metalate precursors. For such an mixed anion new Raman bands should be observed. Therefore, a homogeneous distribution within the polyoxometalate catalyst precursors cannot be expected from such simply mixed solutions as it has been experimentally been confirmed.<sup>297</sup>

## 5.2.7 Mixed Ternary metalate Solutions

### 5.2.7.1 Mo(60%)/V(30%)/W(10 %) Solution

The Raman spectra of the Mo(60%)/V(30%)/W(10%) solution are shown in Figure 5.18. This composition has been chosen because of its relevance for the preparation of industrially used catalysts like the one presented in Chapter 2. At pH 9.1, the Raman spectrum shows Raman bands at 308, 376, 643, 829, 842, 872, 897, 929, 945 and 977  $\text{cm}^{-1}$ . The intense Raman band at 897  $\text{cm}^{-1}$  and the weak bands at 827, 945 and 977  $\text{cm}^{-1}$  identify  $[\text{MoO}_4]^{2-}$ ,  $[\text{VO}_4]^{3-}$  and  $\text{H}_2[\text{W}_{12}\text{O}_{42}]^{8-}$  in the pH range from 9.1 to 5.9, respectively. These anions were observed in pure Mo, V and W solutions too. However, the Raman band at 927  $\text{cm}^{-1}$  points to the formation of a species which was not found in pure solutions. This Raman band

at 927  $\text{cm}^{-1}$  is observed for solutions with pH values from 9.1 to 2.1. The appearance of this new, probably mixed species in solution at pH values  $< 8$  points to a low degree of condensation

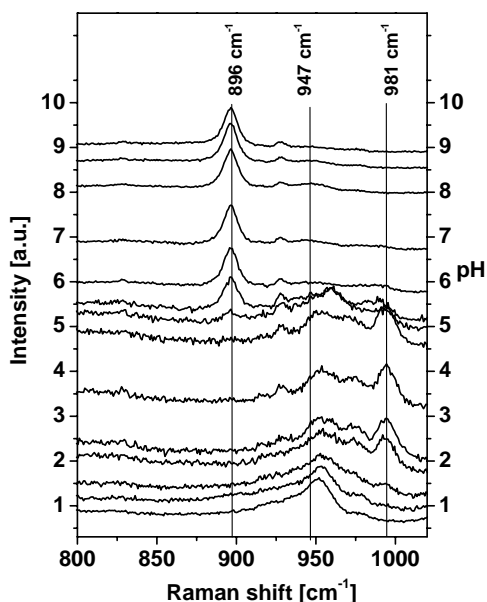


**Fig. 5.18:** Selected Raman spectra recorded during the titration of a mixed solution of AHM (0.3 M), AMV (0.15 M) and AMW (0.05 M). Spectra are normalised and vertically shifted for better visualisation. The intensity at 1020  $\text{cm}^{-1}$  corresponds to the pH value of the solution.

of this species. However, the observation of only one weak Raman band renders an assignment impossible of this band to a specific mixed polyoxometalate. Upon acidification to a pH value of 6.0, new Raman bands arise at 948, 988 and 995  $\text{cm}^{-1}$ , while the Raman bands of the  $[\text{MoO}_4]^{2-}$  at 897  $\text{cm}^{-1}$  and of the  $[\text{VO}_3]_n^{n-}$  at 945  $\text{cm}^{-1}$  vanish. These new bands which are observed for solutions with pH values between 6.0 to 1.5 and are attributed to the  $[\text{Mo}_7\text{O}_{24}]^{6-}$  and  $[\text{V}_{10}\text{O}_{28}]^{6-}$  anions. In contrast to pure molybdate solution only minor amounts of  $[\text{Mo}_7\text{O}_{24}]^{6-}$  are formed.

The obtained Raman spectra of solutions with pH values smaller 6 are in general broader and strongly overlapping which points to the formation of a mixture of differently mixed polyoxometalates or unresolved symmetry splits of mixed polyoxometalates. At pH 4.9, Raman bands are observed at 381, 796, 827, 928, 953, 963, 970 and 994  $\text{cm}^{-1}$ . The observed positions indicate a mixture consisting of  $\text{H}[\text{V}_{10}\text{O}_{28}]^{5-}$  (Raman bands at 970, 994  $\text{cm}^{-1}$ ) and  $[\text{Mo}_8\text{O}_{26}]^{4-}$  (Raman bands at 953 and 963  $\text{cm}^{-1}$ ) to be present in solution. The broad Raman bands of the probably mixed polyoxometalate  $[\text{M}_8\text{O}_{26}]^{4-}$  and  $[\text{M}_{10}\text{O}_{28}]^{6-}$  are observed in the pH range from 5.5 to 1.5. The obviously minor influence on the formation of a mixed  $[\text{M}_8\text{O}_{26}]^{4-}$  as compared to the  $[\text{M}_7\text{O}_{24}]^{6-}$  formation may be explained by the different structures of these polyoxometalates as shown in Figure 3.7 on page 92. The  $[\text{Mo}_7\text{O}_{24}]^{6-}$  anion consists of seven edge and vertex linked  $\text{MoO}_6$  octahedra, while the  $[\text{Mo}_8\text{O}_{26}]^{4-}$  anion consists of six octahedral and two tetrahedral coordinated  $\text{MoO}_x$  polyhedra. It may be assumed that the tetrahedral coordinated Mo is preferentially replaced by V and that the incorporation of V has a lower influence on the formation and stability of  $[\text{Mo}_8\text{O}_{26}]^{4-}$  as compared to  $[\text{Mo}_7\text{O}_{24}]^{6-}$ . The appearance of the  $[\text{V}_{10}\text{O}_{28}]^{6-}$  anion and its protonated forms suggests only minor amounts of V to be present in the mixed polyoxometalates. The Raman spectra obtained from Mo(90%)/V(10%) proved the  $[\text{V}_{10}\text{O}_{28}]^{6-}$  to be present in this solution too. Therefore, it is concluded that less than one third of the vanadium cations in the Mo6V3W1 solution are incorporated into mixed Mo-V-O clusters. More than two third of the vanadium in solution form polyoxovanadates, which is experimentally indicated by the intense Raman bands of the decavanadate. This finding is in agreement with results of Dupont et al.<sup>198</sup> who found in hexagonal precipitates of mixed Mo/V solutions an amount of vanadia of only one third to one half of the vanadate concentrations in solutions with pH values of  $\sim 1.5$ . At pH < 1.5, Raman bands are observed at 381, 937, 952 and 973  $\text{cm}^{-1}$ , which may be attributed to the formation of a

mixed  $[\text{Mo}_{36}\text{O}_{112}]^{8-}$  and a *cis*- $[\text{VO}_2(\text{NO}_3)_4]^{3-}$  (Raman band at  $937\text{ cm}^{-1}$ ) polyoxometalate. The observed broad and strongly overlapping Raman bands point to the formation of differently mixed polyoxometalates.

Raman bands of polyoxotungstates as observed for pure tungstate solution could not be detected. This may point to the formation of mixed Mo/W polyoxometalates. However, this interpretation is ambiguous because of the low concentration of W in the mixed solution combined with a in general lower Raman cross section of the tungstate complexes as compared to the molybdate or vanadate complexes. Because new Raman bands could not be observed and because the observed Raman spectra mainly resemble those of the pure molybdate and vanadate solution, a final decision about the incorporation of W into the molybdenum oxygen clusters cannot be drawn.

The obtained Raman spectra of mixed Mo6V3W1 solutions indicate isopolyoxovanadates, isopolyoxomolybdates and minor amounts of mixed polyoxometalates. These combined results explain the observed elemental inhomogeneities of molybdenum oxide based catalyst prepared from aqueous solutions.

#### **5.2.7.2 Mo(60%)/V(30%)/W(10 %)/Ammonium Acetate Solution**

Selected Raman spectra of the Mo6V3W1/ammonium acetate solutions are presented in Figure 5.19. As shown above, only minor amounts of the vanadium present in solution are incorporated into the formed polyoxometalates. Mixed carboxylate solutions are therefore investigated in order to control the spatial arrangement of the different cations in the catalyst precursor. It was shown above, that the addition of acetate, oxalate or tartrate had a strong impact on the metal-oxygen cluster formed in solution. The formation of acetate, oxalate or tartrate complexes inhibited the condensation of polyoxometalates as compared to the pure solutions. Therefore, the stabilisation of monomeric species in solution seems to be one way to improve the element homogeneity of the catalyst precursor.

The Raman spectra of the mixed Mo6V3W1/acetate solutions resemble the Raman spectra of the Mo6V3W1 solution. For solutions in the pH range from pH 9.0 to 6.7 changes have not been observed for the Raman band positions as compared to the Mo6V3W1 solution. At pH 6.1, Raman bands are observed at 302, 376, 896, 927, 949, 960, 974 and  $993\text{ cm}^{-1}$ . However, minor changes

of the intensity ratio of the Raman bands are detected. The Raman bands at 896 and 927  $\text{cm}^{-1}$  point to the presence of the  $[\text{VO}_2(\text{ac})_2]^-$  complex, which was also observed in the V/acetate solution. The more intense Raman bands at 927, 949 and 960  $\text{cm}^{-1}$  as compared to the Mo6V3W1 solution indicate  $[\text{VO}_2(\text{ac})_2]^-$  and higher concentration of the  $[\text{Mo}_7\text{O}_{24}]^{6-}$  and  $[\text{Mo}_8\text{O}_{26}]^{4-}$ . At pH values below 5.0, the obtained Raman spectra resemble those of the solution without acetate and are therefore not described or discussed in detail. The presence of the  $[\text{VO}_2(\text{ac})_2]^-$  complex in the Mo6/V3W1/acetate solution beside mainly isopolyoxomolybdates is expected to lead to a catalyst precursor with a better elemental distribution as compared to one from solutions without acetate, because the formation of larger isopolyoxovanadates is disfavoured by the acetate addition.

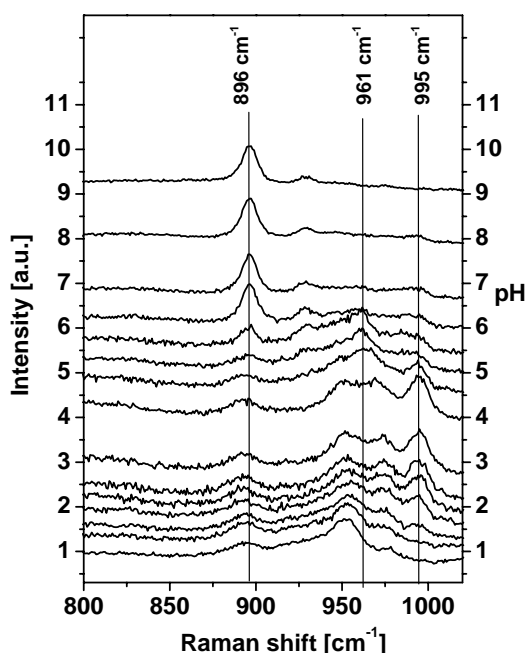


**Fig. 5.19:** Selected Raman spectra recorded during the titration of a mixed solution of AHM (0.3 M), AMV (0.15 M), AMW (0.05 M) and ammonium acetate (0.5 M). Spectra are normalised and vertically shifted for better visualisation. The intensity at 1020  $\text{cm}^{-1}$  corresponds to the pH value of the solution.

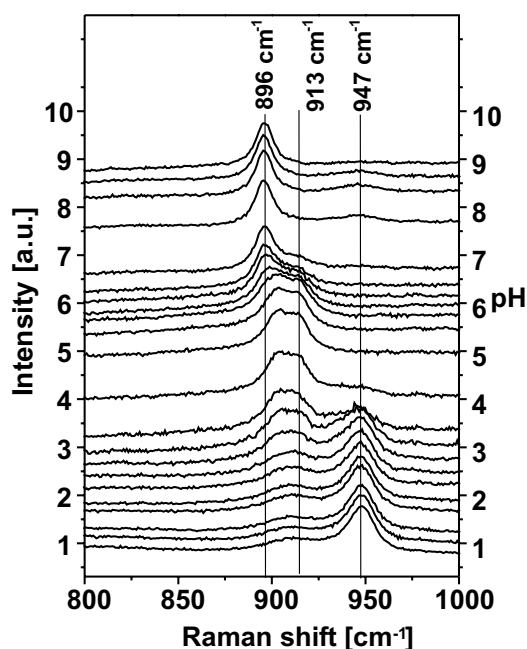


**Fig. 5.20:** Selected Raman spectra recorded during the titration of a mixed solution of AHM (0.3 M), AMV (0.15 M), AMW (0.05 M) and ammonium oxalate (0.5 M). Spectra are normalised and vertically shifted for better visualisation. The intensity at 1020  $\text{cm}^{-1}$  corresponds to the pH value of the solution.

### 5.2.7.3 Mo(60%)/V(30%)/W(10 %)/Ammonium Oxalate Solution

The Raman spectra of the Mo6/V3/W1/oxalate solutions are shown in Figure 5.20. The addition of ammonium oxalate leads to a dramatic change in the appearance of the different polyoxometal-

lates in the mixed Mo6V3W1/oxalate solution. At pH 9.1 Raman bands are observed at 842, 897 and 947  $\text{cm}^{-1}$ , which indicate a mixture of the  $[\text{MoO}_4]^{2-}$  (Raman bands at 897 and 947  $\text{cm}^{-1}$ ) and  $[\text{VO}_3]_n^{n-}$  (Raman band at 842  $\text{cm}^{-1}$ ). A decrease of the pH value of the solution to 7.7 leads to an intensity increase of the band at 947  $\text{cm}^{-1}$ . At pH 6.7, a new Raman band arises at 913  $\text{cm}^{-1}$  replacing the band at 947  $\text{cm}^{-1}$ . At pH 6.7, Raman bands are observed at 842, 897 and 913  $\text{cm}^{-1}$ . Upon acidification to a pH value of 5.0, a shift is observed of the Raman band at 897  $\text{cm}^{-1}$  by 8  $\text{cm}^{-1}$  to 905  $\text{cm}^{-1}$ . The Raman bands at 905 and 913  $\text{cm}^{-1}$  are attributed to the formation of a mixture of a  $[\text{MoO}_3(\text{ox})]^-$  (Raman bands at 905 and 914  $\text{cm}^{-1}$ ) and a  $[\text{VO}_3(\text{ox})]^{2-}$  (Raman bands at 896 and 913  $\text{cm}^{-1}$ ). From pH 4.7 to 2.0, Raman bands are observed at 653, 721, 905 and 913  $\text{cm}^{-1}$ , while at pH 4.0 new Raman bands arise at 717, 910 and 948  $\text{cm}^{-1}$  which replace the former ones. These Raman bands are observed from pH 4.0 to 0.8 and are attributed to the formation of protonated oxalate complexes. Interestingly, Raman bands of polyoxovanadates could not be detected. Therefore, a catalyst precursor with a better elemental distribution may be expected from the mixed metalate/oxalate solutions. Mainly monomeric oxalate complexes are observed in such a solution which should lead to a statistical distribution of the elements within the catalyst precursor and, hence, the final catalyst.

#### 5.2.7.4 Mixed Mo(60%)/V(30%)/W(10 %)/Ammonium Tartrate Solution

The Raman spectra of the Mo6V3W1/tartrate solution are shown in Figure 5.21. The addition of tartrate leads to similar changes as compared to the oxalate addition. At pH 9.1, Raman bands are observed at 308, 369, 840, 896, 914, 927 and 934  $\text{cm}^{-1}$ . The Raman bands at 897 and 934  $\text{cm}^{-1}$  are detected in solutions with pH values between 9 to 2.93 and indicate the formation of a  $[\text{MoO}_2(\text{tart})]$  (Raman bands at 896 and 934  $\text{cm}^{-1}$ ) and  $[\text{VO}_2(\text{tart})]^+$  (Raman bands at 915 and 927  $\text{cm}^{-1}$ ) complexes. The Raman spectrum of the solution with pH 5.55 shows Raman bands at 378, 646, 717, 828, 897, 915, 927 and 934  $\text{cm}^{-1}$ . Upon acidification to pH 2.55, the Raman band at 897  $\text{cm}^{-1}$  loses intensity and a shift is observed for the Raman band at 934  $\text{cm}^{-1}$  by 4  $\text{cm}^{-1}$ . The Raman bands are located at 386, 558, 581, 719, 823, 852, 901, 916, 938, and 995  $\text{cm}^{-1}$  at pH 2.55 and do not change upon further acidification. These Raman bands are attributed to the formation of polyoxovanadates (Raman band at 995  $\text{cm}^{-1}$ ) and a mixture of protonated tartrate complexes of the



metal cations present in solution. The addition of either oxalate or tartrate favours the formation of a highly stable monomeric carboxylate species in solution, which suppresses the formation of isopolyoxometalates. Therefore, the elemental distribution of the catalyst precursor and, hence, the final catalyst is expected to be positively influenced by the addition of such carboxylates.

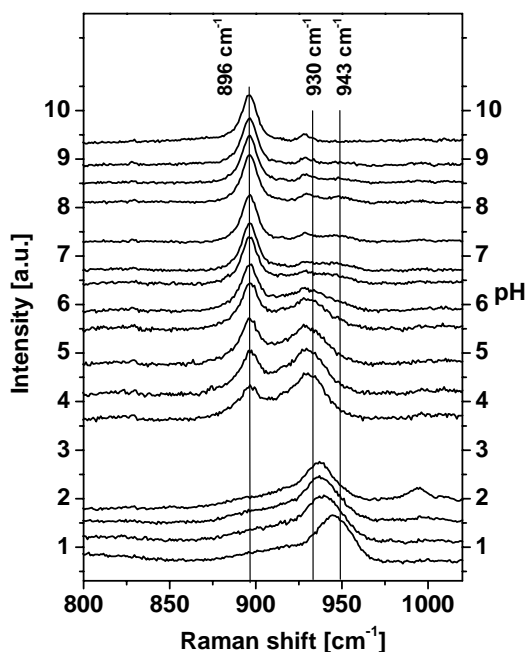


**Fig. 5.21:** Selected Raman spectra recorded during the titration of a mixed solution of AHM (0.3 M), AMV (0.15 M), AMW (0.05 M) and ammonium tartrate (0.5 M). Spectra are normalised and vertically shifted for better visualisation. The intensity at 1020 cm<sup>-1</sup> corresponds to the pH value of the solution.

### 5.3 Conclusions

The formation of Mo, V and W polyoxometalates in solution was investigated by *in situ* Raman spectroscopy. For Mo solutions, [MoO<sub>4</sub>]<sup>2-</sup>, [Mo<sub>7</sub>O<sub>24</sub>]<sup>6-</sup>, [Mo<sub>8</sub>O<sub>26</sub>]<sup>4-</sup> and [Mo<sub>36</sub>O<sub>112</sub>]<sup>8-</sup> and their protonated species were identified. The [VO<sub>4</sub>]<sup>3-</sup>, [V<sub>10</sub>O<sub>28</sub>]<sup>6-</sup> and [V<sub>2</sub>O<sub>7</sub>]<sup>3-</sup> and their protonated species were identified in V solutions. For W solutions, the observed Raman spectra indicated the presence of [WO<sub>4</sub>]<sup>2-</sup> and [W<sub>12</sub>O<sub>42</sub>]<sup>10-</sup>. The pH dependence of the observed species is in good agreement with literature data.

Further, carboxylate complexes of Mo and V could be identified. The stability of the observed complexes increases in the order acetate, oxalate and tartrate for Mo carboxylates. The stability for V carboxylate complexes increases in the order oxalate, acetate and tartrate. The formation of these carboxylate complexes, which are observed over a broader pH range strongly inhibits the condensation of larger polyoxometalates found in carboxylate-free solutions.

The Raman spectra which were observed for the mixed Mo/V, Mo/W and Mo<sub>6</sub>/V<sub>3</sub>/W<sub>1</sub> solutions pointed to the presence of mixed polyoxometalates. However, a structural characterisation of these mixed oxides was not possible due to broad, weak and strongly overlapping Raman bands. These uncharacterised mixed polyoxometalates are only present in minor concentrations in solution. The observed Raman spectra proved mainly isopolyoxomolybdates and isopolyoxovanadates to be present in these mixed solutions. This observation explains the observed elemental inhomogeneities of catalysts with similar composition. Due to the molecularly heterogeneous mixed solutions the preparation of a catalyst precursor with a homogeneous element distribution is not expected from such solutions.

In order to control the presence of a defined species in solution, the influence of carboxylate additions in mixed solutions was investigated. In these mixed metalate/carboxylate solutions, oxalate or tartrate stabilised the formation of monomeric oxometalates. Because the formation of larger polyoxometalates is suppressed a polyoxometalate catalyst precursor and, hence, an activated catalyst with a more homogeneous spatial elemental distribution is expected. Due to the low stability of the acetate complexes the addition of acetate leads only to minor amounts of monomeric species in solution apart of mixed and pure polyoxometalates.

## Chapter 6

# Summary

Selective oxidation reactions require multifunctional catalysts, which are capable of the activation of the organic molecule, of the oxygen activation, the oxygen insertion and of the regeneration of the catalyst. The structure and composition of such catalysts determines their physico-chemical and catalytic properties. Therefore, the compositional and structural changes as well as the catalytic properties of a mixed Mo/V/W oxide catalyst were investigated by XRD, TEM, SEM and Raman spectroscopy in this PhD work.

The catalytic activity of this Mo/V/W mixed oxide in selective oxidation of methanol increased by a factor of three upon thermal activation in inert atmosphere at 813 K. XRD, TEM and Raman spectroscopic characterisation of the initial material showed the presence of nanocrystalline oxides of  $\text{Mo}_5\text{O}_{14}$  and  $\text{MoO}_3$  structure. SEM/EDX analysis proved elemental inhomogeneities to be present, which are explained by the presence of different isopolyoxometalates in the precursor solutions.

After thermal activation in inert gas, the mixed oxide consisted of a mixture of a majority of oxides of  $\text{Mo}_5\text{O}_{14}$  structure and a minority of crystalline oxides of  $\text{MoO}_3$  structure. XRD, TEM and Raman spectroscopic characterisation of the mixed oxide thermally activated at different temperatures revealed that the crystallisation of the oxide of  $\text{Mo}_5\text{O}_{14}$  structure occurs only in a rather narrow temperature regime between 800 and 820 K. For activation temperatures above 820 K, the metastable oxide of  $\text{Mo}_5\text{O}_{14}$  structure increasingly disproportionated into oxides of  $\text{MoO}_3$  and  $\text{MoO}_2$  structure. The combined XRD, TEM and Raman spectroscopic identification of the oxide of  $\text{Mo}_5\text{O}_{14}$  structure points to its relevant role for the observed increase of the catalytic activity for formaldehyde formation by a factor of three after thermal activation.

It can be concluded from the physicochemical characterisation that it is of paramount importance to monitor and fully control the elemental composition and the atomic structure of the MoVW oxide in order to fully understand its catalytic activity and selectivity. It is suggested that vanadium on one hand generates the catalytic activity of the mixed oxide but on the other destabilises the presumably active oxide of  $\text{Mo}_5\text{O}_{14}$  structure due to its high reducibility. The tungsten promoter is seen as necessary to counterbalance the inherent, and V-enhanced instability of the  $\text{Mo}_5\text{O}_{14}$  structure.

In order to unravel these suggested different roles of the W and V promoters, their influence has been investigated on the thermal activation process of the catalyst precursors and their catalytic properties by *in situ* XRD and *in situ* Raman spectroscopy.

Only a minor influence of V could be observed on the structures formed during the activation processes as compared to the AHM activation process. For the W promoter it was found that minor amounts of W in the molybdenum oxides matrix inhibit structural reorganisation processes. Such an inhibition is explained by the octahedral coordination of the redox stable W which shares only O-vertices with its neighbour cations. This is believed to strongly affect the oxygen vacancy mobility in the material and, hence, the evolution of long range ordering of defects.

Due to strong absorption in the visible of the catalyst materials investigated, experimental conditions had to be found for the combined *in situ* Raman/TPRS experiments to couple the Raman scattering to an electronic transition in order to enhance the low Raman cross section by resonance Raman enhancement. Indeed, a resonance Raman effect was proven to be operative in oxygen defective molybdenum oxides. For an excitation wavelength of 632 nm (1.96 eV), the observed Raman cross section varied as a function of the degree of reduction of five different  $\text{MoO}_{3-x}$  samples. A model of the electronic transitions in  $\text{MoO}_{3-x}$  based on crystal field theory was proposed to explain the electronic transitions observed by DR-UV/VIS spectroscopy. The observed resonant Raman scattering is coupled to the IVCT transition at about 2 eV arising from oxygen vacancies present in the materials. Due to the local nature of the absorption process, the developed model is valid for intermediate oxides too in agreement with literature. Accordingly, resonant Raman scattering was proven too for  $\text{Mo}_4\text{O}_{11}$  and  $\text{MoO}_2$ . Not only the intensity of this IVCT transition is a function of the degree of reduction but also its position. Accordingly, the experimentally observed Raman intensity

is a complex function of resonance enhancement and re-absorption of the Raman scattered light. Hence, the experimentally observed Raman intensity bears information about the degree of reduction of the molybdenum oxide provided proper referencing and thus exclusion of trivial effects like defocusing during the experiment.

*In situ* Raman spectroscopy of  $\text{MoO}_{3-x}$  catalysts during propene partial oxidation indicates that the propene conversion and the selectivities are a function of the degree of reduction of the catalyst. The higher the degree of reduction, the higher is the total activity and the selectivity to acetic acid. The consecutive oxidation of acrolein to acetic acid seems to be linked to the presence of larger oxygen vacancy clusters, while the formation of acrolein and its consecutive total oxidation over the  $\text{MoO}_{3-x}$  catalyst presumably is related to the presence of isolated oxygen vacancies.

The role of W as a structural promoter is confirmed by the *in situ* Raman/TPRS experiments and explained by a lower mobility of oxygen vacancies in the catalyst due to the presence of the redox stable  $\text{W}^{6+}$ . As a consequence of the lower oxygen mobility, the formation of larger oxygen vacancy clusters does not occur and a higher selectivity to acrolein is observed as compared to the unpromoted catalyst. V addition is found to increase the propene conversion and, hence, induces the formation of active centres for the selective oxidation of acrolein to acrylic acid. V acts as well structural promoter as it destabilises the found structures and lowers the temperature of defect formation. At high propene conversions, *i.e.* for catalysts containing V, the formation of an oxide of  $\text{Mo}_5\text{O}_{14}$  structure is observed, which does not structurally change during the consecutive TPRS cycles. However, deactivation combined with changes of the selectivities are observed for all V-containing catalysts which are explained by irreversible reduction of the catalysts during the TPRS cycles.

It was concluded on the basis of the observed catalytic performances of the differently promoted catalysts that the primary reaction product of propene partial oxidation over all catalyst samples is acrolein as proven by the high selectivity to acrolein for low propene conversions. The maximum selectivities to acetic and acrylic acid at higher propene conversions indicate different active centres for the consecutive oxidation of acrolein in agreement with literature. The presence of larger oxygen vacancies clusters is seen as being strongly related to the formation of acetic acid. The presence of

the V promoter favours the formation of acrylic acid. The at least three different active sites seem to responsible for the formation of acrolein, acrylic acid and total oxidation products and underline the multifunctional catalytic properties of the investigated mixed Mo/V/W catalysts.

The combination of all measured physicochemical properties of  $\text{Mo}_5\text{O}_{14}$  oxide catalysts suggests a core-shell model, the core being mostly of an oxide of  $\text{Mo}_5\text{O}_{14}$  structure while the shell is formed by stoichiometrically ill-defined metal oxide clusters and having a higher degree of reduction. The core and the shell may act differently in the catalytic process. During partial oxidation catalysis, the crystalline core of  $\text{Mo}_5\text{O}_{14}$  structure is suggested to play the role of an electron reservoir for the fast catalytic redox reactions. The shell provides a high number of active sites and allows fast surface oxygen diffusion.

Precursor preparation and catalyst activation definitely is of importance for the final structure of the active catalyst, its degree of reduction and its elemental and structural heterogeneity. In order to control the spatial elemental distribution within the polyoxometalate catalyst precursor and, hence, the final catalyst it was attempted to control the formation of molecularly defined species in solution. Pure and mixed Mo, V or W solutions have been studied by *in situ* Raman spectroscopy as a function of the solution pH. The Raman spectra which were obtained from the mixed Mo9V1, Mo9W1 and Mo6/V3/W1 solutions indicated mainly isopolyoxomolybdates and isopolyoxovanadates and minor amounts of mixed polyoxometalates to be present in these mixed solutions. However, a structural characterisation of these mixed polyoxometalates was not possible due to broad, weak and strongly overlapping Raman bands. The observation of a mixture of mainly isopolyoxomolybdates, isopolyoxovanadates and minor amounts of mixed isopolyoxometalates present in solution explains the observed elemental inhomogeneities of catalyst precursors and, hence, catalysts of similar composition. Due to the molecularly heterogeneous solutions, the preparation of catalyst precursors with a homogeneous element distribution is not expected from such simply mixed metalate solutions.

The influence of carboxylate additions in mixed and pure metalate solutions was investigated in order to control the formation of defined species in solution. Due to the low stability of the acetate complexes, the addition of acetate only leads to minor amounts of monomeric species beside mixed and pure polyoxometalates. The formation of stable monomeric oxometalate oxalate and

tartrate complexes was observed. The formation of larger polyoxometalates, like  $[\text{Mo}_7\text{O}_{24}]^{6-}$  is suppressed, polyoxometalate catalyst precursors and, hence, activated catalysts of homogeneous spatial elemental distributions are expected.

Based on the studies presented in this PhD thesis additional investigations on the preparation (solutions and thermal activation) as well the catalytic properties of mixed Mo/V/W oxide catalysts may be useful to improve existing Mo/V/W oxide catalysts systems. Starting with the preparation, the conditions in mixed solutions (pH, concentrations) may further be optimised with respect to molecularly defined solid mixed polyoxometalate catalyst precursors. The activation process of this defined mixed polyoxometalate catalyst precursor into the final catalyst still needs to be optimised in order to obtain a monophasic catalyst material of  $\text{Mo}_5\text{O}_{14}$  structure and to avoid the formation of oxides of  $\text{MoO}_3$  structure being active in total oxidation. Finally, *in situ* Raman results may be used to monitor the structure and reduction degree of the catalyst in order to find optimum conditions with respect to the feed composition or the contact time.

# Bibliography

- [1] R. K. Grasselli, *Catal. Today* **49**, p. 141 (1999).
- [2] S. K. Deb and J. A. Chopoorian, *J. Appl. Phys.* **37**, p. 4818 (1966).
- [3] S. K. Deb, *Proc. Roy. Soc. A* **304**, p. 211 (1968).
- [4] V. R. Porter, W. B. White, and R. Roy, *J. Solid. State. Chem.* **4**, p. 250 (1972).
- [5] H. Gruber and E. Krautz, *Phys. Stat. Sol. A* **62**, p. 615 (1980).
- [6] G. Blasse and M. Wiegel, *J. Alloys And Comp.* **224**, p. 342 (1995).
- [7] K. Bange, *Solar Energy Materials & Solar Cells* **58**, p. 1 (1999).
- [8] C. G. Granquist, *Appl. Phys* **57**, p. 3 (1993).
- [9] R. K. Grasselli and J. D. Burrington, *Adv. Catal.* **30**, p. 133 (1981).
- [10] G. Mestl and T. K. K. Srinivasan, *Catal. Rev.-Sci. Eng.* **40**, p. 451 (1998).
- [11] J. B. Moffat, *Appl. Catal. A* **146**, p. 65 (1996).
- [12] U. S. Ozkan, M. R. Smith, and S. A. Driscoll, *J. Catal.* **134**, p. 24 (1992).
- [13] J. C. Volta, O. Bertrand, and N. Floquet, *J. Chem. Soc. Chem. Commun.* , p. 1283 (1985).
- [14] G. Mestl, Ch. Linsmeier, R. Gottschall, M. Dieterle, J. Find, D. Herein, J. Jäger, Y. Uchida, and R. Schlögl, *J. Mol. Catal. A* **162**, p. 455 (2000).
- [15] J. Haber, In G. Ertl, H. Knözinger, and J. Weitkamp, editors, *Handbook of Heterogeneous Catalysis* Volume V , p. 2244. Wiley-VCH, Weinheim (1997).
- [16] E. Gallei and E. Schwab, *Catal. Today* **51**, p. 535 (1999).
- [17] L. C. Glaeser, J. Brazdil, M. A. Hazle, M. Mehicic, and R. K. Grasselli, *J. Chem. Soc. Farad. Trans.* **81**, p. 2903 (1985).
- [18] K. Weissmehl and H.-J. Arpe, *Industrial Organic Chemistry*, VCH, Weinheim (1997).
- [19] N. Nojiri and Y. Watanabe Y. Sakai, *Catal. Rev.-Sci. Eng.* **37**, p. 145 (1995).
- [20] H. Knözinger and G. Mestl, *Topics Catal.* **8**, p. 45 (1999).
- [21] T. Ressler, O. Timpe, T. Neisius, J. Find, G. Mestl, M. Dieterle, and R. Schlögl, *J. Catal.* **191**, p. 75 (2000).



- [22] Y. Zhang, M. Meisel, A. Martin, B. Lücke, K. Witke, and K.-W. Brzezinka, *Chem. Mater.* **9**, p. 1086 (1997).
- [23] J. Melsheimer, S. Mahmoud, G. Mestl, and R. Schlögl, *Catal. Lett.* **60**, p. 103 (1999).
- [24] B. S. Clausen, *Catal. Today* **39**, p. 293 (1998).
- [25] I. E. Wachs, *Topics Catal.* **8**, p. 57 (1999).
- [26] G. Mestl and H. Knözinger, In G. Ertl, H. Knözinger, and J. Weitkamp, editors, *Handbook of Heterogeneous Catalysis Volume II*, p. 539. Wiley-VCH, Weinheim (1997).
- [27] H. Knözinger, *Catal. Today* **32**, p. 72 (1996).
- [28] L. Kihlborg, *Adv. Chem.* **37**, p. 39 (1963).
- [29] L. Kihlborg, *Acta Chem. Scand.* **13**, p. 954 (1959).
- [30] M. A. Py and K. Maschke, *Physica B* **105**, p. 376 (1981).
- [31] M. A. Py, Ph. E. Schmid, and J. T. Vallin, *Il Nuovo Cimento* **38**, p. 271 (1976).
- [32] P. A. Spevack and N. S. McIntyre, *J. Phys. Chem.* **97**, p. 11020 (1993).
- [33] T.V. Andrushkevich, *Catal. Rev.-Sci.Eng.* **35**, p. 213 (1993).
- [34] H. Werner, O. Timpe, D. Herein, Y. Uchida, N. Pfänder, U. Wild, and R. Schlögl, *Catal. Lett.* **44**, p. 153 (1997).
- [35] J. Tichy, *J. Appl. Catal. A* **157**, p. 363 (1999).
- [36] H. Knözinger, *Catal. Today* **32**, p. 71 (1996).
- [37] K. Nakamoto, *Infrared and Raman Spectra of Inorganic and Coordination Compounds*, Wiley New York (1997).
- [38] B. Schrader, *Vibrational Spectroscopy - Methods and Application*, Wiley-VCH, Weinheim (1995).
- [39] M. Cardona, In M. Cardona and G. Güntherodt, editors, *Topics in Applied Physics, Light Scattering in Solids II* Volume 50, Springer, Berlin (1982).
- [40] Hollemann-Wiberg, *Lehrbuch der Anorganischen Chemie*, deGruyter Berlin (1985).
- [41] M. T. Pope, *Heteropoly and Isopolyoxometalates*, Springer, Berlin (1983).
- [42] Th. Ekström and M. Nygren, *Acta Chem. Scand.* **26**, p. 1827 (1972).
- [43] E. Salje, R. Gehlig, and K. Viswanathan, *J. Solid State Chem.* **25**, p. 239 (1978).
- [44] T. Ekström, E. Salje, and R. J. D. Tilley, *J. Solid State Chem.* **40**, p. 75 (1981).
- [45] L. Kihlborg, *Acta. Chem. Scand.* **23**, p. 1834 (1969).
- [46] K. Brückman, R. Grabowski, J. Haber, A. Mazurkiewicz, J. Slocynski, and T. Wiltowski, *J. Catal.* **104**, p. 71 (1987).

- [47] T. Ekström and M. Nygren, *Acta Chem. Scand.* **26**, p. 1836 (1972).
- [48] N. Yamazoe and L. Kihlberg, *Acta Cryst.* **B31**, p. 1666 (1975).
- [49] K.-H. Tytko and B. Schönfeld, *Z. Naturforsch.* **30B**, p. 471 (1975).
- [50] Gmelin, *Molybdenum Supplement Volume B3a*, Springer, Berlin (1987).
- [51] M. A. Vuurman, D. J. Stufkens, A. Oskam, G. Deo, and I. E. Wachs, *J. Chem. Soc. Faraday Trans.* **92**, p. 3259 (1996).
- [52] H. Schmalzried, *Chemical Kinetics in Solids*, VCH, Weinheim (1995).
- [53] P. L. Gai-Boyes, *Catal. Rev.-Sci. Eng.* **34**, p. 1 (1992).
- [54] P. L. Gai-Boyes, *J. Solid State Chem.* **104**, p. 119 (1993).
- [55] K. Eda, *J. Solid State Chem.* **95**, p. 34 (1991).
- [56] R. A. Hernandez and U. S. Ozkan, *Ind. Eng. Chem. Res.* **29**, p. 1454 (1990).
- [57] M. R. Smith and U. S. Ozkan, *J. Catal.* **141**, p. 124 (1993).
- [58] M. Abon, J. Massardier, B. Mingot, J. C. Volta, N. Floquet, and O. Bertrand, *J. Catal.* **134**, p. 542 (1992).
- [59] J. C. Volta, *J. Catal.* **93**, p. 467 (1985).
- [60] J. C. Vedrine, In R. K. Grasseli, S. T. Oyama, A. F. Gaffney, and J. E. Lyons, editors, *3<sup>rd</sup> World Congress on Oxidation Catalysis*, p. 61, Elsevier, Amsterdam (1997).
- [61] B. Mingot, N. Floquet, O. Bertrand, M. Treileux, J. J. Heizmann, J. Massadier, and M. Abon, *J. Catal.* **118**, p. 424 (1989).
- [62] J. C. Volta and B. Moraweck, *J. Chem. Soc. Chem. Commun.*, p. 338 (1980).
- [63] J. M. Tatibouet and J. E. Germain, *J. Catal.* **72**, p. 37 (1981).
- [64] J. M. Tatibouet, J. E. Germain, and J. C. Volta, *J. Catal.* **82**, p. 240 (1983).
- [65] M. Abon, B. Mingot, J. Massadier, and J. C. Volta, *Stud. Surf. Sci. Catal* **67**, p. 67 (1991).
- [66] G. Wu., B. Bartlett, and W. T. Tysoe, *Surf. Sci.* **383**, p. 57 (1997).
- [67] K. F. Andrew, F. A. Brassart, and E. A. Gulbransen, *J. Electrochem. Soc.* **110**, p. 242 (1963).
- [68] G. Mestl, N. F. D. Verbruggen, E. Bosch, and H. Knözinger, *Langmuir* **12**, p. 2961 (1996).
- [69] P. A. Spevack and N. S. McIntyre, *J. Phys. Chem.* **96**, p. 9029 (1992).
- [70] G. Mestl, P. Ruiz, B. Delmon, and H. Knözinger, *J. Phys. Chem.* **98**, p. 11269 (1994).
- [71] B. Stein, C. Weimer, and J. Gaube, In R. K. Grasseli, S. T. Oyama, A. F. Gaffney, and J. E. Lyons, editors, *3<sup>rd</sup> World Congress on Oxidation Catalysis*, p. 393, Elsevier, Amsterdam (1997).
- [72] A. Kuzmin, J. Purans, Ph. Parent, and H. Dexpert, *J. Phys. IV France* **7**, p. C2-891 (1997).

- [73] A. Magnéli, *Acta Chem. Scand.* **2**, p. 861 (1948).
- [74] T. Ressler, R. E. Jentoft, J. Wienold, M. M. Günter, and O. Timpe, *J. Phys. Chem. B* **104**, p. 6360 (2000).
- [75] L. Kihlborg, *Ark. Kemi* **21**, p. 357 (1963).
- [76] H. Seemann, *Kolloidzeitschrift* **107**, p. 190 (1942).
- [77] M. Łabanowska, *Phys. Chem. Chem. Phys.* **1**, p. 5385 (1999).
- [78] G. Mestl, N. F. D. Verbruggen, and H. Knözinger, *Langmuir* **11**, p. 3035 (1995).
- [79] G. Kortüm, *Reflektionspektroskopie*, Springer, Berlin (1969).
- [80] F. Delannay, editor, *Characterization of heterogeneous Catalysts*, Marcel Dekker, New York (1984).
- [81] R. B. Dzhanelidze, I. M. Purtseladze, L. S. Khitarishvili, R. I. Chikovani, and A. L. Shkolnik, *Phys. Solid State* **7**, p. 2082 (1966).
- [82] L. A. Bursill, *Proc. Roy. Soc. A* **311**, p. 267 (1969).
- [83] M. R. Tubbs, *Phys. Stat. Sol. A* **21**, p. 253 (1974).
- [84] O. Krylov, *Catalysis by Non-Metals*, Academic Press, New York (1980).
- [85] R. Erre, M. H. Legay, and J. J. Fropiat, *Surf. Sci.* **127**, p. 69 (1983).
- [86] J. B. Goodenough, In H. F. Barry and P. C. H. Mitchell, editors, *Proc. Climax 4<sup>th</sup> Int. Conf. on the Chemistry and Uses of Molybdenum*, p. 1, Climax Molybdenum, Ann Arbor, Michigan (1982).
- [87] L. G. J. Haart, A. J. de Vries, and G. Blasse, *J. Solid State Chem.* **59**, p. 291 (1985).
- [88] B. W. Faughnan, R. S. Crandall, and P. M. Heyman, *RCA Rev.* **36**, p. 177 (1968).
- [89] T. G. Souza-Cruz, A. Gorenstein, R. Landers, G. G. Kleiman, and S. C. deCastro, *J. Electron Spectr. and Rel. Phenom.* **101-103**, p. 397 (1997).
- [90] G. Blasse, G. J. Dirkesen, M. P. Crosnier-Lopez, and J. L. Fourquedt, *Solid State. Commun.* **90**, p. 595 (1994).
- [91] G. Hollinger, T. M. Duc, and A. Deneuve, *Phys. Rev. Lett.* **37**, p. 1564 (1976).
- [92] G. Mestl, N. F. D. Verbruggen, and H. Knözinger, *Langmuir* **11**, p. 1 (1995).
- [93] F. D. Hardcastle and I. E. Wachs, *J. Raman Spectros.* **21**, p. 83 (1990).
- [94] L. Seguin, M. Figlarz, R. Cavagnat, and J.-C. Lassgues, *Spectr. Acta* **A51**, p. 1323 (1999).
- [95] G. A. Nazri and C. Julien, *Solid State Ionics* **53**, p. 376 (1992).
- [96] L. A. Nafie, *Annu. Rev. Phys. Chem.* **48**, p. 357 (1997).
- [97] M. Yoshikawa, N. Nagai, M. Matsuki, H. Fukuda, G. Katagiri, H. Ishida, and A. Ishitani, *Phys. Rev.* **B46**, p. 7169 (1992).

- [98] J. B. Goodenough, *Prog. Solid. State Chem.* **5**, p. 145 (1971).
- [99] K. Hermann, M. Witko, and A. Michalak, *Catal. Today* **50**, p. 567 (1999).
- [100] J. S. Anderson, In L. Eyring and M. O'Keefe, editors, *The Chemistry of extended defects in Non-Stoichiometric Solids*, p. 1, North-Holland, Amsterdam (1970).
- [101] P. L. Gai, W. Thöni, and P. B. Hirsch, *J. Less Common Met.* **54**, p. 263 (1979).
- [102] L. C. Dufour, O. Bertrand, and N. Floquet, *Surf. Sci.* **147**, p. 396 (1984).
- [103] P. L. Gai-Boyes and R. J. Tilley, *Phil. Mag.* **43**, p. 1 (1983).
- [104] P. L. Gai and P. A. Labun, *J. Catal.* **94**, p. 79 (1985).
- [105] G. Mestl and H. Knözinger, *Langmuir* **14**, p. 3964 (1998).
- [106] B. Pispisa, *Z. Phys. Chem.* **76**, p. 1 (1971).
- [107] P. J. Gellings and H. J. M. Bouwmeester, *Catal. Today* **58**, p. 1 (2000).
- [108] T. R. Griffiths, D. A. Nerukh, and S. A. Eremenko, *Phys. Chem. Chem. Phys.* **1**, p. 3199 (1999).
- [109] Powder Cell 2.2 Software Federal Institut of Materials Research, Berlin (1995).
- [110] L. Kihlborg, *Ark. Kemi* **21**, p. 443 (1963).
- [111] R. Tokarz-Sobieraj, K. Hermann, M. Witko, A. Blume, G. Mestl, and R. Schlögl, *to be submitted to Surf. Sci.*
- [112] N. Sotani, K. Eda, M. Sadamatu, and S. Takagi, *Bull Soc. Chem. Jpn.* **62**, p. 903 (1989).
- [113] H.-L. Krauss and W. Huber, *Chem. Bericht* **94**, p. 2864 (1961).
- [114] E. Canadell and M.-H. Wangbo, *Chem. Rev.* **91**, p. 965 (1991).
- [115] R. Rousseau, E. Canadell, P. Alemany, D. H. Galvan, and R. Hoffmann, *Inorg. Chem.* **36**, p. 4627 (1997).
- [116] E. Iguchi and H. Miyagi, *J. Phys. Chem. Solids* **54**, p. 403 (1993).
- [117] D. Tinet, P. Canesson, H. Estrade, and J. J. Fripiat, *J. Phys. Chem. Solids* **41**, p. 583 (1979).
- [118] W. Meyer and H. Neddel, *Phys. Z.* **38**, p. 1014 (1937).
- [119] C.A. Catlow, In O.T. Sorensen, editor, *Nonstoichiometric Oxides*, Academic Press, (1981).
- [120] A. Magnéli, B. Blomberg-Hansen, L. Kihlborg, and G. Sundkvist, *Acta Chem. Scand.* **9**, p. 1382 (1955).
- [121] S. Barber, J. Booth, D. R. Pyke, R. Reid, and R. J. Tilley, *J. Catal.* **77**, p. 180 (1982).
- [122] L. Kihlborg and A. Magnéli, *Acta Chem. Scand.* **9**, p. 471 (1955).
- [123] J. S. Anderson, In M. W. Roberts and J. M. Thomas, editors, *Surface and Defect Properties of Solids* Volume 1, p. 1, Burlington House, London (1972).

- [124] L. Kihlborg, *Acta Chem. Scand.* **14**, p. 1612 (1960).
- [125] L. A. Bursill, *Acta Chem. Scand.* **A 28**, p. 187 (1972).
- [126] S. Himeno, H. Niiya, and T. Ueda, *Bull. Chem. Soc. Jpn.* **70**, p. 631 (1997).
- [127] W. P. Griffith, *J. Chem. Soc.(A)* , p. 286 (1970).
- [128] K. A. Olson and G. L. Schrader, In B. M. Clemens and W. L. Johnson, editors, *Thin Films Structures and Phase Stability* volume 187 , p. 167, Materials Research Society, Pittsburgh (1990).
- [129] L. Kihlborg, *Ark. Kemi* **21**, p. 471 (1963).
- [130] L. Kihlborg, *Adv. Chem.* **39**, p. 37 (1963).
- [131] I. E. Wachs and F. D. Hardcastle, *J. Raman Spectros.* **21**, p. 683 (1990).
- [132] A. A. Bolzan, B. J. Kenned, and C. J. Howard, *Austr. J. Chem.* **48**, p. 1473 (1995).
- [133] A. Magnéli, *Acta Chem. Scand.* **2**, p. 501 (1948).
- [134] T. Klotzbücher, M. Mergens, D. A. Wesner, and E. W. Kreutz, *Surf. Coat. Technol.* **100-101**, p. 388 (1998).
- [135] G. Mestl, *PHD thesis*, LMU München (1994).
- [136] J. S. Cross and G. L. Schrader, *Thin Solid Films* **259**, p. 5 (1995).
- [137] R. Böhlting, A. Drochner, M. Fehlings, D. König, and H. Vogel, *Chem. Ing. Techn.* **71**, p. 226 (1999).
- [138] Y. Tong and J. H. Lunsford, *J. Am. Chem. Soc.* **113**, p. 4741 (1991).
- [139] P. Mars and D. W. van Krevelen, *Chem. Eng. Sci. Special Suppl.* **1**, p. 41 (1954).
- [140] A. R. Adams and T. J. Jennings, *J. Catal.* **3**, p. 549 (1964).
- [141] A. B. Anderson, D. W. Ewing, Y. Kim, R. K. Grasselli, J. D. Burrington, and J. F. Brazdil, *J. Catal.* **96**, p. 222 (1985).
- [142] A.R. Adams and T.J. Jennings, *J. Catal.* **1964**, p. 549 (3).
- [143] G. Hägg and A. Magnéli, *Ark. Kemi* **19**, p. 1 (1944).
- [144] A. Magnéli, B. Blomberg, and L. Kihlborg, *Ana. Chem.* **24**, p. 1998 (1952).
- [145] L. Kihlborg, *Ark. Kemi* **21**, p. 365 (1963).
- [146] A. Magnéli, *Acta Crystall.* **6**, p. 495 (1953).
- [147] L. Kihlborg, *Acta Chem. Scand.* **17**, p. 1485 (1963).
- [148] L. Kihlborg, *Adv. Chem.*, p. 37 (1981).
- [149] L. Kihlborg, *Ark. Kemi* **21**, p. 427 (1963).
- [150] L. Kihlborg, *Ark. Kemi* **21**, p. 461 (1963).

- [151] S. Åsbrink and L. Kihlberg, *Acta Chem. Scand.* **18**, p. 1571 (1964).
- [152] P. F. Cornaz, J. H. C. van Hooff, F. J. Plujim, and G. C. A. Schuit, *Discuss. Faraday Soc.* **41**, p. 290 (1966).
- [153] L. A. Bursil, *Acta Crystall.* **A28**, p. 187 (1972).
- [154] N. N. Greenwood, *Ionic Crystals, Lattice Defects and Nonstoichiometry*, Butterworth, London (1968).
- [155] T. G. Kuznetsova, G. K. Boreskov, and T. V. Andrushkevich, *React. Kinet. Catal. Lett.* **12**, p. 531 (1979).
- [156] T. V. Andrushkevich, *Kinet. Catal.* **38**, p. 289 (1997).
- [157] T. V. Andrushkevich, L. M. Plyasova, , and T. G. Kuzetsova, *React. Kinet. Catal. Lett.* **12**, p. 463 (1979).
- [158] J. Tichy, J. Kusta, and J. Venkl, *Coll. Czechos. Chem. Commun.* **39**, p. 1797 (1974).
- [159] J. Tichy, J. Kusta, and J. Machek, *Coll. Czechos. Chem. Commun.* **47**, p. 698 (1982).
- [160] M. Ai, *Appl. Catal.* **27**, p. 167 (1986).
- [161] L. M. Plyasova, L. P. Solovéva, G. N. Kryukova, and T. V. Andrushkevich, *Rect. Kinet. Catal. Lett.* **31**, p. 1253.
- [162] T. V. Andrushkevich, V. M. Bondareva, G. Y. Popova, and L. M. Plyasova, In P. Ruiz and B. Delmon, editors, *New Developments in Selective Oxidation by Heterogeneous Catalysis* Volume 72, p. 91, Wiley-VCH, Weinheim (1992).
- [163] T.V. Andrushkevich, V.M. Bondareva, G.Y. Popova, and L.M. Plyasova, In P.Ruiz and B. Delmon, editors, *New Developments in Selective Oxidation by Heterogeneous Catalysis* Volume 72, p. 91, Wiley-VCH, Weinheim (1992).
- [164] S. Breiter, M. Estenfelder, H.-G. Lintz, A. Tenten, and H. Hibst, *Appl. Catal. A* **134**, p. 81 (1996).
- [165] M. Niwa, M. Mizutani, M. Takahashi, and Y. Murakami, *J. Catal.* **70**, p. 14 (1981).
- [166] F. Trifiro and I. Pasquon, *J. Catal.* **12**, p. 412 (1968).
- [167] F. Trifiro and I. Pasquon, *React. Kinet. Katal. Lett.* **15**, p. 389 (1980).
- [168] T. Wadayama, T. Saito, and W. Suetaka, *Appl. Surf. Sci.* **20**, p. 199 (1984).
- [169] J. S. Chung, R. Miranda, and C. O. Benett, *J. Catal.* **114**, p. 398 (1988).
- [170] H. Adkins and W.R. Peterson, *J. Amer. Chem. Soc.* **53**, p. 152 (1931).
- [171] E. Hums, *Catal. Today* **42**, p. 25 (1998).
- [172] K. DeBraekeleer and D.L. Massart, *Chemomet. Intell. Lab. Syst.* **39**, p. 127 (1997).
- [173] W. Windig, *Chemomet. Intell. Lab. Syst.* **36**, p. 3 (1997).
- [174] W. Windig and J. Guilment, *Anal. Chem.* **63**, p. 1425 (1991).
- [175] W. Windig, *Chemomet. Intell. Lab. Syst.* **23**, p. 71 (1994).

- [176] W. Windig, *Simplisma Manual*.
- [177] W. Windig and D. A. Stephenson, *Analy. Chem.* **64**, p. 2735 (1992).
- [178] M. Kraus, In G. Ertl, H. Knözinger, and J. Weitkamp, editors, *Handbook of Heterogeneous Catalysis* Volume V , p. 2129, Wiley-VCH, Weinheim (1997).
- [179] A. Blume, G. Mestl, and R. Schlögl, *to be published*.
- [180] B. G. Hyde and M. O'Keefe, *Acta Cryst. A* **29**, p. 243 (1969).
- [181] T. Ekström, *Acta Chem. Scand.* **26**, p. 3381 (1972).
- [182] R.C. Weast and M.J. Astle, editors, *Handbook of Chemistry and Physics*, CRC Press, Boca Raton 63<sup>rd</sup> edition (1984).
- [183] E. Ma, *Bull. Soc. Chem. Jpn.* **37**, p. 649 (1964).
- [184] K. Isa and H. Ishimura, *Bull. Soc. Chem. Jpn.* **54**, p. 328 (1981).
- [185] M. Dieterle and G. Mestl, *in preparation*.
- [186] T. Ilkenhans, B. Herzog, T. Braun, and R. Schlögl, *J. Catal.* **153**, p. 275 (1995).
- [187] H. Böhnke, J. C. Petzold, B. Stein, C. Weimer, and J. W. Gaube, In *Proc. of the DGMK Conference: Selective Oxidations in Petrochemistry* , p. 65 Hamburg (1998), DGMK.
- [188] M. Dieterle, G. Mestl, J. Jäger, Y. Uchida, and R. Schlögl, *J. Mol. Catal. A* *in press*.
- [189] A. J. Hegedüs, K. Sasvari, and J. Neugebauer, *Z. Anorg. allg. Chem.* **293**, p. 57 (1957).
- [190] E. Ma, *Bull. Chem. Soc. Jpn.* **37**, p. 171 (1964).
- [191] E. Ma, *Bull. Chem. Soc. Jpn.* **37**, p. 648 (1964).
- [192] F. Duval, *Inorganic Thermogravimetric Analysis*, Elsevier, Amsterdam (1953).
- [193] W.-D. Hunnius, *Z. Naturforsch.* **30b**, p. 63 (1975).
- [194] Z. M. Hanafi, M. A. Killa, and M. H. Askar, *Therm. Acta.* **45**, p. 221 (1981).
- [195] A. B. Kiss, P. Gads, I. Aszatalos, and A. J. Hegedüs, *Acta Chim. Acad. Sci. Hung.* **66**, p. 235 (1970).
- [196] K. Isa, *Chem. Soc. Jpn.* **54**, p. 3628 (1981).
- [197] J.-C. Valmalette and J.-R. Gavarri, *Eur. J. Solid State Inorg. Chem.* **32**, p. 71 (1995).
- [198] L. Dupont, D. Larcher, F. Portemer, and M. Figlarz, *J. Solid State Chem.* **121**, p. 339 (1996).
- [199] M. Dieterle, Ch. Bouchy, E. Derouane, and G. Mestl, *in preparation*.
- [200] N. Sotani and M. Hasegawa, *Polyhedron* **5**, p. 71 (1985).
- [201] N. Sotani, *Polyhedron* **5**, p. 67 (1986).

- [202] E. Eda, *J. Solid State Chem.* **83**, p. 292 (1989).
- [203] W. P. Griffith and P. J. B. Lesniak, *J. Chem. Soc. (A)*, p. 1066 (1969).
- [204] J. Fuchs, H. Hartl, W.-D. Hunnius, and S. Mahjour, *Angew. Chem.* **87**, p. 634 (1975).
- [205] J. Haber, In R. K. Grasseli, S. T. Oyama, A. F. Gaffney, and J. E. Lyons, editors, *3<sup>rd</sup> World Congress on Oxidation Catalysis*, p. 1, Elsevier, Amsterdam (1997).
- [206] O. V. Krylov, N. T. Tai, and B. V. Rozentuller, In R. K. Grasseli, S. T. Oyama, A. F. Gaffney, and J. E. Lyons, editors, *3<sup>rd</sup> World Congress on Oxidation Catalysis*, p. 275, Elsevier, Amsterdam (1997).
- [207] D. L. Stern and R. K. Grasselli, In R. K. Grasseli, S. T. Oyama, A. F. Gaffney, and J. E. Lyons, editors, *3<sup>rd</sup> World Congress on Oxidation Catalysis*, p. 357, Elsevier, Amsterdam (1997).
- [208] B. Stein, C. Weimer, and J. Gaube, In R. K. Grasseli, S. T. Oyama, A. F. Gaffney, and J. E. Lyons, editors, *3<sup>rd</sup> World Congress on Oxidation Catalysis*, p. 393, Elsevier, Amsterdam (1997).
- [209] H. Vogel, R. Böhling, and H. Hibst, *Catal. Lett.* **62**, p. 71 (1999).
- [210] B. Delmon, *HCR Adv. Edu. Rev.* **1**, p. 219 (1994).
- [211] N. Yamazoe, T. H. Ekström, and L. Kihlberg, *Acta Chem. Scand.* **A29**, p. 404 (1975).
- [212] R.C. Weast and M.J. Astle, editors, *Handbook of Chemistry and Physics*, CRC Press, Boca Raton 79<sup>th</sup> edition (1998).
- [213] H. Gruber, E. Krautz, H. P. Fritzer, K. Gatterer, and A. Popitsch, *Phys. Stat. Sol. (a)* **86**, p. 749 (1984).
- [214] H. T. Evans Jr., B. M. Gatehouse, and P. Leverett, *J. Chem. Soc. Dalton Trans.*, p. 505 (1975).
- [215] G. Tammann, *Z. Elektrochem.* **35**, p. 21 (1929).
- [216] R.C. Weast and M.J. Astle, editors, *Handbook of Chemistry and Physics*, CRC Press, Boca Raton 69<sup>th</sup> edition (1988).
- [217] I. E. Wachs, *Catal. Today* **27**, p. 437 (1996).
- [218] G. Mestl, M. P. Rosynek, and J. H. Lunsford, *J. Phys. Chem. B* **101**, p. 9321 (1997).
- [219] H. Zeilinger, *PhD thesis*, LMU München (1991).
- [220] E. Payen, M. C. Dhamelinourt, P. Dhamelinourt, J. Grimblot, and J. P. Bonnelle, *Appl. Spectr.* **36**, p. 30 (1982).
- [221] J. C. Volta, In T.S. Oyama and J. Hightower, editors, *Catalytic Selective Oxidation ACS Symp. Ser. 523*, Washington DC (1993).
- [222] I. E. Wachs, F. D. Hardcastle, and S. S. Chan, *Spectrosc.*, p. 1 (1986).
- [223] P. E. York, C. Pham-Huu, P. Del Gallo, and M. J. Ledoux, *Catal. Today* **35**, p. 51 (1997).
- [224] M. J. Ledoux, F. Meunier, B. Heinrich, C. Pham-Huu, M. E. Harlin, A. Ooutiand, and I. Krause, *Appl. Catal. A* **181**, p. 157 (1999).



- [225] T. Matsuda, T. Hirata, S. Sugo, H. Sakagami, and N. Takahashi, *Appl. Catal. A* **193**, p. 185 (2000).
- [226] M. A. Vuurman, I. E. Wachs, P. J. Stufkins, and A. Ozkan, *J. Mol. Catal.* **80**, p. 209 (1993).
- [227] P. G. Dickens, J. J. Birtill, and C. J. Wright, *J. Solid State Chem.* **28**, p. 185 (1979).
- [228] R. C. T. Slade, C. K. Halstead, and P. G. Dickens, *J. Solid State, Chem.* **34**, p. 1983 (1980).
- [229] Cl. Ritter, W. Müller-Warmuth, and R. Schöllhorn, *J. Chem. Phys.* **83**, p. 6130 (1985).
- [230] M. Łabanowska, *Phys. Chem. Chem. Phys.* **2**, p. 3307 (2000).
- [231] J. Haber and E. Lalik, *Catal. Today* **33**, p. 119 (1997).
- [232] R. L. McCormick and G. L. Schrader, *J. Catal.* **113**, p. 529 (1988).
- [233] A.A. Davydov, V. G. Mikhaltchenko, V. D. Sokolovskii, and G. K. Borekov, *J. Catal.* **55**, p. 299 (1978).
- [234] Y. Iwasawa, Y. Nakano, and S. Ogasawara, *J. Chem. Soc. Faraday. Trans I* **74**, p. 2968 (1978).
- [235] M. Fehlings, *PhD thesis*, TU Darmstadt (D17) (1997).
- [236] R. Böhnke, *PhD thesis*, TU Darmstadt (D17) (1997).
- [237] M. Estenfelder and H.-G. Lintz, *J. Catal.* **195**, p. 38 (2000).
- [238] A. Müller, J. Meyer, E. Krickemeyer, and E. Diemann, *Angew. Chem.* **108**, p. 1296 (1996).
- [239] O. Ovsitzer, G. Mestl, and R. Schlögl, *to be published*.
- [240] E. Gaigneaux, *PHD thesis*, Universite Catholique De Louvain (1997).
- [241] M., Abon, J. Massardier, B. Mingot, J. C. Volta, N. Floquet, and O. Bertrand, *J. Catal.* **134**, p. 542 (1992).
- [242] J. Petzold, *PhD thesis*, TU Darmstadt (D17) (1999).
- [243] G. S. Rohrer, W. Lu, L. Smith, and A. Hutchinson, *Surf. Sci.* **292**, p. 261 (1993).
- [244] R. L. Smith and G. S. Rohrer, *J. Catal.* **173**, p. 219 (1998).
- [245] J. Haber, In R. K. Grasseli, S. T. Oyama, A. F. Gaffney, and J. E. Lyons, editors, *3<sup>rd</sup> World Congress on Oxidation Catalysis*, p. 1, Elsevier, Amsterdam (1997).
- [246] J. Purans, A. Kuzmin, P. H. Parent, and H. Dexpert, *Physica B* **208/209**, p. 373 (1995).
- [247] E. Broclawik and J. Haber, *J. Catal.* **72**, p. 379 (1981).
- [248] T.V. Andrushkevich, V.M. Bondareva, G.Y. Popova, and L.M. Plyasova, *Stud. Surf. Sci. Catal.* **72**, p. 91 (1992).
- [249] J. J. Hastings and O. W. Howarth, *J. Chem. Soc. Dalton. Trans.*, p. 2891 (1995).
- [250] T. V. Andrushkevich T. Kuznetsova, L. Plyasova, *React. Kinet. Catal. Lett.* **20**, p. 303 (1982).
- [251] L.M. Plyazova, L.P. Solovyeva, and T.V. Andrushkevich, *Kinet. Catal.* **31**, p. 1430 (1990).

- [252] L.B. Levy and P.B. DeGroot, *J. Catal.* **76**, p. 385 (1982).
- [253] P.B. DeGroot and L.B. Levy, *J. Catal.* **76**, p. 393 (1982).
- [254] J.L. Callahan and R.K. Grasselli, *Am. Inst. Chem. Eng. J.* **9**, p. 755 (1963).
- [255] C. C. McCain, G. Gough, and G. W. Godin, *Nature* **4884**, p. 989 (1963).
- [256] A. Blume and G. Mestl, *unpublished results*.
- [257] BASF AG, *Offenlegungsschrift DE 4405514 A1*.
- [258] BASF AG, *Offenlegungsschrift DE 4405058 A1*.
- [259] BASF AG, *Offenlegungsschrift DE 4405060 A1*.
- [260] R. Böhling, A. Drochner, M. Fehlings, D. Knig, and H. Vogel, *Chem. Ing. Tech.* **71**, p. 3199 (1999).
- [261] J. Livage, *Catal. Today* **41**, p. 3 (1988).
- [262] R. Krabetz, W. Ferrmann, H. Engelbach, P. Palm, K. Sommer, and H. Spahn, *EP 17 000* , p. A1 (1980).
- [263] F. Gonzales-Vilchez and W. P. Griffith, *J.Chem. Soc. Dalton Trans.* **2**, p. 1416 (1972).
- [264] K.-H. Tytko, G. Petridis, and B. Schönfeld, *Z. Naturforsch.* **35b**, p. 45 (1980).
- [265] K.-H. Tytko and B. Schönfeld, *Z. Naturforsch.* **30b**, p. 471 (1975).
- [266] K. H. Tytko and J. Mehmke, *Z. anorg. allg. Chem.* **503**, p. 67 (1983).
- [267] K. H. Tytko, G. Baethe, E. R. Hirschfeld, K. Mehmke, and D. Stellhorn, *Z. Anorg. allg. Chem.* **503**, p. 43 (1983).
- [268] G. L. Schrader, M. S. Batista, and C. B. Bergman, *Chem. Eng. Commun.* **12**, p. 121 (1981).
- [269] L. C. W. Baker, In S. Kirschner, editor, *Advances in the Chemistry of Coordination Compounds* , p. 604, Macmillan, New York (1961).
- [270] A. Müller, J. Meyer, E. Krickemeyer, Ch. Beugholt, H. Boegge, F. Peters, M. Schmidtman, and M. J. Koop, *Chem. Eur. J.* **4**, p. 1000 (1998).
- [271] A. Müller, E. Krickemeyer, H. Bögge, M. Schmidtman, CH. Beugholt, P. Kögeler, and Ch. Lu, *Angew. Chem.* **110**, p. 1278 (1998).
- [272] A. Müller, E. Krickemeyer, H. Bögge, M. Schmidtman, and F. Peters, *Angew. Chem.* **100**, p. 3567 (1998).
- [273] A. Müller, E. Krickemeyer, H. Bögge, M. Schmidtman, Ch. Beugholt, S. K. Das, and F. Peters, *Chem. Eur. J.* **5**, p. 1496 (1999).
- [274] K. Schmidt and A. Müller, *Coord. Chem. Rev.* **14**, p. 115 (1974).
- [275] O. W. Howarth, L. Petterson, and I. Anderson, *J. Chem. Soc. Dalton. Trans.* , p. 1799 (1991).
- [276] J. J. Hastings and O. W. Howarth, *J. Chem. Soc. Dalton. Trans.* , p. 209 (1992).

- [277] O. W. Howarth, L. Petterson, and I. Anderson, *J. Chem. Soc. Dalton. Trans.* , p. 1061 (1994).
- [278] B. Krebs and I. Paulat-Böschén, *Acta. Cryst.* **B32**, p. 1697 (1976).
- [279] K.H. Tytko and O. Glemser, *Adv. Inorg. Chem. Radiochem.* **19**, p. 239 (1976).
- [280] C. Baes and R.E. Mesmer, In F.A. Cotton, editor, *The Hydrolysis of Cations*, p. 258. John Wiley and Sons, New York (1976).
- [281] J. Aveston, E. W. Anacker, and J. S. Johnson, *Inorg. Chem.* **5**, p. 735 (1964).
- [282] C. P. Cheng and G. L. Schrader, *J. Catal.* **60**, p. 276 (1979).
- [283] G. Johanson, L. Petterson, and N. Ingri, *Acta Chem. Scand.* **A 33**, p. 305 (1979).
- [284] S. S. Saleem and G. Aruldhas, *Pramana* **21**, p. 283 (1983).
- [285] K. H. Tytko, B. Schönfeld, V. Cordis, and O. Glemser, *Z. Naturforsch* **B30**, p. 471 (1975).
- [286] K.H. Tytko, B. Schönfeld, V. Cordis, and O. Glemser, *Z. Naturforsch.* **B30**, p. 834 (1975).
- [287] W. P. Griffith and T. D. Wickins, *J.Chem. Soc. A* , p. 675 (1967).
- [288] K. Y. Ng and E. Gulari, *Polyhedron* **3**, p. 1001 (1984).
- [289] D.L. Kepert, In F.A. Cotton, editor, *Prog.Inorg. Chem.* Volume 4 , p. 199. Wiley, New York (1962).
- [290] O. V. Krylov, N. T. Tai, and B. V. Rozentuller, In R. K. Grasseli, S. T. Oyama, A. F. Gaffney, and J. E. Lyons, editors, *3<sup>rd</sup> World Congress on Oxidation Catalysis* , p. 275, Elsevier, Amsterdam (1997).
- [291] M. A. Vuurman and I.E. Wachs, *J. Phys. Chem.* **96**, p. 5008 (1992).
- [292] K. H. Tytko and O. Glemser, *Z. Naturforsch.* **26B**, p. 659 (1971).
- [293] I. Böschén, B. Buss, and B. Krebs, *Acta. Cryst.* **B30**, p. 48 (1974).
- [294] H. T. Evans Jr., *Inorg. Chem.* **5**, p. 967 (1966).
- [295] K. H. Tytko, B. Schönfeld, B. Buss, and O. Glemser, *Angew. Chem.* **85**, p. 305 (1973).
- [296] W. P. Griffith and T. D. Wickins, *J.Chem. Soc. A* , p. 400 (1968).
- [297] O. Timpe, *personal communication*.

# Publications

1. Ch. Schalley, M. Dieterle, D. Schröder, H. Schwarz and E. Uggerud, **On the Cleavage of the Peroxide O-O-Bond in Methylhydroperoxide and Dimethylhydroperoxide upon Protonation**, *Int. J. Mass Spectr. Ion Proc.*, **1997**, 169, 101.
2. M. Dieterle, J. N. Harvey, Ch. Heinemann, J. Schwarz, D. Schröder and H. Schwarz, **Equilibrium Studies of Weakly Bound  $\text{Fe(L)}^+$  Complexes with  $\text{L} = \text{Xe}$ ,  $\text{CO}_2$ ,  $\text{N}_2$  and  $\text{CH}_4$** , *Phys. Chem. Lett.*, **1997**, 277, 399.
3. G. Hornung, Ch. Schalley, M. Dieterle, D. Schröder and H. Schwarz, **Gas Phase Reactivity of Alkoxy Radicals as Studied by Mass Spectrometry:  $\alpha$ -Cleavages and Barton-type Hydrogen Migration**, *Chem. Eur. J.*, **1997**, 3, 1865.
4. E. M. Gaigneaux, M. Dieterle, P. Ruiz, G. Mestl, B. Delmon, **Catalytic Performances and Stability of Three Sb-Mo-O Phases in the Selective Oxidation of Isobutene to Methacrolein**, *J. Phys. Chem. B*, **1998**, 102, 10542.
5. T. Ressler, O. Timpe, T. Neisius, J. Find, G. Mestl, M. Dieterle, and R. Schlögl, **Time-Resolved XAS Investigation of the Reduction/Oxidation of  $\text{MoO}_{3-x}$** , *J. Catal.* **2000**, 191, 75.
6. G. Mestl, Ch. Linsmeier, R. Gottschall, M. Dieterle, J. Find, D. Herein, J. Jäger, Y. Uchida and R. Schlögl, **Molybdenum Oxide based Partial Oxidation Catalysts: 1. Thermally induced Deficiency, Element and Structural Heterogeneity and the Relation to catalytic Performance**, *J. Mol. Catal. A.*, **2000**, 162, 455.
7. M. Dieterle, G. Mestl, J. Jäger, Y. Uchida, H. Hibst and R. Schlögl, **Mixed molybdenum oxide based partial oxidation catalyst: 2. Combined X-ray Diffraction, Electron Microscopy and Raman Investigation of the thermal Stability of  $(\text{MoVW})_5\text{O}_{14}$ -type Oxides**, submitted, *J. Mol. Catal. A.*.
8. G. Mestl, T. Ilkenhans, D. Spielbauer, M. Dieterle, O. Timpe, J. Kröhnert, F.C. Jentoft, H. Knözinger and R. Schlögl, **Thermally and Chemically induced structural Transformations of Keggin-type Heteropoly acid catalysts**, in press, *Appl. Catal. A*.
9. M. Dieterle, G. Weinberg, G. Mestl, **Raman spectroscopy of molybdenum oxides (Part I): Structural Characterisation of oxygen defects in  $\text{MoO}_{3-x}$  by DRUV/VIS-, Raman Spectroscopy and X-ray Diffraction**, submitted to *Phys. Chem. Chem. Phys.*.

10. M. Dieterle and G. Mestl, **Raman spectroscopy of molybdenum oxides (Part II): Resonance Raman spectroscopic characterisation of the molybdenum oxides  $\text{Mo}_4\text{O}_{11}$  and  $\text{MoO}_2$** , submitted to *Phys. Chem. Chem. Phys.*.
11. E. Sanchez-Cortezon, M. Dieterle, M. Schur, G. Mestl and R. Schlögl, **On the positive Correlation of the D and D' bands in the first-order Raman Spectrum of Graphite with the XRD Coherence Length in [110]- and [110]- crystallographic Direction**, submitted to *Carbon*.
12. Sanchez-Cortezon, E., M. Dieterle, M. Schur, G. Mestl and R. Schlögl, **NO Effect in the Partial Oxidation of Methanol to Formaldehyde over Graphite Catalysts. The Role of Homogeneous Gas Phase Reactions**, submitted to *Appl. Catal. A*.
13. M. Dieterle, G. Mestl, R. Schlögl, ***In situ* Raman Studies on Mixed Metal-Oxygen-Clusters (Mo, V, W) and Carboxylates in Aqueous Solution**, in preparation.
14. M. Dieterle, G. Mestl, R. Schlögl, **Thermal Activation of V and W promoted Molybdenum Polyoxometalates**, in preparation.
15. M. Dieterle, G. Mestl, R. Schlögl, ***In situ* Raman Spectroscopy Studies Combined with Temperature Programmed Reaction Spectroscopy of V and W Promoted Molybdenum Oxide Catalysts**, in preparation.

# Curriculum Vitae

## LEBENS LAUF

**Martin Dieterle**

Geburtsdatum	6.10.1968	in Alpirsbach
Promotion	9/1997- 2/2001	am Fritz-Haber-Institut (Berlin) in der Abteilung von Prof. Schlögl
Studium	1997	Diplom (Diplomarbeit im AK Schwarz)
	1991 - 1997	Grundstudium Chemie an der TU-Berlin
	1994 - 1995	Universität Nanjing, VR China
	1996 - 1997	Hauptstudium Chemie an der TU-Berlin
Zivildienst	1988 - 1990	Lebenshilfe Heidelberg
Schule	1979 - 1988	Gymnasium Hausach
	1975 - 1979	Grundschule Wolfach